

Measurements of sea ice by satellite and airborne altimetry

Kildegaard Rose, Stine; Forsberg, René; Toudal Pedersen, Leif

Publication date:
2013

Document Version
Publisher's PDF, also known as Version of record

[Link back to DTU Orbit](#)

Citation (APA):
Kildegaard Rose, S., Forsberg, R., & Toudal Pedersen, L. (2013). Measurements of sea ice by satellite and airborne altimetry. Kgs. Lyngby: DTU Space.

DTU Library

Technical Information Center of Denmark

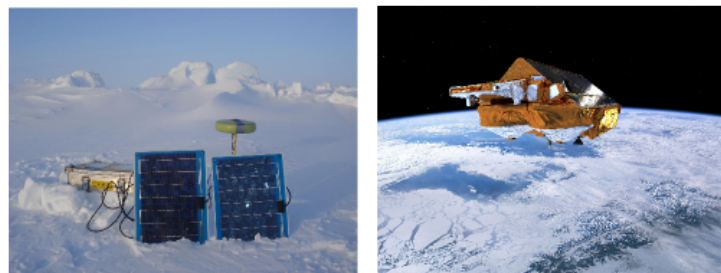
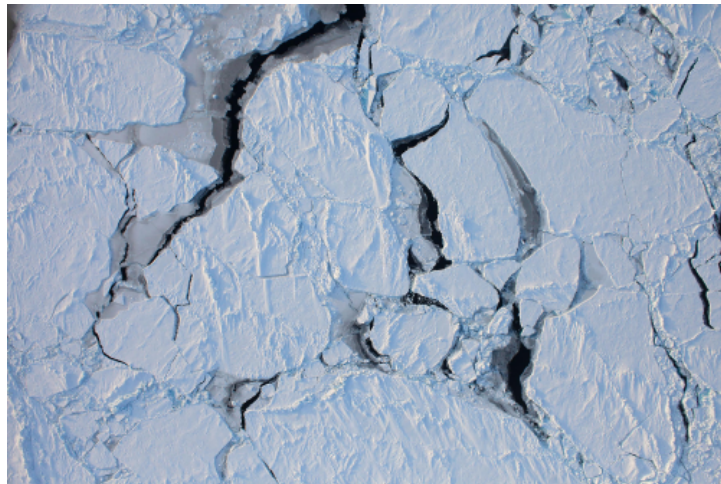
General rights

Copyright and moral rights for the publications made accessible in the public portal are retained by the authors and/or other copyright owners and it is a condition of accessing publications that users recognise and abide by the legal requirements associated with these rights.

- Users may download and print one copy of any publication from the public portal for the purpose of private study or research.
- You may not further distribute the material or use it for any profit-making activity or commercial gain
- You may freely distribute the URL identifying the publication in the public portal

If you believe that this document breaches copyright please contact us providing details, and we will remove access to the work immediately and investigate your claim.

Measurements of sea ice by satellite and airborne altimetry



STINE KILDEGAARD ROSE
DTU Space, National Space Institute

SUPERVISORS:
René Forsberg, DTU Space
Leif Toudal Pedersen, DMI

Measurements of sea ice by satellite and airborne altimetry

Stine Kildegaard Rose
DTU Space - National Space Institute
Ph.D. Thesis, Kgs. Lyngby,

Financed by National Space Institute, Technical University of Denmark and The Danish Council for Independent Research, Natural Sciences (FNU) from the international polar year.

Supervised by:
René Forsberg, DTU Space - National Space Institute, Technical University of Denmark
Leif Toudal Pedersen, Danish Meteorological Institute.

<http://www.space.dtu.dk>

Title page fotos:

Top: Leads in between sea ice. Credit: NASA Earth Observatory

Bottom left: GPS site on the sea ice north from Greenland. Credit: Jørgen Skaffe, Århus University.

Bottom right: CryoSat-2 illustration. Credit: ESA.

Dansk Resumé

Havisen har en stor indflydelse på klimaet, og når det globale klima forandres, er havisen den første indikator på at noget er i forandring. Variationer af havisdækket er blevet observeret fra satellit siden 1979, og siden dengang er der kun observeret en tilbagetrækning af isens udbredelse. Massebalancen af havisen er en vigtig faktor i klimamodeller, hvor istykkelsen er den mest usikre parameter.

CryoSat-2, der er en radar altimetri satellit, har målt over det Arktiske Ocean siden 2010, men der er stadig usikkerheder i nøjagtigheden af dens højdebestemmelser. I dette studie er data fra CryoSat-2 blevet anvendt, og en algoritme til at udlede overfladehøjder fra satellitten er udviklet. Den viser gode resultater for hele havisdækket.

For at validere satellitmålingerne er en sammenlignende analyse præsenteret, hvor flybåren data fra DTU Space/ESA og NASA er udnyttet i to områder i det Arktiske Ocean. I det første område fra Lincoln-havet forventes forekomsten af flerårs is. I det andet område nord for Svalbard forventes mere blandede isforhold men hovedsageligt førsteårs is. Da havisen driver i tid, og målingerne ikke er foretaget på præcis samme tid, er der beregnet en havis drift korrektion mellem de forskellige datasæt, hvilket resulterede i en bedre korrelationen mellem data. De luftbårne datasæt består af laser scanner målinger, hvor laserstrålen reflekteres fra sneoverfladen, hvor satellitten måler med en radar, der teoretisk set reflekteres fra sne/is grænsen. Havis fribordet (højden af isen over havoverfladen) er i første område beregnet til 55 cm for de luftbårne datasæt, og 25 cm for satellitten. Dette giver en snedybde på 30 cm, hvilket stemmer overens med den forventede snedybde i området. I det andet området er havis fribordet beregnet til 35 cm, hvilket svarer til fribordet for den luftbårne måling. Det indikerer at radar signalet fra CryoSat her bliver reflekteret fra sneoverfladen, højst sandsynligt pga. vejrforhold.

Pga. isens dynamik, opstår der sprækker med åbent vand mellem isflagerne. Disse sprækker er meget vigtige i bestemmelsen af havis fribordet, da de udgør det lokale havniveau, dvs. reference rammen. I dette studie er sprækkerne med åbent vand detekteret fra CryoSat, og herfra er havniveauet bestemt. I et selvstændigt studie af GPS bøjler placeret på havisen nord for Grønland, er havniveauet bestemt ud fra kendskab til forskellige geofysiske korrektioner. Desuden er tidevands højden bestemt og sammenlignet med en tidevands model AOTIM-5. Studiet viser, at tidevands modellen giver gode resultater i det åbne Arktiske Ocean, men har problemer tæt ved kysten og i fjordsystemer.

De grønlandske fjorde regulerer udvekslingen af ferskvand fra gletsjerne i fjorden til det åbne hav. Målinger med luftbåren laser altimetri er foretaget i foråret foran hovedgletsjeren Kangeriata Nunata Sermia i sydvest Grønland. Det giver et øjebliksbillede af den is, der er frosset fast foran gletsjerne siden sidste efterår. Det totale volumen er blevet fundet til 1.70 ± 1.26 GT is, hvilket svarer til 38% af den årlige isflux fra gletsjerne.

Som en del af et foreløbigt studie er distributionen af havis fribordet og tykkelsen for hele Arktis bestemt ud fra CryoSat datasættet for hhv. efterår og forår for perioden 2010 til 2013. Årstidsvariationer er observeret; med mindre isudbredelse i efteråret efter en hel sommers smelteperiode, hvor havisen opbygges på ny hen over vinteren, og det kan ses ved større udbredelse og tykkere is. Der er i perioden observeret udtynding af havis fribordet på 1.5 cm/år. Konverteringen fra fribord til istykkelse bygger på antagelsen om isostatisk ligevægt og er associeret med mange usikkerheder, der blandt andet stammer fra varierende densiteter og snedybder. I dette studie er to metoder testet. Resultaterne viser at tykkelsen af havisen udtyndes mellem -8.1 og -11.6 cm/år om efteråret, hvor det om foråret udtyndes mellem -15.7 og -16.9 cm/år.

Abstract

A changing sea ice cover in the Arctic Ocean is an early indicator of a climate in transition, the sea ice has in addition a large impact on the climate. The annual and interannual variations of the sea ice cover have been observed by satellites since the start of the satellite era in 1979, and it has been in retreat every since. The mass balance of the sea ice is an important input to climate models, where the ice thickness is the most uncertain parameter.

In this study, data from the CryoSat-2 radar altimeter satellite are used. CryoSat-2 has been measuring the sea ice in the Arctic Ocean since 2010, but there remain uncertainties in the accuracy of its elevation retrieval. A threshold retracker is developed to derive surface elevations and shows good results over the sea ice cover.

To validate the satellite measurements, a comparative assessment of sea ice freeboard is presented, where airborne laser altimeter data from DTU Space together with data from the European Space Agency's (ESA) CryoSat Calibration and Validation Experiment (CryoVEx) and the National Aeronautics and Space Administration's (NASA) Operation IceBridge (OIB) are used over a first and multi-year ice area. Comparing the modal freeboard heights of 55 cm retrieved from the laser scanner data with the 25 cm retrieved from CryoSat-2 indicates a snow layer of 30 cm, due to the theory that a laser is reflected at the air/snow interface, while the radar is reflected at the snow/ice interface. In the other area, the modal freeboard is found to be 35 cm for both the airborne and satellite data implying, that the radar signal is here reflected from the snow surface, probably due to weather conditions. CryoSat-2 is very sensitive to returns from specular surfaces, even if they appear off-nadir. This contaminates the "true" signal resulting in off-ranging elevations. Filtering out these off-ranging elevations are succeeded and results in more than 60% rejection of CryoSat observations. The correlation between the radar satellite and airborne laser measurements is improved after a drift correction is applied, and at an acceptable level ($r=0.604$), but more knowledge of the datasets are needed to improve this correlation.

Leads are used to form the local sea surface height, and are crucial in the freeboard retrieval. Leads are detected from the CryoSat data by looking at the waveforms. In an independent study, the sea surface height is obtained by using Global Positioning System (GPS) measurements and geophysical parameter corrections on the sea ice north of Greenland. In the same study the ocean tides are examined and show, that the ocean tide model AOTIM-5 works good in the Arctic Ocean, but less good in costal areas and in fjord systems.

The Greenland fjords exchange freshwater between the glaciers and the ocean. Measuring a snapshot of the ice mélange in front of Kangeriata Nunâ Sermia in southwest Greenland with airborne LiDAR, gives an estimate of the ice discharge since last autumn. The total volume of 1.70 ± 1.26 GT ice in the inner fjord is found, which is 38% of the yearly ice flux.

In a preliminary study, the freeboard and ice thickness distribution over the entire Arctic Ocean are computed for the CryoSat record for autumn and fall, respectively in the period from 2010 to 2013. Annual and interannual variations are observed and a mean freeboard thinning of 1.5 cm/year is found. For the ice thickness determination, two methods are tested using climatology snow depths or an empirical relationship for the ice thickness distribution. The autumn mean thickness trend varies between -8.1 to -11.6 cm/year between the two methods, and -15.7 to -16.9 cm/year for the spring trends.

Preface

This thesis is submitted in fulfilment of the requirements for obtaining a Ph.D. degree at DTU Space - National Space Institute. The research presented is carried out at the Division of Geodynamics under supervision of State geodesist and head of department René Forsberg at DTU Space and senior scientist at the Danish Meteorological Institute Leif Toudal Pedersen. I started the Ph.D January 1, 2010 and have had nine months of maternity leave.

The title “Measurements of sea ice by satellite and airborne altimetry” cover measurements on the sea ice by GPS, of sea ice freebord, and glacial ice freeboard by radar satellite and laser airborne altimetry. In the beginning of the study, prior to the launch of CryoSat-2, I worked with several GPS studies, especially focusing towards advancing in processing GPS in the Arctic. One of the studies is presented in [Rose et al. \[2013c\]](#) and at a conference as a poster. When CryoSat-2 finally was launched in April, 2010 it took eight months before the first data were released to the community. DTU Space was part of CryoVEx, getting the opportunity to look at the data in the commissioning phase. I have presented two posters, and one proceedings paper [[Rose et al., 2011](#)] based on the first releases. During this time I mainly studied CryoSat-2 in depth, but worked on the side with processing of laser altimetry data over a Greenland fjord containg both sea ice and icebergs [[Rose et al., 2013d](#)]. The current CryoSat-2 processing version was released in February, 2012. With this release one poster, one proceedings paper [[Rose et al., 2013a](#)], and one journal paper [[Rose et al., 2013b](#)] are presented.

This study is based on CryoSat-2 Level 1B (L1B) and Level 2 (L2) data, and the three data versions from the commissioning phase, baseline A to the latest Baseline B. [Rose et al. \[2011\]](#) show results from Baseline A and results from L2 data are shown in [Rose et al. \[2013a\]](#). The results based on Baseline A and L2 data are not presented in the thesis, because they are either outdated or not yet usable for sea ice research.

As part of the Ph.D. program I had the opportunity to stay two weeks in Barcelona at Institute for Space Science, National Research Council (CSIC) visiting Pedro Elosegui. During the stay I learned about TRACK and GPS processing. Furthermore, I stayed three months at NOAA, Silver Spring, MD, USA, where I got a first hand knowledge of the airborne topographic mapper (ATM) from Operation IceBridge, and further knowlegde of CryoSat’s SAR altimeter. This stay was partly granted by: Mærsk, Knud Højgaard, Otto Mønsted and Oticon.

Acknowledgments

I am deeply grateful to all the people who have been involved in the process, both my family and colleagues. I am indebted to thank my supervisors for letting me have this opportunity, I especially enjoyed our joint meetings. I will give my deepest thanks to Henriette Skourup for the everyday support and guidance. I would like to thank Pedro Elosegui and Julia de Juan Verger at CSIC for their hospitality. Furthermore, I am grateful to Laurence Connor, Laury Miller, Sinead Farrell, Walter Smith, Thomas Newman, Eric Leuliette and colleagues for the wonderful stay at NOAA and their extraordinary hospitality and help to me and my family.

I acknowledge: NSIDC for distributing Operation IceBridge data, ESA for providing and processing CryoSat-2 data and ASAR images, NASA for MODIS images, the IceBridge Arctic and CryoVEx 2012 teams.

*Stine Kildegaard Rose
Kgs. Lyngby, September 2013.*

Contents

Contents	ix
List of Figures	xiii
List of Tables	xvii
1 Introduction	1
1.1 Scientific Objectives	2
1.2 Structure of the Thesis	2
2 Scientific Papers	5
3 The State of the Arctic Sea Ice	9
3.1 The Arctic Sea Ice Cover	10
3.1.1 Dynamic Forcing	10
3.2 The Arctic Sea Ice Extent	12
3.2.1 Interannual Variation	13
3.3 Thickness Distribution and Measurements	15
3.4 Sea Ice in a Climate Perspective	17
4 The Principles of GPS	19
4.1 The Concept of GPS	19
4.1.1 The Signals	20
4.1.2 GPS Receivers and Estimation of Position	21
4.1.3 Measurements	21
4.2 GPS Errors	21
4.2.1 Signal Propagation Errors	21
4.2.2 Impact of Geometry	22
4.2.3 Measurement Errors	23
4.2.4 Combining Measurements	23
4.3 Augmentations	23
4.3.1 Differential GPS	24
4.3.2 Precise Point Positioning	25

4.4	Processing Software	25
4.5	GPS in the Arctic	25
5	Description of Data	29
5.1	Airborne Campaigns	29
5.1.1	CryoVEx	29
5.1.2	Operation IceBridge	30
5.2	Satellite Imagery	31
5.2.1	Advanced Synthetic Aperture Radar	31
5.2.2	Moderate-Resolution Imaging Spectroradiometer	31
5.3	Sea Ice Data	32
5.3.1	Ice Edge and Ice Type Data	32
6	Satellite Altimetry	33
6.1	Satellite Altimeter Missions	33
6.1.1	CryoSat	33
6.2	Basic Principle of Radar Altimetry	35
6.2.1	The reflected signal - Waveforms	36
6.2.2	Pulse and Beam Limited Altimeters	38
6.2.3	SAR Altimeter Principles	40
6.3	Retracking	40
6.3.1	Threshold Retracker	43
6.3.2	Typical Errors over Sea Ice	43
7	Geophysical Parameter Corrections	45
7.1	Atmosphere	45
7.1.1	Tropospheric Correction	45
7.1.2	Ionospheric Correction	46
7.1.3	Inverse Barometric Correction	46
7.2	Tides	46
7.2.1	Ocean Tide	47
7.2.2	Long-Period Equilibrium Tide	47
7.2.3	Ocean Loading Tide	47
7.2.4	Solid Earth Tide	47
7.2.5	Geocentric Polar Tide	47
7.2.6	Permanent Tides	48
7.3	Geoid	49
7.4	Dynamic Topography	50
8	Sea Ice Measurements by Satellite Radar Altimetry	53
8.1	Sea Ice Measurements	53
8.1.1	Freeboard Determination	54
8.1.2	Freeboard to Ice Thickness	55
8.1.3	Error Sources in thickness Retrieval	57

9 CryoSat Data Development	61
9.1 Access and Read Data	61
9.2 Threshold Retracker Development	62
9.3 Retracker Performance	64
9.3.1 The Residual SSH	64
9.3.2 Beam Behavior	66
10 Evaluating CryoSat Observations - A Comparative Assessment	69
10.1 Comparing ALS and ATM Elevations	70
10.2 Averaging Airborne Data to CryoSat Data Sampling	71
10.3 Lead Detection	73
10.4 Sea Ice Drift	77
10.5 Analyzing CryoSat Observations	78
10.6 Dealing with the Off-ranging Elevations	89
10.6.1 First Attempt: Peak Power Search Routine	89
10.6.2 Second Attempt: Pulse Peakiness Criteria	90
10.6.3 Further Discussion and Enhancements	94
11 Sea Ice Maps from CryoSat	97
11.1 Pre-mapping	97
11.1.1 Filtering Data	98
11.1.2 Gridding	99
11.2 Sea Surface Height and Dynamic Topography	100
11.2.1 Validation	100
11.3 Sea Ice Freeboard Distribution	104
11.3.1 Sea Ice Freeboard Heights	106
11.4 Sea Ice Thickness Distribution	108
11.4.1 Sea Ice Thickness	109
11.5 Sea Ice Trends	113
11.5.1 Annual Freeboard Trends	113
11.5.2 Annual Thickness Trends	114
11.5.3 Interannual Variation	116
11.6 Further Discussions and Enhancements	118
12 Conclusion	121
12.1 Future Work	122
Bibliography	125
Appendices	139
A Snow Depths from Warren's Climatology	139
B Statistics	143
B.1 Standard Deviation of the Mean	143
B.2 A Skew Distribution	143
B.3 Uncertainty in the Slope	143

C	Averaging Airborne Data	145
C.1	Scatter Plots	145
D	CryoSat Elevation Analysis	149
D.1	Ice Drift	149
D.2	CryoSat Elevations over Leads	150
E	Sea Ice Map from CryoSat	155
E.1	Retracking Gate	155
E.2	Number of Points in Grid	155
E.3	Ice Conditions	158
E.4	Ice Edge Detection Maps	159
E.5	Ice Type Detection Maps	160
F	Scientific Papers	163
F.1	Initial Results of CryoSat-2 Data from the Arctic	163
F.2	Arctic Tides from GPS on sea ice	168
F.3	Comparative Analysis of Sea Ice Freeboard	178
F.4	Sea Ice Freeboard in Multi-year and First-year Ice Areas	183
F.5	Ice mélange volume estimates from LiDAR	199
G	Posters	207

List of Figures

3.0.1	The International Bathymetric Chart of the Arctic Ocean	9
3.1.1	Circulation patterns in the Arctic Ocean	11
3.2.1	Average monthly sea ice extent	13
3.2.2	Sea ice extent September 2012 and March 2013	13
3.2.3	Monthly sea ice extent for 1981-2000	14
3.3.1	Sea ice age	16
3.4.1	Linking the processes of climate forcing.	18
4.1.1	The three GPS segments.	20
4.3.1	The GPS concept	24
4.5.1	GPS processing statistics	27
6.1.1	Illustration of CryoSat	34
6.2.1	Corrections on altimeter range measurements and the relation between heights	36
6.2.2	Idealized waveform with descriptions	37
6.2.3	SAR waveforms over various surfaces	38
6.2.4	Beam-limited altimeter footprint	39
6.2.5	Principles of conventional and SAR altimeter	41
7.2.1	Illustration of the permanent tide concepts of the crust and the geoids	49
8.1.1	Schematic picture of sea ice.	54
8.1.2	The first published sea ice map from CryoSat data	58
9.2.1	SAR waveform with a bump in the leading edge.	63
9.3.1	Residual SSH from different retrackers.	65
10.0.1	ASAR image with CryoSat power overlayed	69
10.1.1	Scatter plot of ALS and ATM elevations	70
10.2.1	Comparing methods for averaging airborne altimeter data	73
10.3.1	Surface identification in CryoSat L2 data.	74
10.3.2	Beam parameters	76
10.3.3	The relationship between the stack standard deviation and the pulse peakiness.	77

10.5.1	Elevations and surface description	78
10.5.2	CryoSat elevations overlayed DMS images showing a lead	79
10.5.3	CryoSat waveforms corresponding to the elevations in Fig. 10.5.2	80
10.5.4	CryoSat elevation in rough surface area	82
10.5.5	Zoom of ASAR image showing leads off-nadir.	83
10.5.6	Waveforms corresponding to the elevations in Fig. 10.5.5	84
10.5.7	MODIS image with CryoSat elevations	86
10.5.8	Ranging offset as a function of the distance from nadir.	87
10.5.9	Snagging in CryoSat data	88
10.6.1	Detecting off-ranging elevations in the CryoSat data	89
10.6.2	Freeboard distribution of CryoSat data from the second study area	90
10.6.4	Freeboard distribution of CryoSat data from the first study area	92
10.6.5	Probability distribution of snow depth from OIB.	93
10.6.6	SSH and freeboard distribution from study area 2.	94
11.1.1	Probability Distribution of retracking gate	98
11.1.2	Number of measurements in grid cells distributed over the Arctic Ocean.	99
11.2.1	The dynamic topography based on leads from CryoSat.	101
11.2.2	Arctic Oscillation Index for January 2010 to July 2013	102
11.2.3	The residual sea surface height.	103
11.2.4	Residual SSH probability distribution.	104
11.3.1	Probability distribution comparing grid size and filter.	105
11.3.2	Freeboard distributions from CryoSat	107
11.3.3	Freeboard frequency distributions over the whole Arctic Ocean	108
11.4.1	Thickness distributions from CryoSat, WAT method	110
11.4.2	Thickness distributions from CryoSat, ALT method	111
11.4.3	Thickness probability distributions from CryoSat	112
11.5.1	Mean sea ice freeboard trends	113
11.5.2	Sea ice thickness trends.	115
11.5.3	Arctic sea ice thickness from PIOMAS	116
11.5.4	PIMOAS thickness difference between 2013-2012	119
A.0.1	Coordinate system with astronomical triangles.	140
A.0.2	Snow depth from Warrens climatology, Sep-Dec	141
A.0.3	Snow depth from Warrens climatology Jan-Apr	142
C.1.1	Scatter plots of ATM versus CryoSat, no interpolation.	145
C.1.2	Scatter plots of ATM versus CryoSat, surface gridding	146
C.1.3	Scatter plots of ATM versus CryoSat, nearest neighbor gridding	147
D.1.1	Ice drift	149
D.1.2	CryoSat drift based on ASAR drift vectors.	150
E.1.1	Map of the retracking gate in the Arctic Ocean	155
E.2.1	Number of points in each lead grid cell.	156
E.2.2	Number of total points in each grid cell.	157
E.3.1	Drift pattern in the Arctic Ocean from March 2013	158

E.3.2	Average sea ice extent for November.	158
E.4.1	Sea ice edge from OSI SAF.	159
E.5.1	Sea ice type from OSI SAF.	160
E.5.2	Ice type detection.	161

List of Tables

6.1.1	CryoSat facts	35
7.4.1	Geophysical corrections to the range	51
8.1.1	Typical snow depths and snow and ice densities	57
10.2.1	Correlation between averaged airborne and satellite data	72
10.3.1	Lead and ice floe detection parameters	75
10.6.1	Freeboard statistics after filtering.	92
11.1.1	Filtering statistics of monthly CryoSat data	99
11.2.1	Statistics for residual SSH	102
11.3.1	Sensitivity of grid and filter choice	105
11.3.2	Freeboard statistics from CryoSat derived elevations.	108
11.4.1	Sea ice thickness statistics from CryoSat derived elevations.	109
11.5.1	Sea ice freeboard trends.	114
11.5.2	Sea Ice thickness trends.	115

Nomenclature

AGC	Automatic Gain Control	43
ALS	Airborne Laser Scanner used in CryoVEx campaigns	30
ALT	Ice thickness with Alexandrov's empirical relationships	109
AO	Arctic Oscillation	11
ASAR	Advanced Synthetic Aperture Radar, instrument on the Envisat satellite	31
ASIRAS	Airborne Synthetic Aperture and Interferometric Radar Altimeter System	94
ATM	The Airborne Topographic Mapper	30
CryoVEx	CryoSat Calibration and Validation Experiment	1
DGPS	Differential GPS	24
DMI	Danish Meteorological Institute	12
DMS	Digital Mapping System camera on-board IceBridge flights	31
DOP	Dilution of Precision	22
DORIS	Doppler Orbit and Radio positioning Integration by Satellite	36
DT	Dynamic Topography	50
ECMRWF	European Centre for Medium-range Weather Forecasts	45
EM	Electromagnetic	15
ESA	European Space Agency	1
GBAS	Ground-Based Augmentation Systems	23
GIM	Global Ionospheric Model	46
GNSS	Global Navigation Satellite System	19

GPS	Global Positioning System	2
ICESat	Ice, Cloud, and land Elevation Satellite (NASA)	33
IFREMER	French Institute for Exploration of the Sea	158
IGS	International GNSS Service	22
LMS	Least Median of Squares or the estimated mode	65
LRM	Low Resolution Mode	34
MODIS	Moderate-Resolution Imaging Spectroradiometer	31
MSS DTU10	Mean Sea Surface, DTU10	64
NASA	National Aeronautics and Space Administration	1
NSIDC	National Snow and Ice Data Center, Boulder, CO.	14
OIB	Operation IceBridge	1
OSI SAF	Norwegian Meteorological Service Ocean and Sea Ice Satellite Application Facilities	32
PIOMAS	Pan-Arctic Ice-Ocean Modelling and Assimilation System	57
POD	Precise Orbit Determination	36
PP	Pulse Peakiness	73
PPP	Precise Point Positioning	25
PPS	Precise Positioning Service	20
PRF	Pulse Repetition Frequency	33
PRN	Pseudo-Random Noise	20
SAR	Synthetic Aperture Radar	10
SARIn	SAR Interferometry	34
SBAS	Satellite-Based Augmentation System	23
SIRAL	CryoSat's SAR / Interferometric Radar Altimeter	34
SPS	Standard Positioning Service	20
SSH	Sea Surface Height	2
TEC	Total Electronic Content	46
ULS	Upward Looking Sonar	15
WAT	Ice thickness with Warren's snow thicknesses	108

Introduction

A changing sea ice cover is a strong indicator of a changing climate. The sea ice variability can both reflect and affect climate changes and is therefore an important component in climate models. The sea ice in the Arctic is an early indicator of global climate change, and this is happening through feedback mechanisms associated with the high albedo of ice and snow [Curry et al., 1995], exchanges of heat, moisture and momentum between the atmosphere and the polar oceans [Laxon et al., 2004], and it affect the thermohaline circulation [Aagaard and Carmack, 1989]. The warming ocean [Johannessen et al., 2004] has extended the summer melt period [Smith, 1998], and minimized the coverage of multi-year ice [Fowler et al., 2004; Maslanik et al., 2007; Nghiem et al., 2007; Stroeve et al., 2012].

The mass balance of the Arctic sea ice is an important input to the coupled atmosphere-ocean models, and it is therefore crucial to understand the ice volume i.e. the sea ice extent and thickness. The first satellites (passive microwave) started to monitor the sea ice extent in 1979 [Comiso et al., 1991], and the monthly linear trend in the sea ice extent has been negative ever since [Serreze et al., 2007]. The sea ice thickness is more difficult to measure than the extent, and satellite altimetry is the only type of measurements for continuously observing the seasonal and spatial sea ice thickness variations on large scale.

In April 2010, European Space Agency (ESA) launched the CryoSat-2 satellite (hereafter simply referred to as CryoSat), dedicated to monitor the Earth's cryosphere changes. It is measuring more of the Arctic Ocean than ever before due to its high inclination. CryoSat is a key component in this study. In this study CryoSat Level 1B (L1B) data are retracked with a threshold retracker [Davis, 2002].

The retrieved CryoSat observations are analyzed, and to verify the satellite measurements, data needs to be validated. One approach is to use airborne altimetry data, and another is to use airborne and satellite imagery. In this thesis, airborne laser altimetry data from the ESA CryoSat Calibration and Validation Experiment (CryoVEx) and National Aeronautics and Space Administration's (NASA) Operation IceBridge (OIB) are used, together with various imagery to verify the observations.

The CryoSat elevations are in a preliminary study converted to sea ice freeboard heights (height above a local sea surface), and ice thicknesses over the entire Arctic Ocean, and the annual and interannual variations are studied for the period from 2010 to 2013.

Sea ice thickness estimates are crucial to determine the sea ice reduction and accordingly

the freshwater discharge into the Arctic circulation [Aagaard and Carmack, 1989]. As part of this thesis, a case study from a fjord in the southeast Greenland, demonstrates how airborne laser altimetry can be used to estimate the ice discharged from a glacier into the fjord.

Besides the scientific interest in monitoring sea ice as a climate indicator, the exploration, shipping, and fishery industry are interested to know about the ice cover and ice types for a more safe and efficient transport [Ulaby et al., 1986]. Especially due to recent reduction in ice cover.

In order to determine the sea ice thickness from altimetry, it is very important to acquire an accurate local sea surface height (SSH). This can be achieved by locating the leads (open water in between the ice floes) and subsequently approximate the local SSH. Sea ice thickness is very sensitive to the SSH and different datasets can lead to large differences in thickness [Connor et al., 2013].

Another method for obtaining the SSH is to use the Global Positioning System (GPS) in combination with various geophysical parameters. In this study, it is shown [Rose et al., 2013c] how the vertical component in the GPS measurements can be computed to assimilate the SSH. Furthermore, the ocean tides in the Arctic Ocean are studied. The ocean tides are damped in the Arctic due to the sea ice cover. In this thesis, it is shown, that large scale tide models perform well in the open Arctic Ocean compared to the ocean tide model AOTIM-5 by Padman and Erofeeva [2004], but less good in fjord systems and in coastal areas.

1.1 Scientific Objectives

Overall the outcome of the Ph.D. will be an improved understanding and description of CryoSat data, which is a new type of satellite measurements, how they can be used in practice to monitor height changes in sea ice thickness, and how the use of airborne campaign data can help validate the satellite data and provide a better understanding of inherent errors. In other words, the results of this Ph.D. study contribute to a more accurate monitoring of climate-related cryosphere changes.

1.2 Structure of the Thesis

The thesis is based on five papers, which are briefly described in Chapter 2, and attached in full length in Appendix F. The content of this thesis is supplementary to the papers. Discussions of the work are carried out throughout the thesis when appropriate.

The background and motivation of the sea ice study is described in Chapter 3, which covers the state of the Arctic sea ice in the sense of; description of the ice cover and its dynamics, sea ice extent, thickness distribution and sea ice related to the climate.

The theory behind GPS will briefly be described in Chapter 4, covering the fundamental concept of the signal, GPS errors, general improvements to the measurements and a short teaser for GPS applications in the Arctic.

This is followed by a chapter (Chapter 5) describing the data used in the sea ice study, except the CryoSat data, which will be described in Section 6.1.1.

Satellite altimetry is an essential part of the work, and the theory behind it is described in Chapter 6. This will, beside the description of CryoSat data contain an overview of satellite

missions measuring over sea ice, give a review of the theory behind radar altimetry, including SAR altimetry and the principles behind retracking of altimetry data are outlined.

The following chapter, Chapter 7 is about geophysical corrections used in altimetry as well as GPS to derive surface elevations. Next, Chapter 8 is dedicated to measurements of sea ice by radar altimetry including freeboard retrieval, thickness estimates, and the error sources arising in the process.

In Chapter 9 the implementation of the CryoSat retracker is described together with a validation of the retracker over the SSH.

A comparative assessment is carried out to validate the CryoSat observations. This is described in Chapter 10. The chapter starts with a description and validation of the averaging of airborne laser scanner data, description of a lead detection algorithm, and sea ice drift correction. After this follows an in-depth analysis of the CryoSat observations over different ice surfaces. The chapter is closing with a review and discussion of filtering off-ranging elevations.

Chapter 11 delineate the making of sea ice freeboard and thickness maps, with the preparations and considerations that follows. The results are shown, and the preliminary state of this work is stressed. This work was carried out in the very final stage of the Ph.D study.

Chapter 12 concludes the thesis by summarizing the most important findings and lists suggestions for continuing the work done with natural extensions.

Chapter 2

Scientific Papers

The work carried out in this Ph.D. thesis is partly described in the scientific papers shortly summarized below.

Initial Results of CryoSat-2 Data from the Arctic

Rose, S. K., Stenseng, L., Skourup, H., Pedersen, L. T., and Forsberg, R. (2011). Initial results of CryoSat-2 data from the Arctic. In *CryoSat Validation Workshop 2011*, volume SP-693. ESA. See Appendix [F.1](#).

This paper is based on CryoSat data from the commissioning phase. We describe the CryoVEx campaign from 2011, and analyze the SAR L1B waveforms by evaluating the coherence between Envisat ASAR images and the CryoSat observations. The surface elevations are retrieved with a 80% threshold retracker and a five parameter β -retracker, and we find a vertical offset of 10 m, (which was later encountered as an atmospheric correction error in the product). At this stage, the CryoSat product is very noisy, but it was possible to detect the leads, and the freeboard shows good agreement with the ASAR images. The freeboard height in the track was between 0.1 to 1.1 m corresponding to an ice thickness of 1.5-3 m, indicating that the ice was predominantly multi-year ice.

Arctic Tides from GPS on sea ice

Rose, S., Skourup, H., and Forsberg, R. (2013c). Arctic Tides from GPS on Sea-ice. *J. Geodyn.*, 63:45–53. See Appendix [F.2](#).

This study uses GPS data collected from the sea ice north of Greenland to study the ocean tides in the Arctic Ocean. We prove that the tidal defined zero level can be retrieved from GPS by applying geophysical corrections to the data. The vertical height of the GPS measurements are compared with an Arctic tide model AOTIM-5. The results show good agreement between the data in the central Arctic, but less good in coastal areas and in fjord systems. Furthermore, the SSH is determined with an offset between 3-52 cm.

A Comparative Analysis of the Sea Ice Freeboard From CryoSat, CryoVEx and ICEBridge

Rose, S., Conner, L. N., Farrell, S. L., Forsberg, R., Newman, T., Pedersen, L. T. Smith, W. H. F., Skorup, H., and Stenseng, L. (2013a). A Comparative Analysis of the Sea Ice Freeboard from CryoSat, CryoVEx and IceBridge. In *CryoSat Third User Workshop*. ESA. See Appendix F.3.

In this paper, CryoSat data are compared from a small satellite track in the Lincoln Sea and north of Svalbard. CryoSat level 2 (L2) data are analyzed, and show how the ESA retracker fails, when a small peak in the waveform is followed by a tall peak. A rough routine to correct the off-ranging elevations is developed, which improve the L2 results. L1B data are retracked to retrieve surface elevations. Various thresholds of the threshold retracker are studied, and thresholds of 40% and 50% seem to perform best over the sea ice cover. Data still contains off-ranging elevations, which affect the retrieved freeboard heights.

A sea ice freeboard analysis from CryoSat, CryoVEx and ICEBridge over first- and multi-year ice areas

Rose, S., Conner, L. N., Farrell, S. L., Forsberg, R., Newman, T., Smith, W. H. F., and Skorup, H. (2013b). A Sea Ice Freeboard Analysis from CryoSat, CryoVEx and IceBridge over First- and Multi-year Ice Areas. *IEEE T. Geosci. Remote*, Rejected, with resubmission after major revision:1–13. See Appendix F.4.

This manuscript show a comparative assessment between CryoSat, CryoVEx and OIB for an area with multi-year ice and between CryoSat and CryoVEx for an area with first-year ice. Data are successfully corrected for drift, where the laser scanner dataset shows a very good correlation $r = 0.905$, while the correlations between CryoSat and the laser scanner datasets are less good, but acceptable considering the different kinds of data.

Five methods for deriving the SSH are shown, and they show how sensitive the SSH retrieval can be. The method derived from the lead detection algorithm, based on the retracked power peak show the best results. The resulting modal freeboard heights for the multi-year ice area are between 43-53 cm for a threshold of 40% and between 28-53 cm for a threshold of 50% after a snow layer from OIB is applied to data. Comparing the freeboard to the laser scanner data with modal freeboard of 53 cm, the threshold retracker of 40% shows the best results. In the second area with first-year ice, a freeboard between –3 to 13 cm was found for the 40% threshold retracker, while the 50% retracker gave a result between –3 to 8 cm. The laser scanner freeboard was found to be 33 cm. The difference between the observations could be verified by considering a snow layer from a snow model. Off-ranging elevations were not filtered out, which may bias the results.

Ice mélange volume estimates from LiDAR - A snapshot of ice discharge in the Godthåbsfjord, Greenland

Rose, S. K., Forsberg, R., Hvidegaard, S. M., Nielsen, K., Pedersen, L. T., Simonsen, S. B., and Sørensen, L. S. S. (2013d). Ice mélange volume estimates from LiDAR - A snapshot of ice discharge in the inner Godthåbsfjord, Greenland. *J. Glaciol.*, Submitted. See Appendix F.5.

In this paper, submitted to Journal of Glaciology, we use airborne laser scanner data to map the topography in the inner Godthåbsfjord, Greenland, with the purpose of studying the glacier discharge into the fjord. This is built on the synthesis that the calved ice from the glacier is trapped in the frozen-in sea ice in front of the glacier, the *ice mélange*.

The data are collected in spring, where we suppose the ice has not yet broken up. We use a lowest level filtering method to define the local sea level, from where the ice freeboard (sea ice and glacial ice) is found. The scanner lines are interpolated to cover the whole fjord, and with an assumption of buoyancy the total volume of the ice is calculated. We find a volume of 1.70 ± 1.26 GT found in the fjord, corresponding to 38% of the yearly ice flux from the glaciers.

The State of the Arctic Sea Ice

The Arctic Ocean (Fig. 3.0.1) is partly covered with sea ice which vary with the season. The sea ice mass balance is a crucial factor in climate models. To estimate the mass balance; the sea ice volume, extent, and thickness needs to be determined together with the dynamics of the ice. The thickness is by far the most difficult factor to measure while the bottom of the ice is highly variable and difficult to assess.

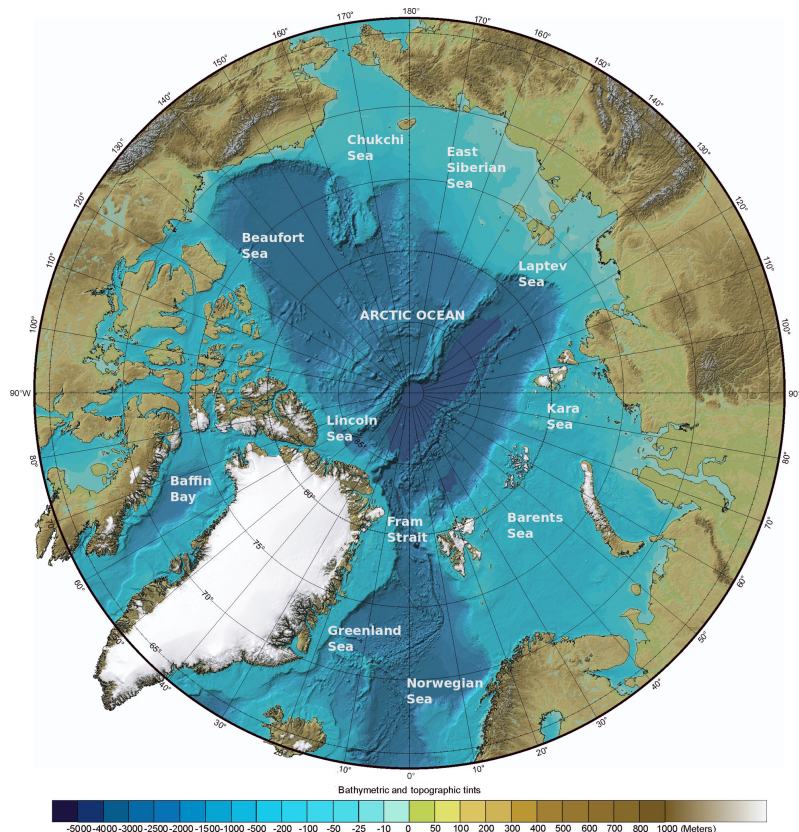


Figure 3.0.1: *The International Bathymetric Chart of the Arctic Ocean (IBCAO) [Jakobsson et al., 2012] modified with location names.*

This chapter aims at describing the sea ice cover, main ice types, extent, thickness distribution, and how the sea ice cover changes due to dynamic forcing. The chapter is closed with a review of the sea ice in a climate perspective.

3.1 The Arctic Sea Ice Cover

The Arctic sea ice cover is usually measured as ice concentration and ice extent. The ice concentration is a measure of the fractional coverage of an area, while the sea ice extent is the area covered by a certain ice concentration, usually above 15% [Bamber and Kwok, 2004]. Passive microwave satellites are the preferred tool for monitoring the sea ice concentration by measuring the emitted radiation from the surface, but also Synthetic Aperture Radar (SAR) and visible sensors can be used to determine the surface type (water/ocean) by counting the pixels. For a description of the two most widely used sea ice concentration algorithms see Cavalieri et al. [1984, 1991]; Comiso [1995]; Markus and Cavalieri [2000].

The physical properties of sea ice depend on the salinity of the ocean water when formed, ice temperature, pressure, and porosity. Sea ice is categorized by its thickness defined by World Meteorological Organization [1970]. New ice is less than 0.2 m thick. First-year ice is of one winter's growth and is between 0.2 - 2 m thick. Multi-year ice is perennial ice surviving more than one summer's melt and is over 2 m thick, typically between 3-4 m. First-year ice normally has a smooth surface, and is more saline than multi-year ice. Multi-year ice has a more rough surface due to surface thawing and refreezing during the season. Furthermore, there exist hummocks and ridges up to 30 m on the ice (with sail and keel), resulting from stresses acting on the ice. [Rouse, 1969].

Besides the thickness, the mechanical strength distinguish first- and multi-year ice. This is due to the lower brine volume and larger thickness resulting in a larger energy loss from the surface and therefore more growth by freezing. It is important to know the relative proportions of first- and multi-year ice, to give an adequate description of the Arctic sea ice cover. The different ice types can be found from active microwave satellites by measuring the backscatter. Multi-year ice has a higher backscatter than first-year ice based on physical characteristics as salinity, porosity, layering, and surface properties [Kwok et al., 1999].

In the icepack there are openings due to local melt and divergence. These are respectively called polynyas and leads. These are important sources for distributing heat and moisture to the atmosphere, for wild life, [Smith et al., 1990], and for this thesis they are crucial in thickness determination, because they are used to obtain a local SSH. Throughout this thesis there is no discrimination between polynyas and leads, the term leads are used to describe open water in between the sea ice floes.

3.1.1 Dynamic Forcing

The mass balance of sea ice in the Arctic is influenced by local growth and melt, horizontal transport and deformation. The local mean sea ice thickness changes due to these processes and involve exchanges of mass and energy with the atmosphere and ocean. The general pattern of sea ice circulation is mainly driven by the anticyclonic *Beaufort Gyre*, and a weaker circulation system in the Eurasian basin, in between these currents the *transpolar drift* transports sea ice from the Laptev Sea and the East Siberian Sea towards Fram Strait (Fig. 3.1.1). Warm salty

ocean water is transported into the Arctic Ocean from the eastern Fram Strait subducting beneath the fresh, less dense and cold surface water to form an intermediate layer. Cold and less dense water is transported into the Arctic Ocean through the Bering Strait. In winter, when the seawater freezes, salt is released into the surface, and the water becomes more dense, sink, and create the inter median layer called the halocline [Dijkstra, 2008].

More than 70,000 km³ of freshwater is stored in the upper layer of the Arctic Ocean, due to river run-offs, melting sea ice and glacial ice, and precipitation, leading to very low salinity in the upper layer. The freshwater content in the circulation system, play a role in the global thermohaline circulation, where models predict a disrupt due to the increased freshwater input. The largest freshwater accumulation is observed in the Canadian Arctic [Serreze et al., 2006, 2007].

This is related to the prevailing wind patterns. Wind-driven motion in the Arctic Ocean, changes between anticyclonic and cyclonic circulation. This is called the *Arctic Oscillation* (AO), and the strength and location of the surface currents are mainly controlled by this wind pattern, i.e. changes in atmospheric pressure. The AO reflects an exchange of atmospheric mass between the Arctic Ocean and mid-latitudes.

The *AO-index* is a measure of the principle time varying component of the Northern Hemisphere sea level pressure [Thompson and Wallace, 1998]. A positive index is associated with stronger prevailing winds (*westerlies*) in mid-latitudes, and lower than usual sea level pressure. This is causing cyclonic winds, and make a slowdown of the anticyclonic circulation of the Beaufort Gyre and a strengthening of the transpolar drift. Sea ice is transported away from the

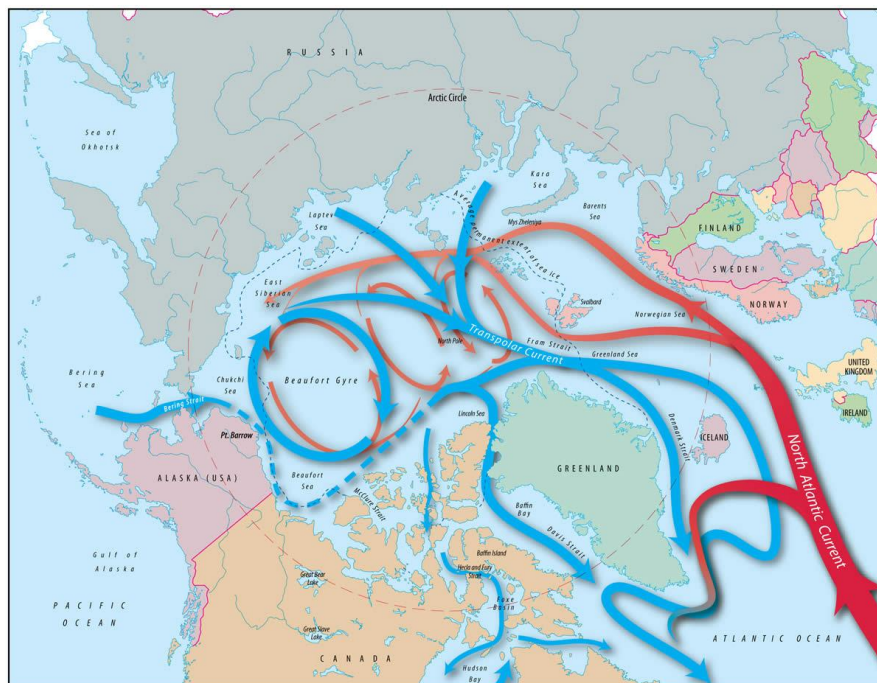


Figure 3.1.1: Circulation patterns in the Arctic ocean. Blue arrows are cold and fresh water, while red arrows are warm salty water from the North Atlantic. Illustration by Jack Cook, Woods Hole Oceanographic Institute.

coast and the sea ice transport out of the Fram Strait increases, leads and openings occur, and the production of new ice increases in the East Siberian and Laptev Seas, and increase the diverges in the Canadian Arctic. This all results in a decrease in the sea ice extent and a general sea ice thinning [Rigor et al., 2002].

A negative AO-index represents, on the other hand, lower than usual pressure at mid-latitudes and higher than normal atmospheric sea level pressure in the Arctic. This is causing anticyclonic winds, and favor thicker sea ice. In anticyclonic regimes, freshwater is stored in the Beaufort Gyre. This changes the SSH and depth of the halocline accordingly [Proshutinsky and Johnson, 1997]. Giles et al. [2012] suggest that the Beaufort Gyre is steepening with an increase in the freshwater storage due to wind-driven spin-up. Spreen et al. [2011] examine how the wind-system affects the sea ice thinning and enhances the deformation. They find that the change in wind speed explain a fraction of the increased sea ice thinning in the central Arctic. Even though a negative AO-index normally favors a sea ice thickening it is not always the case, as seen during winter 2009/2010 Stroeve et al. [2011].

The circulation pattern leads to deformation and thickening of the ice along the Canadian Arctic islands, the coast north of Greenland, and corresponding thin ice along the central Eurasian coast and Canadian mainland. Following the already described circulation pattern and ice transport, the largest concentration of multi-year ice is in the central part of the Arctic, and in the already mentioned deformation or thickening areas. The highest first-year ice concentration in the Arctic Ocean is near the coast of Eurasian and the Canadian mainland [Flato, 2004]. The largest export of multi-year ice is through the Fram Strait. From here it is transported into the Greenland Sea and the North Atlantic, where the sea ice deteriorates.

In the years up to the extreme sea ice minimum in September 2007, the sea ice cover was shrinking and thinning, and made the ice cover vulnerable to the extra powerful atmospheric pressure system located over the Beaufort Sea and the Canadian Basin [Maslanik et al., 2007; Lindsay et al., 2009; Perovich et al., 2008]. For a much more detailed review of this subject see Stroeve et al. [2012].

An extreme melting season as in 2007 [Comiso et al., 2008] and 2012 [Parkinson and Comiso, 2013], is followed by an increase in the first-year ice extent in spring. First-year ice is more vulnerable to melt away during summer. In August 2012 a major storm in the central Arctic Ocean likely evoked the record September 2012 minimum. The storm facilitated the vulnerable ice pack to melt by bringing warm and moist winds from the south and furthermore shearing-off a large portion of the ice in the Bering Strait/Chukchi Sea inducing fracturing and further melt.

3.2 The Arctic Sea Ice Extent

The Danish Meteorological Institute (DMI) was in 1890 the first to produce annual sea ice charts based on ship and coastal reports [DMI, 1930]. As mentioned in the introduction, Chapter 1, passive microwave satellites started to monitor the sea ice extent in 1979 [Comiso et al., 1991], and the sea ice extent has retreated ever since with a decrease in September extent of -13.0% (Fig. 3.2.1(a)) per decade in the period from 1979 to 2012, and -2.5% per decade for the minimum extent in March (Fig. 3.2.1(b)) for the same period [Stroeve et al., 2012; Perovich et al., 2012].

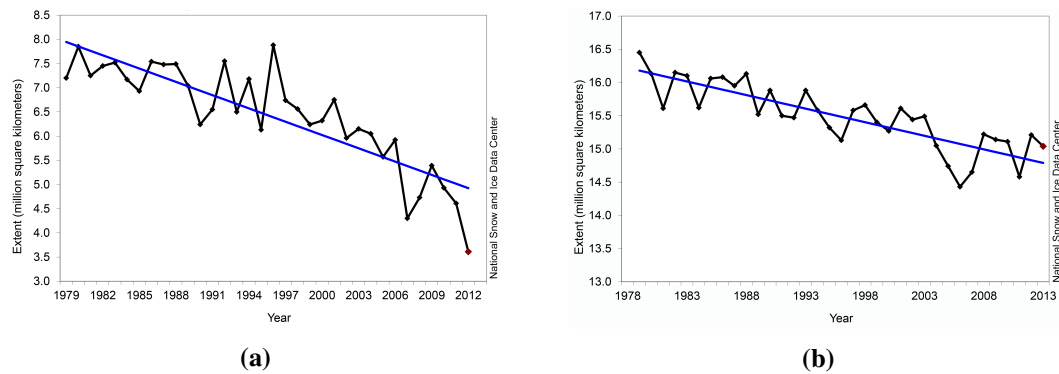


Figure 3.2.1: Average monthly sea ice extent (black curve) from 1979 to (a) September 2012 and (b) March 2013. The fitted linear trend (blue curve) is -13.0% and -2.5% per decade, respectively. With courtesy National Snow and Ice Data Center, Boulder, CO.

3.2.1 Interannual Variation

The Arctic sea ice cover reaches its maximum in March, this is the end of the growth season and the beginning of the melt season, which continues until September, where the sea ice cover reaches its minimum extent. At this time about 2/3 of the sea ice has melted.

Summer melt makes it difficult to measure sea ice thickness, ice concentration and distinguish between the ice types during the summer months, because surface melt cannot be distinguished from open water.

The lowest record since 1979 of ice extent was observed September 16, 2012 with an extent

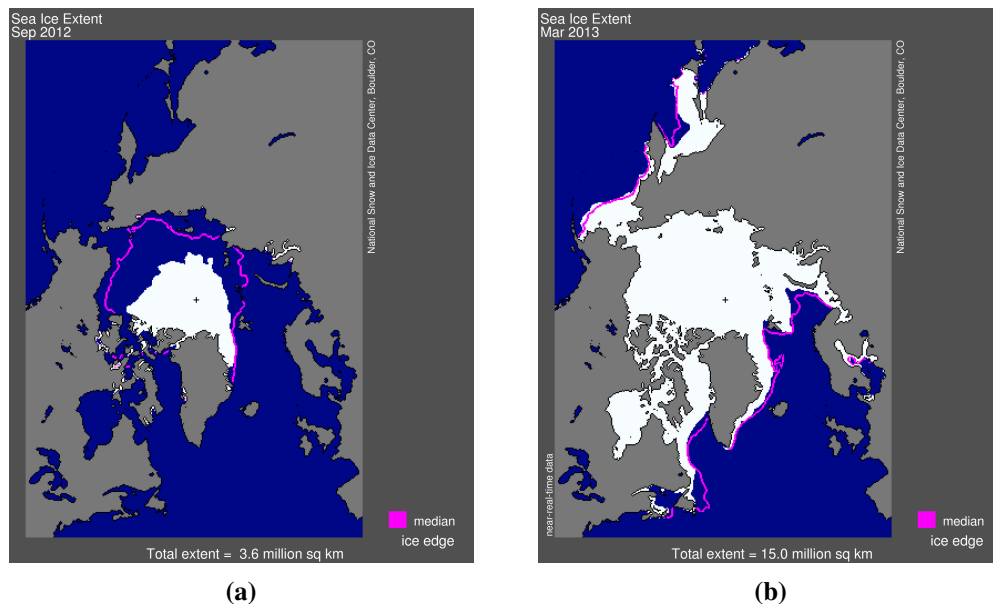


Figure 3.2.2: Sea ice extent. (a) Minimum extent in September 2012, and (b) maximum extent in March 2013. The magenta line show the median extent from 1979 to 2000. Image credits: National Snow and Ice Data Center, Boulder, CO.

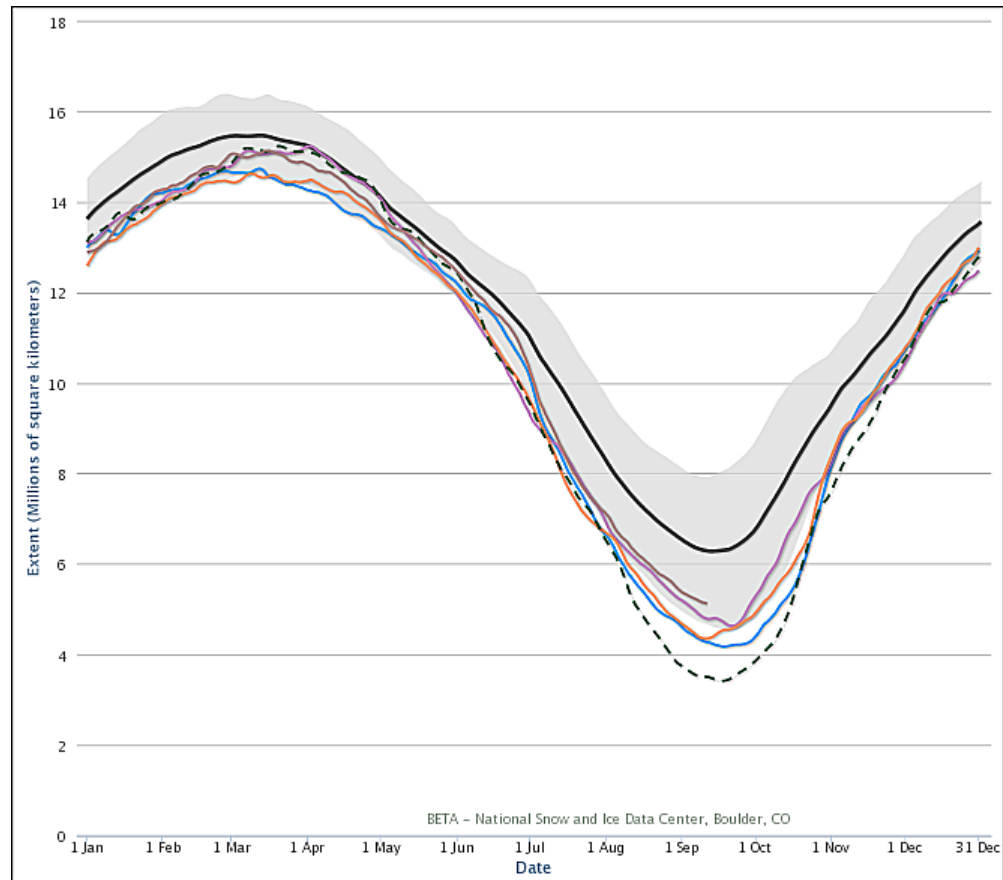


Figure 3.2.3: Monthly sea ice extent for 1981-2000 (black curve) with standard deviation (gray), 2007 (blue), 2010 (purple), 2011 (orange), 2012 (dashed) and 2013 (red). Image credits: NSIDC, Boulder, CO.

of $3.41 \cdot 10^6 \text{ km}^2$ (Fig. 3.2.2(a)), and this was $3.29 \cdot 10^6 \text{ km}^2$ lower than the 1979-2000 average minimum extent. In the following spring in 2013 (on March 15), the maximum extent reached $15.04 \cdot 10^6 \text{ km}^2$ (Fig. 3.2.2(b)), and this is $710,000 \text{ km}^2$ below the 1979-2000 maximum average extent (credit: National Snow and Ice Data Center (NSIDC), Monthly Archives, September 19, 2012 and March 25, 2013). The 2012 record was 18% lower than the former record minimum observed in 2007 [Perovich et al., 2012].

The interannual extent is shown in Fig. 3.2.3 for the period 1981-2000 (black) with standard deviation (gray), 2007 (blue), 2010 (purple), 2011 (orange), 2012 (dashed green), and 2013 up to now (red). 2007 and 2012 are the extreme melt years, while 2010, 2011, and 2013 are included because they are part of the analysis in Chapter 11.

Comiso et al. [2008]; Stroeve et al. [2012] are suggesting an acceleration in the September decline from 1996 and 1999, respectively. The latter finds a trend of $-0.032 \pm 0.017 \cdot 10^6 \text{ km}^2/\text{year}$ in the period 1979-1999, and $-0.154 \pm 0.038 \cdot 10^6 \text{ km}^2/\text{year}$ in 1999-2010.

3.3 Thickness Distribution and Measurements

Measuring sea ice thickness is the most difficult and uncertain parameter to measure on large scale and over time. The bottom of the sea ice is highly variable, and not very assessable. There exist various ways of measuring sea ice thickness. The most commonly used are; in-situ measurements, Upward Looking Sonars (ULS), Electromagnetic (EM) sensors, airborne and satellite altimetry. In-situ and airborne remote sensing techniques are very good at determining the sea ice thickness, but is limited in spatial and temporal coverage. That can only be provided by satellite altimetry.

In-situ measurements give the best estimate of the thickness, but are mainly useful in validating other datasets [e.g. Haas et al., 1997], as the method is arduous over long distances.

Rothrock et al. [1999] used ULS and found a thickness decrease of 42% by comparing measurements from 1958 and 1976. A similar study by Wadhams and Davis [2000] found a 43% thinning in the period from 1976-1996, corresponding to 1 m thinning in both studies. Perovich et al. [2008] found a 2 m thinning in the Beaufort Sea in the extreme warm summer of 2007, based on autonomous ice mass balance buoys observing the ice growth's bottom and surface melt.

Helicopter EM measurements over the Transpolar Drift show a modal sea ice thickness reduction of 53% from 2001-2007 [Haas et al., 2008]. More recently Haas et al. [2010b] made an extensive airborne EM survey in 2009 and compared with data from 2007. The results show stable multi-year ice thickness or thickening following a natural variability.

Satellite altimetry for estimating sea ice thickness has recently become available [Laxon et al., 2003], and other studies [Kwok, 2004; Lindsay and Zhang, 2005; Giles et al., 2008, and more] agree on the thinning of the sea ice. The satellite altimetry missions and the theory behind altimetry will be covered in Chapter 6, and the methods of measuring over sea ice will be covered in more details in Chapter 8.

Thinning of the ice and decreasing ice extent is linked. A thinning of the sea ice eventually causes the ice to break and makes it easier for the ice to drift away. This is due to less mechanical strength of the thin ice. When more open water occurs, it amplifies the albedo effect; more radiation from the sun is absorbed in the ocean, and the temperature of the ocean increases, this causes the albedo to decrease and enhance further melt of the sea ice.

Sea ice thinning is caused by various factors; surface melt due to higher temperatures, bottom melt, which could be caused by advection of warm water into the Arctic, extension of the summer melt season and the composition of the ice cover with less multi-year ice [Wadhams, 2013]. ULS observations indicate a linear relationship between the melt rate and the sea ice thickness, where bottom melt is the main factor to thinning [Wadhams, 1997].

Stroeve et al. [2012] observed an increased variability of sea ice thickness after 1990, which may be coupled with a shift in the partial fraction of first- and multi-year ice in spring, linked to a period with a strong AO causing more first-year ice. Furthermore, the oldest and thickest ice has declined, so now 58% of the multi-year ice is relative young ice (2-3 years), compared with 35% in the 1980s. The most profound changes are found in the eastern Arctic Ocean [Fowler et al., 2004; Maslanik et al., 2007; Nghiem et al., 2007]. In Fig. 3.3.1 the extent of sea ice age is shown from 1983 to 2012 together with age maps from the two record low September extents; 2007 and 2012.

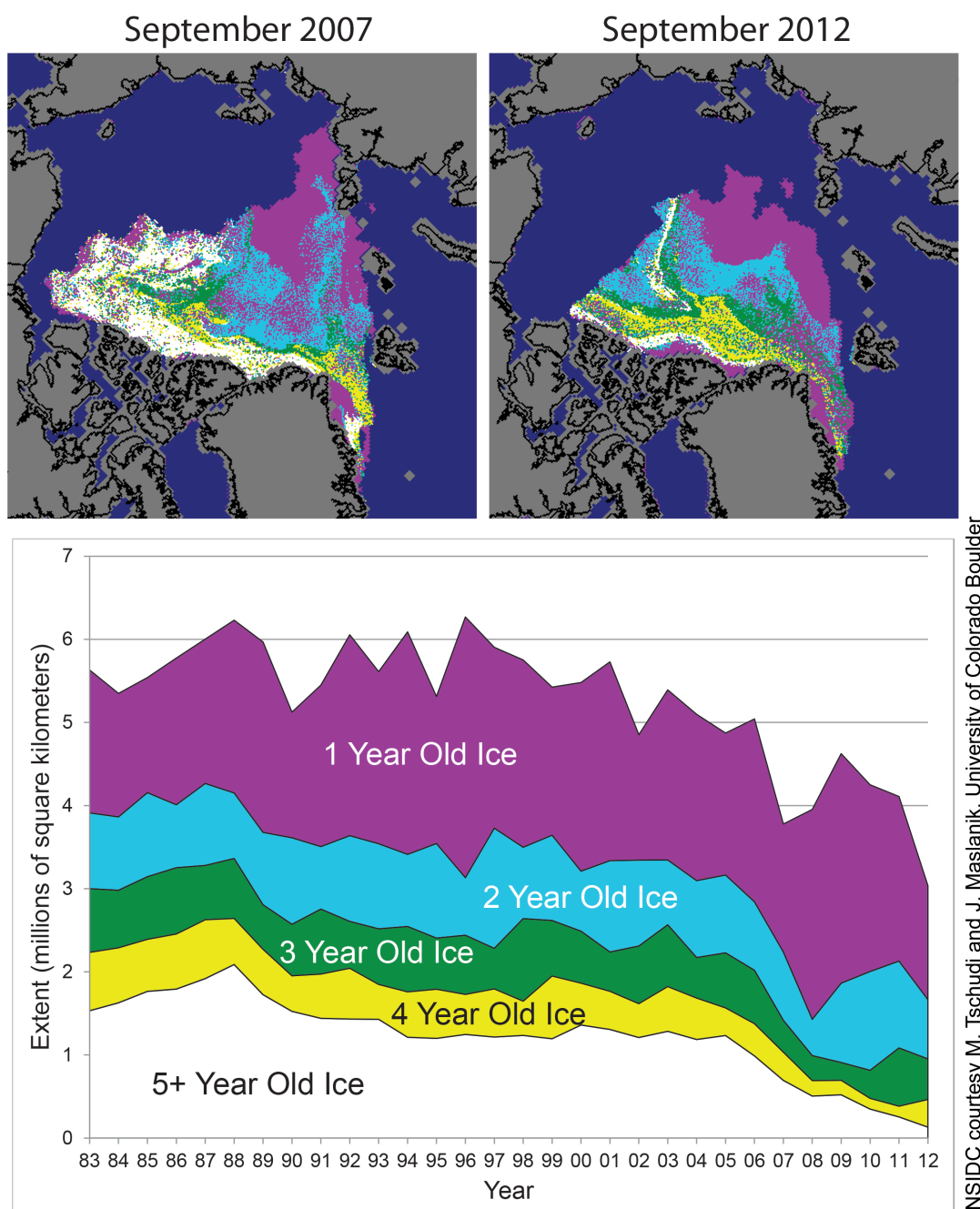


Figure 3.3.1: Top: sea ice age map from September 2007 and September 2012. Bottom: The Arctic sea ice age extent from 1983 to 2012. The figure shows a large decrease in the old ice. Ice older than 5 years has almost disappeared from the Arctic Ocean, making the ice pack thinner and more vulnerable to weather. Credits: NSIDC and M. Tschudi and J. Maslanik, University of Colorado Boulder.

3.4 Sea Ice in a Climate Perspective

Following the 2007 IPCC report, there exists three important sea ice components related to the global climate:

1. The albedo feedback mechanism, which enhances climate response at high latitudes.
2. Exchanges of heat, moisture and momentum between the atmosphere and the polar oceans.
3. Alterations of the ocean stratification and deep-water formation forcing via redistributing freshwater by transport and melt.

These components are explained from a combination of natural variability in temperature, atmosphere, and ocean circulation and anthropogenic forcing, i.e. rise in atmospheric greenhouse gases [Serreze et al., 2007]. Observations show a much faster decline in the sea ice extent than all the 13 models included in the 2007 IPCC report [Stroeve et al., 2007]. New models represents the sea ice extent better, [see e.g. Wang and Overland, 2012; Overland and Wang, 2013] predicting an ice free summer in the 2030s or even before. They now capture the rapid decline, but the extrapolation for future scenarios is uncertain. As seen with the 2007 and 2012 minimum extents a large storm can quickly change the sea ice pack.

The coverage of multi-year ice is significant in the climate perspective, due to its relation to summer ice concentration [Comiso, 1990]. Reduction of multi-year ice coverage could be due to increased melt and export out of the Arctic. The decrease in summer ice coverage enhances the summer heating of the ocean by insolation and changes the outflow of sea ice to the Arctic Ocean. This will (as described in Section 3.1.1) increase the transport of fresh water to the Greenland, Icelandic and Norwegian Seas and may affect the thermohaline circulation [Aagaard and Carmack, 1989].

An external climate forcing will enhance the linked processes in accelerating the September downward trend in the sea ice extent (Fig. 3.4.1). An atmospheric warming gives rise to a thinner sea ice cover in spring and more open water in autumn, and these effects mutually enhance each other. An accelerated sea ice thinning in summer delays refreezing in winter, therefore decreasing the amount of multi-year ice, and the mechanical strength of the ice cover allowing even more fracturing and faster export of sea ice to the Fram Strait [Rampal et al., 2009].

The solar radiative forcing between the atmosphere, ocean, and ice, has been altered due to the diminishing sea ice cover, which results in decreasing surface albedo. The sea ice extent is inversely correlated with the latitude of maximum warming, and models with thin ice do have a higher polar amplification [Holland and Bitz, 2003].

The upper layer of the Arctic Ocean has been getting warmer in the past decades, and more thin ice gives a more broken ice cover with more open water and therefore an increased albedo feedback. A 500% positive solar heating anomaly was observed in 2007 in the Beaufort Sea as an input to the upper ocean layer [Perovich et al., 2007, 2008]. From 1979 to 2009 the melting season in the Arctic has increased by 20 days, i.e. the Arctic has warmed in all seasons since the satellite started to monitor the sea ice, and there is no evidence for a cold season to appear [Markus et al., 2009].

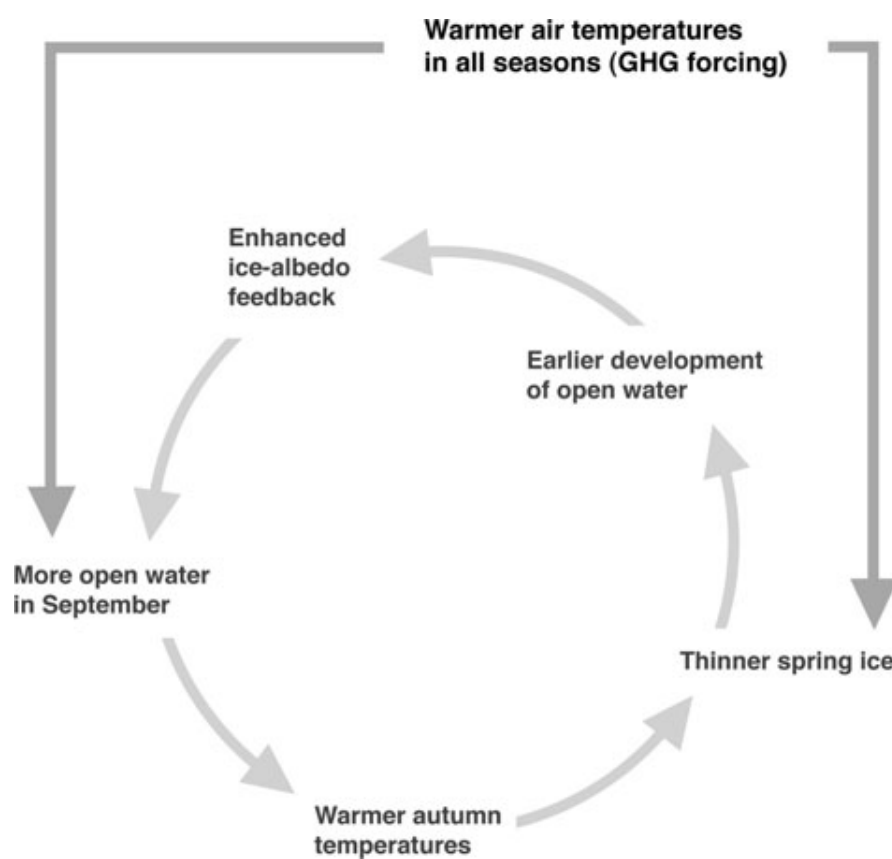


Figure 3.4.1: An external climate forcing enhance the linked processes in accelerating the September downward trend in sea ice extent. Credits: *Stroeve et al. [2012]*.

The Principles of GPS

This introductory chapter, addresses the theory behind the work done regarding the Global Positioning System (GPS) data. For scientific processing, an understanding of the GPS signal and the associated errors is necessary. During this study a lot of effort has been put into GPS processing and analysis. A fraction of this work is described in the paper [Rose et al. \[2013c\]](#) in Appendix F.2, and a short summery can be found in Chapter 2.

This chapter is a concise description of the GPS concept (Section 4.1). The errors arising when measuring with GPS (Section 4.2) are briefly addressed, methods for improving the accuracy are described (Section 4.3), and examples of processing software (Section 4.4) are listed. The chapter is closed with a section about the issues when working with GPS in the Arctic (Section 4.5). For a more thorough background information of GPS I recommend reading the books by [Kaplan and Hegarty \[2006\]](#); [Hofmann-Wellenhof et al. \[2008\]](#); [Misra and Enge \[2011\]](#).

4.1 The Concept of GPS

GPS is a space-based Global Navigation Satellite System (GNSS) started in 1973, and was declared fully operational in 1995. The objective was to provide the U.S. military with position, velocity and time information anywhere near the Earth. Since May 1, 2000 civilians have been able to use the same precision as the military. Today it is about 10 cm and with a good receiver it can be much better. GNSS is the generic name for systems similar to the GPS system, for example the Russian GLONASS, the Chinese BaiDou, and the European system Galileo. GPS and GLONASS are the only operating GNSS, where BaiDou and Galileo are under construction [[Misra and Enge, 2011](#)]. The focus will be on the GPS system, while it is the only GPS system used in this thesis. Following, the official U.S. Government information about GPS (www.GPS.gov) there are currently 31 satellites in operation.

In determination of the four dimensional position (space and time) a GPS receiver needs to determine the ranges to at least four satellites, and their positions at time of transmitting. The position of the satellites can be estimated with an error less than a few centimeters based on the precision of their predicted orbits. The basic measurement made by the GPS receiver is the apparent transit time, the time it takes the signal to travel from a satellite to the receiver, defined as the difference between the reception time determined by the receiver and satellite

clock, respectively. The time it takes a signal to travel from a satellite to a receiver is biased due to non-synchronous clocks. This bias in the receiver clock affects the observed transit time for all satellites equally, because the receiver measures the range to different satellites nearly at the same time. The corresponding measured ranges are called *pseudo-ranges*. By finding the pseudo-range for the fourth satellite, the time error can also be estimated.

There exist three segments in GPS (Fig. 4.1.1); the space segment, the control segment and the user segment. The space segment is the constellation of the satellites. A user will have at least four satellites in sight with a clear view of the sky. The control segment consist of the master control station in Colorado, where the system is operated and controlled, and several monitor stations around the world, where the satellites are tracked. The user segment is all the GPS receivers that are used in every day life, in science, and in commercial applications.

4.1.1 The Signals

The GPS satellites transmit in the ultra-height L-band using radio frequencies named Link 1 (L1: $f_{L1} = 1575.42$ MHz) and Link 2 (L2: $f_{L2} = 1227.60$ MHz). Each signal comprises of three components; the *carrier*, the *ranging code* and the *navigation data*. The carrier is the radio signal with frequencies f_{L1} and f_{L2} . The ranging code is a system of *Pseudo-Random Noise* codes. These PRN codes are constructed with properties such that all satellites can transmit at the same frequency without interfering with each other. Furthermore, they allow precise range measurements, and diminish reflected and interfering signals received by the GPS antenna. The *Standard Positioning Service* (SPS) code called the coarse/acquisition codes (C/A-codes) is unique on L1 for every satellite. The Precise Positioning Service (PPS) code is called the precision (encrypted) codes (P(Y)-codes) transmitting a unique code on both L1 and L2. The navigation data mainly consists of the satellite health status, the position and velocity, referred to as ephemeris, clock bias, and an almanac given reduced ephemeris of the other satellites in

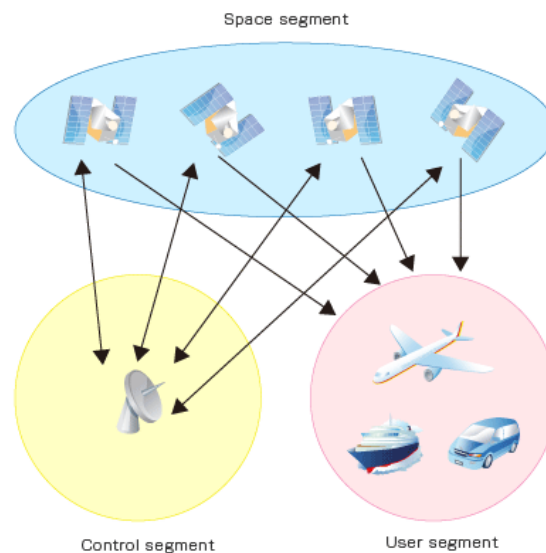


Figure 4.1.1: The three GPS segments; the space, control and user segment. credit: FURUNO (Manufacturer of marine electronics, GPS receiver chips/modules and medical appliances).

the constellation [Misra and Enge, 2011].

4.1.2 GPS Receivers and Estimation of Position

A GPS receiver must be able to capture and separate the radio frequency signal transmitted by various satellites. The receiver is performing measurements of the signal travel time and Doppler shift. Furthermore, the receiver should be able to decode the navigation code in determination of the satellite position, velocity and clock parameters, and finally estimate the users position, velocity and time.

The precision of the estimated position, velocity and time is basically determined by 1) the number of satellites and the satellite geometry i.e. the satellite position in the sky w.r.t the user. An even distribution of satellites in the view of the user gives the best geometry. 2) the quality of the pseudo range and Doppler measurements. These errors can arise as signal-in-space errors, which are errors in the navigation message parameters concerning satellite position and time, and in propagation delays due to atmospheric distortion, multipath, and receiver noise [Misra and Enge, 2011].

4.1.3 Measurements

There exist two measurement modes in GPS, code phase and carrier phase tracking. In the code phase measurement the transit time is estimated. The pseudo-ranges are found by multiplying the transit time received from a satellite with the speed of light in vacuum. Code tracking gives an unambiguous pseudo-range, which is a crude measure of distance. For real-time positioning, using a single receiver, the only option is to use code-based pseudo-ranges.

The carrier phase tracking compares the phases of the receiver generated carrier signal and the carrier received from the satellite at the measurement moment. The measure is counted in terms of cycles received since the starting point of an interval. This method is much more precise than the code phase measurements. The receiver needs to be able to lock its phase with the satellite signal, measure the initial phase difference between the receiver and receiver-generated signals, and keep on tracking the difference. The number of full cycles is tracked together with the fractional cycle at each measurement epoch.

This is much more precise than code tracking, but it is corrupted by the integer ambiguities, which is the integer number of wavelength between the satellite and the receiver doing the travel time of the signal [Misra and Enge, 2011].

4.2 GPS Errors

4.2.1 Signal Propagation Errors

The GPS signal travels between 20,000- 26,000 km through the atmosphere (ionosphere and troposphere) to the receiver. 95% of this distance is in vacuum, where the signal travels with the speed of light. The last 5% changes the velocity (speed and direction) of the signal, this is referred to as refraction. The bending effect of the signal is insignificant, while the change of speed alter the signal several meters [Misra and Enge, 2011]. With a single frequency the ionospheric RMS error can range from 1 to 50 m depending on the quality of the model, but with

two frequencies the RMS error can be lowered to centimeter or decimeter level. Also the tropospheric RMS error is in the decimeter level [Seeber, 2003]. For more about the atmospheric corrections, see Section 7.

Satellite Clock Errors

The receiver and satellite clocks are crucial in precise GPS surveying. Small errors can lead to very large code and phase errors. Inaccuracies are modeled by the control segment and send via the broadcast signal. The satellites have atomic clocks on-board for precise timing. For a single range observation the clock RMS range error is 1-2 m [Seeber, 2003].

Orbital Errors

The GPS satellites orbit position are well known, but small perturbations due to gravitational forces from the sun and the moon influence the orbit. The GPS orbital information (*ephemeris*) is available in three different ways; almanac data, broadcast ephemeris, and precise ephemeris. *Almanac data* are Keplerian orbit and perturbation parameters with an uncertainty of some kilometers (depending on the age of data). They are regularly updated and the data are broadcasted as part of the satellite signal. They contain information of the orbit and satellite clock corrections for all satellites. It is also available from various information services.

The *broadcast ephemeris* are also produced from Keplerian orbit and perturbation parameters at the monitor stations at the respective control segment. The broadcast ephemeris are predicted satellite positions within the navigation message transmitted from the satellites in real time. The message is used at the monitor station to calculate new orbital parameters and transferred back to the satellite [Hofmann-Wellenhof et al., 2008]. The accuracy is about 1 m.

Precise ephemeris are post-processed from the actual tracking data to improve the satellite position accuracy. The precise ephemeris are available from the International GNSS Service (IGS) in ultra rapid processing (3-9 hours), rapid (17-41 hours) and a final product (12-18 days). The final product has an accuracy of about 2.5 cm. Credit: IGS <http://igscb.jpl.nasa.gov/>, April 2013. During this study, the final precise ephemeris are used as orbit parameters.

4.2.2 Impact of Geometry

In GPS positioning the accuracy is depending on the accuracy of the range measurement (σ_r) and the satellite geometry expressed by the Dilution of Precision (DOP). The standard deviation of the position (σ^*) can be written as

$$\sigma^* = \text{DOP} \sigma_r . \quad (4.2.1)$$

The standard deviation of the range measurement is based on the errors described earlier. DOP is an unit less measure of the satellites number and distribution in the sky. DOP can be expressed in various ways e.g. horizontal (HDOP), vertical (VDOP), 3D positioning (PDOP), and time (TDOP), with the combined effect: $\text{GDOP} = \sqrt{\text{PDOP}^2 + \text{TDOP}^2}$ [Seeber, 2003].

DOP is computed from the covariance matrix used in GPS positioning. In this thesis, GPS is mainly used for height determination, and VDOP is minimized when satellites close to the

horizon are distributed evenly in azimuth, and when a satellite is close to zenith. An even distribution and more satellites minimizes DOP, but does not necessarily give a better estimate of the position. A higher DOP gives more scatter in the position error, it is as likely to get a low as a high position error. The RMS position error and DOP are linear. HDOP is typically smaller than VDOP, and VDOP gets larger at high latitudes because there are no satellites overhead due to the GPS satellite inclination of 55° . In the beginning of the GPS era DOP was a very important tool for accessing the data quality, but today with more GPS satellites in the constellation and receivers, which better track the satellites, smaller DOP values are achievable and the DOP measure is used in lesser extend [Misra and Enge, 2011].

4.2.3 Measurement Errors

Receiver noise is the random measurement noise coming from the antenna, cables, amplifiers, interference from other GPS signals, and signal quantization noise. The effect is small, the observation noise is 0.2 - 1 m [Seeber, 2003].

Multipath is when the GPS signal is altered via one or more paths, typically when the antenna is close to buildings, mountains etc. The error is dependent on the strength of the reflected signal and the delay between the direct and the reflected signal. The phenomena has to be taken into account when placing the GPS antenna, but the effect is already reduced in many antenna designs and by receiver manufactures.

These measurement errors are getting two magnitude lower for the carrier phase than for the code phase, and both errors are getting larger with low elevation satellites, which often are the case in the Arctic [Misra and Enge, 2011]. For a single range observation the error is 1-2 m [Seeber, 2003].

4.2.4 Combining Measurements

The carrier phase is measuring with great precision, but the measurements include satellite clock and ephemeris errors, ionospheric and tropospheric refraction, and receiver clock bias. With the carrier phase, the receiver noise and the multipath effects are getting smaller compared to the pseudo-range measurements, but the integer ambiguity complicates the matter. This problem can be surpassed by combining the carrier and code phase measurements by using single or dual-frequency. But there are other and better methods for improving the GPS measurements e.g. by using differential GPS (Section 4.3.1) or precise point positioning (Section 4.3.2).

4.3 Augmentations

Augmentation of GPS is available to improve the stand alone GPS performance. These can be Satellite-Based (SBAS) or Ground-Based Augmentation Systems (GBAS). The satellite-based augmentation system use geostationary satellites to enhance the accuracy, availability, and integrity through additional broadcast messages, where the ground-based system uses a network of reference stations.

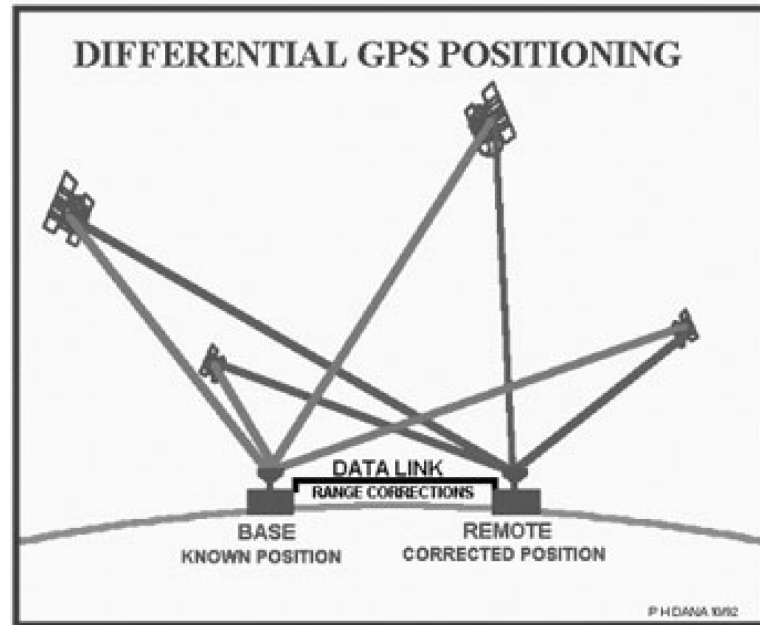


Figure 4.3.1: The basic concept of differential GPS.

4.3.1 Differential GPS

By using GPS in geodetic research, we need to improve the accuracy even more than stand alone GPS can provide. This can be achieved by using *differential GPS* (DGPS), which is taking advantage of a GPS network of ground-based reference stations. The reference stations broadcast the difference between measured satellite pseudo ranges and the actual pseudo ranges. The basic concept is shown in Fig. 4.3.1. The measurement errors are the same for users located “not far” apart, i.e. the errors correlate in both time and space, and the error estimate can be used as differential corrections to mitigate errors. This will give a decimeter-to-meter level accuracy. The closer a user is to a reference station, the shorter latency (the delay of received corrections), the higher the advantages of differential correction [Misra and Enge, 2011].

For surveys in this thesis, we have, when possible, deployed a local reference station for using DGPS or we have used permanent GPS stations, when a local station was not suitable (e.g. over long distances) or because of malfunction of the local station. Furthermore, we have post-processed data to further achieve a better accuracy. By using a reference station and post-processing we get down to a millimeter-to-centimeter level positioning accuracy.

In differential mode a lot of the errors are mitigated. Many of the GPS errors introduced in Section 4.2 correlate over space and time. The satellite clock errors are in differential mode becoming almost negligible, because the errors are the same for the pseudo-range and the carrier-phase measurements, disregarding the location of the user. The errors on the satellite ephemeris are also small. The errors change very slowly with time with an error of 2 - 6 cm/min [Olynik et al., 2002]. This will give a RMS error of ~ 0.1 m if the user is tens of kilometer from the receiver and the signal latency is tens of seconds. The measurements errors are uncorrelated in DGPS, therefore the location and the equipment are very important at the reference and user stations [Misra and Enge, 2011].

4.3.2 Precise Point Positioning

It is possible to make a centimeter-level position estimate from a single receiver by using carrier phase measurements, i.e. GPS satellite ephemeris. This method is referred to as *Precise Point Positioning* (PPP). Besides the normal errors induced in DGPS, PPP measurements induce errors which by 1. order is eliminated in DGPS. First of all the Earth's center of mass is changing with time, and solid Earth tides and ocean tides have to be considered in the processing. Other error sources in PPP are: Phase wind-up correction and satellite antenna off-set, for more information on this see [Misra and Enge \[2011\]](#).

4.4 Processing Software

For scientific processing, an understanding of the GPS signal and the associated errors are necessary. There exists a variety of processing softwares developed for scientific purposes, e.g. Bernese [\[Hugentobler et al., 2001\]](#), GIPSY-OASIS [\[Gregorius, 1996\]](#), GAMIT-GLOBK [\[Herring et al., 2008\]](#), TriP [\[Zhang, 2005\]](#) and others.

GrafNav

During this thesis, NovAtel's Waypoint GrafNav and GrafNet software are the most frequently used softwares. GrafNav is the software DTU Space use for their aircraft tracking in gravity and altimeter field campaigns. Following [Skourup et al. \[2013a\]](#) it has an accuracy down to 10 cm, and in individual cases down to 3 cm [\[Skourup et al., 2013b\]](#).

Online Positioning Services

There exist several online positioning services where it is possible to submit a GPS data file (in RINEX format) to be processed, mainly for static positioning. During this study two of those services have been used to fix the reference station coordinate: Jet Propulsion Laboratory's APPS (The Automatic Precise Positioning Service of the Global Differential GPS System). They are using the widely used processing software GIPSY (<http://apps.gdgps.net/>). Most of all I have used AUSPOS which is provided by Geoscience Australia (<http://www.ga.gov.au/bin/gps.pl>).

4.5 GPS in the Arctic

GPS is now widely used in cryosphere sciences, e.g. for glacial isostatic adjustment [\[Khan et al., 2008\]](#), ice mass loss [\[Khan et al., 2010\]](#) and icesheet flow [\[Zwally et al., 2002\]](#) and Greenland uplift and sea level rise [\[Spada et al., 2012\]](#).

In the Arctic Ocean buoys tracked by GPS are used in various applications, i.e. sea ice motion [e.g. [Kwok et al., 1998](#); [Rigor et al., 2002](#)], sea ice age [\[Rigor and Wallace, 2004](#); [Nghiem et al., 2007\]](#), ocean circulation, and for several meteorological and oceanographic applications. The buoys are provided by the International Arctic Buoy Programme managed by the Polar Science Center at University of Washington, <http://iabp.apl.washington.edu>. The buoys are besides GPS containing various other instruments. Another buoy program is the Arctic Ocean sea ice and ocean Circulation using Satellite Methods (SATICE) project, experimenting

with high-rate, high precision GPS aiming at studying the arctic sea ice dynamics and physical oceanography including ocean tide variation, freeboard heights, ice thickness, ocean dynamic topography, freshwater storage and calibration and validation of CryoSat measurements. For more information see the SATICE homepage <http://satice.icm.csic.es>.

Rivas et al. [2010] use a bistatic GPS radar for investigating the presence and condition of the sea ice cover in Arctic by extracting the permittivity and roughness of the surface from the reflected GPS waveforms.

Working with GPS in the Arctic can be challenging, and with the receding Arctic sea ice it is not only used by the scientific community, but also for navigation in a broader perspective. The limitations of using GPS in the Arctic are due to the ionospheric effects, which highly affect the satellites in these latitudes, and the positioning is also effected by the lack of SBAS satellites, which are not visible in high latitudes, and the general geometry of the GPS satellites (c.f. Section 4.2.2). For more information about GPS in high latitudes see Jensen and Sicard [2010]; Gao et al. [2012].

In Fig. 4.5.1 two examples of processing in the Arctic are shown. The GPS data are processed differentially in (a) the permanent GPS stations Kap Morris Jessup (KMJP) is processed with Jørgen Bjørnlund Fjord (JGBL) as reference. The baseline between them is 163 km. In (b) Station Nord (NORD) processed differentially with JGBL as reference. The baseline is 329 km. The figures shown from bottom to top are; the vertical elevation w.r.t. WGS84 ellipsoid, the linear residual of the filtered height, the number of satellites used in the processing, the standard deviation of the vertical position, and the PDOP. This shows how there is more noise in the longer baseline processing and a higher standard deviation.

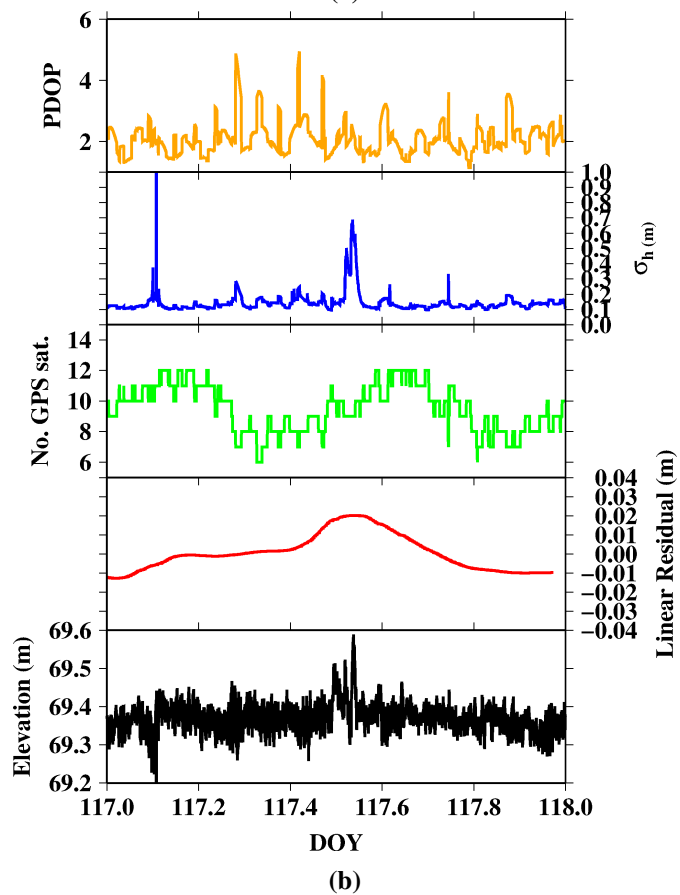
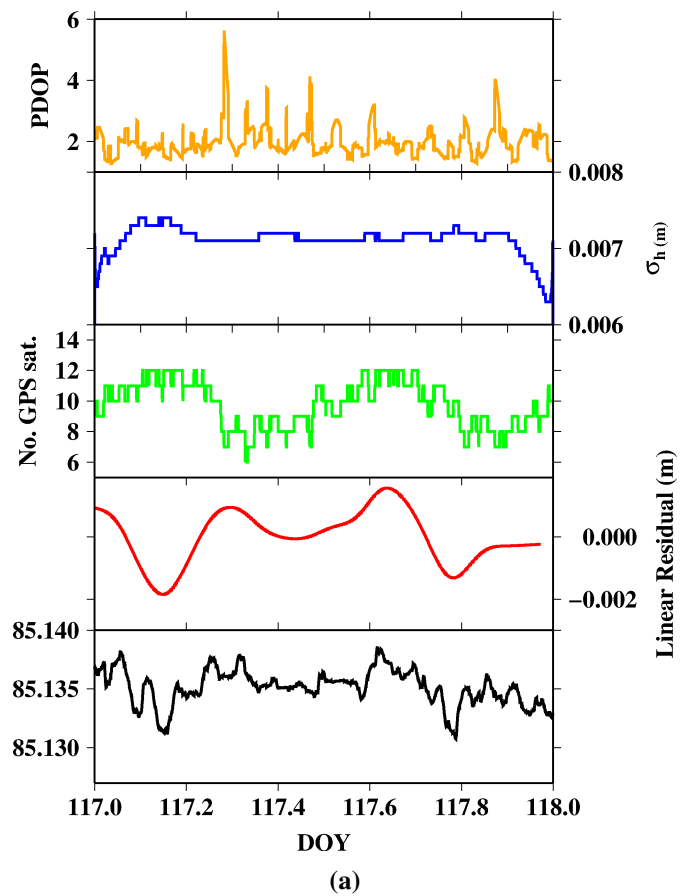


Figure 4.5.1: GPS statistics for (a) the UNAVCO site KMJP processed differentially with reference station JGBL with a baseline of 163 km., and (b) NORD processed with JGBL with a baseline of 329 km.

Description of Data

In this chapter the data used in the thesis related to the CryoSat validation are described with an exception of the actual CryoSat data. The CryoSat satellite facts will be described in Section 6.1.1, and in Section 9.1 it is described how to access and read data.

During this study several data products are used mainly for validating the CryoSat data. This includes airborne laser altimetry data from the airborne campaigns CryoVEx (Section 5.1.1) and OIB (Section 5.1.2). Airborne and satellite imagery are also used in this study; DMS imagery from OIB and ASAR images from Envisat (Section 5.2.1) and MODIS from the Terra and Aqua satellites (Section 5.2.2).

Ice data in form of ice edge and ice type are also used (Section 5.3) to make sea ice thickness maps from CryoSat data. First, the Airborne Campaigns are described.

5.1 Airborne Campaigns

In this section, data from the airborne campaigns are described, with focus on their airborne laser altimeter systems. A scanning airborne laser is measuring the elevation of the surface by timing the laser pulses from the aircraft, reflected from the ground and returned to the aircraft.

5.1.1 CryoVEx

The CryoSat Calibration and Validation Experiment (CryoVEx) started in 2003 with extensive validation campaigns to gather a multitude of ground truth measurements carried out in the Arctic prior to the launch of the first CryoSat mission. It now continues for CryoSat-2. Since the first CryoVEx campaign there have been several campaigns. The last one was in spring 2012, and a new campaign is planned for spring 2014.

The objective of CryoVEx is to provide pre-launch and post-launch reference datasets for CryoSat. Measurements of ice sheet elevations and sea ice thickness are undertaken, and ice profiles from the measurements are done. The campaign is in particular aimed at understanding miscellaneous sources of error: snow loading, ice density, radar penetration, preferential sampling and various freeboard measurement errors. CryoVEx is a joint effort of ESA, DTU Space, Alfred Wegener Institute (AWI), and other European and Canadian Institutes.

The campaigns consist of airborne radar and laser altimetry, EM sounding, and in-situ observations. After the successful launch, underflights of CryoSat were performed together with overflights of ground teams performing in-situ measurements over both sea ice and ice caps and glaciers. OIB has also been part of the calibration and validation campaigns in several coordinated surveys, and data from one of these joint surveys April, 2 2012 are in focus in this thesis.

Airborne Laser Scanner

The Airborne Laser Scanner (ALS) instrument is a Riegl LMS Q-240i type laser scanner operating at a wavelength of 904 nm and with a pulse repetition frequency of 10 kHz. It has an opto-mechanical scan mechanism providing linear and parallel scan lines with a 60° scan angle. In both study areas the Twin Otter flew with an average altitude of about 340 m (1000 feet) yielding a horizontal point resolution of 0.7 m × 0.7 m at a ground speed of 250 km/hr. The across-track swath corresponds roughly to the altitude of the airplane.

The aircraft location is determined by GPS techniques and the attitude (pitch, roll and heading) recorded by inertial navigation systems (INS). Calibration of the ALS misalignment angles between ALS and INS are estimated by sequential overflights of a building of which the coordinates of its corners are known to high precision. The vertical accuracy of ALS is on the order of 5 - 10 cm depending mainly on the uncertainties in the GPS solutions. Data are provided relative to the WGS-84 reference ellipsoid [Skourup et al., 2013b].

5.1.2 Operation IceBridge

NASA's Operation IceBridge (OIB) mission, initiated in 2009, is the largest airborne survey of Earth's polar ice ever flown. It is supposed to collect airborne remote sensing measurements to bridge the gap between NASA's Ice, Cloud and Land Elevation Satellite (ICESat) mission and the upcoming ICESat-2 mission. Data are provided by NSIDC, and it is planned to continue for a six-year period. Just to mention a few, OIB is, besides the instruments described below, flying with an accumulation radar, snow radar, magnetometer, K_u-band radar, infrared radiation pyrometer, and meteorological instruments.

Airborne Topographic Mapper

The Airborne Topographic Mapper (ATM) is the OIB LiDAR instrument mainly used for mapping the topography of the changing Arctic and Antarctic icecaps, glaciers and sea ice. The topography is measured by the ATM as sequences of points scanned conically in a swath along the aircraft flight track at rates up to 5000 measurements per second.

Here the OIB Narrow Swath ATM L1B Qfit Elevation and Return Strength dataset [Krabill, 2012] is used. The processing done by NSIDC in this level is: applying the calibration factor to convert time of flight to range; scan pointing angles and interpolate attitude to each LiDAR measurement; processing GPS data into the aircraft trajectory and determine the biases and offsets; finally the surface elevation (with respect to the ellipsoid) is given by the qfit program provided by NSIDC with all the biases and offsets incorporated. The elevation is given for each laser pulse without any re-sampling. The elevation measurement files contain qfit 32 bit binary data. Here the c-version of the qfit program to read the qfit files is used.

The ATM operates at 532 nm with a pulse repetition frequency of 5 kHz. It is a conically scanning device with a 22.5° scan angle. The nominal across-track resolution is 400 m with an average point density of one laser shot per 10 m^2 . OIB also has an ATM narrow swath scanning device with an angular swath width of 2.7° off-nadir, giving a nominal ground swath of 45 m with a frequency of 3 kHz. The aircraft's attitude was also monitored by an INS. The surface elevation accuracy over sea ice is expected to be better than 10 cm [Farrell et al., 2012] and given relative to the WGS-84 reference ellipsoid [Krabill, 2012].

DMS Imagery

The L1b product of the Digital Mapping System (DMS) camera consists of geolocated and orthorectified images [Dominguez, 2012]. The DMS image resolution varies with aircraft height. The pixel size is about $10 \times 10\text{ cm}$, and at an altitude around 480 m, this results in an image size of about $690 \times 775\text{ m}$.

5.2 Satellite Imagery

Satellite imagery is a very useful tool for monitoring sea ice and validating satellite data, especially in the context of ice movement, deformation and in lead detection. In this study the imagery is used to validate leads.

5.2.1 Advanced Synthetic Aperture Radar

Envisat carried, besides the radar altimeter (see Section 6.1), the Advanced Synthetic Aperture Radar (ASAR). ASAR images are widely used by the sea ice community, e.g. to calculate daily sea ice drift patterns (Section 10.4), and are very useful for a visual inspection of the current sea ice conditions. The instrument operates in the C-band and can operate in different modes of polarization. The pixels in the radar images are represented by the backscatter from the ground. A low backscatter is shown as dark areas, implying that little energy is reflected back to the satellite, whereas high backscatter is represented with a brighter color, and large amounts of the data are transferred back to the satellite, i.e. the brighter the backscatter on the image, the rougher the surface is. The resolution of the images used in this study is about 100-150 m [Resti et al., 1999; ESA, 2007a, 2013]. Unfortunately, ESA lost contact to Envisat April, 8 2012, and the data were therefore not available for the second study area April 27, 2012. Credit: NASA at <http://modis.gsfc.nasa.gov>.

5.2.2 Moderate-Resolution Imaging Spectroradiometer

MODIS is a Moderate-Resolution Imaging Spectroradiometer and is a payload on-board the NASA satellites Terra and Aqua. The satellites cover together the entire Earth in one to two days. The satellites are operating in 36 spectral bands, two bands are imaged at a resolution of 250 m. This is the resolution used in this study, where the MODIS Level 3 datasets are used. The images are in the visible spectrum and therefore affected by cloud cover. Changes in cloud cover are actually one of the instrument's main objectives but ambiguous to sea ice observations.

5.3 Sea Ice Data

In the making of sea ice thickness maps in the Arctic, knowledge of the ice edge and ice type (first-year or multi-year ice) is crucial to filter out unwanted data and to apply the right snow and ice densities to the thickness retrieval (Section 8.1.2).

5.3.1 Ice Edge and Ice Type Data

The sea ice type (Fig. E.5.1) is classified using gridded data from the Norwegian Meteorological Service Ocean and Sea Ice Satellite Application Facilities (OSI SAF) system.

OSI SAF are using data from the Special Sensor Microwave/Imager (SSM/I) and the Advanced Scatterometer (ASCAT) to classify the ice edge together with the sea ice in first-year ice and multi-year ice. SSM/I is carried on the United States Air Force Defense Meteorological Satellite Program (DMSP) to measure the brightness temperature, and the polarization ratio (19 and 85 GHz), i.e. the normalized difference between horizontal and vertical brightness temperature. It also measures the gradient ratio, i.e. the normalized difference in brightness temperature between 37 and 19 GHz. ASCAT is flown on-board the Meteorological Operational satellite programme (Metop) by ESA. ASCAT measures the backscatter, and takes advantage of the difference between the relative isotropic behavior over sea ice and the anisotropic behavior over water.

A multi-sensor system of both SSM/I and ASCAT data are used to detect the ice edge and identify the perennial and annual ice types. In the ice type classification, the internal scattering of multi-year ice is used to separate the ice types by looking at the change in radiation. For scatterometers, the normalized backscatter is dependent on the ice age, rough multi-year ice giving larger backscatter. In winter, the multi-year ice will also have an enhanced scatter compared to first-year ice due to volume scatter. In Summer (June-September), it is difficult to classify the ice types mainly due to melt. For more information about the multi-sensor system used at OSI SAF, see Eastwood et al. [2012].

Chapter 6

Satellite Altimetry

This chapter aims at describing the principles of satellite altimetry, namely radar altimetry, and its applications to sea ice analyzes. It is the intension only to describe the basic principles of radar altimetry to give an overview of the different retracking methods, and in more detail to describe the threshold retracker used in this thesis.

6.1 Satellite Altimeter Missions

Laxon et al. [2003] were the first to show a sea ice thickness map over the Arctic Ocean from satellite altimetry. The results were carried out from the European Remote Sensing Satellites ESR-1 and ESR-2, carrying a Ku-band (13.8 GHz) Radar Altimeter (RA), extending to 81.5°N/S. ESR-1 operated from 1991-2011 and ERS-2 from 1995-2011 [ESA, 2011b].

Envisat is another ESA satellite launched in 2002, as a successor to ERS-2, with an improved radar altimeter (RA-2, 13.575 GHz) and a higher *Pulse Repetition Frequency* (PRF). This gives the number of pulses per second, which means more measurements per second resulting in a better accuracy. The nominal footprint was 2-10 km. Unfortunately, ESA lost contact to Envisat in April 2012. There exists several sea ice thickness studies based on data from the Envisat satellite [see e.g. Giles et al., 2008; Connor et al., 2009].

NASA's Ice, Cloud, and Elevation Satellite (ICESat), operating between 2003-2010, was the first satellite dedicated for measuring the cryosphere. The satellite carried a laser altimeter system on-board and was suppose to measure the elevations of the ice sheets, ice caps, glaciers, and their elevation changes. ICESat had a geographical coverage up to 86°N/S with a footprint size of about 65 m [Schutz et al., 2005] and an elevation precision over a flat sea ice surface of about 2 cm [Kwok et al., 2006]. References for sea ice elevations based on ICESat measurements are e.g. Kwok [2004]; Forsberg and Skourup [2005]; Kwok et al. [2007]; Zwally et al. [2008]; Connor et al. [2013] and others.

6.1.1 CryoSat

The only ongoing altimeter satellite suitable for measuring sea ice elevations, is CryoSat. It is an ESA satellite, and was launched April, 8 2010. CryoSat is dedicated to monitor the changes in the sea ice thickness as a primary objective, and the mass balance of the ice sheets and

variations of major glaciers as a secondary objective. It has, however, proven to be valuable for other applications including marine gravity, sea level, coastal areas, inland waters, and land. The mission duration was originally estimated to be three years after eight months of commissioning phase. This time is soon exceeded, and the ground team expects the satellite to keep monitoring until at least 2020. CryoSat has a non-sun-synchronous orbit with inclination of 92° , which resolves in a geographical coverage up to 88°N/S , and it is now possible to observe more of the Arctic Ocean than ever before. CryoSat has a mean altitude of 717 km and a repeat cycle of 369 days, with a sub-cycle of 30 days. This gives a very dense track coverage, yielding a equatorial track spacing of 8 km.

The K_u -band (13.6 GHz) radar altimeter on-board the satellite is called SIRAL (SAR / Interferometric Radar Altimeter) and it measures in one of three modes at a time: The *Low Resolution Mode* (LRM), the SAR mode, and the *SAR Interferometry* (SARIn) mode. The LRM mode is a conventional pulse-limited radar altimeter operating over the oceans and the interior of the ice sheets. The SAR mode is mainly operating over the sea ice covered regions, and by taking advantage of the Doppler effect to divide the footprint into several slices along-track the radar bursts can be combined to reduce the instrument footprint and the speckle noise. Using this technique the footprint becomes about 300 m along-track and 1500 m across-track. The SARIn mode is operating over areas with steep terrain, such as the margins of the ice sheets. In this mode, SIRAL is using its two antennas where the signal between the two phases are used to derive the echo.

In the Arctic Ocean there is a test area called the “Wingham box” after Duncan Wingham, a British scientist who originally proposed the CryoSat mission to ESA, where the SARIn mode is switched on. Here, the use of CryoSat’s two antennas are tested over a sea ice covered region to evaluate the signals from off-nadir specular surfaces. In the SAR/SARIn mode, the across-track direction is defined as LRM by the pulse-limited width. In the along-track direction the illuminated area for SIRAL is defined as the sharpened beam-limited area. In this study, only data from the SAR mode are used, and therefore the focus will be on this mode. Satellite facts of the SAR mode are summarized in Table 6.1.1. The satellite requirements of residual

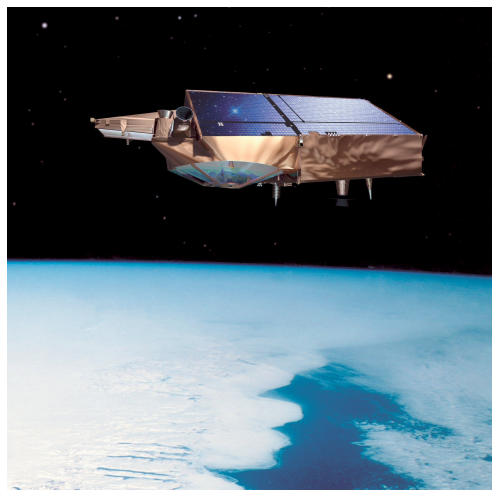


Figure 6.1.1: Artistic picture of CryoSat in orbit, adapted from *European Space Agency* [2010].

Parameter	Value
Mean altitude	717.242 km
Inclination	92.00°
Orbit	Non sun-synchronous
Repeat cycle	369 days, 30 days sub-cycle
Antenna footprint	15 km
Antenna gain	42 dB
Radio frequency	13.575 GHz
Pulse bandwidth	320 MHz
PRF	18.181 kHz
Burstmode PRF	85.7 Hz
Wavelength	2.2 cm
Sample interval	0.2342 m
Samples per echo	128
Pulses per burst	64
Burst repetition interval	11.8 ms
Size of range window	30 m

Table 6.1.1: Facts about CryoSat SAR mode, [ESA, 2007b; ESA and UCL, 2013a]

uncertainty and measurement error are 3.5 and 1.6 cm/year, respectively, for an areal extent of 10^5 km^2 Arctic sea ice in the end of the mission. The residual error is a relationship of the natural variability and the measurement error [ESA, 2003; ESA and UCL, 2013a].

6.2 Basic Principle of Radar Altimetry

Satellite altimeters are nadir-pointing active microwave instruments, emitting signals with a frequency range of 2 – 18 GHz and receiving the echo from the surface after its reflection.

The altimeter measures the range (R_0) from the satellite to the ground by measuring the time it takes the transmitted electromagnetic pulse to reach the surface at nadir and return to the altimeter. This is the two-way travel time (t). As the electromagnetic waves travel with the speed of light c (in vacuum), the range can be written to a first approximation as

$$R_0 = \frac{ct}{2} . \quad (6.2.1)$$

In reality, the electromagnetic waves travel through the atmosphere where they are refracted by particles, which reduce the speed of the wave. Therefore, the range R_0 has to be corrected for atmospheric refraction and instrument errors (R_i) in order to obtain the true range R [Fu and Cazenave, 2001].

$$R = R_0 - \sum_i R_i . \quad (6.2.2)$$

The corrections are described in more details in Section 7. The ellipsoidal height (h), i.e. the elevation of the surface above a reference ellipsoid, where the reference ellipsoid is defined as

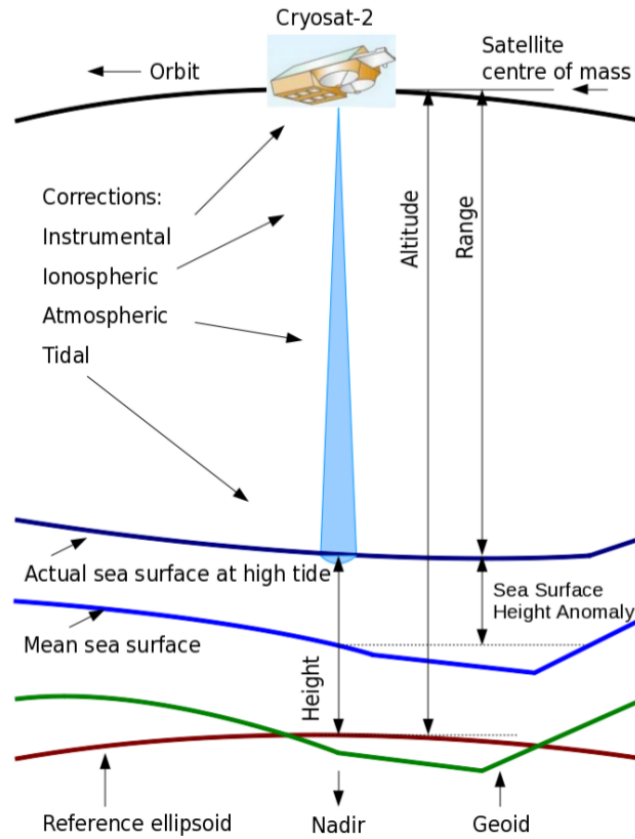


Figure 6.2.1: Corrections on altimeter range measurements and the relation between heights, [ESA and UCL, 2013a].

the ellipsoidal surface approximating the mean SSH, is given by

$$h = H - R \quad , \quad (6.2.3)$$

where H is the satellite altitude above the reference ellipsoid. These heights are schematically shown in Figure 6.2.1 together with the various corrections. The altitude is determined by a very accurate *precise orbit determination* (POD) system such as GPS, Doris or laser telemetry. CryoSat is using Doris (Doppler Orbit and Radio positioning Integration by Satellite), which is based on the principle of the Doppler effect with a transmitting terrestrial beacons network and on-board instruments on the satellite's payload. For more information about DORIS visit <http://ids-doris.org/> and <http://www.avis.oceanobs.com>.

6.2.1 The reflected signal - Waveforms

The shape of the reflected signal is called a *waveform* (Fig. 6.2.2), and it represents the time progress of the reflected power as the radar pulse reaches the surface. It is processed by the

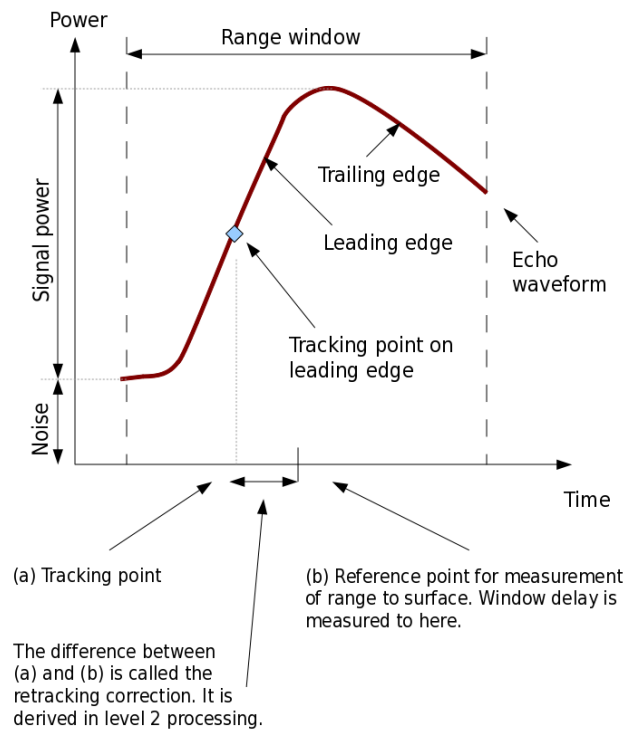


Figure 6.2.2: Idealized altimeter waveform from a diffuse scattering surface such as open ocean and its characteristics with a sharp rising leading edge and a slow decaying trailing edge. Also the tracking point is marked, this is the mean surface. Credits ESA and UCL [2013a].

on-board tracker system to derive the range and power within the *range window* specified by the width of the frequency spectrum. The altimeter maintains acquisition around the orbit by keeping the signal within the range window. In the CryoSat SAR mode, the range window is about 30 m and covered by 128 samples. There is 23.24 cm between each sample or *range bin*. By measuring the range and shape of the waveform, knowledge of the reflecting surface can be achieved. In other words, the waveform shape depends on the scattering surface.

The waveforms illustrated in Fig 6.2.2 are often called *ocean-like* or *Brown-like* with a characteristic sharp rise, the *leading edge*, up to maximum power, followed by a slowly decreasing slope, the *trailing edge*. The *retracking point* is a specific point on the leading edge used to mark the point for measuring the range to the surface. This is described in more details in Section 6.3. This waveform-type is a typical waveform over a diffuse surface such as ocean or sea ice for a conventional altimeter. Samples from the leading edge correspond to the time, where the pulse first hits the surface (at nadir). Samples from the trailing edge represent the received power from points further and further away from nadir.

Small changes (mm-scale) in surface roughness change the shape of the waveform [Laxon, 1994a]. The radar signal is scattered when hitting a rough surface, and the surface is said to be diffuse. Therefore, the power return from a rough surface gives a waveform with asymmetric shape, and with a slow trailing edge.

Over a smooth, flat surface the radar return is characterized by a high power, a sharp leading edge followed by a rapid decaying trailing edge. The power can be three times larger in such

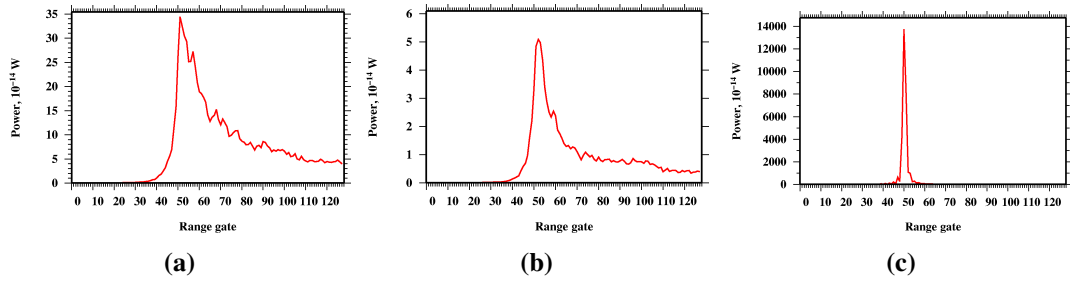


Figure 6.2.3: Example of “real” CryoSat SAR waveforms over ocean (a), ice (b) and lead (c). The waveforms are given by the power as a function of range gates i.e. range measurement.

a return. The peaks in the waveform may come from specular and coherent reflections from smooth surfaces near nadir, while diffuse reflections from rough surfaces occur in later off-nadir gates [Fetterer et al., 1992].

The open ocean is a typical diffuse surface, and the shape of the waveforms are very similar, but varies due to e.g. wave height. The sea ice waveforms are more varied, and contains both diffuse (ice floes and ridges) and specular waveforms (leads and new ice). Waveforms over first-year ice will typically have a higher power compared with multi-year ice, due to its smoother surface. Particularly occurring in areas with small ice floes and leads, echoes from specular surfaces off-nadir tend to influence the waveform; this is known as *snagging*.

In Fig. 6.2.3 three “real” waveforms from CryoSat SAR mode are shown for (a) ocean, (b) ice and (c) over a lead. The waveforms are given as return power in watt as a function of range gates (i.e. time).

Comparing the ocean waveform from SAR and conventional altimetry (Fig. 6.2.2) clearly show a more sharp waveform from SAR. The waveforms shown are carefully picked to best resemble the most idealized waveforms for each surface type, however many of the CryoSat waveforms are not this nice. They often have multiple peaks, a slow rise and kinks in the leading edge.

6.2.2 Pulse and Beam Limited Altimeters

In principle two altimeters exist; the beam-limited and the pulse-limited. Most radar altimeters are pulse-limited, while laser altimeters are beam-limited.

The beam-limited altimeter’s return pulse is given by the width of the beam. The corresponding footprint is defined as the whole area on the Earth surface illuminated by the beam echo. The footprint size depends only on the satellite altitude (H) and the beam width (ϑ) at -3 dB (Fig 6.2.4). Assuming a flat Earth, the beam-limited footprint can be approximated as

$$D = 2H \tan \frac{\vartheta}{2} . \quad (6.2.4)$$

A narrow beam requires very large antennas, which are physically difficult in satellite constructions. This results in difficulties in getting large horizontal resolutions. An advantage of the beam-limited altimeter is the range insensitivity of the small (≈ 1 degree) pointing errors [Fu and Cazenave, 2001; ESA and UCL, 2013a].

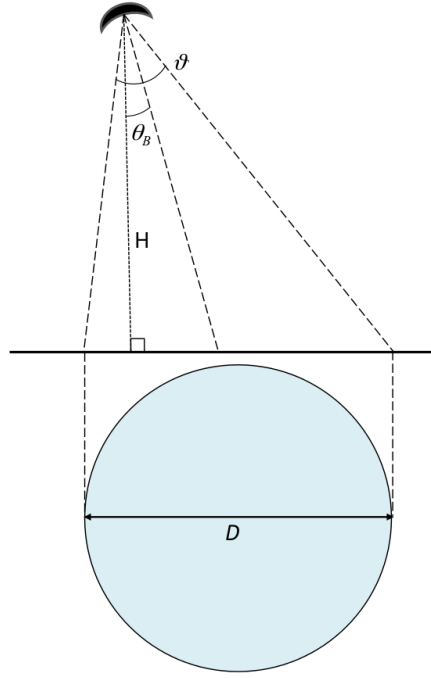


Figure 6.2.4: Footprint D of the beam-limited altimeter. H is the satellite altitude, θ_B the beam width at -3 dB, and θ is the beam direction w.r.t. nadir [ESA and UCL, 2013a].

A pulse-limited altimeter has a wide beam, however it is limited by its pulse. For conventional altimetry, the footprint only depends on the compressed pulse duration. The principle of the pulse-limited altimeter is shown in the left-hand side of Fig 6.2.5. This is an idealized example of a calm ocean surface. The top of the figure shows the spherical expansion of the altimeter pulse as it approaches the surface. Blue indicates the time t where the pulse hits the surface. The middle figure shows the area on the surface illuminated by the radar pulse, which varies linearly in intensity over time until the back of the pulse arrives at the surface (the blue circle, $t = \tau$, τ is the pulse duration). This corresponds to the area illuminated by the leading edge of the pulse until the time the trailing edge first intersects the surface. Afterwards, an annulus of constant area, increasing diameter and thinner thickness is illuminated, and the time $t = t + \tau$, $t = t + 2\tau$, \dots . The received power decay due to the antenna beam width and off-nadir scattering corresponds to the waveforms trailing edge.

The radius r_p of the circular area of the pulse-limited footprint can be approximated to

$$r_p = \sqrt{H \frac{c}{B}}, \quad (6.2.5)$$

given by the satellite altitude H , the speed of light c and the pulse bandwidth B [Walsh et al., 1978; ESA and UCL, 2013a]. The waveforms are typically averaged by the ground processing team to reduce fluctuation and eventually to make a better height estimate.

6.2.3 SAR Altimeter Principles

The first principle objectives of the SAR altimeter were to operate more efficiently and more effectively i.e. to sharpen the pulse in the along-track direction, so the SAR altimeter could use more of the instrument's radiated energy than was the case for a conventional beam-limited altimeter [Raney \[1998\]](#). The objective of having a SAR altimeter as the principle payload on CryoSat was to utilize the sharpened pulse to narrow the along-track resolution to better fit the diversities of a typical lead in the Arctic [\[Wingham et al., 2006\]](#).

The SAR altimeter, sometimes called the *delay/Doppler altimeter*, is taking advantage of the forward motion of the altimeter, by using the Doppler effect to divide the radar footprint into many along-track strips. The PRF is large, and each burst of pulses is coherently correlated, superimposed on each other, pointing on a specific strip of the Earth surface, this is called *stacking*. The Doppler beams are averaged to reduce the speckle noise. The averaging of a stack of beams into one waveform are called *multi-looking*.

The Doppler principle results in a narrow along-track footprint and together with the signal processing of the multiple looks. This results in a waveform with a steeper leading edge, a faster decaying trailing edge, and a response more than 10 dB stronger at the peak power than when compared to the conventional altimeter [\[Raney, 1998\]](#). This is shown on the right-hand side of Fig. 6.2.5.

The width of the illuminated area in CryoSat SAR/SARIn modes is, as mentioned in Section 6.1.1, defined independently in the along-track and the across-track direction. In the across-track direction, the area width is defined as the pulse-limited width in LRM (Eq. 6.2.5), and in the along-track direction the illuminated area is defined as the sharpened beam-limited area. This is the *pulse-Doppler-limited* area, and it can be approximated as a rectangle area given by the pulse-limited and the sharpened beam-limited area. The along-track sharpened beam-limited area x_D is given by

$$x_D = H \frac{\lambda}{2v} \frac{\text{PRF}}{64} , \quad (6.2.6)$$

where H is the satellite altitude, λ is the wavelength, and PRF is the pulse repetition frequency [\[ESA and UCL, 2013a\]](#).

For CryoSat, $\lambda = 2.2$ cm, $\text{PRF} = 18.181$ kHz, and the pulse-limited across-track width is about 1.64 km, calculated using Eq. 6.2.5 as the double radius. The sharpened beam-limited area width in the along-track directions is 299 m ($2x_D$), which yields an area of 0.49 km² with a satellite height of 717 km and a speed of 7500 m/s.

6.3 Retracking

It is out of the scope of this study to describe retrackers in detail, and the goal is merely to give a short overview of the concept and the most widely used methods.

As already mentioned in Section 6.2.1, the on-satellite processor, or on-board tracker, is used to gain information about the range the signal travels from the radar to the surface and back. The on-board tracker is biased due to the surface roughness and the size of a sampling bin, and therefore the on-board range estimate is coarse.

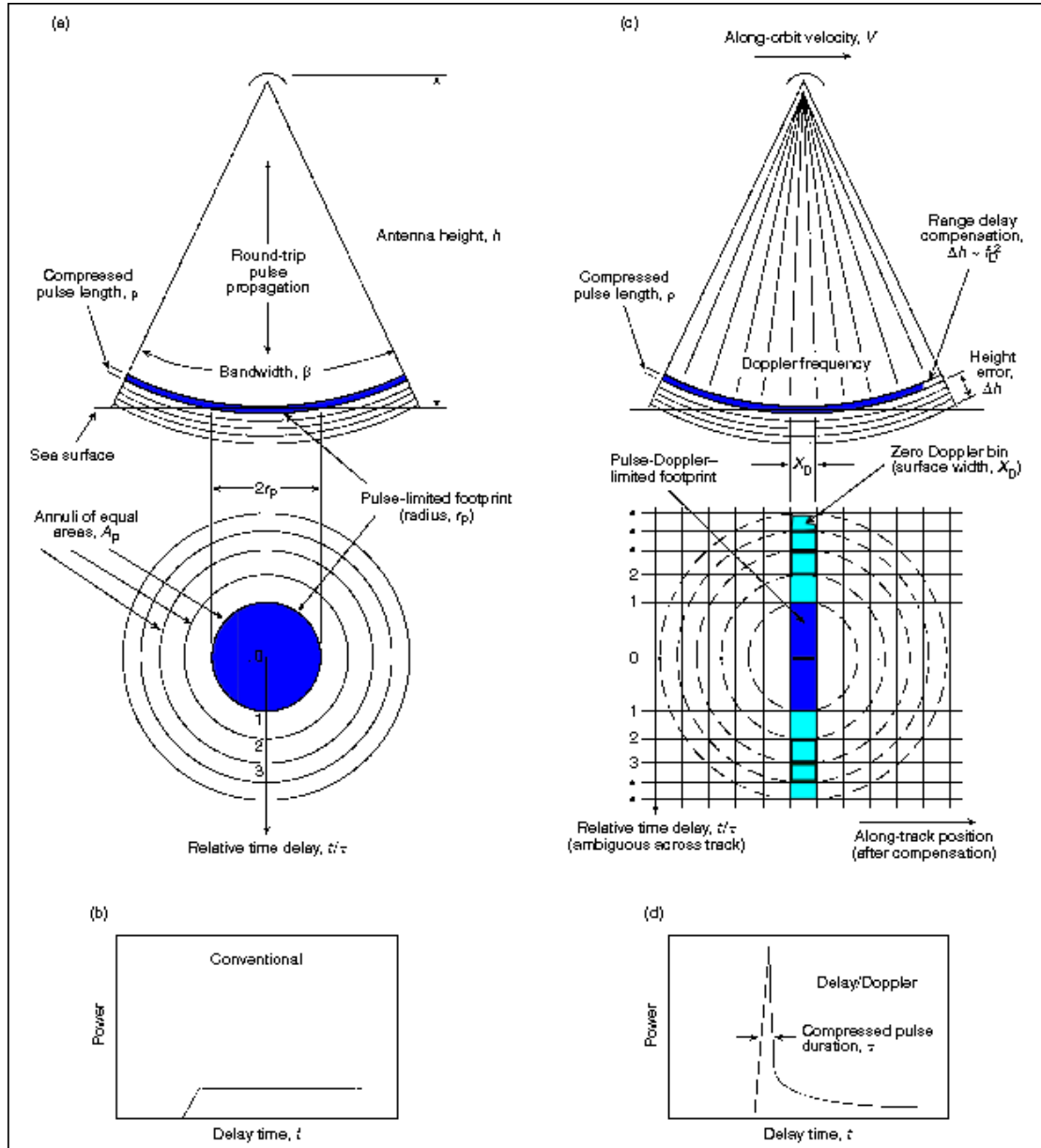


Figure 6.2.5: Principles of conventional altimetry (left) versus SAR altimetry (right). With courtesy Johns Hopkins University/Applied Physics Laboratory and ESA. The top part of (a) and (c) shows the geometry of the spherical expansion of the radar pulse. The bottom part shows the area illuminated by the radar pulse as a function of the relative time delay. (b) and (d) show the difference of a waveform from a conventional altimeter and from a SAR. The SAR waveform is more spiked, and has a much higher power.

The aim of the ground-based retracking is to fit a model or functional form to the waveforms and then to retrieve geophysical parameters such as the range, echo power, etc. By combining the range measurement of the tracker range with the retrieved epoch by retracking gives the final range measurement.

Retracking altimeter data is achieved by estimating the departure of the waveform's leading edge from the altimeter tracking gate and then correcting the satellite range measurement accordingly.

Following [ESA and UCL \[2013b\]](#), the surface height with respect to the reference ellipsoid is then

$$h = H_{sat} - (R_r + \text{Geophysical Corrections}) . \quad (6.3.1)$$

Two methods of waveform retracking exist; physical and empirical methods. The physically-based retrackers are computed from physical models with knowledge of microwave scattering at nadir. They often include the Brown-type waveforms as a convolution of the average impulse response from a flat surface, the surface elevation probability density function of specular points within the altimeter footprint, and the radar system point target response. The method is described in more details in [Brown \[1977\]](#). This type of retracking is often more comprehensive than the empirical methods and need a great deal of information of for example the physics of the sea ice. Furthermore, the Brown-model does not deal properly with the diverse ice cover, [\[Deng, 2003\]](#).

The empirical methods can be divided into statistically based properties and those based on fitting empirical functions to the waveform. The offset center of gravity (OCOG) retracking is of the statistical kind and developed by [Wingham et al. \[1986\]](#). It is simple, robust, and easy to implement. In short, the principle of the OCOG retracker is to define a rectangle about the center of gravity of the waveform and then to calculate the amplitude and the width of the waveform. The resulting output is the position of the leading edge.

[Davis \[2002\]](#) has developed the threshold retracker, which was originally intended for measuring ice-sheet elevations. The position of the leading edge of the return waveform is derived by locating the first range bin to exceed a percentage of the maximum waveform amplitude. This could be achieved by the OCOG amplitude. This is the retracker developed in this study. It is described in more details in Section 6.3.1.

Another widely used retracker is the β -retracker developed by [Martin et al. \[1983\]](#). This is a fitting algorithm given with a 5- or 9-parameter functional form of the returned power to fit single or double-ramped waveforms, respectively. The Ice Altimetry Group at NASA's Goddard Space Flight Center (GSFC) has developed a series of retracing algorithms for ice sheet and sea ice waveforms based upon this method.

Due to the complexity of the sea ice cover with a mixture of ice and water, the normal approach is to use a simple statistical retracker over the ice and to make a Gaussian fit over the over leads. This is done to pick the same part of the specular form every time, which could be a problem for a threshold retracker due to discrete waveform sampling and the diffuse part of the waveform [\[Armitage and Davidson, 2013\]](#). For CryoSat there is also developed a special empirical CryoSat retracker by [Wingham et al. \[2006\]](#), which is based on six fitting parameters and five segments to represent the waveform. It is developed to simulate the theoretical model

of a multi-looked SAR altimeter echo. A simplified version is developed by [Giles et al. \[2007\]](#) with only three segments. In [Laxon et al. \[2013\]](#) they use a 50% threshold retracker over the ice floes and a Gaussian fitting algorithm over the leads.

6.3.1 Threshold Retracker

We have chosen the threshold retracker to be implemented as the waveform model. To implement this the thermal noise (P_N), is determined as

$$P_N = \frac{1}{5} \sum_{i=\tilde{n}}^{\tilde{n}+4} P_i , \quad (6.3.2)$$

where P_i is the power at the i th gate and \tilde{n} is the first unaliased waveform (sometimes the first data is aliased and should not be used in the thermal noise estimate). The threshold level can be computed as

$$T_l = P_N + \alpha(A - P_N) . \quad (6.3.3)$$

α is the threshold value, i.e. the percentage of the maximum waveform amplitude above the thermal noise level, A is the maximum amplitude. Finally, the retracking gate can be written as

$$G_r = (\hat{n} - 1) + \frac{T_l - P_{\hat{n}-1}}{P_{\hat{n}} - P_{\hat{n}-1}} , \quad (6.3.4)$$

where \hat{n} is the location of the first gate exceeding the threshold level T_l . In the case of $P_{\hat{n}-1} - P_{\hat{n}} = P_{\hat{n}-1}$, the fraction in Eq. (6.3.4) is undefined, and the retracking gate is set to $(\hat{n} - 1)$.

[Davis \[2002\]](#) found that a threshold level from 7 – 10% gives the values with the smallest standard deviations due to the more noisy higher amplitude waveforms. The low standard deviation is especially the case for ice-sheets due to their irregular nature.

The first return of the waveform, from the leading edge, is the only unambiguous point in the waveform as it comes from the surface closest to the satellite. This value is good when looking at elevation changes, but looking at sea-ice we are more interested in an average surface elevation. When the altimeter waveform is dominated by surface scattering, the half-power or threshold value of 50% represents the mean surface elevation. This is also the value used in various studies when determining the range from the satellite to the sea-ice (see [Peacock and Laxon \[2004\]](#) among others).

6.3.2 Typical Errors over Sea Ice

CryoSat is using Automatic Gain Control (AGC), where AGC constantly adjust the gain of the on-board receiver from the previous measurements to achieve the maximum signal-to-noise ratio. In practice this means that over the ocean the half-power of the waveform should be in the middle of the range gate window. The sea ice waveform has a very rapid rise and fall compared

to ocean waveforms, and the leading and trailing edges can entirely lay within the middle range gate. This could cause a large negative height error, causing the tracker to shift, so subsequent pulses appear later in the range window. This is called *tracker oscillation*. This can of course be corrected for in the retracking if the waveform sampling is performed without errors. Sampling errors in themselves can result in double peaked waveforms when e.g. the topography varies rapidly. A combination of waveform sampling and tracker oscillations also gives rise to shifted and blurred or doubled peak waveforms, referred to as *height glitch*.

Another artifact in radar altimeter data are the off-ranging or the snagging, which result in an underestimation of the elevation. It often occurs in the transition from a high power return at nadir e.g. from a lead to sea ice floe.

In early radar altimeter missions such as Geosat another common error over sea ice was the antenna off-pointing error, where sometimes the waveform disappeared from the range window due to lose of lock [Fetterer et al., 1992].

Geophysical Parameter Corrections

Signals from satellites travel many kilometers from the satellite to the ground and maybe back again. The signal is delayed due to the atmosphere. The Earth is a dynamic place, the oceans level changes in the Arctic Ocean due to the attraction of external objects (Sun, Moon, planets), atmospheric pressure loading, and rotation of the Earth.

These geophysical parameters need to be corrected to retrieve a surface elevation from satellite, whether it is GPS or an altimeter satellite. This chapter deals with these parameters. In the end of the chapter the range of the corrections are summarized (Table 7.4.1) together with the models used and error estimates, if available. The range are an estimate of values from the CryoSat product March 2013 from the Arctic Ocean covering 60°N to 88°N. Typical correction values are in the Chapter referred to the magnitude of a winter value at 80°N averaged over one month and 10^4 km^2 , given by [Wingham et al. \[2006\]](#).

7.1 Atmosphere

The radar pulse and the GPS signal is delayed when traveling through the atmosphere due to refraction. The troposphere is the lower part of the atmosphere, and its depth is varying from about 16 km in the tropics to about 9 km over the poles.

7.1.1 Tropospheric Correction

The troposphere is non-dispersive for the radar signal and GPS frequencies. The troposphere consists of a wet and a dry component, which has to be modeled independently.

The wet tropospheric correction is the delay due to the liquid water in the atmosphere, a typical magnitude for the correction is 0.01 m, and ranging from -0.115 to -0.004 m in the CryoSat product for March 2013. In the CryoSat product the correction is provided from Meteo-France via SSALTO (Segment Sol multi-missions d'Altimétrie, d'orbitographie et de localisation précise) and based on data from the European Centre for Medium-range Weather Forecasts (ECMWF) [[ESA and UCL, 2013a](#)].

For radar altimetry the dry tropospheric correction is the correction for the dry component of the atmosphere refraction and path delay. The March 2013 range is from -2.4 to -1.9 m,

and is the largest correction in the CryoSat product. A typical correction magnitude for 80° is 2.3 ± 0.02 m.

The dry tropospheric correction is computed by the CryoSat processor from the dynamic mean surface pressure grids and monthly S1 and S2 tide grids from the same source as above [ESA and UCL, 2013a].

A GPS network can estimate the water vapor content over larger areas. The GPS signal is slower than in free air, appearing 2.5-25 m longer due to the troposphere depending on the satellite elevation angle [Misra and Enge, 2011].

7.1.2 Ionospheric Correction

The ionosphere is reaching from about 50 km to about 10000 km above the earth, and is a region of ionized gas, and the Total Electronic Content (TEC) of the ionosphere is primarily dependent on the solar activity. Therefore the ionosphere is changing between day and night, and the magnetic poles and the equator. The region with highest ionospheric delay is $\pm 20^\circ$ of the magnetic poles. Especially therefore are the Arctic regions affected by magnetic storms, creating large and quickly varying electron densities, which result in rapid fluctuations. This can cause difficulties in tracking the GPS signals continuously.

For radar signals, the ionosphere correction takes the path delay into account due to the electronic content in the atmosphere. The range is -0.083 to -0.007 m. In the CryoSat product there are two sources available; the Global Ionospheric Model (GIM) and the Bent model. GIM (<http://iono.jpl.nasa.gov/gim.html>) using ionospheric data from GPS, computed every second along the satellite tracks (source: CNES). The Bent model (<http://modelweb.gsfc.nasa.gov/ionos/bent.html>) depends on the solar activity index, ionospheric correction file, and a modified magnetic dip map (source: CLS and CNES [ESA and UCL, 2013a]).

In the CryoSat retracking in this thesis the same standard as in L2 is used, where GIM is preferred to the Bent model. A typical magnitude is 0.015 cm.

Using dual-frequency measurements in GPS can eliminate the first order ionospheric effect (1-50 m). The second-order effect is 1000 times smaller and usually ignored, but it is causing up to a 0.5 cm shift in the latitude on diurnal, seasonal, and decadal scales [Kedar et al., 2003].

7.1.3 Inverse Barometric Correction

The atmosphere loads a pressure force on the SSH. The ocean is easy to compress, the spatial and temporal atmospheric variations are compensated by changes in the SSH. This is the inverse barometer effect. For March 2013 it ranges from -0.065 to 0.0 m. In the CryoSat product, the correction is computed using the dry tropospheric correction. A typical magnitude is 0.03 m.

PPP measurements can be used to detect atmospheric pressure loading in the vertical positions over GPS stations. The pressure loading is largest at higher latitudes [Van Dam and Wahr, 1998].

7.2 Tides

Working with data from the Arctic Ocean it is obvious that the ocean tides can play a significant role, but also the other tidal effects have to be taking into account in satellite and airborne altimetry and GPS height time series.

Penna et al. [2007] shows how unmodelled subdaily periodic signals for GPS processing such as ocean tide loading and solid earth tides, can propagate in to substantial errors in semi-annual and annual signals.

7.2.1 Ocean Tide

The ocean tides correction removes the effect of local tides caused by the moon, and it ranges in the CryoSat product from -4.289 to 3.509 m. This is higher than expected, but it has to be stated, that the majority of the ocean tide corrections is within -0.50 to 0.50 m. The FES2004 ocean tide model is available in the CryoSat product, and the typical average value for 80°N is 0.03 m.

There exists a new ocean tide model FES2012 with a better resolution compared to FES2004. In a study by Forsberg et al. [2007] various tide models (CSR4.0, GOT00.2, AOTIM-5) were tested in the Arctic Ocean, yielding AOTIM to perform best in the Arctic Ocean. Unfortunately FES was not included in this study, but a similar study by Renganathan [2010] showed, that AOTIM-5 performed better than FES2004 and GOT99.2 in the Arctic Ocean. This conclusion lies behind the choice of using AOTIM-5 in the ocean tide study from GPS made during this Ph.D. The uncertainty of the tide models are around 10 cm.

7.2.2 Long-Period Equilibrium Tide

The long periodic equilibrium tide removes the long period ocean tide effects due to the Sun. A model estimate of this effect is available from the FES2004 ocean tide model and is given in the CryoSat product. A typical magnitude is 0.0075 m, ranging from -0.049 to 0.010 m in March 2013.

7.2.3 Ocean Loading Tide

The ocean crust is deformed due to the weight of the ocean. The ocean loading tide correction is dealing with effect, and it varies from -0.054 to 0.070 m. The FES2004 model is also used to estimate this correction, with a typical averaged magnitude of 0.002 m at 80°N .

7.2.4 Solid Earth Tide

The Earth deforms due to the attraction from the Sun and the Moon. The solid Earth tide correction ranges from -0.074 to 0.004 m. The Cartwright and Edden model is used in the computation of the surface height from CryoSat data and the SSH from GPS measurements. A typical magnitude is 0.015 m.

The solid Earth tide is often ignored in GPS processing by many commercial softwares. For differential baselines over short baselines (< 100 km) both stations would have nearly the same displacement, and the relative position can therefore be measured with centimeter accuracy [Xu and Knudsen, 2000].

7.2.5 Geocentric Polar Tide

As the Earth rotates the crust deforms as a long-periodic distortion caused by variations in the centrifugal force as the position of the rotation axis move. Typically, this correction ranges from

–0.005 to 0.004 m, with a typical magnitude of 0.0025 m. This is not included in the GPS study, due to the minor effect.

7.2.6 Permanent Tides

The tide-generating potential of the Sun and the moon does not only vary with time, but also has a time-independent term called the permanent tides. The time-varying potential deforms the elastic Earth and causes an indirect change (the permanent tides). The permanent tide is determined by the knowledge of the elastic Earth, i.e. the Love and Shida numbers. This deformation causes a lowering in the polar areas and an increase around the equator. Conventionally, in the definition of the geoid the periodic component of these potentials are averaged out, but it is not zero because of the permanent term.

It is important to distinguish between the various permanent tidal concepts, and to be aware about its difference in the crust/topography and in the geoid. This can be treated in two different ways for the crust and three ways when dealing with a geoid. Figure 7.2.1 is a schematic illustration of the various crusts (dashed lines) and geoids (solid lines).

Tide-free system or non-tidal system, is the system where the effects from the Sun and the Moon are removed, i.e. the permanent deformation is removed from the shape of the Earth. Normally a solid Earth is assumed (conventional tide-free system) but can also be estimated for a secular Love (fluid) numbers (fluid tide-free system). The tide-free system is mainly used in 3-D positions e.g. ITRFxx. The conventional tide-free system is shown in red in Figure 7.2.1 and the fluid tide-free is green.

Mean-tide system In this system, the Sun and the Moon are present, i.e. the permanent effect is not removed. Therefore, the shape corresponds not only to the masses of the Earth but also to the long-time average of of the tidal potential. Following Rapp et al. [1991] this system is recommended working with Topex/Poseidon geophysical data, and furthermore, the MSL is per definition the mean-tide system, i.e. the mean-tide system is appropriate for oceanographic sciences. Shown in blue in Fig. 7.2.1.

Zero-tide system is the system where the direct effects of the Sun and the Moon are removed, and the indirect component of the elastic deformation of the Earth is kept. This is mainly used in gravity studies. The zero-tide is black in Fig. 7.2.1.

The permanent tidal deformation of the geoid (N), rounded to 1 mm from the GRS80 ellipsoid, is given by [Ekman, 1989; Mäkinen and Ihde, 2008]

$$N = \frac{W_2}{g} = 9.9 - 29.6 \sin^2 \phi \quad [\text{cm}] . \quad (7.2.1)$$

W_2 is the tidal potential, g the acceleration of gravity, and ϕ is the geodetic latitude. Using the mean-tide crust as a reference, the conventional tide-free crust is $-hN$, where $h \approx 0.6$. This convention is used in Rose et al. [2013c]. It is recommended to use the mean geoid for studying sea level, because the shape of the ocean in long-term is equivalent, when the semi-permanent sea surface topography are removed.

The difference between going from zero-tide geoid to mean-tide geoid and zero-tide crust to mean-tide crust gives a double as large correction. Going from a zero-tide geoid to a mean-tide

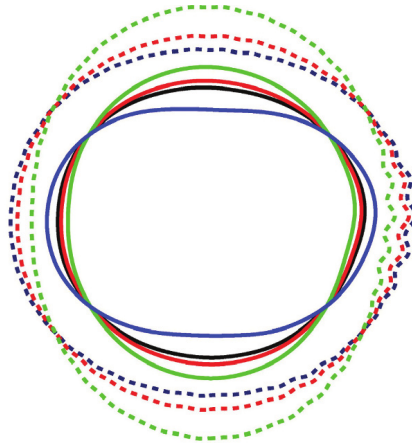


Figure 7.2.1: Crust/topography (dashed line) and geoids (solid lines) of different permanent tides. Mean-tide (blue), tide-free (red), and fluid-tide-free (green). The relative differences in flattening are correctly scaled while the flattening is not. With courtesy Mäkinen and Ihde [2008].

crust gives a zero contribution, where it from a mean-tide geoid to a mean-tide crust gives a $-N$ contribution. For more on the conversions between the different systems see Ekman [1989]; Mäkinen and Ihde [2008]. The permanent tide is not included in the CryoSat product nor in the altimeter calculations.

7.3 Geoid

The geoid is the equipotential surface, which approximates the mean SSH if the only forces acting were the gravity and the centrifugal force. Its spatial variation is connected by the distribution of the masses inside the Earth. The geoid is not applied in the CryoSat L1b product.

In this thesis two geoid models are used; the tide-free Earth Gravitational Model (EGM08) w.r.t. the WGS84 ellipsoid [Pavlis et al., 2008], and the Arctic Gravity Project (ArcGP) with an accuracy of 10 cm in the open basins and 20 cm in coastal areas [Forsberg et al., 2006]. In the Arctic Ocean EGM08 uses the ArcGP data. There exists a difference between ArcGP and EGM08 of 41 cm. In EGM08 a zero-degree term of 41 cm is applied to all geoid undulations derived from a mean-earth ellipsoid [National Geospatial-intelligence Agency, 2013]. In the Arctic Ocean the EGM08 geoid is varying from -49 to 65 m.

Currently the most accurate geoid model (in short scale) is the GOCE geoid based on the GOCE (Gravity field and steady-state Ocean Circulation Explorer) satellite measuring the Earth's gravity field with a geoid accuracy of 1 - 2 cm with 100 km spatial resolution.

7.4 Dynamic Topography

The Dynamic Topography (DT) is the SSH variation due to density changes in the ocean associated with horizontal pressure gradients. In open ocean the variation in DT is related to the general large-scale ocean circulation, because the large-scale oceanic flows are nearly in geostrophic balance (horizontal pressure gradient and Coriolis force). The DT varies globally by 2.5 m relative to the geoid [Fu and Cazenave, 2001] and is approximately 1 m in the Arctic Ocean [Forsberg et al., 2007]. There exists several DT models. One of them, from the University of Washington (UW), is a coupled ice-ocean model driven by atmospheric forcing [Zhang and Rothrock, 2003]. This model is used in Rose et al. [2013c].

The DT can be derived from satellite altimetry with a high precision geoid and SSH model. An Arctic Ocean mean DT is developed from ERS-2, ICESat, ArcGP, and GRACE [Skourup and Forsberg, 2008]. The DT is not derived for the altimetry data but is applied in the GPS study in Rose et al. [2013c].

Parameter	Range (m)	Model/Source	Error	Source
Dry Troposphere	-2.4 to -1.9	CS, ECMWF	0.02	[Saastamoinen, 1972]
Wet Troposphere	-0.12 to -0.004	CS, ECMWF		
Ionosphere	-0.083 to -0.007	GIM/Bent		
IBE	-0.065 to 0.0	CS, ECMWF	0.05	[Renganathan, 2010]
Ocean Tide	-0.50 to 0.50 ^a	FES2004	0.1	[Renganathan, 2010]
Long Periodic	-0.049 to 0.010	FES2004		
Ocean Loading	-0.054 to 0.070	FES2004		
Solid Earth	-0.074 to 0.11	Cartwright and Edden		
Geocentric Pole	-0.005 to 0.004	Historic data ^b		
Geoid	-49 to 65	EGM08	0.1	[Forsberg et al., 2006; Kenyon et al., 2008]
Permanent Tide diff	0.17 to 0.29	Cartwright and Edden		
DT	-0.30 to 0.30	UW	0.15	[Forsberg et al., 2007; Andersen, 2010]

Table 7.4.1: Geophysical correction range measurements taking from the CryoSat product from March 2013. The geoid, permanent tide, and the dynamic topography (DT) are not given in the CryoSat product but written in the table for completion. The permanent tide is given as the difference between a tide-free and a mean-tide system. All the values are from the Arctic Ocean.

^aIn the March 2013 product it varied from -4.3 to 3.5 m, but these are very large values compared to the usual magnitudes.

^bsource unknown

Sea Ice Measurements by Satellite Radar Altimetry

This chapter describes the method for measuring sea ice elevations by using radar satellite altimetry (Section 8.1). From altimeter satellites the freeboard height can be measured (Section 8.1.1). To retrieve the sea ice thickness a multiplication factor k based on assumptions of the snow/ice densities is applied to the freeboard height (Section 8.1.2). This obviously leads to errors in the thickness determination (discussed in Section 8.1.3) as the k -factor may vary between different ice types (seasons and regions), due to the difference in the effective density.

8.1 Sea Ice Measurements

In the Arctic Ocean the satellites measure the sea ice cover. The ellipsoidal height is given by the sea ice freeboard (h_{fb}) and the SSH (h_{SSH})

$$h = h_{fb} + h_{SSH} \quad . \quad (8.1.1)$$

The sea surface height can be expressed by the geoid (N), the dynamic topography (h_{DT}) associated with large ocean currents, the inverse barometric effect (h_{IBE}) due to atmospheric loading, tides (h_{tides}) and height corrections from instruments and model inaccuracies

$$h_{SSH} = N + h_{MDT} + h_{IBE} + h_{tides} + h_{errors} \quad . \quad (8.1.2)$$

The SSH can be modeled by knowing the geophysical parameters in details and as done during

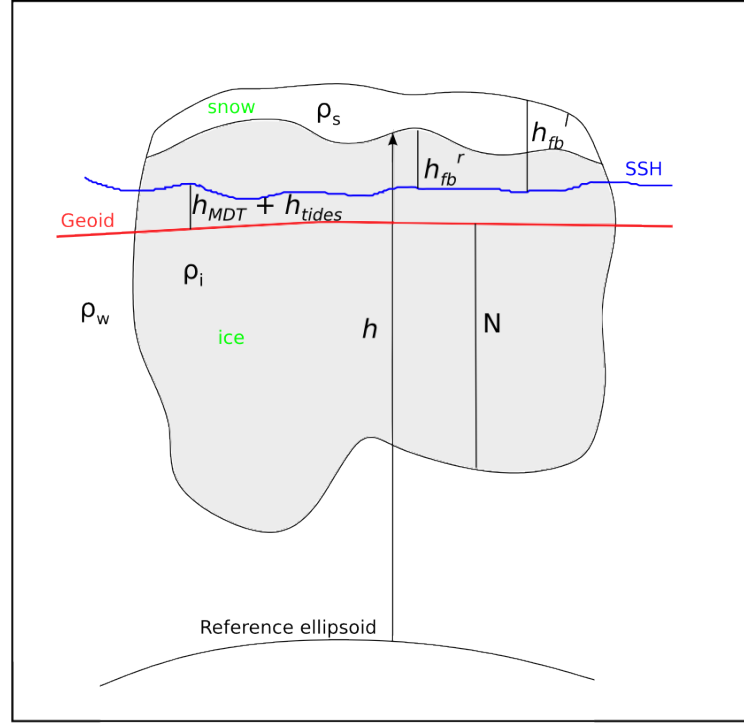


Figure 8.1.1: Schematic picture of sea ice with a snow layer on top. The various heights are shown: h is the ellipsoidal height, N the geoid height, SSH is the sea surface height given by the tides and the dynamic topography. h_{fb}^l and h_{fb}^r are the laser and radar freeboard heights, respectively. ρ_w , ρ_s and ρ_i are the densities of water, snow, and ice, respectively.

this study the tides [Rose et al., 2013c], or the freeboard [Rose et al., 2011, 2013a,b,d], can be extracted.

Backscatter of the ice surface is dependent on the season and environment such as salinity and density. Furthermore, it is very difficult to interpret the observations of summer sea ice due to melt.

8.1.1 Freeboard Determination

The sea ice freeboard is defined as the part of the sea ice above the local sea level. In laser altimetry the laser beam reflects from the top of the snow surface, while in radar altimetry the signal penetrates into the snow layer (see Section 8.1.3). In this thesis we discriminate between ice freeboard as the layer from the local sea level to the snow/ice interface, whereas the snow freeboard is the layer of the local sea level to the top of the snow layer (Fig. 8.1.1). From Eq. 8.1.1 the freeboard height is

$$h_{fb} = h - h_{SSH} , \quad (8.1.3)$$

where h is the ellipsoidal height, or the retracked height given by Eq. (6.3.1) in Section 6.3, and the SSH (h_{SSH}) can be determined from the leads. The advantage of CryoSat is its sensitivity to measure specular surfaces as leads. The uncertainty in the total freeboard can be estimated by using Eq. (8.1.1) and (8.1.2), and by assuming the variables are uncorrelated

$$\delta h_{fb}^2 = \delta h^2 + \delta N^2 + \delta h_{DT}^2 + \delta h_{IBE}^2 + \delta h_{tides}^2 \quad (8.1.4)$$

For CryoSat SAR mode the elevation errors δh are estimated to 11.6 cm for a “single shot” [Wingham et al., 2006], that gives for an area with 100 measurements an error of 1.2 cm. Using this and the values from Table 7.4.1 in Section 7, the freeboard uncertainty yields 21 cm. The error from the last four terms i.e. the SSH are 21 cm, and the freeboard error can never be smaller than this if these correction errors stays the same. The normal approach for determining the freeboard error, with many measurements are to use the regular expression of the standard deviation of the mean given in Appendix B.1.

The typical values for the freeboard error is between 3-5 cm, [Giles and Hvidegaard, 2006; Giles et al., 2007; Kwok et al., 2007; Alexandrov et al., 2010], these are measurement errors derived from comparison studies, and are much smaller than what is possible from Eq. 8.1.4, The freeboard error in OIB ATM data is estimated to 1-10 cm. [Kurtz et al., 2013].

8.1.2 Freeboard to Ice Thickness

It is described above how the freeboard can be estimated from altimeter measurements, but the sea ice keel can not be measured by altimetry satellites. To calculate the sea ice thickness, bottom estimates or assumptions about the sea ice thickness are needed. Analyzes of coincident laser and ULS measurements [Comiso et al., 1991; Wadhams et al., 1992] yields that the sea ice thickness can be derived by assuming the sea ice is in hydrostatic equilibrium with the surrounding water. Thus the sea ice thickness (h_{ice}) can be estimated from the radar freeboard (h_{fb}^r) by

$$h_{ice} = \frac{\rho_w}{\rho_w - \rho_i} h_{fb}^r + \frac{\rho_s}{\rho_w - \rho_i} h_s \quad (8.1.5)$$

where ρ_w , ρ_i , and ρ_s are the density of water, ice and snow, respectively, and h_s is the snow depth. This thickness estimate does not include a snow layer. All the parameters from the equations can be seen in Fig. 8.1.1, but the sea ice model is a rectangular shape, and not inhomogeneous as seen in the figure. The sea ice thickness (Eq. 8.1.5) is sometimes written with the multiplication factor k

$$h_{ice} = k h_{fb} \quad (8.1.6)$$

which is called the effective snow ice density factor. This factor is around 10, and it is obvious that even small errors in the freeboard height, lead to large errors in the sea ice thickness.

By assuming uncorrelated uncertainties the sea ice thickness errors can be determined with an error propagation analysis of Eq. 8.1.5 [Giles et al., 2007]

$$\epsilon_r^2 = \epsilon_{fi}^2 \left(\frac{\rho_w}{\rho_w - \rho_i} \right)^2 + \epsilon_{hs}^2 \left(\frac{\rho_s}{\rho_w - \rho_i} \right)^2 + \epsilon_{\rho s}^2 \left(\frac{h_s}{\rho_w - \rho_i} \right)^2 \quad (8.1.7)$$

$$+ \epsilon_{\rho w}^2 \left(\frac{f_i}{\rho_w - \rho_i} - \frac{f_i \rho_w}{(\rho_s - \rho_i)^2} - \frac{h_s \rho_s}{(\rho_s - \rho_i)^2} \right)^2 \quad (8.1.8)$$

$$+ \epsilon_{\rho i}^2 \left(\frac{f_i}{(\rho_w - \rho_i)^2} + \frac{h_s \rho_s}{(\rho_s - \rho_i)^2} \right)^2 . \quad (8.1.9)$$

By using typical error values [Giles et al., 2007] for ice and snow freeboard, water, ice, and snow densities an error of 46 cm are found for the radar altimeter sea ice thickness retrieval. It does not include penetration of the radar signal into the snow. An expected performance for CryoSat sea ice thickness is 6.8 cm for one month sampling over a 10^5 km^2 at 70° [Wingham et al., 2006].

The sensitivity of the ice thickness retrieval depends on the SSH estimation. This is presented in an ICESat and OIB's ATM laser altimeter study [Connor et al., 2013]. They find a mean sea ice freeboard of about $5.5 \pm 0.61 \text{ m}$ for ICESat and $4.5 \pm 0.56 \text{ cm}$ for the ATM data over a 250 km flight track in the northern Canada Basin. This shows a sensitivity of 1 m in the derivation of ice thickness to accurate freeboard and SSH measurements.

Ice thickness measurements from the Sever expeditions in a 65 year period are used to determine an ice thickness relationship for first- and multi-year ice from the equation above. The expeditions were mainly conducted in Spring from March to May and covered only the Eurasian Russian Arctic. Substituting the ice, snow, and water densities with typical values (Table 8.1.1) and using Sever data to calculate the snow thickness, a linear relationship between the ice thickness and the sea ice freeboard for first-year ice is given [Alexandrov et al., 2010] by

$$h_{ice} = 9.46 h_{fb}^r + 0.15 , \quad (8.1.10)$$

and for multi-year ice

$$h_{ice} = 6.24 h_{fb}^r + 1.07 . \quad (8.1.11)$$

The error depends on the ice thickness. Alexandrov et al. [2010] finds that a thickness retrieval error is smaller for multi-year ice than for first-year ice due to the smaller relative freeboard error and because the uncertainty in ice density is smaller for multi-year ice. Assuming a freeboard error of 0.03 m and using the numbers from Table 8.1.1, a first-year ice a freeboard of 0.01 m gives a thickness of $1.10 \pm 0.48 \text{ m}$ which corresponds to an error of 44%. Equivalent for multi-year ice with a freeboard of 0.21 m gives a thickness of $2.04 \pm 0.75 \text{ m}$ which corresponds to an error of 37%. The relationship for the first-year ice Eq. (8.1.10) agree with other studies [Forsstrom et al., 2011] north of Svalbard, whereas the relationship for the multi-year

Parameter	FYI	MYI
Snow depth (m)	0.05 ± 0.05	0.35 ± 0.06
Ice density (kg/m^3)	916.7 ± 33.7	882 ± 23
Snow density (kg/m^3)	324 ± 50	320 ± 20

Table 8.1.1: Typical snow depths and snow and ice densities [Alexandrov et al., 2010].

ice Eq. (8.1.11) shows inconsistency with similar studies [Wadhams et al., 1992]. This may be due to a larger variability of multi-year ice over large scale.

Laxon et al. [2013] were the first, to publish a sea ice thickness map based on CryoSat data. The maps are with courtesy presented in Fig. 8.1.2. In the left hand-side maps from February-March are shown, and on the right-hand side maps from October-November are shown. The top of the figure ((a) and (b)) shows the ICESat maps from 2003-2007 and the bottom ((g) and (h)) shows sea ice thickness maps from the Pan-Arctic Ice-Ocean Modelling and Assimilation System (PIOMAS). Based on the ICESat and CryoSat measurements Laxon et al. [2013] finds an average decrease in the sea ice volume of approximately $500 \text{ km}^3/\text{year}$ corresponding to a 0.075 m/year decrease in thickness. Their autumn average is 60% higher than the PIOMAS model.

8.1.3 Error Sources in thickness Retrieval

It is evident from Eq. (8.1.5), how an error in the freeboard will increase the error in sea ice thickness. There exist several error sources in the freeboard retrieval, the error sources are:

1. Freeboard error caused by penetration errors, ocean-tide, geoid, ocean variability and atmospheric refraction error.
2. Snow-loading.
3. Snow/ice/water densities.
4. Preferential sampling of floes.

More freeboard retrieval errors can originate from atmospheric and geophysical correction errors, retracking errors, and on-board tracking errors.

The snow layer on top of the sea ice is the largest error source in thickness determination. Therefore the combination of laser and radar altimetry measurements are very important. The first comparisons of spaceborne radar altimetry (ERS-2) and airborne laser altimetry [Giles and Hvidegaard, 2006] show a difference between the freeboard of -10 to 40 cm , and the difference decreases with increasing air temperature. This suggests that the radar reflection varies with air temperature. Giles et al. [2007] use a combination of airborne laser and radar altimeter measurements over the Fram Strait to estimate the snow thickness. They found a difference in height between the laser and radar measurement to yield 34 cm . The airborne radar measurements were coincident with ERS-2 measurements. Furthermore, Envisat radar measurements and airborne laser altimeter measurements are compared [Connor et al., 2009], and they show good agreement over refrozen leads with a mean difference over the leads of $\approx 1 \text{ cm}$.

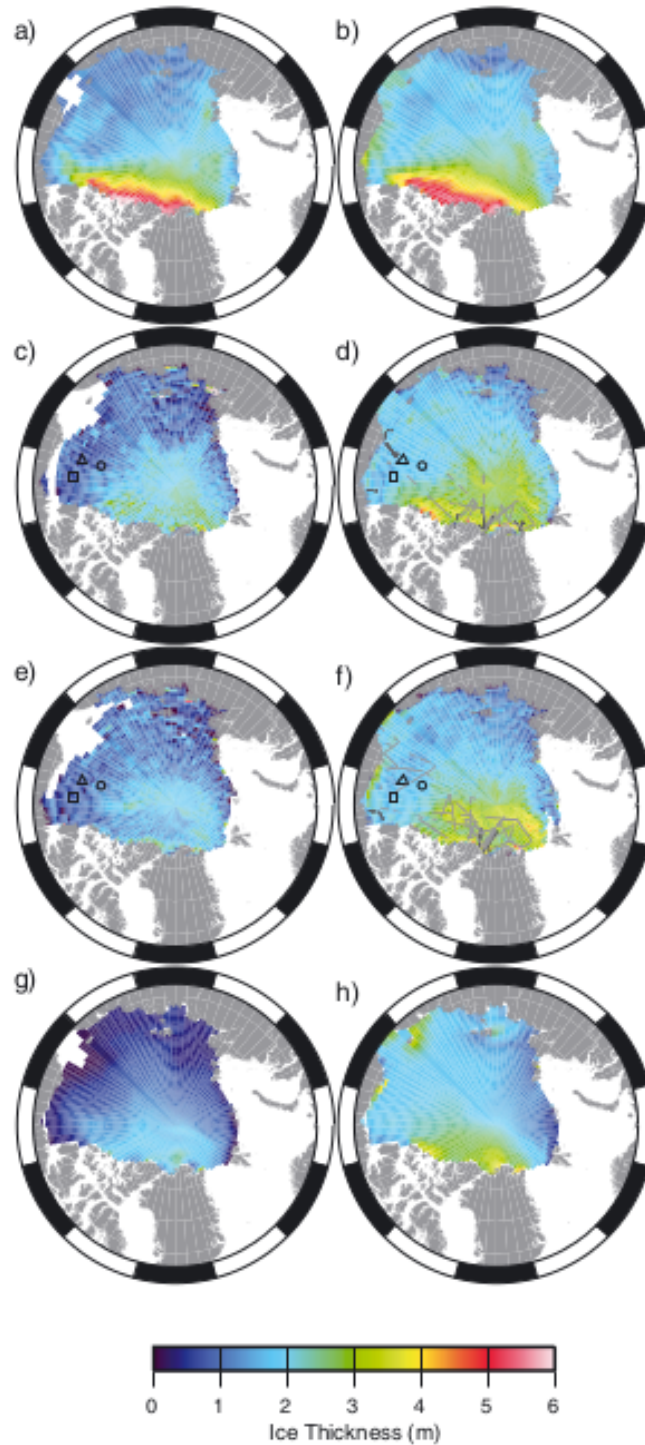


Figure 8.1.2: CryoSat sea ice thickness compared with ICESat and the sea ice model PIOMAS. (a) ICESat from 2003-2007 October-November. (b) ICESat from 2004-2008 February-March. (c) CryoSat from 2004-2008 October-November, (d) CryoSat from 2004-2008 February-March, (e) CryoSat October-November 2011, (f) CryoSat February-March 2011, (g) and (h) are PIOMAS for October-November 2011 and February-March 2012, respectively. The lines (black, gray), triangles, circles and squares indicate areas where data are validated with airborne laser, electro magnetic data and upward looking sonar moorings [Laxon *et al.*, 2013].

A recent study by [Armitage and Davidson \[2013\]](#) states that the freeboard accuracy can be improved by using the CryoSat SARIn mode over the Arctic Ocean, This is tested from the Wingham box where correcting for off-nadir ranging can increase the number of leads in the SSH determination and therefore improve the freeboard accuracy.

Penetration Errors

Laboratory experiments show that a K_u -band radar with normal incidence penetrates to the snow/ice interface of dry, cold snow [[Beaven et al., 1995](#)]. This is confirmed by comparing laser and radar altimetry [[Connor et al., 2013](#)]. When the snow layer is wet the signal does not penetrate the snow, but reflects from the snow surface [[Hallikainen, 1992](#)]. [Willatt et al. \[2011\]](#) show from field experiments, that with lower temperatures of the snow, the closer the K_u -band radar penetration is to the snow/ice interface.

However, the penetration results are not coincident: From an Antarctic field study [[Willatt et al., 2010](#)] the K_u -band radar penetrates 50% of the snow layer in cold dry conditions. This could be due to the various snow types in the field study. It is most widely assumed that the radar signal penetrate to the snow/ice interface [[Laxon et al., 2013](#)]. Theoretical results [[Tonboe et al., 2006](#)] show how the snow depth and density have a significant impact on the leading edge of the radar altimeter waveform where the snow depth increases the half-power time. The penetration depth also varies depending on the surface roughness.

Snow-loading

The snow-loading is important due to the sea ice buoyancy. An overestimation of the snow thickness will result in an underestimation of the sea ice thickness and vice versa. The snow-loading is varying with the seasons [[Warren et al., 1999](#)], and very little is known about the loading on different scales. [Tonboe et al. \[2010\]](#) state from simulations that the buoyancy error may be compensated by the radar penetration to some degree, and therefore moderate the total error. [Warren et al. \[1999\]](#) climatology snow depths is widely used [[Giles et al., 2008](#); [Kwok et al., 2009](#), and many others] based on measurements from the 1950's. The implementation of the model is described in Appendix A, and selected maps of the snow depth are shown. However, recent work by [Kurtz and Farrell \[2011\]](#) based on OIB snow radar shows consistency with Warrens climatology over multi-year ice, but they recommend only to apply half the snow depth over first-year ice.

Densities

The snow, ice, and water densities also have a strong impact on the sea ice buoyancy. A typical value for the snow density is $319.5 \pm 3 \text{ kg/m}^3$ [[Warren et al., 1999](#)] and for ice it is $915.1 \pm 5 \text{ kg/m}^3$ [[Wadhams et al., 1992](#)]. [Alexandrov et al. \[2010\]](#) discriminate between first-year ice and multi-year ice. These values can be seen in Table 8.1.1. The density of sea water is often not considered, but during winter it can vary between about 1024 and 1027 kg/m^3 [[Pavlov, 1998](#)]. [Wadhams et al. \[1992\]](#); [Giles et al. \[2007\]](#) use $1023.8 \pm 0.5 \text{ kg/m}^3$ and [Alexandrov et al. \[2010\]](#) use $1025 \pm 0.5 \text{ kg/m}^3$ for the water density.

Preferential Sampling

The radar does not see the whole footprint, due to spatial backscatter and elevation distributions. This is called *preferential sampling*. The radar may not detect small floes if the thickness distribution is distinctively different from the large floe. In [Tonboe et al. \[2010\]](#) this is called “*the single most important error in thickness retrieval*”. They conclude that the high backscatter from the thinnest ice floe dominates the return signal. This results in underestimation of ridges, which are a significant part of the ice thickness [[Haas et al., 2010a](#)]. The preferential sampling error is minimized in areas dominated by one ice type and few ridges.

CryoSat Data Development

This chapter describes the methods used for reading and retracking CryoSat L1B SAR data. CryoSat data are available in a binary format from the ESA website. The first section of this chapter discloses broadly how the data are read. A threshold retracker is developed to evaluate the CryoSat waveforms (Section 9.2), and the retracker is tested over leads towards other retrackers (Section 9.3). This chapter is finished with a description of the beam parameters included in the CryoSat product (Section 9.3.2).

9.1 Access and Read Data

For registered users, CryoSat data are free and open access, and they are distributed by FTP from <ftp://science-pds.cryosat.esa.int>. For more information about the various data and access, see <http://earth.esa.int/cryosat> or the CryoSat Product Handbook [ESA and UCL, 2013a] (the newest version is available at the address above). Data are currently being reprocessed from baseline A to baseline B, and all the CryoSat SAR data are therefore not (as writing) available in the newest processing version.

The CryoSat SAR L1b data used in this thesis are read with a Python routine inspired by my colleague Louise S. Sørensen's (DTU Space) L2 reader. The product consists of two files, an XLM header file and a product file. Here the XLM file is used to quickly find the files of interest according to orbit or geographical area. The product file is divided into a header followed by a binary data block with big-endian byte order.

The data record contains five groups, and the groups are varying depending on the SIRAL mode. The groups are: The time and orbit group repeated 20 times per record, the measurements group also repeated 20 times, followed by the correction group and the average waveform group both available once per record, and last the waveform group, which is repeated 20 times. Obviously, the time and orbit group contains the CryoSat time and location. The measurements group contains the window delay, the noise on the echo signal, the instrument, and the Doppler corrections. The latter two are applied to the L1b product by the ground team. The correction group contains the atmospheric and the geophysical corrections, the average waveform group contains the 1 Hz waveforms, and the waveform group contains the 20 Hz waveforms together with the beam information (Section 9.3.2). The corrections and the waveforms status and error flags are checked in the reading process. The SAR mode record is consequently 11084 bytes

large. For more information about the data product see the Product Specification manual [ESA, 2011a] or the CryoSat Product Handbook.

9.2 Threshold Retracker Development

The background of the threshold retracker was described in Section 6.3.1. This section aims at describing the retracker developed during this study to derive CryoSat SAR elevations over a sea ice covered ocean. The Python routine reads in the 20 Hz waveform, correction, and beam parameter data for each waveform.

Picking the First Peak

It is crucial to detect the first peak and not the maximum peak to interpret the waveforms correctly. The first peak of the waveform is detected by a peak detection algorithm. The first 10 and last 10 bins are not considered because of aliasing. The first peak must be above 10% for not picking up thermal noise in the beginning of the waveform.

The peak detection algorithm identifies the local maxima in the signal by searching for values, which are surrounded by lower values. It is in this step crucial to choose the right search intervals and the minimum difference between the peaks. This method is good because it allows e.g. to pick up small bumps in the leading edge. This means detecting the true surface when a off-nadir lead contaminates the signal. The negative about this method is that, sometimes it identifies the first peak way too early. This is why the 10% threshold of the maximum peak is incorporated. Sometimes 10% is not enough, but raising this threshold also means discarding the true first return.

Another method for detecting the first peak is tested, and it is suggested by Walter N. F. Smith (NOAA). This method involves taking the gradient of the first point ($P(0)$) to the current point ($P(i)$), and taking the logarithm of the values.

$$P_{\text{firstMAX}} = \frac{\log P(i) - \log P(0)}{i} . \quad (9.2.1)$$

This method is very robust to pick the first peak, if the first peak is a sharp peak, but it cannot detect the bumps described earlier. The difference of the two detection methods are shown in Fig. 9.2.1, where the green dashed curve indicate the first peak picked by the method in Eq. 9.2.1, and the blue dashed curve indicate the picking from the search algorithm used in the final retracker. The importance of picking the bump on the lading edge and not the first “real peak” is described in more details in Section 10.5.

Threshold Retracker

After the first peak is detected the waveform is retracked by Eq. (6.3.4), found in Section 6.3.1, and the threshold determined by Eq. (6.3.3). A threshold coefficient of 40% or 50% performs best over the sea ice cover [Rose et al., 2013a,b].

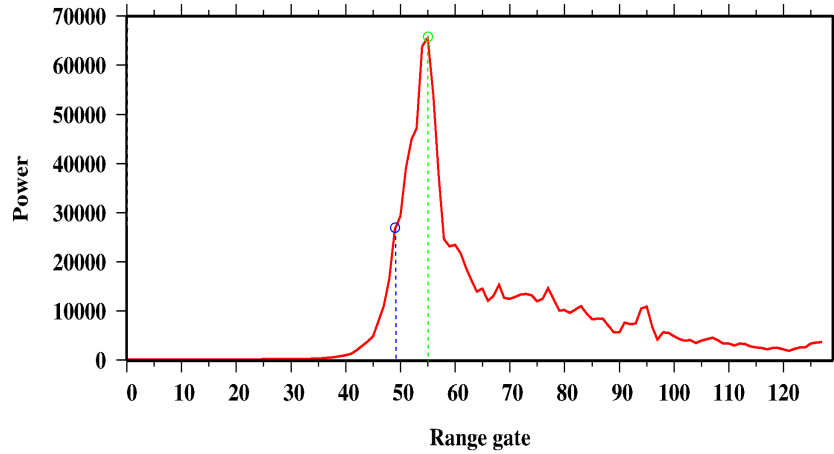


Figure 9.2.1: SAR waveform with a bump in the leading edge. The green dashed curve indicate the picking of the first peak from the method in Eq. 9.2.1, and the blue dashed curve indicate detection from the search algorithm used in the retracker.

From Retracking to Elevation

The ellipsoidal height (h) can be derived from retracking by the satellite altitude (H), the window delay (WD), the speed of light in vacuum (c), the retracking correction (RC), and the atmospheric and geophysical corrections (h_{corr}) described in Chapter 7

$$h = H - \left(\frac{1}{2} c \text{WD} - RC + h_{\text{corr}} \right) . \quad (9.2.2)$$

The equation in the brackets is the range (See Section 6.2). The retracking correction is the difference between the retracking point and the center of the range window. It compensates for the deviation of the waveform's leading edge from the on-board altimeter tracking gate

$$RC = (l_{\frac{1}{2}} - RG) \Delta r , \quad (9.2.3)$$

where $l_{\frac{1}{2}}$ is the center of the range window counting from zero, RG is the retracking, gate and $\Delta r = 0.2342$ m (for SAR) is the sampling interval. Note: the sampling interval is actually the crucial difference of Baseline A and Baseline B. This comes from the computation of the range, where in Baseline A the range to the waveform sample (n) is given by $R_A = \frac{nc}{2B}$, whereas in Baseline B the range is given by $R_B = \frac{nc}{4B}$, where c is the speed of light.

The status and error flags are checked for all correction, and if they are bad the waveform is rejected. Finally, the surface elevation can be achieved by redrawing the geoid. The corrections applied to the CryoSat range estimate are

$$h_{\text{corr}} = \underbrace{h_{\text{dryTrop}} + h_{\text{wetTrop}} + h_{\text{iono}} + h_{\text{IBE}}}_{\text{Atmospheric corrections}} + \underbrace{h_{\text{otide}} + h_{\text{longPtide}} + h_{\text{loadtide}} + h_{\text{setide}} + h_{\text{geoCPTide}}}_{\text{Tidal corrections}} . \quad (9.2.4)$$

Following the tidal adjustments the range is given from a mean ice or tide-free sea surface.

Extra

In addition, the following is calculated:

- TAI seconds is converted to UTC hours of the day.
- The power of the retracked and highest peak is converted to watts.
- Distance in kilometers between the retracked and the highest peak, if the first peak is not the highest.
- The slope of the leading edge.

9.3 Retracker Performance

As pointed out several times, determining the SSH is crucial in the retrieval of the sea ice freeboard height. The SSH is found from detecting the leads in between the ice floes. Lead detection will be described in more details in Section 10.3. This section is dedicated to validating the performance of the threshold retracker developed during this study. This is carried out by comparing the lead elevations from CryoSat towards the mean SSH (MSS) DTU10 by Andersen [2010]. The results from the threshold retracker are compared to three different retrackers provided by my colleague Lars Stenseng. Two of these retrackers are based on fitting a Gaussian function, which are normally used when retracking leads (see Section 6.3), and the third is a 80% threshold retracker, where we by retracking high on the leading edge could expect a more stable lead level.

9.3.1 The Residual SSH

Comparing Eq. (8.1.2) and (9.2.4) in Section 8.1 and 9.2, respectively, we are missing a DT term in the last equation. This means that strictly speaking the leads from CryoSat are not the true SSH but actually the SSH and the effects from the surface topography caused by ocean currents i.e. the DT.

To validate the retracker over the leads the mean SSH (MSS) DTU10 is redrawn. MSS DTU10 is a 17 yearly (1993-2009) average of the SSH, i.e. the geoid and the mean DT. The accuracy is less than 10 cm below 82°N. There may be an issue with the data above 82°N due to the sparse satellite coverage in those latitudes, but it should be accurate to 20 cm.

The performance of the 50% threshold retracker used in this thesis is tested against three different retracker developed by Lars Stenseng, DTU Space. The first is a Gaussian fitting routine, similar to Armitage and Davidson [2013], where a Gaussian function is fitted ± 2 bins from the maximum peak, where the maximum peak is taken as the tracking point. The second is also based on the Gaussian fit, but this time the tracking point is at a 80% threshold. The third retracker tested towards the retracker used in this thesis is a 80% threshold retracker of the OCOG amplitude [Stenseng and Andersen, 2012].

The CryoSat track no. 10520 from April, 2, 2012 from 73.6°N to 88°N is used. This is an expansion of the data used in [Rose et al. \[2013b\]](#). The probability distribution of the residual SSH for all four retrackerers are plotted in Fig. 9.3.1 with a bin size of 0.05 m. The statistics are written in the top left corner of the figure; the number of points, the extreme values of data (Min/Max), the mean, median and the Least Median of Squares (LMS), which is the estimated mode, and the standard deviation (SD), all given in meters.

The standard deviation is the smallest for the 50% threshold retracker (a), but the precision of the probability distribution is lower than for the other retrackerers. Furthermore, the distribution is more symmetric. The Gaussian distributions (b) and (c) are very similar in form, but the mode is shifted due to the retracking point. They have the highest precision. There may be a second mode. The 80% threshold retracker (d) is similar to the Gaussian distributions, which is because they are all retracked at or close to the maximum peak, but the 80% threshold retracker is more fat-tailed to the right.

All the distributions are a little negative skewed, i.e. there is a elongated tail to the left. The definition of a skewed distribution is described in Appendix B.2. This skewness is due to off-ranging elevations detected falsely as leads. The signal comes from specular surfaces off-nadir (see Section 10.6).

For the evaluated track there where 1118 elevations defined as leads. The 50% threshold retracker performed as good as the retrackerers tested against, and it seams like the 50% threshold

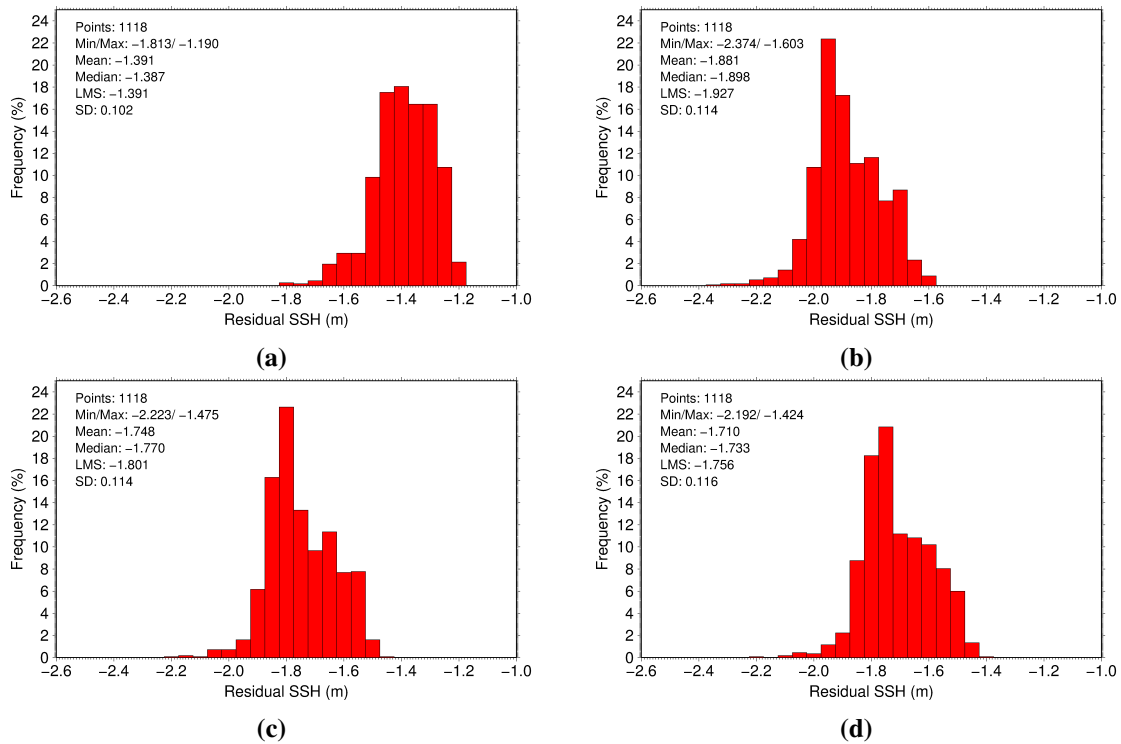


Figure 9.3.1: Residual SSH from (a) the 50% threshold retracker, (b) Gaussian maximum peak, (c) 80% threshold of the Gaussian, and (d) 80% threshold retracker of the OCOG amplitude. The number of points, the extreme value (Max/Min), the mean, the median, the estimated mode (LMS), and the standard deviation (SD) are given in the top left corner. The values are in meters.

retracker can be used over leads. Though, a more comprehensive analysis with more data points are advised.

9.3.2 Beam Behavior

The beam parameters; stack standard deviation, stack center, stack scaled amplitude, stack skewness, stack kurtosis, stack standard deviation in terms of reception angle, and stack center angle are provided in the L1b product and are given as a *stack*, i.e. the collected set of looks returned from a single target surface.

The beam behavior parameters are plotted together with the surface elevation w.r.t. EGM08 (Fig. 9.3.2). The gray dots indicate a peak power above $1.5 \cdot 10^{-12}$ W, and the red dots indicate too low elevations. These are very crude measures of leads and off-ranging points, and should not be thought of as final leads, nor points with too low elevations, respectively, but more as indicators of points of interests.

The power in each look is averaged over all ranges, and the resulting set of points are found with a Gaussian fit. The stack standard deviation (St. SD) is the standard deviation of the fit. The stack center is the mean of the fit. The stack skewness quantifies the asymmetry of the distribution about the mean, and the stack kurtosis is a measure of how peaked or flat the distribution is. The stack standard deviation in terms of reception angle and the stack center angle are the stack of the angle of each burst w.r.t. the surface flying to and away from the measured point, not to be confused with the mispointing angle being the physical angle of the antenna beam.

The normal and angle stack standard deviations are low and close to zero for echoes over leads. Zero is a perfectly smooth surface in all multi-looks. Furthermore, the scaled amplitude, the skewness and the kurtosis have a local maximum over leads. Especially the kurtosis is a good indicator of leads, because of the almost constant low values over non-lead surfaces.

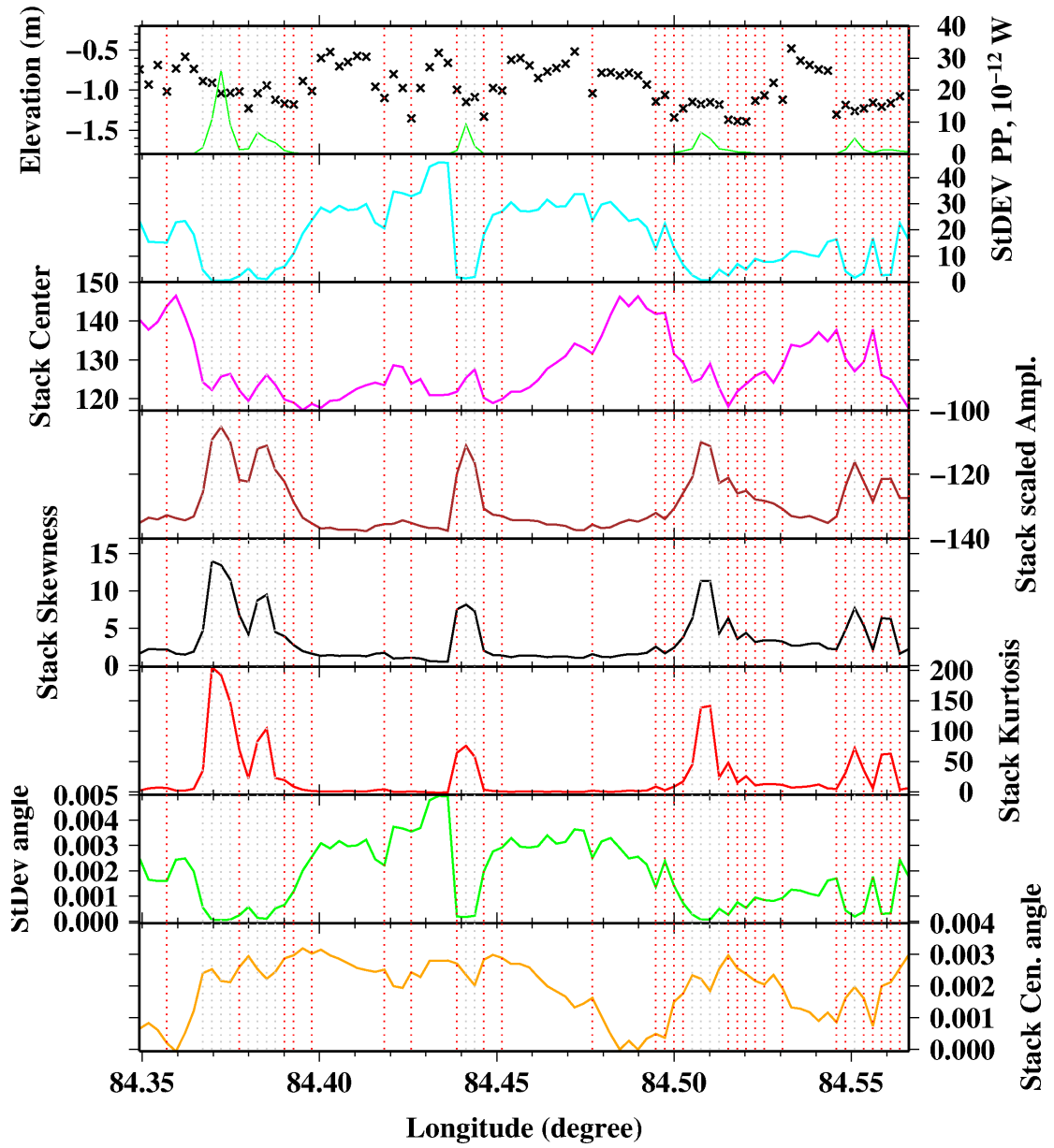


Figure 9.3.2: Beam behavior parameters. From the top and down; elevation w.r.t. EGM08 and the re-tracked peak power, standard deviation of the stack, stack center, stack scaled amplitude, stack skewness, stack kurtosis, stack standard deviation and the stack center of the reception angle. The gray and red dots are crude indicates of leads and off-ranging points.

Evaluating CryoSat Observations - A Comparative Assessment

The results in this chapter are a supplementary and a further development of the results found in [Rose et al. \[2013b\]](#), where a comparative analysis between CryoSat, CryoVEx and OIB were conducted. The goal of this chapter is to validate the retracked CryoSat data by comparing them to CryoVEx, and OIB airborne laser altimeter data and furthermore examine the CryoSat elevations in details by looking at high resolution images.

This will be carried out on the basis of the study areas described in [Rose et al. \[2013b\]](#). The first study area is in the Lincoln Sea, where data from April 2, 2012 are used. The CryoSat orbit is no. 10520. The CryoSat track from April 2, 2012 is shown in Fig. 10.0.1 on top of an Envisat

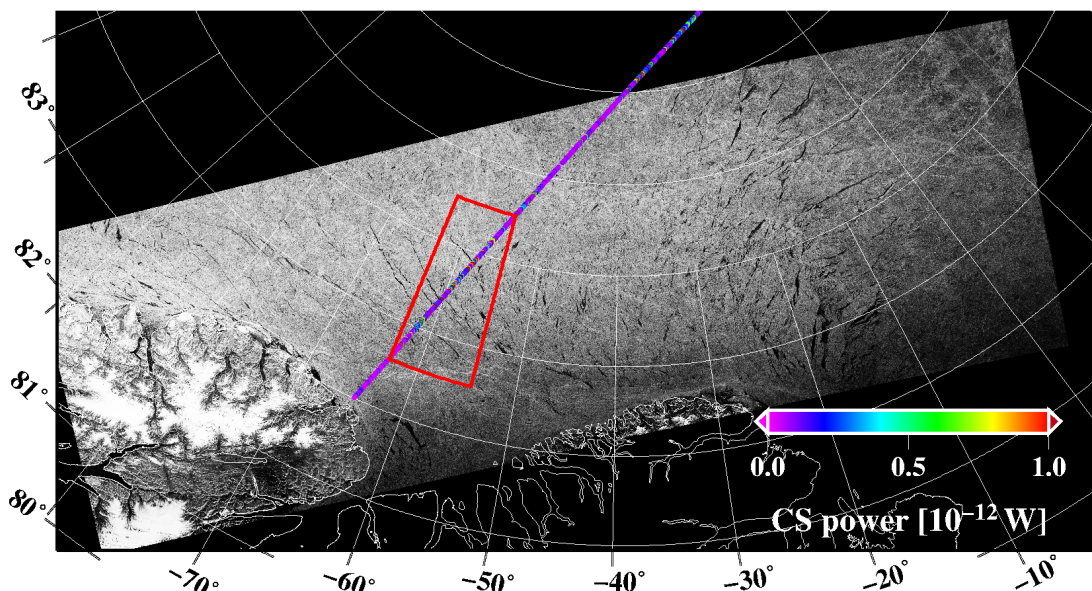


Figure 10.0.1: ASAR image from April 2, 2012 at 17:51:24 overlaid with the peak power from the CryoSat track no. 10520. The red box indicate the study area.

ASAR image from April 2, 2012 at 17:51:24 UTC. The second study area is from April 27, 2012, north of Svalbard. the CryoSat orbit is no. 10885.

Comparisons of the ALS and ATM laser scanner datasets are described in Section 10.1, and the averaging of the laser scanner dataset to the CryoSat ground resolution is discussed in Section 10.2.

In freeboard retrieval it is crucial to find the local SSH. In Section 10.3 lead detection is described. A new drift correction is applied to the CryoSat data (Section 10.4) and discussed (Section 10.6.3). Furthermore, this chapter intent to describe the retracked CryoSat elevations in details (Section 10.5): How does the waveforms look like over different surfaces? How can the leads be found? Why is it sometimes fails with the retracking?

Two methods for filtering off-ranging CryoSat elevations are discussed (Section 10.6) and new freeboard values for the study areas from Rose et al. [2013b] are made with the new filtered data.

10.1 Comparing ALS and ATM Elevations

ALS and ATM are currently the most used airborne laser altimeter missions. Rose et al. [2013b] showed that they have a very good correlation. The correlation results before and after drift is applied are plotted in Fig. 10.1.1. The correlation has improved after drift indicating an effective drift correction. From this test, it is seen, that the two independent datasets are very reliable and good candidates for testing against the CryoSat data.

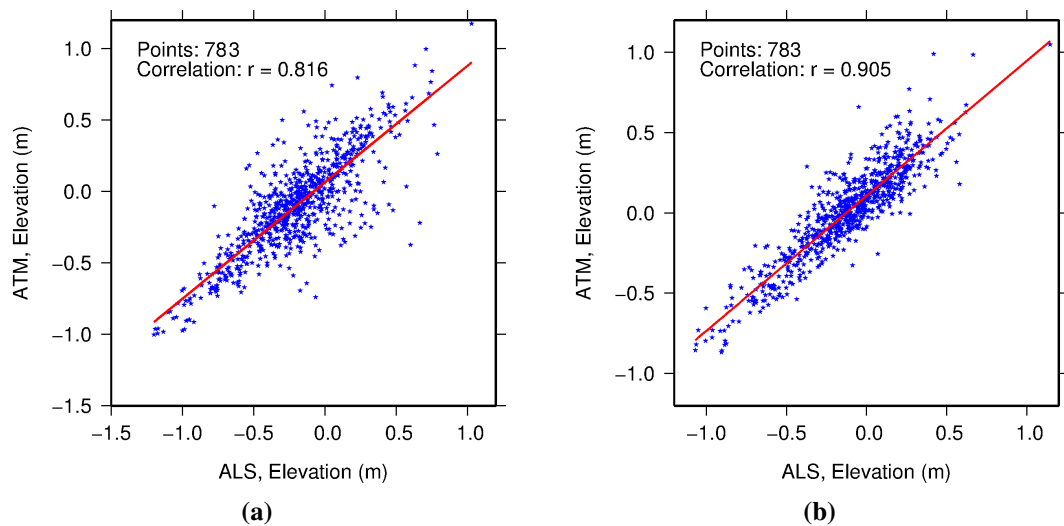


Figure 10.1.1: Scatter plot of ALS and ATM elevations (a) before drift, and (b) after drift (cf. Rose et al. [2013b]).

10.2 Averaging Airborne Data to CryoSat Data Sampling

It is crucial to average data when comparing elevations from airborne laser and radar satellite altimetry. A nearly perfect correlation as seen between ATM and ALS is not expected. Here, the two data sets compared are very different in many ways. The airborne data have a higher data density and a smaller footprint. The satellite data have a larger footprint, and therefore measure more of the sea ice cover along-track, but these data are also averaged. The problem of preferential sampling occurs as described in Section 8.1.3, where the satellite “does not see” the whole footprint.

In the airborne data averaging, a lead can be averaged out because of its small size, whereas CryoSat is very sensitive towards leads even on very small scale. Due to the off-nadir scan angles both the ATM and the ALS do not always pick up the reflections from the very specular open leads. This is a problem because these leads are the true SSH and the single most important leads in the SSH determination. Tracking CryoSat data in the laser scanner dataset may also result in loss of important information if a lead is located in between the CryoSat samples. Furthermore, the laser and the radar altimeter measure in theory, two different surfaces, i.e. the snow and the ice surface (cf. Section 8.1).

The point of averaging the airborne scanner data is to turn it more into a satellite footprint. As mentioned in Section 6.1.1, the pulse-Doppler-limited altimeter SIRAL on-board CryoSat can be seen as pulse-limited in the along-track direction and a sharpened beam-limited altimeter across-track. From this it is not obvious which approach is the best for sampling airborne altimeter data to the CryoSat SAR footprint, because even if the across-track and along-track distances are known, the satellite data are affected by the whole footprint, and even small very specular surfaces far from nadir are observed. This will be described in more details in Section 10.5.

There exists many ways for sampling data. In this study; 1) a non-interpolation, 2) a minimum curvature, and a 3) nearest neighbor method are tested. This is done in a combination of the Generic Mapping Tool (GMT) and shell scripting. To find the corresponding satellite coordinates in the grid the points have to be tracked. The GMT `grdtrack` can do the job by various methods (bicubic, bilinear, B-spline, nearest neighbor or no interpolation) depending on the desired result. Here, the bicubic or the non interpolation methods are normally used.

First, data are divided into blocks and the median of each block is found. This is common for all methods and for the later two methods this is done to avoid aliasing. The mean and the mode are also tested in the averaging, but the median gave a better correlation compared to the mean, whereas the mode gave similar results, therefore the median was chosen.

In the first method, the non-interpolation method, data are gridded without any constraints, but if more points coincide they are averaged.

In the second method, data are gridded with splines in tension as a minimum curvature algorithm. This method is called surface, because it works like fitting a thin elastic surface going through all data points. In this method various tensions are examined, but only shown here for a tension of 0.25.

For a conventional altimeter a nearest neighbor gridding is an obvious choice, because the algorithm search for data in a radius around a center point, and it can be build such that points further away from the center are weighted less in the averaging. The circular area centered on each point is divided into sectors n . An average value is only computed if at least one value is inside at least n_{\min} sectors for a given node. The search radius is not changed in this test study,

Method	Grid	No. Sectors	No. points	r
No interpolation	25	-	419	0.536
No interpolation	50	-	394	0.578
Surface	25	-	422	0.537
Surface	50	-	422	0.561
Surface	100	-	422	0.590
Surface	152.5	-	422	0.617
Near neighbor	25	8/6	399	0.596
Near neighbor	25	8/1	422	0.573
Near neighbor	50	8/4	388	0.603
Near neighbor	50	8/2	421	0.596
Near neighbor	50	4/1	421	0.585
Near neighbor	100	8/1	256	0.648
Near neighbor	100	1/1	401	0.598

Table 10.2.1: Correlation (r) of the various averaged ATM and CryoSat elevations given for different grid sizes, Number of sectors (n/n_{\min}) The corresponding scatter plots are shown in Appendix C.1. The red text indicate the best result for each method (Fig. 10.2.1).

but kept constant at 152.5 m corresponding to the mean point density in the respective CryoSat dataset.

Data used in this comparison are from April 2, 2012 from the Lincoln Sea. Here we only use data from the area with no sea ice drift between longitude -62° to -59° . Data are compared to CryoSat elevations by fitting a linear regression model by least squares. The method is robust in terms of outliers. The results are shown in Table 10.2.1. The correlation coefficient (r) is a regular Pearson correlation.

Overall the results are correlating (> 0.5). The scatter plots are shown in Appendix C.1. The best result for each method is marked with red in the table and plotted for a small area (Fig. 10.2.1). The best results are not chosen entirely on the basis of the correlation coefficient but also on the number of points. There are in total 422 CryoSat data points in the test area, but in the non-interpolation and the nearest neighbor methods, the number of points increases when the grid size gets too large or the sector criteria too strict, i.e. the method or the tracking routine cannot give a suitable result and the value is set to *Not A Number* (NaN).

The surface method gives the overall best correlation for a grid size corresponding to the CryoSat point density. However, this method often smooth the data more than appropriate, especially in areas with low point density. Furthermore, it is more time consuming than the other two methods. Therefore, the nearest neighbor method is preferred during this study.

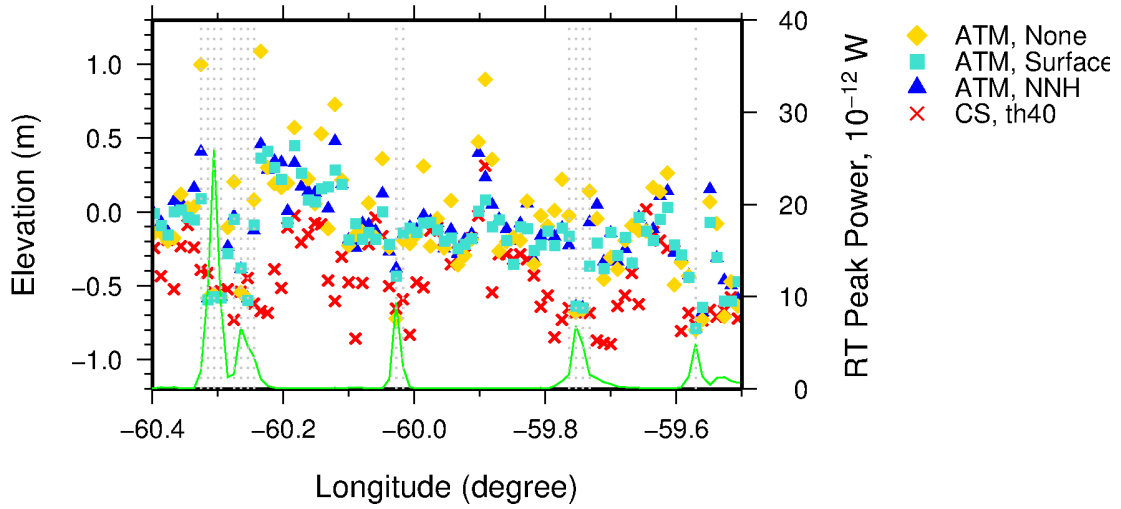


Figure 10.2.1: Comparing methods for averaging airborne altimeter data: No interpolation (yellow diamonds), nearest neighbor (blue triangles), and surface (turquoise squares). The CryoSat elevations (red crosses) are detrended to fit the lowest points in the altimeter data, peak power (green), and the gray dots indicate a peak power above $1.5 \cdot 10^{-12}$ W.

10.3 Lead Detection

Detecting leads is the most important factor in the determination of the sea ice freeboard because they form the SSH. As seen in Connor et al. [2013] the SSH is very sensitive to the freeboard retrieval and in comparison studies. This was also demonstrated in Rose et al. [2013b], where the radar freeboard varied by 15 cm depending on the SSH method used.

The lead detection method in Rose et al. [2013b], used a new peak detection algorithm to locate the leads. Below, an alternative method is described.

The peak power of the first return is used to discriminate leads from ice floes. A high peak power is more likely to originate from a lead, but the peak power alone is an unstable lead detector. The strength of the peak power over a lead is not only a signal of how specular the surface is, i.e. open lead, refrozen, with snow etc., but it also depends on the orientation and the size of the lead. A lead in the across-track direction is sampled over a much larger area than a lead in the along-track direction. Therefore, a lead pointing in the across-track direction will have a higher peak power than a lead pointing in the along-track direction.

The pulse peakiness (PP) is a widely used method for detecting leads [Laxon and Rapley, 1987; Laxon, 1994b; Peacock and Laxon, 2004, and others]. It is a measure of how sharply peaked an echo is. It was first used to filter out anomalous data over ocean, including sea ice. Pulse peakiness is given by

$$PP = \frac{k P_{\max}}{\sum_{i=j}^n P_i}, \quad (10.3.1)$$

where P_{\max} is the peak power, P_i is the power of the i 'th range gate, where the first gates (j) are excluded due to aliased power. k is a factor multiplied to the equation assuming the waveform

is roughly centered in the altimeter range window such that the pulse peakiness approximates one over the ocean. The higher the pulse peakiness ratio, the more peaked the echo. High peakiness indicates a very specular reflection, such as that from leads in sea ice. Due to speckle in the altimeter return the pulse peakiness value is more likely around 1.4 for the ocean surface [Laxon and Rapley, 1987]. In sea ice covered regions this is even greater. Knudsen et al. [1992] removed sea ice with a pulse peakiness < 1.7 and later Peacock and Laxon [2004] assumed a value higher than 1.8 to be a specular return from a lead.

For ERS-1 a k value of 31.5 is used and for Envisat it is 44.5. Different thresholds for defining the surface type from pulse peakiness is used, mainly depending on the satellite. For Envisat Connor et al. [2009] classify a pulse peakiness < 3 as ice floe and a pulse peakiness > 30 for leads. Armitage and Davidson [2013] are using $k = 1$ for CryoSat and are summing over all samples (i.e. $j = 1, n = 128$). For CryoSat SAR data they assign all pulse peakiness > 0.25 as valid ocean elevations. In this study the same values are used in the pulse peakiness calculations.

In Laxon et al. [2013] they detect leads in CryoSat data using pulse peakiness and the stack standard deviation as a surface detector. Leads are identified as pulse peakiness > 18 and stack standard deviation < 4 , while floes are identified as pulse peakiness < 9 and with a stack standard deviation > 4 . It is unknown what they use as the k -value.

In the CryoSat handbook [ESA and UCL, 2013a] the peakiness is defined as: “... essential the ratio of the highest bin value to the mean value of all bins above the retracking point”. The peakiness is used in the CryoSat L2 product for determining the leads and the ice floes. In Fig. 10.3.1 the pulse peakiness is plotted against the backscatter sigma0, and it is clearly shown how the leads (red) and the ice (yellow) are discriminated depending on the peakiness.

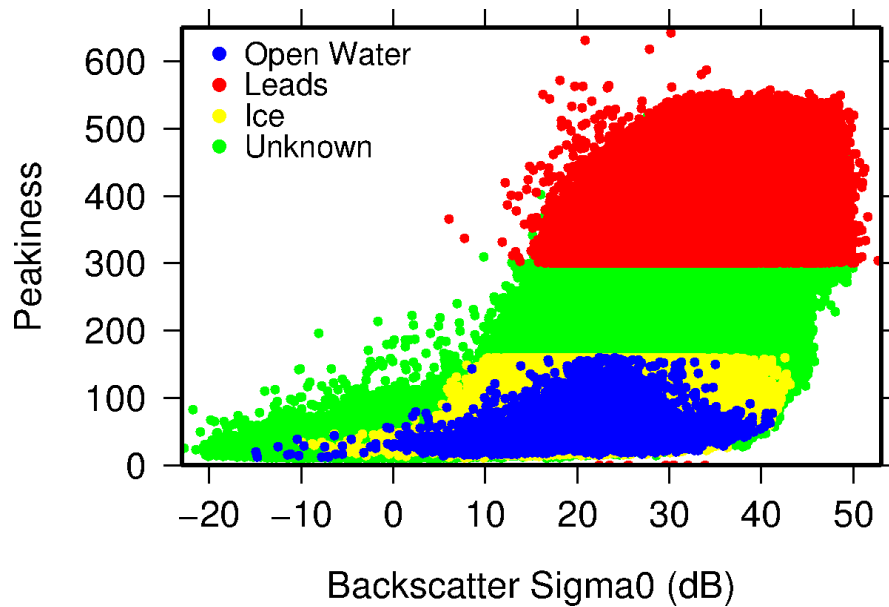


Figure 10.3.1: Surface identification in CryoSat L2 data from March 2012. The pulse peakiness is plotted together with the backscatter Sigma0. The surface types are: Open water (blue), leads (red), ice floes (yellow), and surface classified as unknown (green). Leads are given defined as peakiness higher than 300 and ice floes with peakiness lower than 160.

Parameter	Lead	Ice Floe
Pulse Peakiness	> 0.25	< 0.45
Peak Power	$> 1.5 \cdot 10^{-12} \text{ W}$	$> 8.0 \cdot 10^{-14} \text{ W}$
St. SD.	< 4	> 4
St. Skewness	< 7.5	< 2.5
St. Kurtosis	< 70	< 7
No. Measurements	42	309

Table 10.3.1: Parameters for detecting leads and ice floes. In the study area there are 789 observations, and by using the pulse peakiness and standard deviation as discriminators 56% of the measurements are rejected.

Data are from March 2012. Elevations are identified as leads when the pulse peakiness > 300 , and ice floes when the pulse peakiness < 160 . The peakiness may be a factor 10 too large, but the parameter is applied as written in the documentation. The distribution of points are ocean: 242426 points (5%); leads: 280877 points (6%); ice floes: 3095253 points (66%); and unknowns: 1070585 points (23%). From the baseline processing A and B the surface classifications are changed (not shown here).

Here the pulse peakiness, peak power of the retracked peak, stack standard deviation, stack skewness, and stack kurtosis are studied (the latter is described in Section 9.3.2). The surface detection parameters for leads and ice floes are written in Table 10.3.1. For detecting leads with the pulse peakiness parameter we use the pulse peakiness formula (Eq. (10.3.1)) as formulated in Armitage and Davidson [2013] with $k = 1$ spanning over all waveform bins and their recommendation for ocean surface with pulse peakiness > 0.25 . We also use the stack standard deviation criteria from Laxon et al. [2013]. The remaining parameters are based on trial and error analysis tested in different areas and compared with laser altimeter data and DMS imagery.

In Fig. 10.3.2 the pulse peakiness is plotted together with the peak power of the retracked peak and the beam parameters; stack standard deviation, stack skewness, and stack kurtosis. A high peak power, stack skewness, stack kurtosis, pulse peakiness and a low stack standard deviation are expected over leads. The beam parameters are described in Section 9.3.2. Red indicates a lead while green indicates an ice floe for each detection parameter given in Table 10.3.1.

For the purpose of detecting leads the parameters can be tuned to be very alike, but especially the pulse peakiness shows good results for lead values. The stack standard deviation, stack skewness, and stack kurtosis are also excellent lead detectors but can not alone detect the leads. Here, it is chosen to use a combination of the stack standard deviation as in Laxon et al. [2013] and the pulse peakiness as in Armitage and Davidson [2013]. The relationship between the parameters are shown in Fig. 10.3.3.

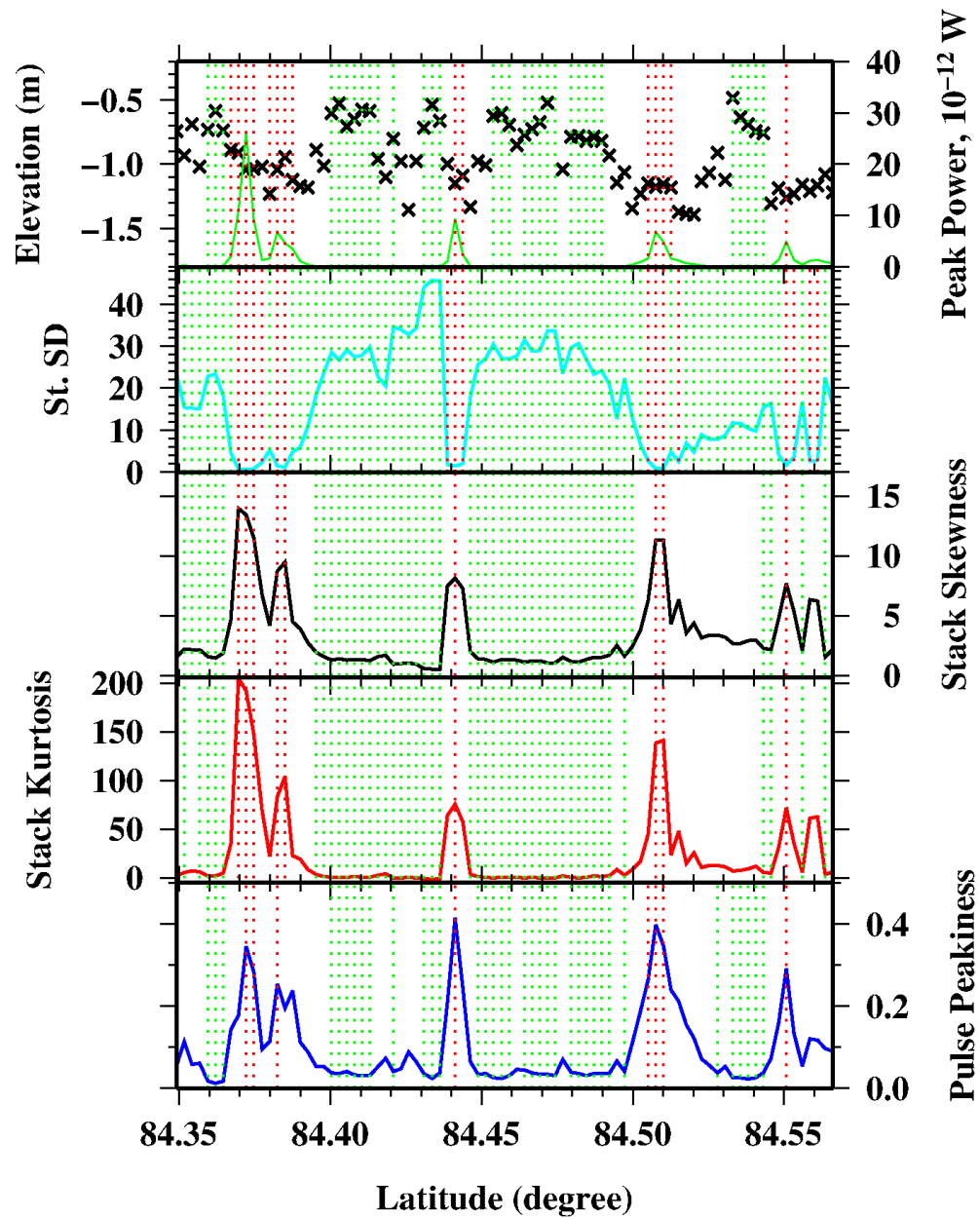


Figure 10.3.2: The CryoSat elevations are plotted together with the peak power of the retraced peak, the stack standard deviation (St. SD), stack skewness, stack kurtosis, and the pulse peakiness. The red dots indicate the lead detection for each parameter given in Table 10.3.1.

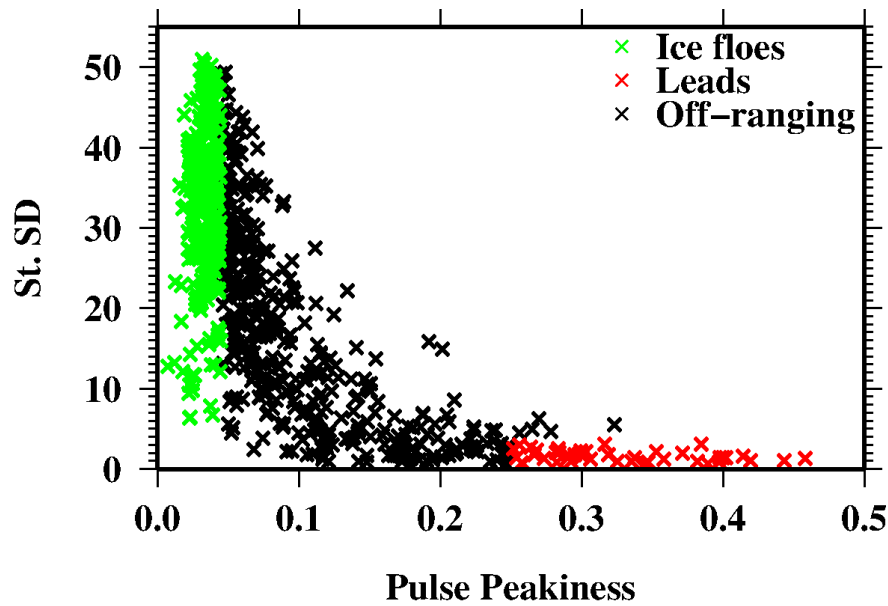


Figure 10.3.3: The relationship between the stack standard deviation (St. SD) and the pulse peakiness. These are the parameters used to discriminate leads (red) (pulse peakiness > 0.25 and stack standard deviation < 4) and ice floes (green) (pulse peakiness < 0.045 and stack standard deviation > 4). The black crosses are unclassified measurements indicating off-ranging elevations.

10.4 Sea Ice Drift

As described in Rose et al. [2013b], no sea ice drift is observed in the first part of the study area. This was based on comparing OIB's DMS and ATM with CryoVEx ALS data, flying the same track in close proximity within half an hour. The time difference between the CryoSat and the OIB and CryoVEx overflights are large (> 1 hour) and in principle the sea ice could have changed in this time frame. The start of the ice drift zone is clearly visible in the ASAR image (Fig. 10.0.1) above 84°N as long fractions in the ice pack.

Here ice drift is calculated from the same area but established from Envisat ASAR images. The drift coordinates are generated by Roberto Saldo, DTU Space, www.seaice.dk, from several ASAR images. There is a time difference between the images of 14 to 47 hours. From these coordinates a set of drift vectors (distance and direction) are calculated. Assuming a linear relationship in time, the ASAR drift is downscaled with the time ratio suitable for the drift between ATM and CryoSat. The drift map is shown in Appendix D.1. In the area shown in Fig. 10.5.1 the drift is about 0.1 km in the direction east-northeast. The drift correction based on the ASAR data are shown in Fig. D.1.2 over a lead in the study area.

Based on the temporal difference of the ASAR images the calculated drift is subject to uncertainties. Theoretically the sea ice can have moved in various directions during the period, and all the drift could have happened in the first hour. This is not likely the case but the reason why a shorter time difference between drift based datasets are preferred.

Making this correction actually strengthens the correlation of data in the first part of the study area where no drift was assumed in Rose et al. [2013b]. This Drift is applied in the following, and the drift is discussed in more details in Section 10.6.3.

10.5 Analyzing CryoSat Observations

CryoSat elevations (red crosses) are plotted in the area from earlier (Fig. 10.2.1 in Section 10.2) in Fig. 10.5.1, but this time with the preferred nearest neighbor algorithm for both ATM (yellow triangles) and ALS (blue diamonds) plus a description of the ice conditions analyzed from DMS and ASAR images. There exists five leads in the area in question (Fig. 10.5.1), they are all refrozen and some with snow on top.

In Fig. 10.5.1 the three datasets have been adjusted vertically for comparison purposes. The three red stars in the figure indicates the areas for further investigation. In the following, CryoSat data are corrected based on the ASAR drift described in Section 10.4.

Lead

The attention in this subsection is around the lead with the highest peak power (green curve) in Fig. 10.5.1. The remaining four leads are not described here, are shown together with CryoSat surface elevations in Appendix D.2. The CryoSat elevations over this lead (the dark gray color) with smooth surface are shown on top of three DMS images in Fig. 10.5.2. CryoSat is descending (i.e. flying from right to left in the figure). Fig. 10.5.3 contains the waveform of each observation, where the stack beam parameters are written in the top right corner.

The first thing to notice in Fig. 10.5.2; CryoSat “sees” the lead, i.e. the elevations are lower here than over the ice floes. The freeboard is around 40 cm, which is typical for multi-year ice. The retracked height furthest north (waveform 7672) has the same elevation level as the lead, which is too low as the retracked observation is outside the lead cf. the DMS image.

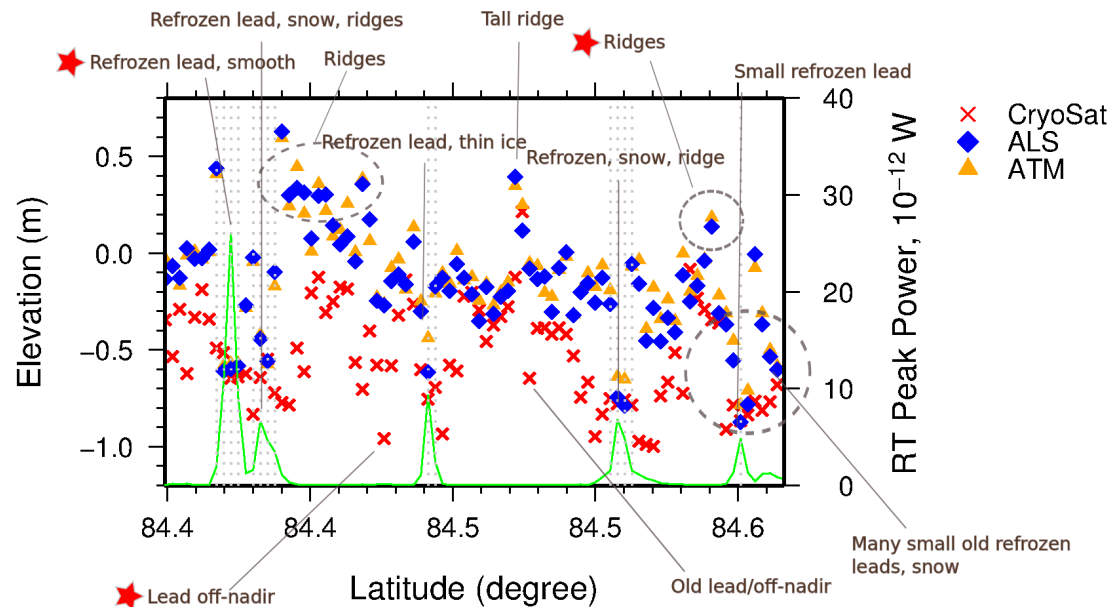


Figure 10.5.1: Elevations from CryoSat (red crosses), ALS (blue diamonds), and ATM (orange triangles) together with a description of the surface based on DMS and ASAR imagery. The green curve is the peak power, and the gray dots indicate a peak power over $1.5 \cdot 10^{-12}$ W. The red stars point out the areas for further investigation.

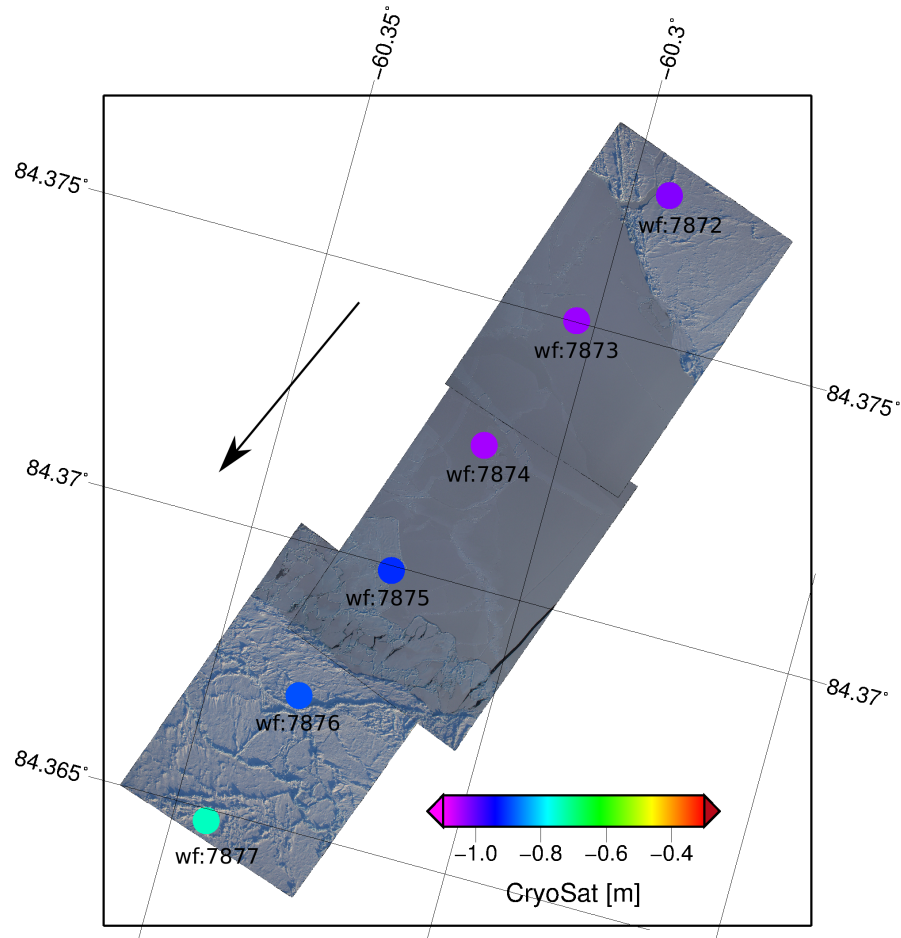


Figure 10.5.2: DMS images from 12:42:04, 12:42:07 and 12:42:12 merged together and overlaid with CryoSat elevations. The satellite is descending i.e. flying from the top right corner to the bottom left corner. The image shows a refrozen lead (dark feature).

Following the descending flight direction the waveforms (Fig. 10.5.3(a)-(f)) will be described one by one. Starting from (a) waveform number 7872, this is a very sharp one peaked waveform with a lead-type waveform. From the DMS image this is not a lead, but the observation is in between two leads, and is contaminated by the strong return signal from these leads. Comparing this and the next waveform, it is seen that the leading edge is less sharp in the beginning and with a relatively low peak power $8 \cdot 10^{-12}$ W. This waveform would have been retracked correctly if it was shifted around 1.5 range gates to the left. One range gate in the waveform corresponds to 23.42 cm in the vertical direction. This means that the true surface is actually the slow rising part of the waveform, the bump, before the second kink, marked with a green circle and an arrow.

The waveforms number 7873 in (b) and number 7874 in (c) are lead-like waveforms with a high peak power and a very sharp leading edge followed by a very sharp trailing edge. They are not perfect textbook examples because of the small kinks (marked with an arrow) just before the sharp rise. (b) also has a kink (marked with an arrow) in the beginning of the trailing edge. This is believed to be due to the snow on top of the refrozen lead and the effect by scattering

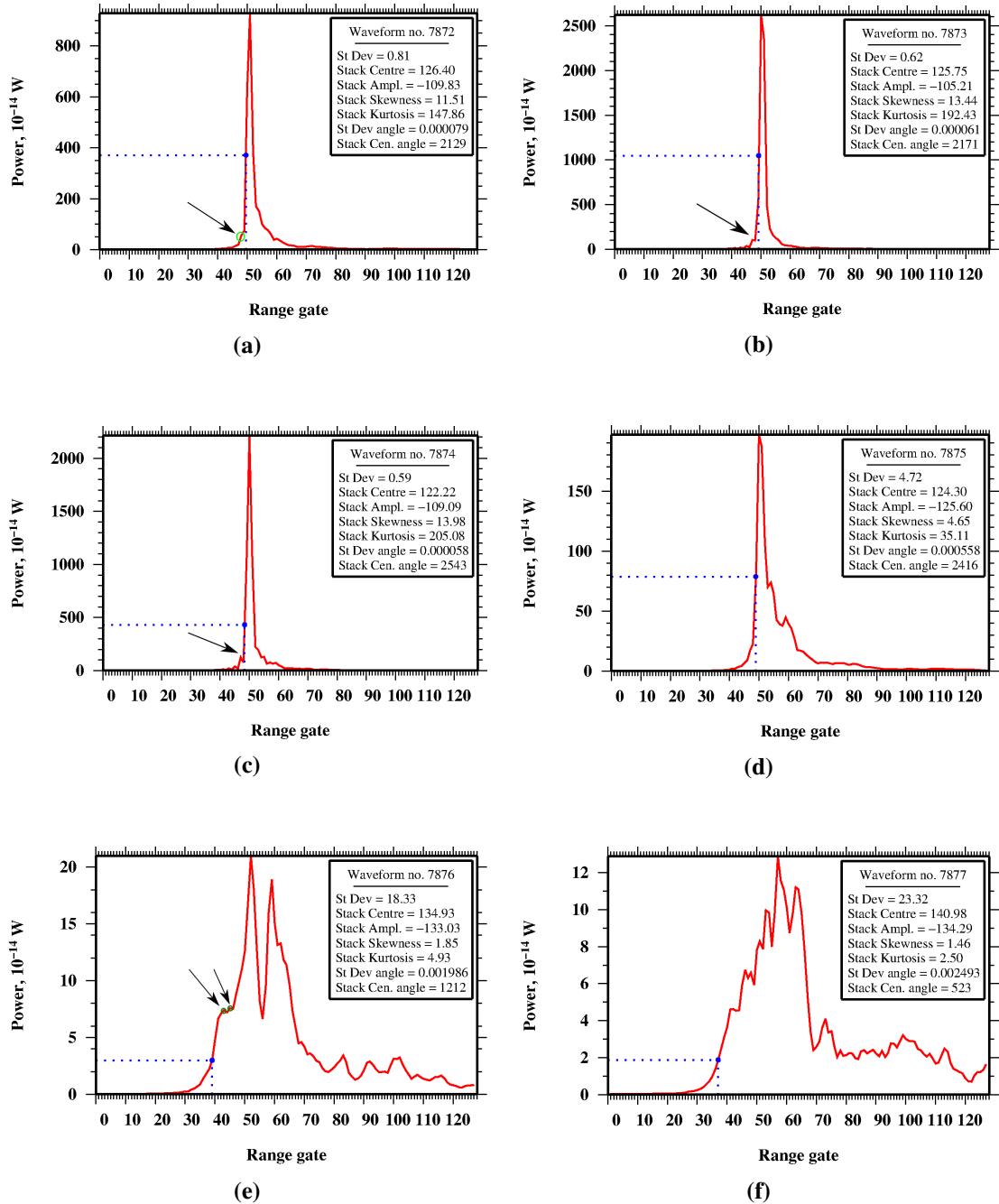


Figure 10.5.3: Waveforms corresponding to the CryoSat elevations in Fig. 10.5.2 from right to left following the flight direction. (b), (c) are typical lead waveforms from a specular surface i.e. from the lead. (e), (f) show returns from a more diffuse surface representing the ice floes. (a), (d) are the waveforms affected by the surrounding specular surfaces resulting in false retracking.

from the surrounding ice floes.

Following the DMS image Fig. 10.5.2, the waveform in (d), waveform number 7875, is over the lead, and therefore a low elevation is expected. The waveform has a small peak power compared with a lead but a nice sharp rise and a trailing edge suggesting a rough surface. From the retracking the elevation is intermediate, which is not what we would expect over a lead. Looking more carefully at the DMS image the surface looks more rough at this part of the lead, which could be the reason for the higher elevations. The stack standard deviation is higher than the previous leads due to more scattering.

Waveform number 7876 (e) is an irregular waveform in different ways. First of all; it has two peaks, and second; there is a soft curve in the maximum of the leading edge around range gate number 42 (a third peak). These are marked in the figure. Comparing the CryoSat surface elevation to the ATM and ALS elevations in Fig. 10.5.1 and to the surrounding ice-type CryoSat elevations, the elevation of this point, is expected to be about 20 cm too low. This corresponds to a shift in one range gate. In this case the retracker detects the first peak as the small sharp peak around gate 43 instead of the soft curvature before, actually being the first return. The two tall peaks are returns from the lead just passed and/or from specular surfaces off-nadir outside the DMS image. Waveform number 7877 (f) is a typical waveform over rough ice, which corresponds to the ridges visible in the DMS image. The stack standard deviation is high and the kurtosis low.

It could be expected that the ASAR drift applied to these data are incorrect. If the observations were moved half the length of the ground resolution in the flight direction, waveform number 7872 and 7875 would fit better to the DMS image. But this does not correspond to the direction of the drift observed by ASAR (Fig. D.1.1 in Appendix D.1), and by the EUMETSAT drift (not shown) provided with courtesy by Thomas Lavergne, LIMSI-CNRS.

Ridges

The area around latitude 84.535°N, marked with a small circle in Fig. 10.5.1, is an area with high surface elevations. The CryoSat elevations are overlayed a DMS image (Fig. 10.5.4(a)), the image shows a rough sea ice surface with ridge-like features. Fig 10.5.4(b)-(d) show the waveforms corresponding to the CryoSat observations in (a) following the descending flight direction (from left to right in the figure).

The maximum peak in the waveforms are likely coming from off-nadir returns. The last observation (outside the DMS image) is affected so much by the off-nadir return that the leading edge is tracked around one range gate too late, resulting in a too low elevation.

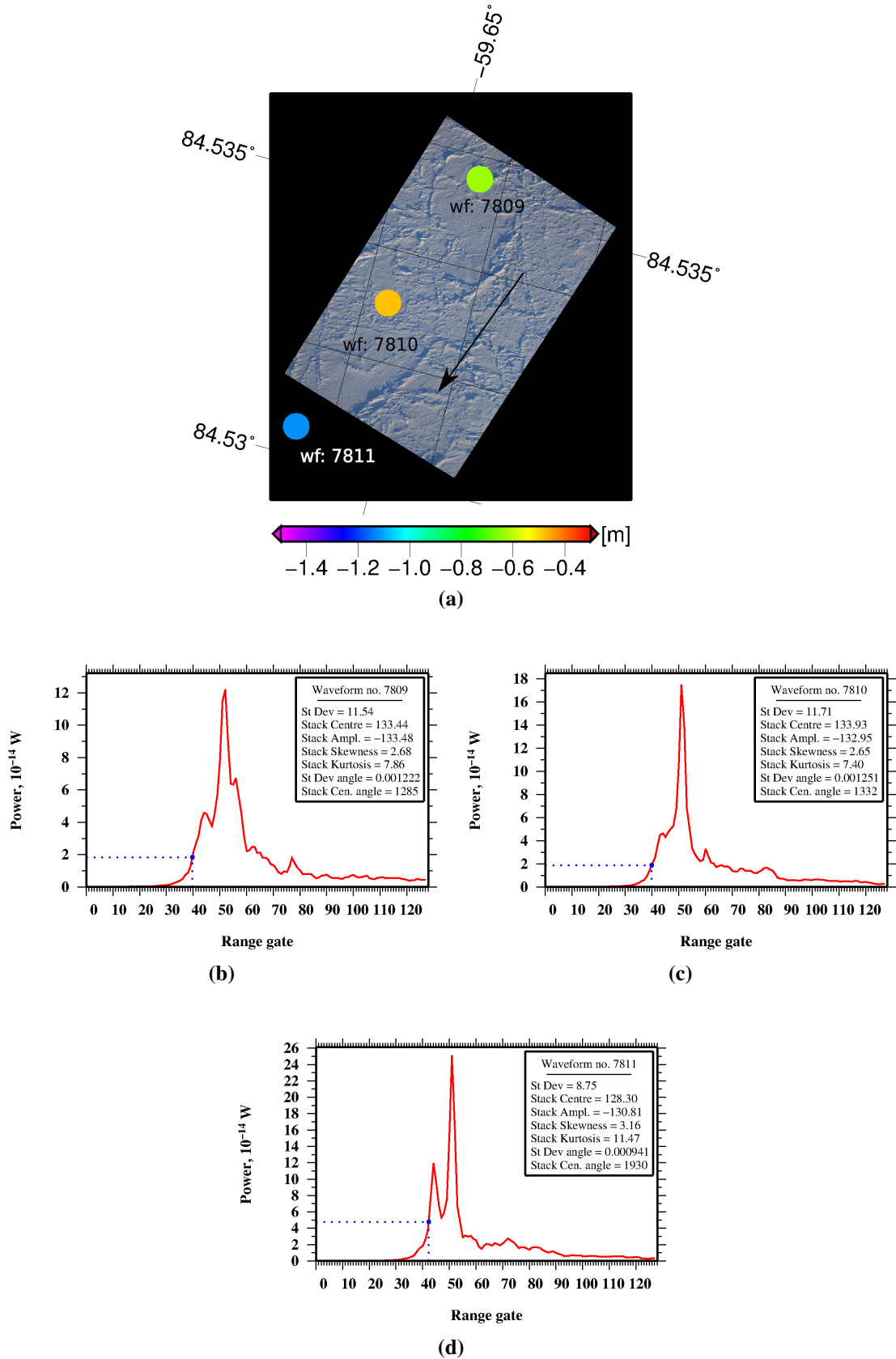


Figure 10.5.4: (a) DMS image from 12:43:51 with CryoSat surface elevations overlaid. This is a rough surface. (d) waveform number 7811, green point further right, (c) waveform number 7810, orange point in the middle, and (b) waveform number 7809 blue point to the left.

Lead off-nadir

This subsection concentrate about the region in Fig. 10.5.1 close to latitude 84.48° with an elevation of -0.96 m. This is a very nice example of a lead off-nadir. On the DMS imagery there is no sign of a lead (not shown here). The elevation of the CryoSat point is lower than the general lead elevations, and it does not look like snagging (cf. next subsection).

A zoom of the ASAR image (Fig. 10.0.1) is shown in Fig. 10.5.5. In the bottom left corner of the image, the lead evaluated earlier, is visible with two branches also seen in Fig. 10.5.1. The purple point in Fig. 10.5.5 in the center of the red circle, is the low CryoSat observation in question. Fig. 10.5.6(a)-(e) show the waveforms for the corresponding encircled points in Fig. 10.5.5. The very low elevation is the waveform in (c). It has a sharp first return and a high peak power compared with a normal ice-type waveform. The standard deviation is high and the stack kurtosis low. This indicates that the power return is coming from off-nadir.

There are marked two leads with black arrows in the ASAR image. The arrow closest to the CryoSat track is pointing at a small dark feature (only one pixel). This is probably the lead causing the high return in the waveform. It is about 6 km from the CryoSat track, i.e. within the CryoSat footprint. This off-nadir lead is also visible in the nearby waveforms with a very strong peak. The second lead, marked with an arrow, is probably causing the disturbance in the trailing edge.

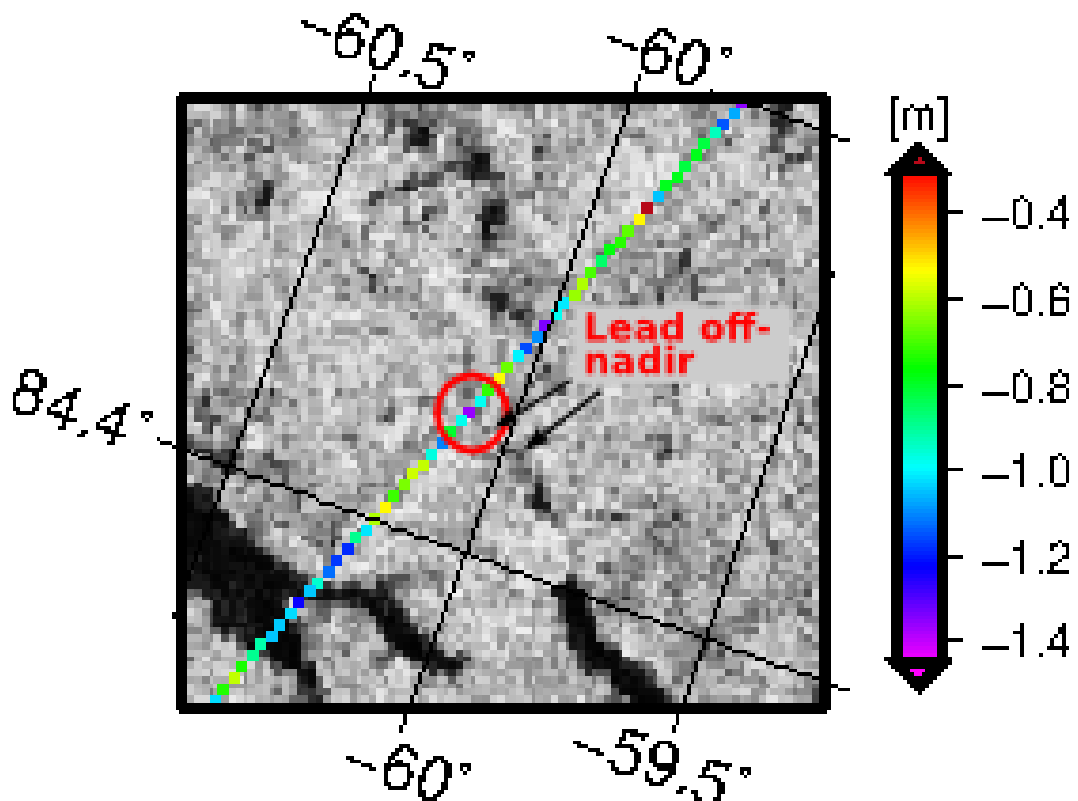


Figure 10.5.5: Zoom of ASAR image from 17:51. A lead off-nadir is affecting the CryoSat observation (purple point) with its high return power.

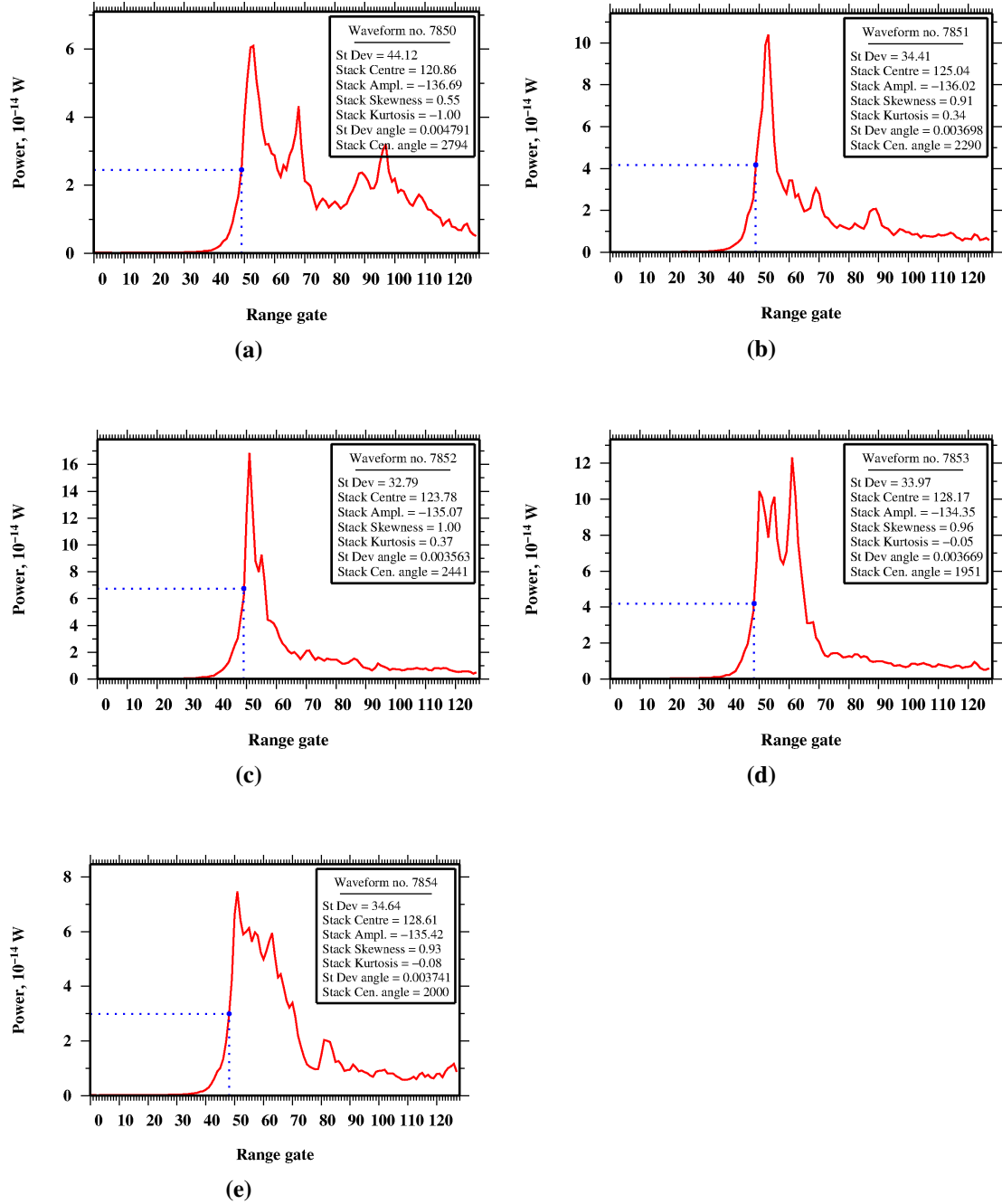


Figure 10.5.6: Waveforms corresponding to the elevations encircled in Fig. 10.5.5 given in the flight direction from right (a) to left (e).

Snagging

In this last subsection data from April 27, 2012 are used, where CryoVEx underflew the CryoSat orbit number 10885, north of Svalbard. The ice conditions are very dynamic and the sea ice is of mixed types, but mainly first-year ice. This dataset is described in more details in [Rose et al. \[2013b\]](#) as study area 2.

To illustrate how dynamic the area is two MODIS images (Section 5.2.2) from the Terra satellite is merged from the subsets r02c04 and r03c04 from April 27, 2012 and cropped to the desired region (large image in Fig. 10.5.7). The image resolution is 250 m. ESA lost contact to Envisat April 8, 2012 therefore no ASAR image is available for this date. The CryoSat surface elevations are overlayed in Fig. 10.5.7. The area in the red box is enlarged showing the area for this investigation. Unfortunately, there is a cloud just above the area of interest (red circle). To enhance the lead features, image processing is conducted. A rough estimate yields a distance of 1.6 km between the lead and the snagging point with the lowest elevation furthest away from the lead (indicated on the figure with a green line).

The range difference between a nadir point and a off-nadir point can be given with simple geometry (Fig. 10.5.8(a)): $R - H = \sqrt{H^2 + x^2} - H$, where R is the range from the satellite to the off-nadir point, H is the satellite altitude, and x is the distance on ground to the off-nadir point. The mean satellite altitude in the study area is 737.14 km. The ranging offset in meters are shown in Fig. 10.5.8(b) as a function of the lead distance from nadir.

In Fig. 10.5.9(a) the CryoSat retracked elevations around the lead are shown together with the corresponding waveforms. Fig. 10.5.9(b) is a zoom of the blue box in (a). There is a clear shift in the maximum peak power of the waveforms when the elevations starts to decay. Furthermore, the snagging waveforms have a double peak indicating the various surfaces picked up in the return signal.

The distance between the two peaks becomes smaller further away from the lead because of less influence from the powerful lead return. In these waveforms the lead has contaminated the waveforms and therefore the retracked elevations. The closer the satellite is to the lead, the higher the peak power of the waveform.

Notice how the CryoSat observations decay in a curve following the shape of the graph in Fig. 10.5.8(b). The lowest CryoSat elevation is 2 m lower than the lead value, corresponding to a distance of -1.6 km to the lead height.

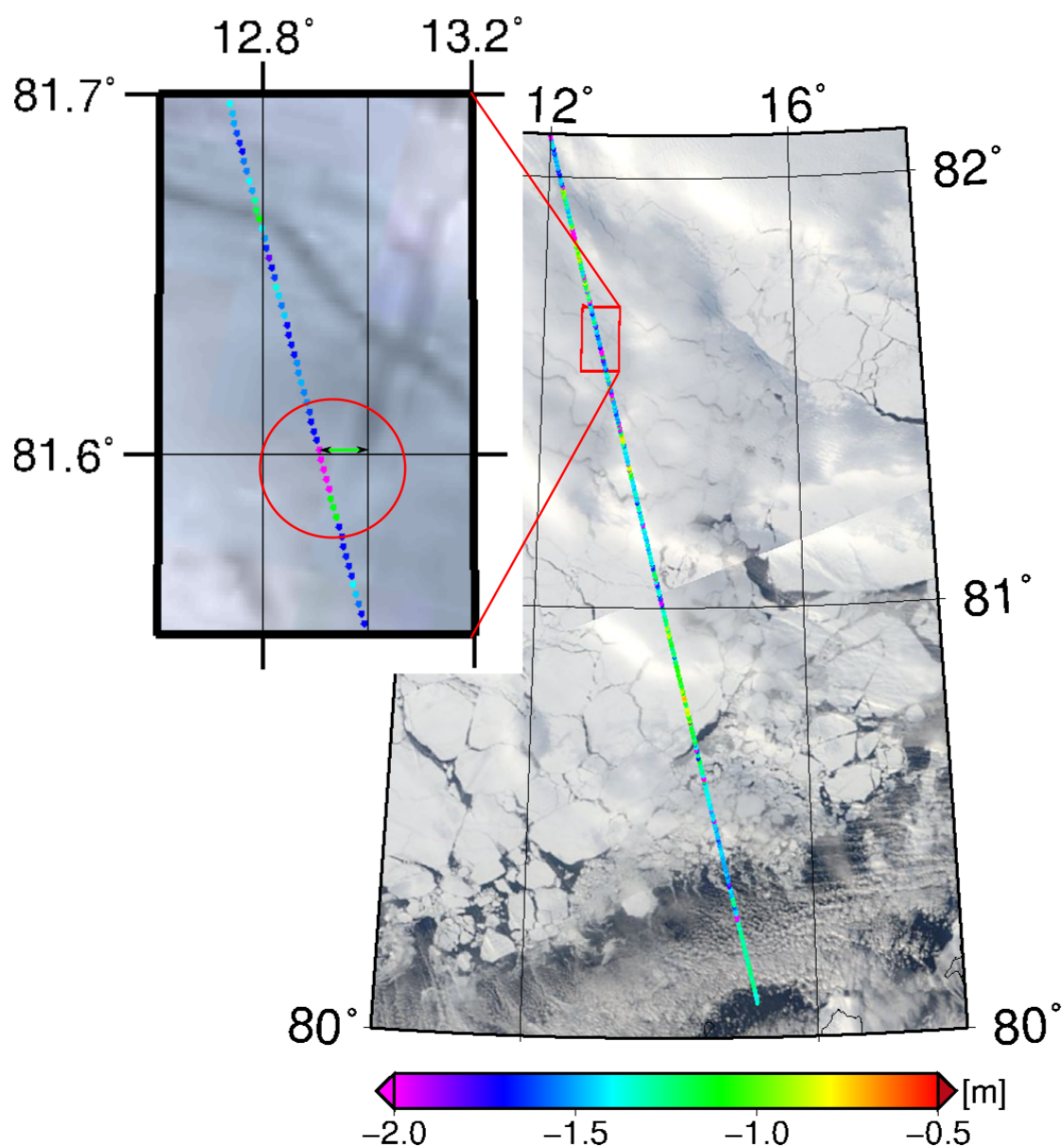


Figure 10.5.7: MODIS image from May 27, 2012 with overlaid elevations from CryoSat orbit number 10885. The sea ice is very dynamic in this region as seen by the many leads (black features) in between the ice floes.

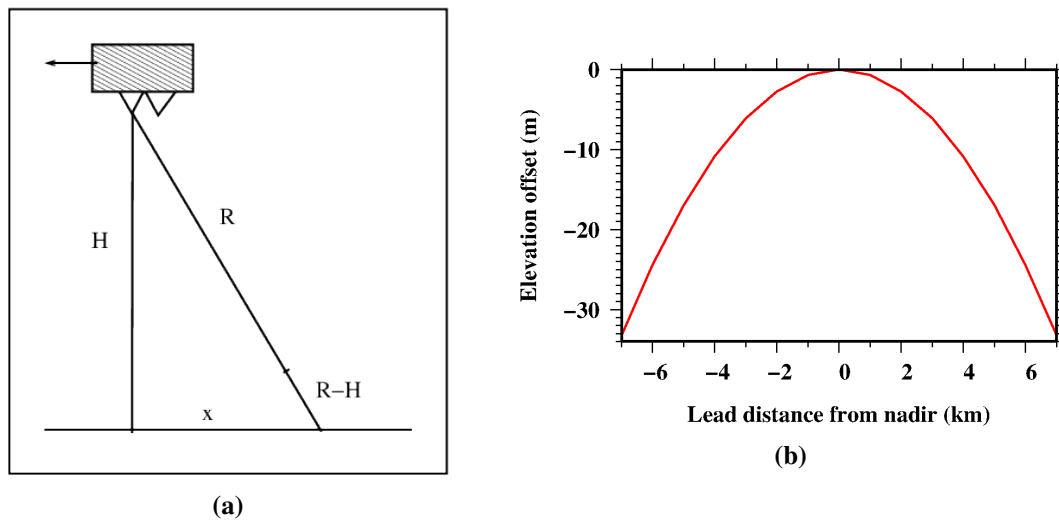


Figure 10.5.8: (a) Sketch of the satellite geometry. H is the satellite altitude, R the range to a point off-nadir, and x is the distance on the ground from nadir to the measurement off-nadir. (b) Ranging offset ($R-H$) as a function of the distance from nadir (x).

Concluding Remarks

In overall, CryoSat gives good elevation results. In ridged areas CryoSat has high elevations and over leads it has low elevations. Furthermore, in the last part of Fig. 10.5.1 the area with a lot of small old refrozen leads are depicted in all three datasets.

The retracking goes wrong when CryoSat is approaching or receding a lead, and if there exist a lead off-nadir. These are typically the points laying around -0.5 m. If these elevations are not filtered out, consequently, the results will have more uncertainties. CryoSat does not perform as good in very dynamic areas with lot of leads and thin ice as in areas with steady ice conditions and few leads.

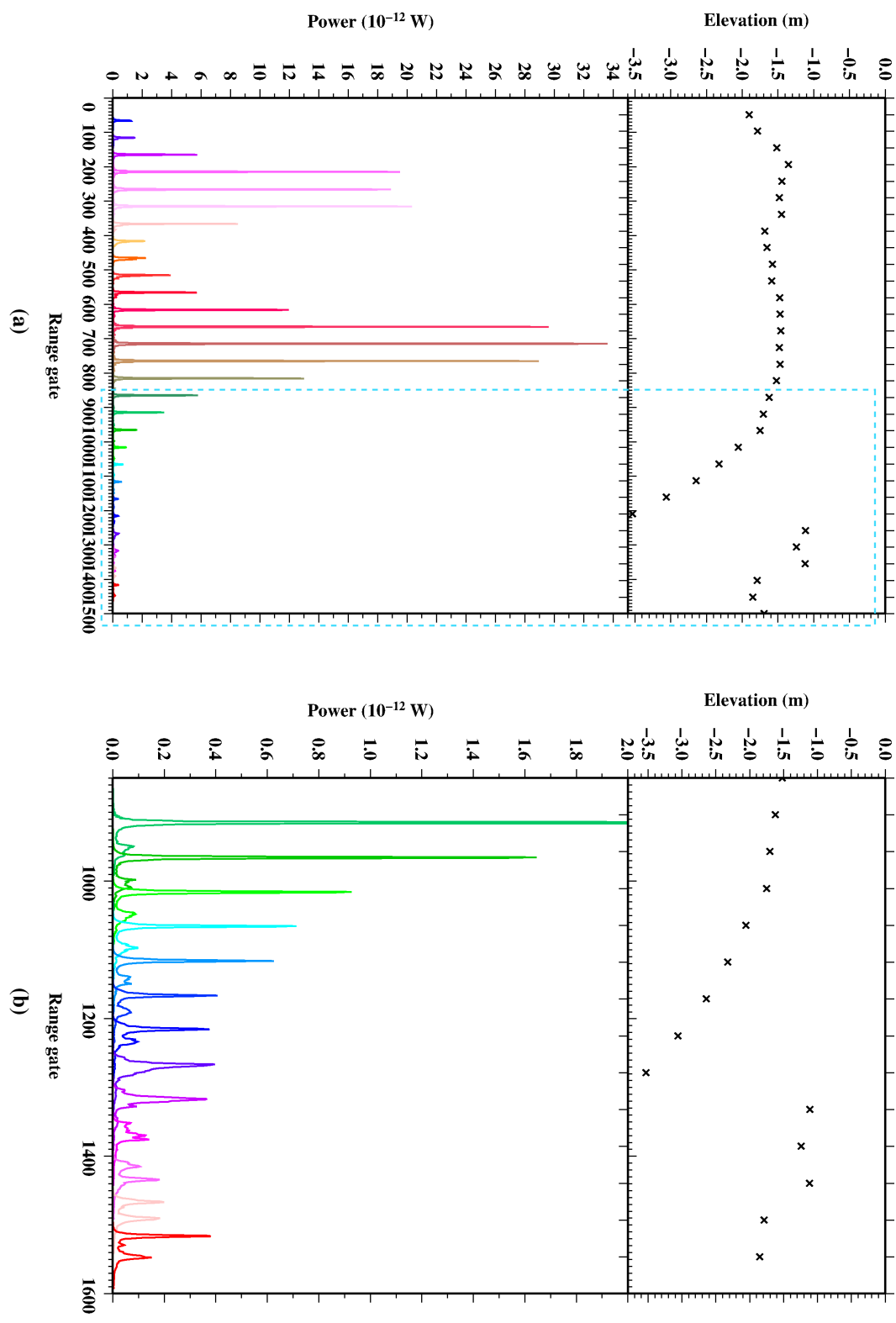


Figure 10.5.9: Top: CryoSat elevations. Bottom: The corresponding waveforms. (a) CryoSat is overflying two leads from right to left. The first lead is observed by the satellite when approaching. The elevation is decaying in a typical pattern, as shown Fig. 10.5.8(b). This is called snagging. There is observed high peak power over the lead. (b) zoom of the snagging elevations and waveforms. The peak power is here less than the power over the leads.

10.6 Dealing with the Off-ranging Elevations

In the following two methods for detecting off-ranging elevations are presented, and a number of optional methods are discussed. The data from study area 1 and 2 from Rose et al. [2013b] are used to filter out the off-ranging elevations, and the new freeboard results are presented. Finally, further improvements to the study are discussed in Section 10.6.3.

10.6.1 First Attempt: Peak Power Search Routine

In the first method leads are selected with the algorithm used in Rose et al. [2013b], and the high peaked waveforms are analyzed to detect off-ranging elevations. The off-ranging elevations are detected as follows:

1. All peaks above a threshold of $1.5 \cdot 10^{-12}$ W are found. The largest peak power is chosen as the central lead.
2. The routine is searching the nearby values, if the elevation is lower than the central lead and the peak power is less than 50% of the power of the central lead, the values are chosen as off-ranging and therefore rejected.

The results are shown in Fig. 10.6.1, where the pink dots indicate the rejected observations, the red triangles are the detected leads, and the green curve is the peak power. Applying this for the whole track in study area 2 from Rose et al. [2013b] gives a new freeboard of 12.0 cm for the 40% threshold retracker. The freeboard distribution is shown in Fig. 10.6.2. Rose et al. [2013b] find a freeboard of CryoVEx's ALS scanner data of 32.5 cm yielding a difference to the CryoSat radar signal of 20.5 cm. The high peak around 37 cm corresponds to the CryoVEx

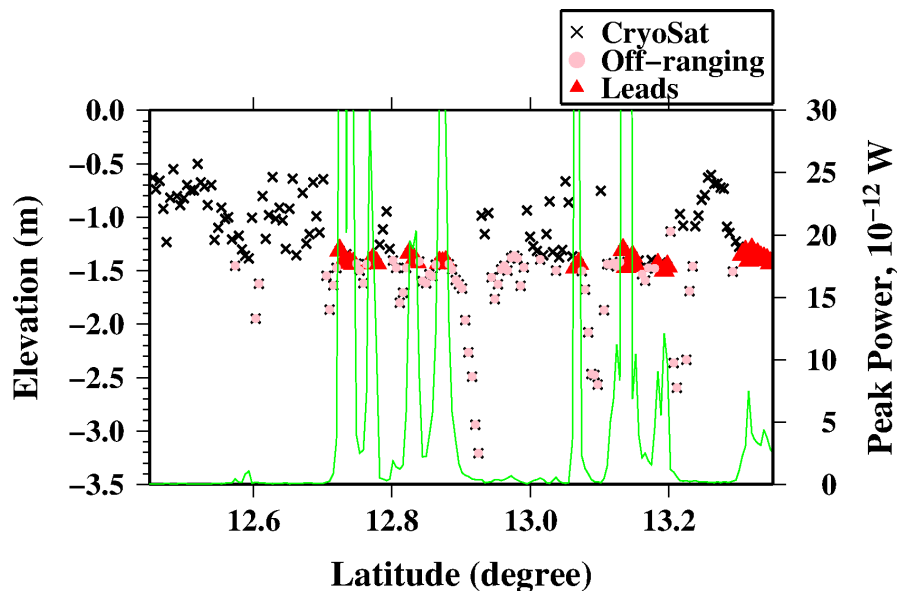


Figure 10.6.1: Detecting off-ranging elevations in the CryoSat data (black crosses). The red triangles are the detected leads, and the pink circles are the elevations classified as off-ranging.

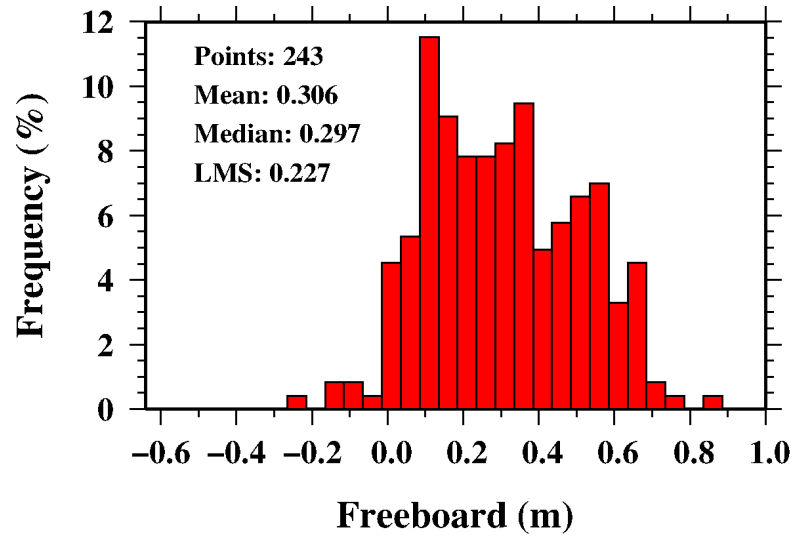


Figure 10.6.2: Freeboard distribution of CryoSat data from the second study area in *Rose et al. [2013b]*. Here, off-ranging data are filtered, and this gives a new freeboard of 12.0 cm.

ALS freeboard. This may be caused by the radar signal reflecting from the snow surface. By using this method 47% of data are rejected.

This is a first attempt of filtering off-ranging elevations. It has to be tested on different CryoSat tracks with various ice conditions. Especially it has to be adjusted to not detect too many off-ranging elevations and thereby losing important signals. But the problem with this method is actually the opposite: This method finds the snagging points, but does not deal with the off-ranging elevations in between the ice floes and the leads. The problem with this method is that there is no statistical evidence for filtering data.

10.6.2 Second Attempt: Pulse Peakiness Criteria

The second method for dealing with off-ranging elevations are by using the same parameters as for detecting leads (Table 10.3.1), but choosing the parameters for ice floes written in Table 10.3.1. For the study area 1 there are 789 measurements for which 42 measurements are leads and 209 are ice floes yielding a rejection of 56% of the dataset.

The new elevation relationship between the airborne datasets and CryoSat with a 40% and a 50% retracker are shown in Fig. 10.6.3. The 40% threshold (top figures) correlates better with the airborne datasets than the 50% threshold (bottom figures). After filtering the correlation relationship has improved (compared to *Rose et al. [2013b]*) about 0.09 for ALS and 0.07 for ATM to the CryoSat elevations from the 40% threshold retracker. The new correlation coefficients (See Fig. 10.6.3) are close to the thickness correlation between ATM and CryoSat in *Laxon et al. [2013]*. They found a correlation of $r = 0.608$.

There is still a large spread between the observations, and Section 10.6.3 discusses why data are not correlating better and further improvements are suggested.

New CryoSat freeboard values after the filtering are calculated for Method 1, 2, and 3 [see *Rose et al., 2013b*] and written in Table 10.6.1. The mean, median, and the freeboard mode are given together with the standard deviation and the difference between the laser scanner mode

(Δ Mode) and the mean of ALS (Δ ALS) and ATM (Δ ATM). The two laser modes are the same, and their mean difference is 3 cm. The modal difference between the laser scanner data and the CryoSat 40% threshold freeboards are 10 cm, where a threshold of 50% yields a 18 to 25 cm difference. The mean difference varies between 20 and 23 cm for the three methods compared to ALS and between 23 to 26 cm compared to ATM. For the freeboard from the 50% threshold retracker the difference is 30 to 31 cm and 33 to 34 cm compared to ALS and ATM, respectively. The standard deviation is a little better for the 50% threshold retracker results than for the 40% threshold.

In Fig. 10.6.4 the probability distribution of the freeboard heights are shown. The three freeboard retrieval methods agree, and we see a second mode around zero representing the leads.

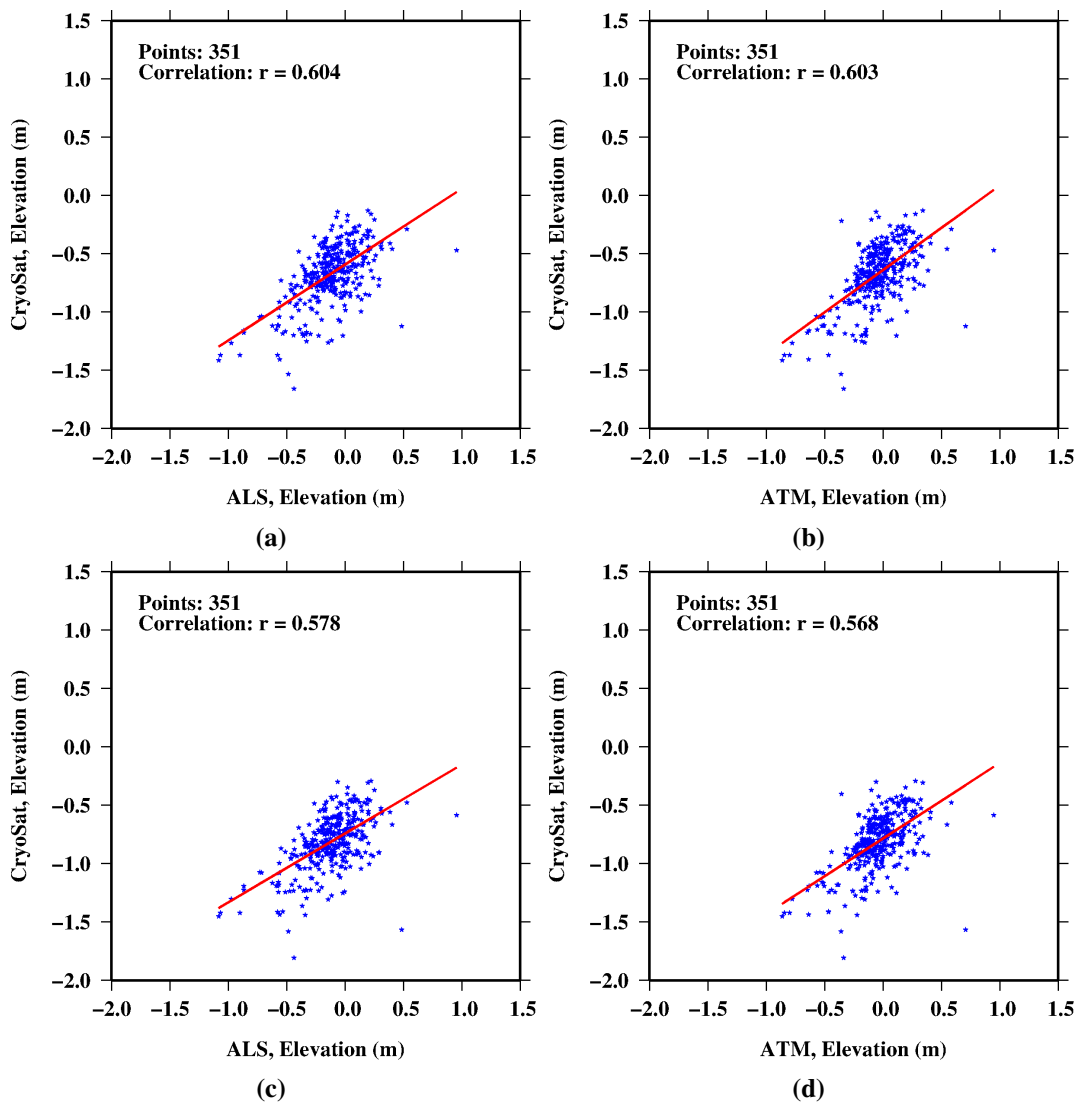


Figure 10.6.3: Scatter plot of (a) ALS and CryoSat elevations w.r.t EGM08 (40% threshold), (b) ATM and CryoSat with a 40% threshold, (c) ALS and CryoSat with a 50% threshold and (d) ATM and CryoSat with a 50% threshold.

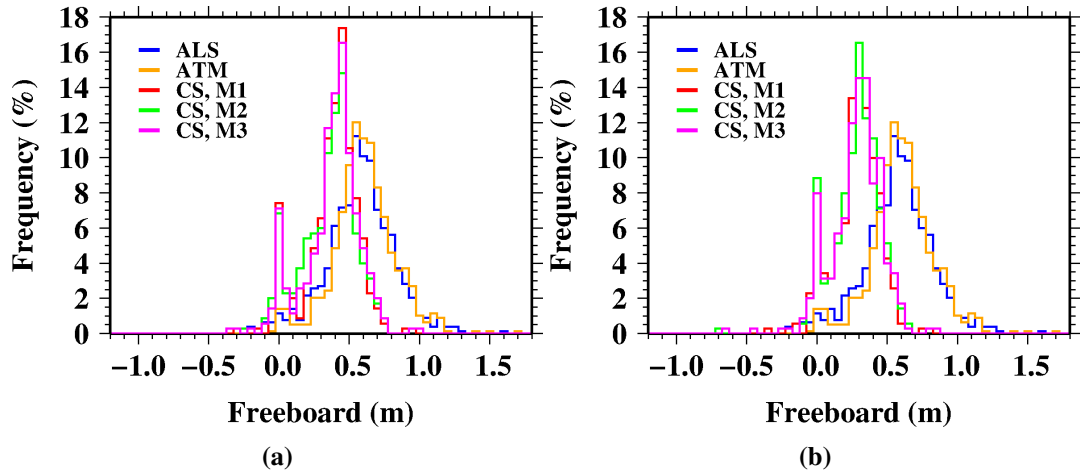


Figure 10.6.4: Freeboard distribution of CryoSat data from the first study area. The off-ranging data are filtered with the second filtering attempt i.e. the criteria from Table 10.3.1.

The frequency of leads are large and will affect the mean and the median values. Therefore, the modal freeboard is the best to compare with the laser scanner datasets.

In Rose et al. [2013b] the snow depths from the OIB Quick Look product were used to apply the CryoSat data. In Fig. 10.6.5 the distribution of snow depth is shown, averaged to the CryoSat sampling rate. The mean snow depth is 28 cm, and the distribution is bimodal having modes at 15 and 25 cm. This is about 10 cm lower than compared to the snow depth from Warren’s climatology yielding 36 cm in April for this study area (See Appendix A).

	Mean (m)	Median (m)	Mode (m)	SD (m)	Δ Mode (m)	Δ ALS (m)	Δ ATM (m)
ALS	0.575	0.581	0.550	0.244	-	-	0.030
ATM	0.605	0.599	0.550	0.222	-	-0.030	-
CryoSat Method 1							
Threshold 40%	0.371	0.403	0.450	0.193	0.100	0.204	0.234
Threshold 50%	0.269	0.293	0.300	0.157	0.250	0.306	0.336
CryoSat Method 2							
Threshold 40%	0.350	0.389	0.450	0.205	0.100	0.225	0.255
Threshold 50%	0.277	0.300	0.300	0.162	0.250	0.298	0.328
CryoSat Method 3							
Threshold 40%	0.373	0.410	0.450	0.198	0.100	0.202	0.232
Threshold 50%	0.279	0.306	0.375	0.161	0.175	0.296	0.326

Table 10.6.1: Freeboard statistics after filtering off-ranging CryoSat elevations. The columns are from left to right: mean, median, mode, standard deviation (SD), the difference w.r.t. the ATM and ALS mode (Δ Mode), mean ALS (Δ ALS), and ATM (Δ ATM) freeboard, respectively.

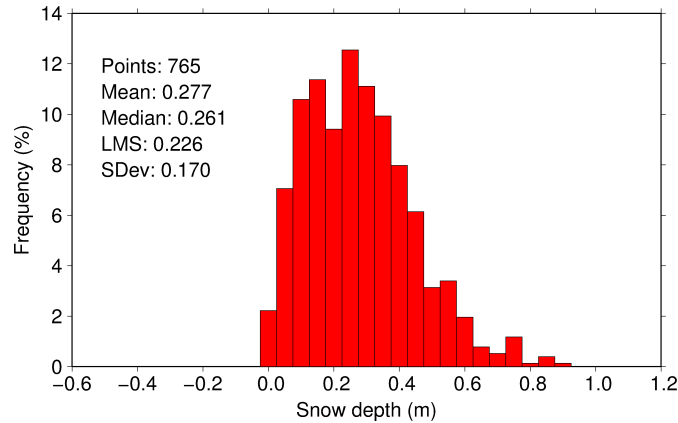


Figure 10.6.5: Probability distribution of snow depth from OIB from April 2, 2012. This is from the Quick Look product averaged to the CryoSat sampling. In the top left corner data statistics are given: Number of points, mean, median, the estimated mode (LMS), and the standard deviation (SDev).

The threshold of the retracker was also tested in [Rose et al. \[2013b\]](#), before any filtering was applied to data. We concluded that the 40% threshold retracker performed best, after applying snow. After this second attempt to filter out off-ranging elevations, a threshold of 40% also correlating best with ALS, but with the snow depth in mind, the freeboard value for the 50% threshold retracker performs best after filtering the off-ranging elevations.

This filtering attempt with the pulse peakiness criteria is also tested for study area 2 based on the threshold retracker of 50%. For this area the pulse peakiness criteria resulted in 59% rejection of observations, resulting in 190 observations left after filtering. As seen in Fig. 10.6.6(a), showing the filtered CryoSat surface elevations (blue) with the detected leads (red) and the derived SSH (green), the rejection criteria does not filter out all the off-ranging elevations, and several leads are falsely detected as leads (red dots in figure below the SSH). This has to be investigated in more details. The leads represent 54% of the dataset and therefore drowns the ice floe signal. Therefore are the leads and the negative freeboard values filtered out from the data. The new freeboard distribution is shown in Fig. 10.6.6(b) in red, whereas the blue distribution is the ALS data.

From the probability distribution of the CryoSat observations there are two or three modes approximately around 15 cm, 37 cm, and 50 cm. This could be representing first- and multi-year and the last peak could represent older multi-year ice or ridges. In [Rose et al. \[2013b\]](#) we speculated that some of the radar signal were returning from the snow surface. At this time of year, late in the season, days with melt occur followed by days of freeze. This would cause frost flowers in the snow, which the radar signal may not penetrate. After this filtering of off-ranging elevations, the conclusion has changed: The two first modes from the CryoSat probability distribution are coincident with the ALS data, from this it seems like most of the CryoSat data are reflected from the snow surface. The model freeboard is 37 cm. The mean freeboard for ALS is 32 cm, whereas the mean freeboard from CryoSat is 29 cm. This is a difference of 3 cm close to the uncertainty reported from laser and radar data comparisons (cf. Section 8.1.1). The result is not shown for the 40% threshold retracker, because this gives a modal freeboard higher than the ALS freeboard, which is not appropriate.

Comparing these findings to the freeboard probability distribution of the first filtering at-

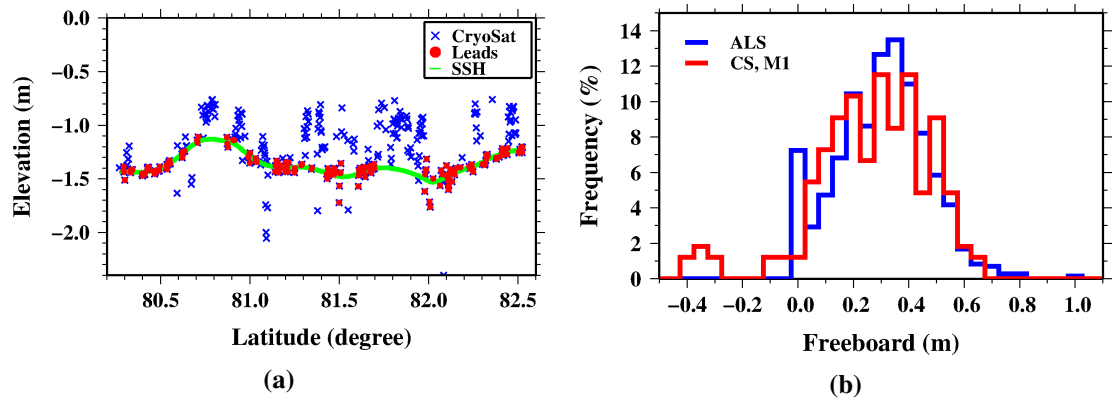


Figure 10.6.6: (a) SSH of study area 2 from north of Svalbard after pulse peakiness filtering. Blue crosses are CryoSat surface elevations, red circles are the detected leads, and the green curve is the retrieved SSH. (b) Freeboard distribution of CryoSat observations from the second study area.

tempt in Section 10.6.1, Fig. 10.6.2, it seems like the large mode around 0.1 is an artifact from off-ranging elevations and not the true nadir sea ice surface.

10.6.3 Further Discussion and Enhancements

In this section the lead detection and the data filtering of the off-ranging elevations are described. The CryoSat and laser scanner data correlations are discussed and possible enhancements to the study are described.

Lead and Off-ranging Elevation Detection

Another way of dealing with off-ranging elevations could be to include the beam parameters described in Section 9.3.2 and 10.3, or by looking at the width and the slope of the leading edge and the trailing edge. Farrell et al. [2009] made a study from ICESat using a combination of surface elevations, reflectivity, the properties of the laser waveform of the transmitted and received waveform including peak power, the width of the waveform from half maximum power, skewness, kurtosis, and the cross correlation between the transmitted and the received waveform.

The width of the leading edge is also used to determine unknowns in the ERS-1 satellite [Laxon, 1994b]. In a recent discussion paper by Zygmuntowska et al. [2013] using the Airborne Synthetic Aperture and Interferometric Radar Altimeter System (ASIRAS), which has a SIRAL like altimeter on-board, various waveform parameters are studied to analyze the waveforms from different sea ice surfaces. They study the pulse peakiness, the trailing edge slope, the leading edge width, the trailing edge width, and the maximum peak power. They find that using the maximum peak power increases the accuracy of lead detection but reduces the detection rate of leads. Furthermore, they find the maximum peak power and the trailing edge width as the most suitable for classifying first- and multi-year ice.

Discussion and Improvements of the CryoSat and Laser Scanner Data correlation

For study area 1, the correlation between CryoSat and the scanner datasets has improved after applying the pulse peakiness criteria for filtering off-ranging elevations (second attempt). The correlation varied from 0.568 to 0.604 and showed better results for a threshold of 40% than for 50%. The freeboard with the 50% threshold retracker gave a more realistic freeboard height.

It is important to stress that the radar and the laser data are different in nature. The radar penetrate (most often) to the snow/ice interface, whereas the laser reflects from the snow surface. Therefore, the snow cover variability is a large error source in the analysis.

A few things may improve the correlation and needs to be investigated in more details. Even though the physical difference of the laser and the radar altimeter, the correlation can probably be improved by various considerations; drift, averaging of laser scanner data, and loss of data over leads. The drift was only applied for the second part of the track, and the CryoSat drift was calculated based on the drift between ATM and ALS by assuming a linear drift in time. The averaging of data is done after the drift correction and is very dependent on a correct drift correction. Furthermore, the laser scanner data tends to loose data over the open leads (Section 10.2), which will cause wrong interpolation of leads between the two datasets. OIB is besides the ATM flying with a narrow swath ATM, with a more nadir pointing scan angle of 2.7° off-nadir, meaning that the scanner is able to pick-up the returns from leads. This data could be used as a supplement to the ATM.

To get an idea of where the problem lies, the relationship between the ATM elevations and the CryoSat elevations (40% threshold) are shown again but this time with the leads (following the CryoSat lead criteria) plotted in Fig. 10.6.7(a) as orange stars. Data are separated in ice floes in Fig. 10.6.7(b) and leads in Fig. 10.6.7(c) and color coded depending on the latitude. In (c) the gray line is the linear correlation from the total dataset in (a).

The first thing to notice is how much the leads in (c) are scattered. In a good correlation, one would especially expect the leads to be nicely aligned, assuming no snow on the leads, where both the radar satellite and the laser airborne altimeter would measure the same surface.

In (c), looking at the total correlation (gray line), the blue and dark blue points from low latitudes correlate the best. This is CryoSat observations from the area before the ice drift begins. The dark blue and purple leads are lower in ALS than in the CryoSat observations. This is following the DMS imagery refrozen leads with snow on top. These observations are 10 to 20 cm from the correlation line, corresponding well with a possible snow layer.

Fig. 10.6.7(d) shows all the observations but with the three largely deviating points in (b) rejected. Removing these outliers improve the total correlation to $r = 0.629$.

The CryoSat drift in respect to ALS and ATM are subject to further investigation. It has already been pointed out that the ASAR drift in the first part of the track showed ice movements. This was not corrected for in Rose et al. [2013b], because it was not visible between the short period between the ALS and ATM flights. Either the drift calculated based on ASAR drift vectors should be applied to the CryoSat data, or an other possibility is to find a direct drift between the ATM and the CryoSat measurements by looking at the lead locations in the datasets.

In the end of this section, it is important to emphasis that even with a less good correlation the freeboard heights can rightfully be compared to each other. Also if the datasets are not measuring the exact same surface due to drift, the mean freeboard would be comparable for the area in question.

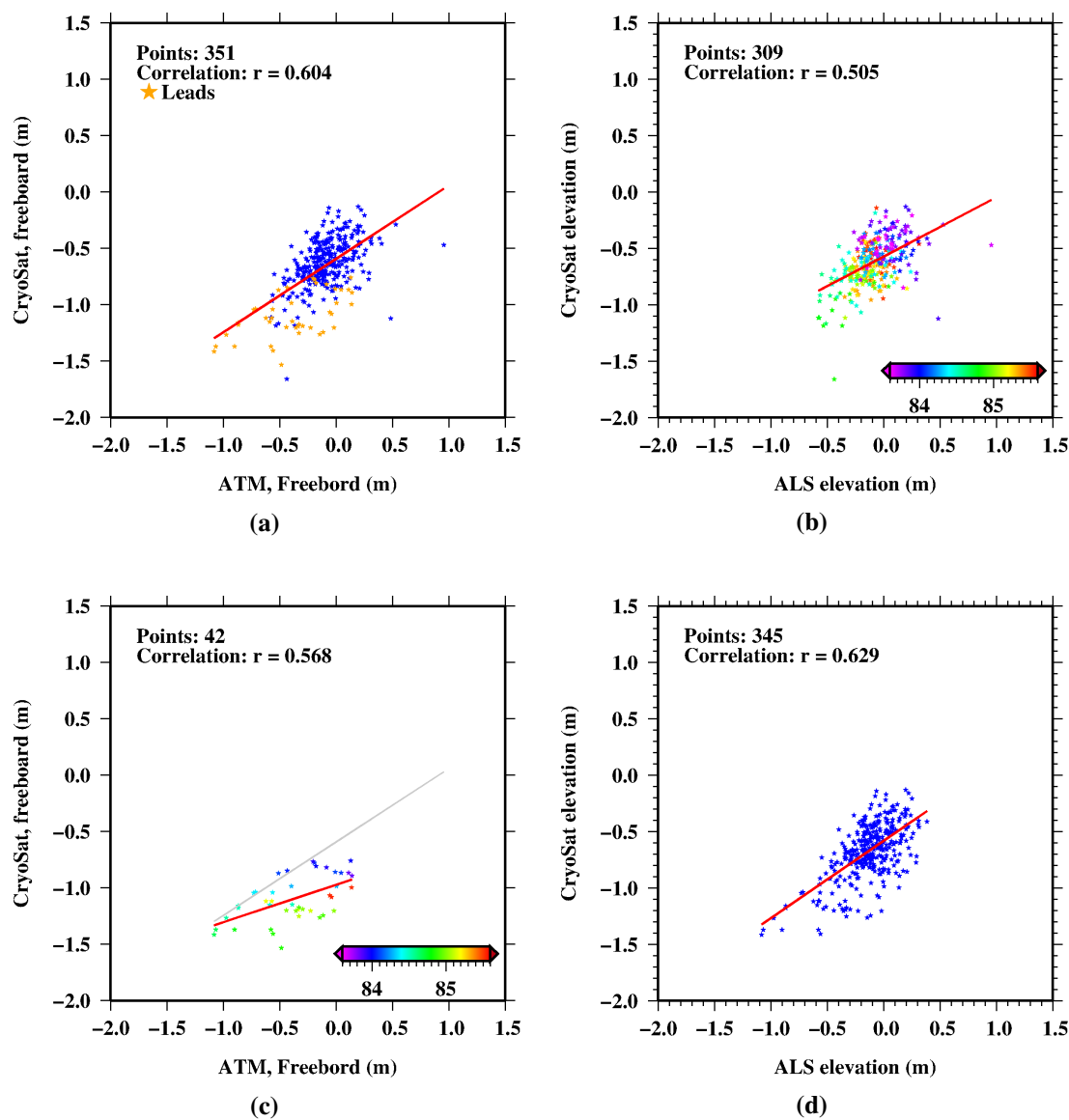


Figure 10.6.7: Scatter plots of ATM versus CryoSat 40% elevations w.r.t. the EGM08 geoid.

Sea Ice Maps from CryoSat

The results in this chapter focus on sea ice mapping in the Arctic Ocean from the CryoSat satellite. The process of making a sea ice map is described (Section 11.1), the SSH with DT is retrieved and validated (Section 11.2), and the results of the respective freeboard (Section 11.3) and ice thickness (Section 11.4) distributions in the Arctic Ocean are presented and discussed. In Section 11.5 the annual and interannual trends are discussed.

The sea ice maps are presented for autumn and spring from 2010 to 2013 to analyze the annual and interannual variations of the Arctic sea ice cover. March is chosen as the spring month due to maximum sea ice cover and November as the autumn month. September is the month with minimum sea ice extent (Section 3.2) but there can be issues with the measurements due to melt (Section 3.2.1). Therefore October would have been more appropriate to choose as an autumn month, but November is chosen due to lack of October data availability of the newest processing version baseline B (cf. Section 9.1).

The results presented in this chapter were carried out in the final stage of the Ph.D. and is considered as preliminary. The potential of large uncertainties of the thickness retrieval is stressed, and suggestions for improvements are discussed in Section 11.6.

In the presented maps from the Arctic Ocean a box of no data are visible in the Canadian Arctic (except for March 2011). This is the Wingham box (Section 6.1.1), where CryoSat is flying in the SARIn mode, and the data from there are not processed during this study.

11.1 Pre-mapping

To prepare a distribution of sea ice elevations data needs to be filtered and gridded. Data are filtered in three steps based on:

1. Pulse peakiness criteria to remove off-ranging elevations (Section 11.1.1).
2. Retracking correction to remove failures from the retracking (Section 11.1.2).
3. Residual SSH to remove the off-ranging lead elevations (Section 11.2.1).

Alternative methods for filtering data are discussed in Section 11.6.

11.1.1 Filtering Data

The detection of leads is based on the method described in Section 10.3 and data filtering in Section 10.6. To summarize the procedure; the pulse peakiness > 0.25 and the stack standard deviation < 4 are used for detecting leads, and pulse peakiness of $0.25 < PP < 0.45$ is used to filter off-ranging CryoSat elevations.

Furthermore, the second filtering is applied here. This filtering step is rejecting data points which are retracked wrongly or in another way are having a very low or high retracking gate. This rejection is based on a criteria of the retracking correction of the leads. The retracking gate of leads are expected to be centered in the range window due to its specular return. The mode of the probability distribution of the lead values are found, and an example from November 2010 is shown in Fig. 11.1.1(a). The distributions from the rest of the months are similar in form. Values lower than 5 m (~ 22 range gates) from the mode of the probability distribution are filtered out in the ice floe dataset (Fig. 11.1.1(b)), along with retracking gates higher than the highest lead retracking gate (around gate 51). The 5 m threshold is conservatively chosen such that ridges are not filtered out. A ridge can be up to 30 m in thickness and sometimes even more, see Section 3.1, and this corresponds to a freeboard of about 3 m. By this, it is assumed that the ice floes can not be lower than the lowest lead value.

The distribution of the lead retracking gates is bimodal distributed, while the distribution of the floe values only has one mode. The second mode in the leads distribution could be the mode of off-ranging elevations not filtered out with the pulse peakiness criteria. The elevations in this second mode are lower than the elevations in the first mode and therefore typical off-ranging elevations. This is only a speculation and is not confirmed, and therefore these values are not rejected. The lead distribution has a very sharp beginning and end, and thus the lead values are filtered at these ends.

The majority of rejected elevations are located in the margin of the data coverage. This is where the satellite is flying from ocean to ice, and vice versa, and close to land. The retracking filtering is therefore a rough ice edge detection. A map of the geographical distribution of the retracking gates can be seen in Appendix E.1. The statistics of the total number of data points (before filtering), the number of leads (after filtering), rejected values from the pulse peakiness criteria, and the retracking corrections criteria are shown in Table 11.1.1.

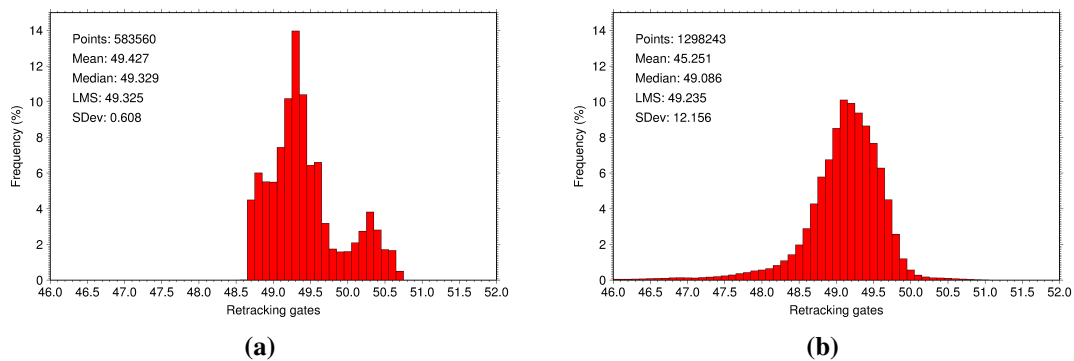


Figure 11.1.1: Frequency distribution of the retracking gate in (a) lead-points and (b) floe-points before the last filtering step. This is an example from November 2010.

Year/month	No. Points	No. Leads	Rejected PP	Rejected RG
2010 Nov	1,711,167	583,320	2,650,695	170,636
2011 Mar	1,764,413	457,577	3,361,318	342,322
2011 Nov	1,997,077	660,843	2,727,161	212,697
2012 Mar	1,850,154	419,049	3,266,580	333,451
2012 Nov	2,109,566	627,062	2,532,717	193,685
2013 Mar	1,561,028	496,108	3,372,815	324,507

Table 11.1.1: Filtering statistics of the monthly CryoSat data. The table contains from left to right; the year/month of data, total number of points and number of lead values after applying the first two filtering steps, rejected values due to the first filtering step; based on the pulse peakiness criteria, and rejected values due to second filtering; based on the retracing gate (RG).

11.1.2 Gridding

Data are gridded using the same procedure as described in Section 10.2. Firstly, data are divided into blocks of $25 \text{ km} \times 25 \text{ km}$, and a median average filter is applied. A modal and a mean average filter are also tested, but the median filter showed the best results which is typically recommended for a skewed distribution [Taylor, 1997].

Secondly, the nearest neighbor algorithm is used to grid data with a search radius of 100 km, and with dividing the search circle into eight sectors with at least one value inside a minimum of six sectors.

The number of points in each block are plotted in Fig. 11.1.2 for March 2013, and the

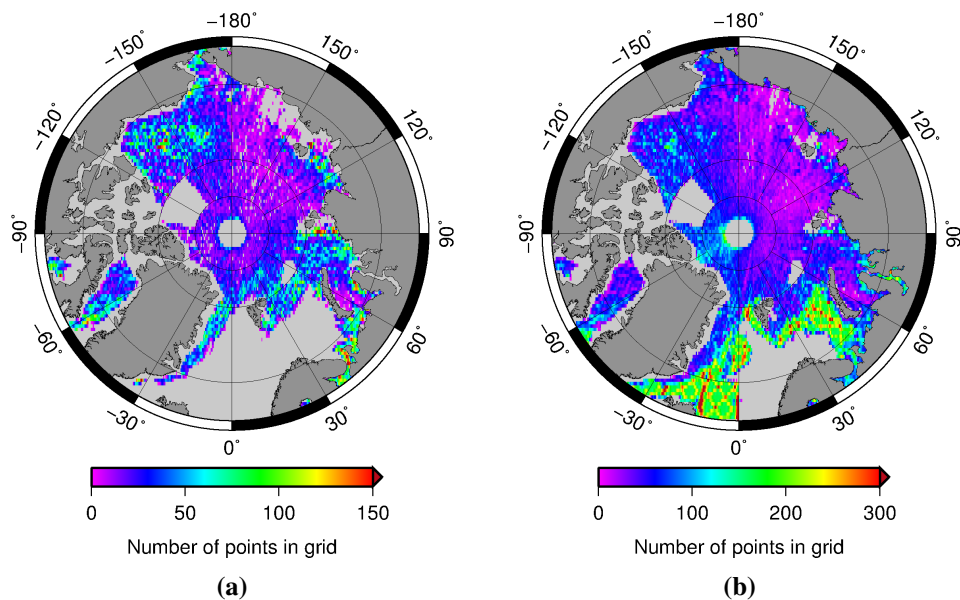


Figure 11.1.2: Number of measurements in grid cells distributed over the Arctic Ocean for (a) leads and (b) ice floes. The magenta color indicates a block with less than 25 lead measurements and 50 ice floes measurements. Notice the different color scales. This is an example of data from March 2013, and the remaining months are shown in Appendix E.2.

remaining months are shown in Appendix E.2. The distribution of points in each block could be a measure of the reliability of the elevation results, i.e. few measurements in an area can lead to false interpretations. Comparing the number of leads distributed over the Arctic Ocean in autumn and spring there are clearly less leads in March when the ice cover is thicker after a whole winter growth. Furthermore, there are less than 50 points in the majority of grid cells in the Russian Arctic for March 2012 and 2013. Also, notice the large amount of leads in the Beaufort Sea, this will be discussed later in Section 11.5.

The number of data points (Fig. 11.1.2) is again divided into a lead distribution (a) and a distribution of all data (b). Not surprisingly there are few leads in the area north of Greenland stretching to the central Arctic. This is an area with thick multi-year ice and relative calm conditions. The ice is pressed towards the north coast of Greenland by the transpolar drift stream, giving rise to many pressure ridges. The drift patterns for March 2013 from the ASCAT and SSMI datasets are shown in Fig. E.3.1, Appendix E.3. The Russian Arctic is expected to have a lot of leads, because it is a very dynamic area, but as seen in the Fig. 11.1.2 the leads are very sparse (below 50 data points). This may be due to a generally sparse data distribution in this area. Furthermore, there are many leads in the Canadian Arctic, around the Beaufort Gyre, and in the ice margin areas. Again a clear ice edge is visible in the lead distribution when comparing the two figures.

11.2 Sea Surface Height and Dynamic Topography

From Eq. (8.1.3) in Section 8.1.1 the sea ice freeboard can be determined by subtracting the SSH. The precision of the SSH is crucial in this step (Section 9.3). The leads from the CryoSat data are detected and filtered as described above. The CryoSat data do not give the SSH, but actually the SSH including the DT. This DT w.r.t. the EGM08 geoid is plotted in Fig. 11.2.1.

In all six maps there is a clear signal from the Beaufort Gyre. It is strongest in November 2011 and weakest in November 2012. As described in Section 3.1.1, a strong negative AO-index causes the occurrence of anticyclonic winds and tends to enhance the Beaufort Gyre and a positive AO-index tends to weaken the Beaufort Gyre, and more ice is transported out of the Arctic Ocean. The negative AO-index is confirmed for November 2010 (Fig. 11.2.2) and in November 2011 the AO-index seems to change from negative to positive phase, which is a weather system persisting to spring 2012 (credit: NSIDC), corresponding well with the weaker Beaufort Gyre in these month. The index is strongly positive during the spring and summer 2012 which enhance the ice export out of the Fram Strait corresponding to the well with the large Summer melt in 2012. In November 2012 the AO-index is negative again throughout the winter and spring months. This is seen by a strengthening of the Beaufort Gyre from November 2012 to March 2013 favoring ice growth.

11.2.1 Validation

To validate the DT, the MSS DTU10 is subtracted (Section 9.3), and shown in Fig. 11.2.3. The figure represents the monthly variation of the SSH and DT to the 17 yearly average. This residual SSH covers the static and time-varying components of the sea surface (cf. Eq. (8.1.2)) as well as errors and noise introduced in the estimation process.

The residual SSH is approximately between -1.8 to -0.8 m. It is negative due to the vertical

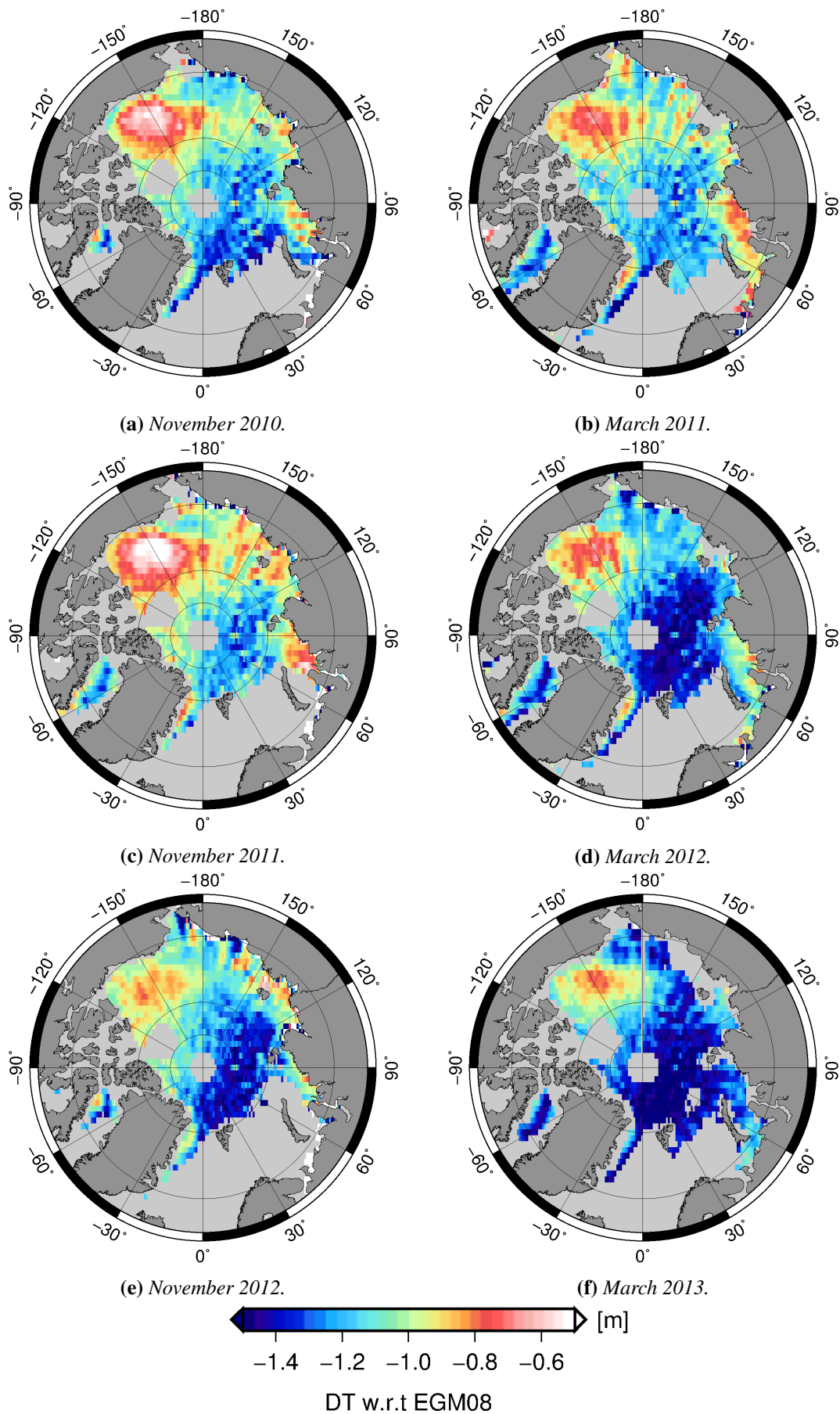


Figure 11.2.1: The dynamic topography based on lead detection from CryoSat in November/March 2010-2013 w.r.t. the EGM08 geoid.

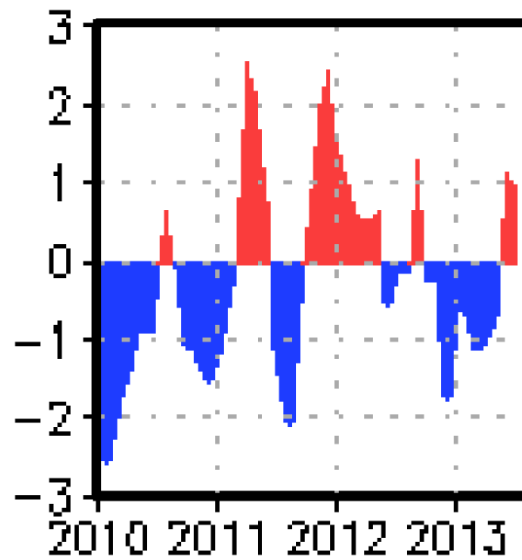


Figure 11.2.2: A standardized 3-month running mean value of the AO-index from January 2010 to July 2013. Adapted with courtesy: NOAA/ National Weather Service.

bias in the CryoSat data mentioned earlier. There is a higher SSH in the Beaufort Gyre, and sporadically in the Russian Arctic, and in the Barents Sea between Svalbard and Arkhangelsk Oblast and a low north of Greenland.

The knowledge of the residual SSH is used to improve the data quality in the third filtering step. If a CryoSat DT grid cell deviates more than ± 0.5 m from DTU10, it is rejected. The standard deviation of the residual, together with the mean, the mode, and the percentage of rejected grid cells are given in Table 11.2.1.

The probability distributions of the SSH residual are shown in Fig. 11.2.4. The mode of the first three residuals (November 2010, March 2011 and November 2012) are almost identical and especially the two first distributions are nearly normal distributed around -1.3 m. From March 2012 there is a shift in the distributions. NSIDC writes that in the second part of March 2013 the AO-index was in a strongly negative phase, with an unusual high sea level pressure over the entire Arctic Ocean. The shift in weather patterns may be the cause of the bimodal distribution.

Year/month	Mean (m)	Mode (m)	SD (m)	Δ SSH rejection (%)
2010 Nov	-1.293	-1.307	0.124	2.6
2011 Mar	-1.291	-1.301	0.153	1.3
2011 Nov	-1.228	-1.266	0.133	2.7
2012 Mar	-1.419	-1.475	0.130	1.4
2012 Nov	-1.382	-1.408	0.123	4.2
2013 Mar	-1.508	-1.525	0.122	1.0

Table 11.2.1: For each month the mean, the mode, and the standard deviation (SD) of the residual SSH (Δ SSH) are given. Also, the percentages of rejected grid cells are given in the table.

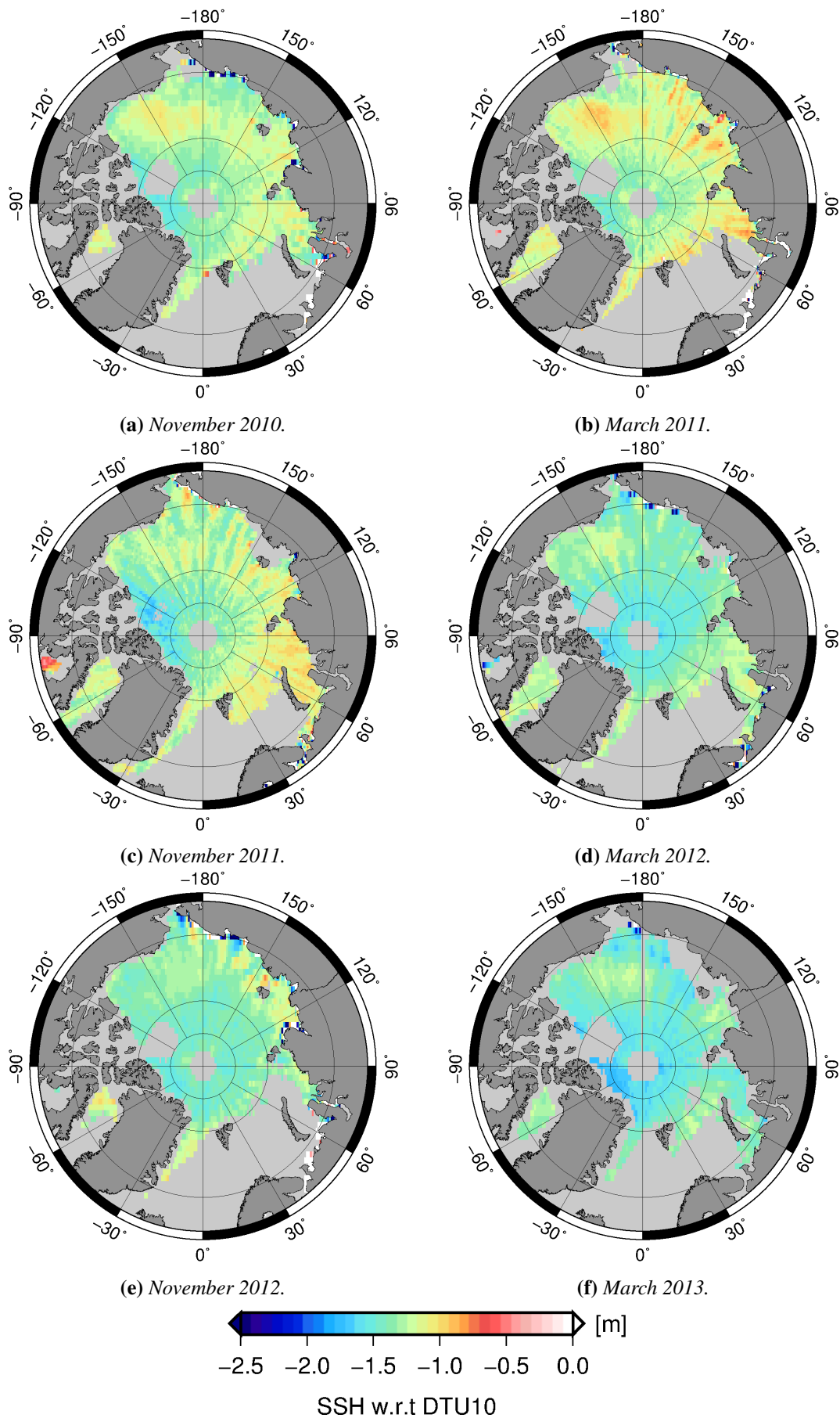


Figure 11.2.3: The residual sea surface height (and dynamic topography) from CryoSat leads November/March 2010-2013 w.r.t. MSS DTU10.

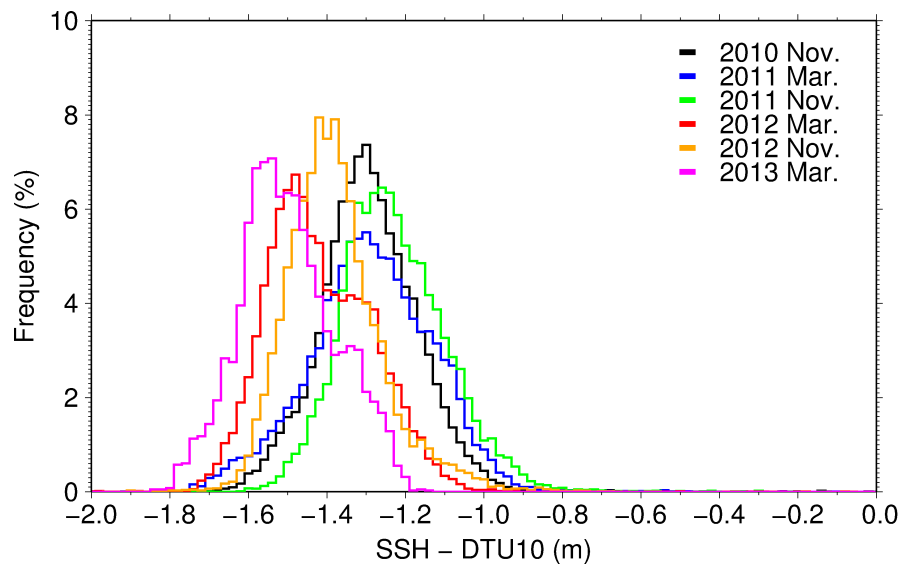


Figure 11.2.4: The residual SSH distributions of the CryoSat derived DT and the MSS DTU10.

11.3 Sea Ice Freeboard Distribution

The freeboard is calculated using Eq. (8.1.3) in Section 8.1.1, where h is the total dataset (with leads and ice floes). A grid spacing of 25 km and search radius of 100 km is chosen. The impact of changing the gridding parameters in the nearest neighbor algorithm is illustrated in Fig. 11.3.1, where grid spacings of 25 km and 50 km and search radii of 50 km and 100 km are tested. The grid size could not be lowered below 25 km before losing too much information as there would not be enough points in each cell to make a reliable result. Furthermore, by increasing the grid size to above 100 km would result in a too coarse product, where you may lose information as the sea ice cover changes over 100 km.

A Gaussian filter is applied to the data to distinguish between first- and multi-year ice. Normally only one clear peak around zero is visible in the freeboard probability distribution. This is due to the many lead values in data. Two distinct peaks occur when the filter is applied, one representing first-year ice and one multi-year ice. The filter amplifies the various signals in the sea ice cover and fills out areas with missing data depending on the filter width. From Fig. 11.3.1 the freeboard is varying depending on the chosen grid size and smoothing filter. By increasing the filter width, the different modes become more distinct, however this also increases the standard deviation.

The freeboard statistics are shown in Table 11.3.1. In the middle columns, two numbers appear: The first number represents freeboard heights without negative values and freeboard heights over 3 m, including leads, first-year ice, multi-year ice, and (small) ridges. The second number represents freeboard statistics, where the lead-values are extracted and the elevation data only contain ice floes. Again, only freeboard values higher than 0 m and lower than 3 m are used in the statistics calculations. The grid used in the study is marked by red in the table.

The modal first-year ice freeboard varies from 10.5 cm to 12.5 cm and the multi-year ice from 29.5 to 31.5 cm. From this test it is concluded that the mean freeboard height is depending on the choice of grid and filter size, with an estimated uncertainty of the freeboard retrieval of

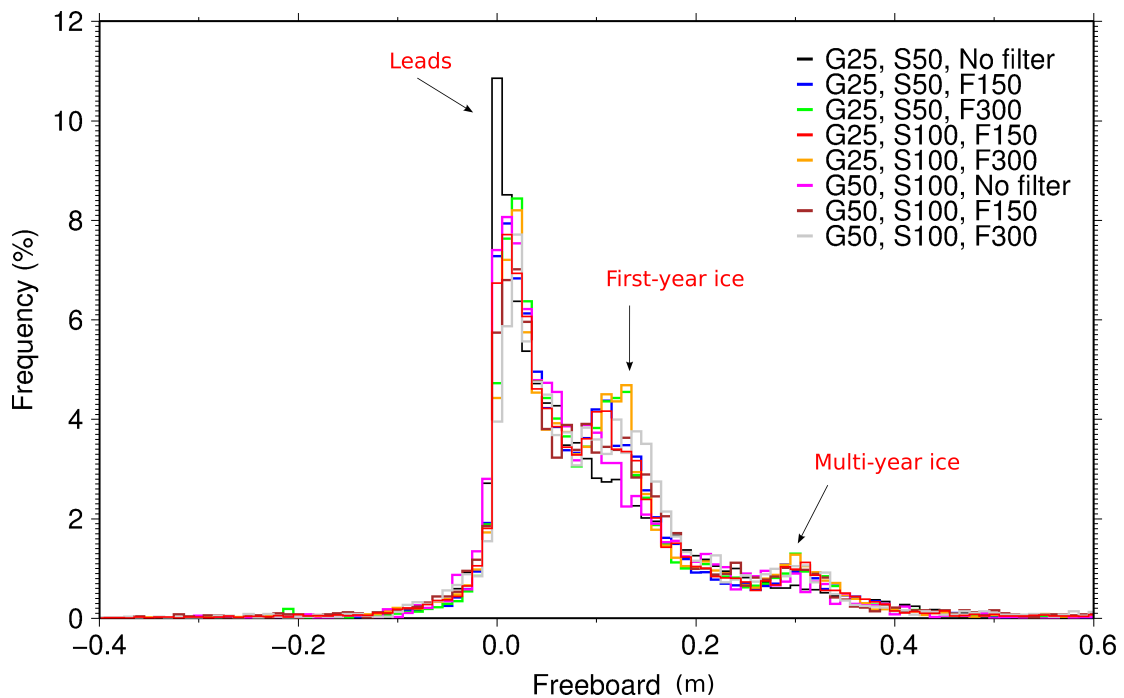


Figure 11.3.1: Comparing the freeboard distributions for various grid sizes (G), search radius (S) in the nearest neighborhood gridding and the width of the Gaussian filter (F). The bin width of distribution is 1 cm. This example data are from March 2013.

+2 cm for the first-year ice and ± 1 cm for multi-year ice.

It is here important to state that the Gaussian filter is only applied as a independent test in the following freeboard retrieval to distinguish between first- and multi-year ice. It is not applied to the total statistics nor to the thickness analysis. To work around the large signal from the leads

Grid/Radius/Filter	No. Blocks	Mean	Median	SD	FY	MY
G25, S50, No	1,4725 / 7,193	11.8 / 21.0	7.7 / 16.3	16.3 / 19.9	-	-
G25, S50, F150	1,8491 / 9,876	13.4 / 22.3	8.9 / 14.7	22.4 / 27.6	10.5	29.5
G25, S50, F300	2,1579 / 1,1732	15.3 / 25.3	9.3 / 14.9	27.4 / 34.1	12.5	31.5
G25, S100, F150	1,8852 / 1,0203	14.2 / 23.5	9.1 / 15.2	24.2 / 30.0	10.5	30.5
G25, S100, F300	2,1338 / 1,1971	15.7 / 25.3	9.7 / 15.0	28.0 / 34.3	12.5	29.5
G50, S100, No	3396 / 1676	11.5 / 19.8	7.8 / 15.5	15.2 / 18.0	-	-
G50, S100, F150	4,608 / 2,592	15.1 / 24.2	9.5 / 15.8	24.6 / 29.7	12.5	30.0
G50, S100, F300	5,304 / 3,102	17.7 / 27.7	10.2 / 15.9	31.0 / 37.3	11.5	30.5

Table 11.3.1: Sensitivity of grid and filter choice. The first row represents grid (G), Search radius (S) in the nearest neighbor gridding, and the width of the Gaussian filter applied, if any. The next rows are; the number of blocks, mean, median, standard deviation (SD), first-year ice (FY) mode and multi-year ice (MY) mode. In the middle columns two numbers are present, representing 1.) the statistics for freeboard with the first mode (the leads), removing negative freeboards, and freeboards over 3 m and 2) without the first peak > 0.08 m and freeboards over 3 m. All values are given in cm.

seen in Fig. 11.3.1, h in Eq. (8.1.3) in Section 8.1.1 is in the remaining analysis only containing ice floe data and not the total dataset.

11.3.1 Sea Ice Freeboard Heights

The resulting CryoSat freeboard elevation maps are shown in Fig. 11.3.2 for autumn and spring months from November 2010 to March 2013.

Overall, the freeboard elevation maps show a typical geographical pattern of the sea ice cover in the Arctic Ocean with thicker ice (up to 1 m) north of Greenland and towards the Canadian Archipelago, which are pushed towards the coast due to the transpolar drift. Thinner ice is found in the Russian Arctic with a freeboard height of 5 to 20 cm. The maps also show interannual variations with especially less and thinner first-year ice in the November months (left-hand side of the figure) compared to spring (right hand-side of the figure).

In November we are in the beginning of the growth season, and there may still exist areas with open water in the Arctic basin.

Data are cut due to the OSI SAF ice edge detection algorithm, described in Section 5.3, to dispose the boundary problems in the margins and to eliminate the open water in order not to bias the freeboard retrieval. The ice edge maps are shown in Appendix E.4. One ice mask is chosen for each month. For the autumn months an ice mask in the beginning of the month is chosen, and for the spring months an ice mask in the middle of the month is chosen. Especially for November there is a large difference between the start and end of the month due to sea ice growth. This issue, and other issues with the maps, are discussed in Section 11.6.

Freeboard Statistics

The freeboard statistics are shown in Table 11.3.2. The mean freeboard varies from 19 to 25 cm, with the highest value in March 2011 and the lowest in November 2011. The standard deviation varies between 11 and 14 cm. The statistics are calculated based on freeboard values from 0 to 1 m only including first- and multi-year ice, i.e. this will not account for negative freeboard values or ridges. The main reason for this is to avoid open water bias in the freeboard calculations and to use incorrectly retracked heights. Removing data will in turn change the mean freeboard values. The modal first-year ice derived from the Gaussian filter is between 17 and 22 cm, and the multi-year ice is between 24 and 35 cm.

The freeboard distributions for all months are plotted in Fig. 11.3.3 with a resolution of 0.02 m. The trailing edge represents the thick multi-year ice. The distributions are discussed in more details in Section 11.5.1.

The standard deviation is given for each month and varying between 10.5 and 13.0 cm. It is a measure of the amount of dispersion of the freeboard. This value will always be large when looking at different sea ice surfaces, because we are dealing with thin first-year ice and thick multi-year ice. The theoretical uncertainty from Eq. 8.1.4 is calculated to be 21.3 to 21.5 cm, where the error in the measurements (δh) is calculated for each block and by assuming the uncertainties, given by Table 7.4.1, cover the whole Arctic Ocean.

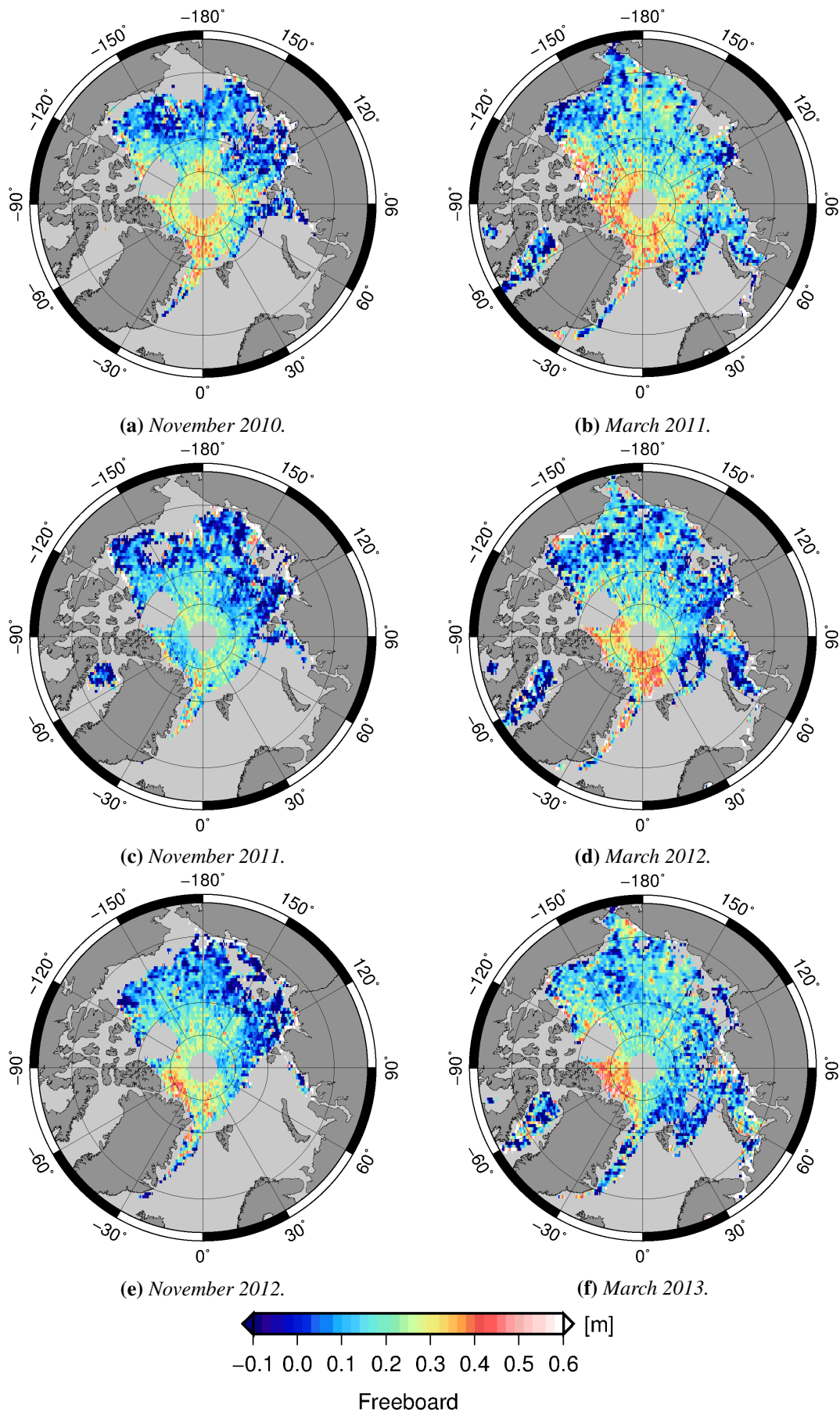


Figure 11.3.2: Freeboard distributions from CryoSat from 2010 to 2013. Left is for November, right is for March.

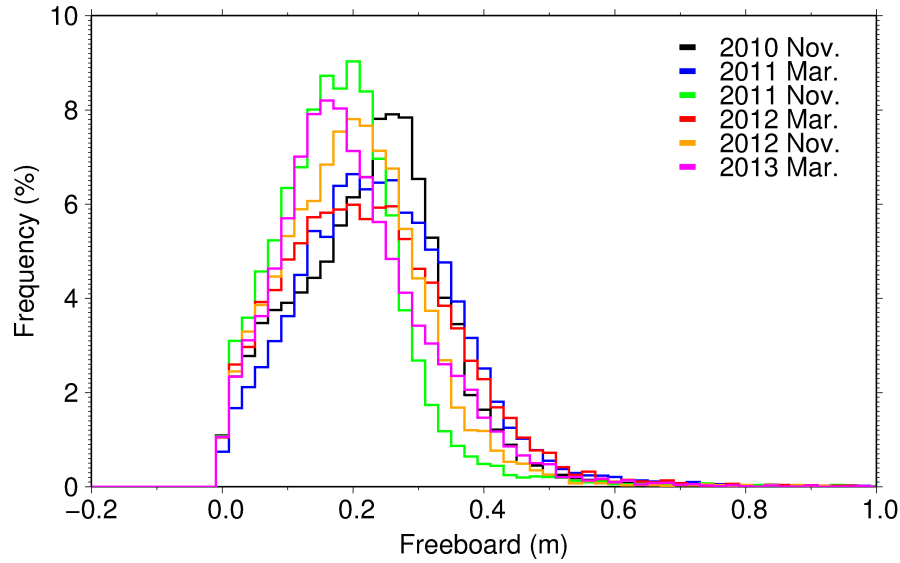


Figure 11.3.3: Freeboard elevation distributions over the whole Arctic Ocean for all months in the study. The bin width of the distribution is 2 cm.

11.4 Sea Ice Thickness Distribution

The principle of converting the freeboard height to sea ice thickness is described in Section 8.1.2 and Eq. (8.1.5). A first attempt of converting the sea ice freeboard to ice thickness are shown and discussed in this section. The thickness retrieval is subject to many errors (cf. Section 8.1.3).

The most problematic term in the conversion is the snow depth. In this study, two approaches of handling the snow depths are carried out. The first method is the most widely used; typical values for the densities (Table 8.1.1, Section 8.1.3) and snow depths from Warren’s climatology (Appendix A) are used. Data are differentiated in first- and multi-year ice, where only half of the snow depth from the Warren snow model is used over first-year ice [c.f. Kurtz and Farrell, 2011]. Furthermore, the different densities are applied for the two ice types. This method is from now on termed WAT.

The second method is based on Alexandrov et al. [2010] (see Section 8.1.2, Eq. (8.1.10))

Year/month	No. Blocks	Mean (cm)	Median (cm)	SD (cm)	FY (cm)	MY (cm)
2010 Nov.	13,033	22.7	23.8	11.5	18.5	-
2011 Mar.	16,450	24.5	23.5	12.5	17.5	27.5
2011 Nov.	12,560	19.2	17.9	10.5	20.5	34.6
2012 Mar.	14,274	23.2	21.9	13.0	21.5	34.5
2012 Nov.	12,250	19.6	17.7	11.0	18.5	23.5
2013 Mar.	15,280	21.1	19.1	11.7	16.8	34.5

Table 11.3.2: Freeboard statistics from CryoSat derived elevations for all six processed months. The columns are; the number of 25×25 km blocks, the mean, the median, the standard deviation, the modal first- and multi-year ice derived from the Gaussian filter; however, no distinct signal was found for multi-year ice in November 2010.

and (8.1.11)), where two empirical relationships of the freeboard to thickness equation (Eq. (8.1.5)) are adapted, one for first-year ice and one for multi-year ice. From now on this method is termed ALT.

In order to discriminate first- and multi-year ice, the OSI SAF's ice type classification (Section 5.3) is used. One day for every month is carefully selected based on comparisons of other datasets (AMSR, OSCAT, NSIDC), if available. The OSI SAF data are shown in Appendix E.5 together with the comparison data.

11.4.1 Sea Ice Thickness

The retrieved sea ice thickness for WAT is shown in Fig. 11.4.1 and for ALT in Fig. 11.4.2. The thickest ice north of Greenland is up to 6 m, whereas the thin first-year ice in the Russian Arctic is 0 to 2.5 m. The mean, median, mode, and standard deviation for the total ice thickness and for first- and multi-year ice thicknesses are summarized in Table 11.4.1.

The freeboard values for the individual ice types are assumed only to contain one ice type, and therefore values above 2 m are rejected in the first-year ice statistics, whereas values above 2 m and below 10 m are used for multi-year ice statistics. The values are chosen based on the definition of first- and multi-year ice from WMO (Section 3.1). This filtering is only carried out for the ice type separation statistics and not in the total sea ice thickness determination.

The thickness distributions from WAT and ALT are shown in Fig. 11.4.3(a) and 11.4.3(b), respectively. The distributions are slightly negatively skewed. In (a), March 2011 and 2012 have low precisions (the frequency of the mode is lower) compared to the other distributions, and the same is valid for all the March distributions in (b). Applicable to all the lower precision distributions are the lack of a clear mode. November 2010 in the ALT thickness distributions

Year/month	No. Blocks	Mean (m)	Median (m)	Mode (m)	SD (m)	FY (m)	MY (m)
WAT							
2010 Nov.	14,130	2.13	2.23	2.25	1.02	1.06	2.59
2011 Mar.	17,830	2.48	2.50	2.53	1.02	1.40	2.98
2011 Nov.	13,631	1.83	1.83	1.92	0.95	1.12	2.35
2012 Mar.	15,940	2.38	2.36	2.32	1.16	1.26	3.01
2012 Nov.	13,209	2.00	2.02	2.14	0.99	1.22	2.57
2013 Mar.	16,947	2.18	2.09	2.07	1.01	1.40	2.80
ALT							
2010 Nov.	14,092	2.27	2.48	2.73	1.02	1.04	2.71
2011 Mar.	17,663	2.35	2.40	2.6	1.03	1.39	3.02
2011 Nov.	13,657	1.97	2.06	2.23	0.98	1.10	2.42
2012 Mar.	15,633	2.22	2.21	2.34	1.15	1.19	2.97
2012 Nov.	13,253	2.07	2.15	2.38	1.01	1.20	2.67
2013 Mar.	16,633	2.02	1.96	1.83	1.04	1.30	2.78

Table 11.4.1: Sea ice thickness statistics from CryoSat derived elevations for all six months. The number of blocks of 25×25 km, mean, median, and mode are given together with the standard deviation, and the modal first- and multi-year ice derived from the OSI SAF ice type detection.

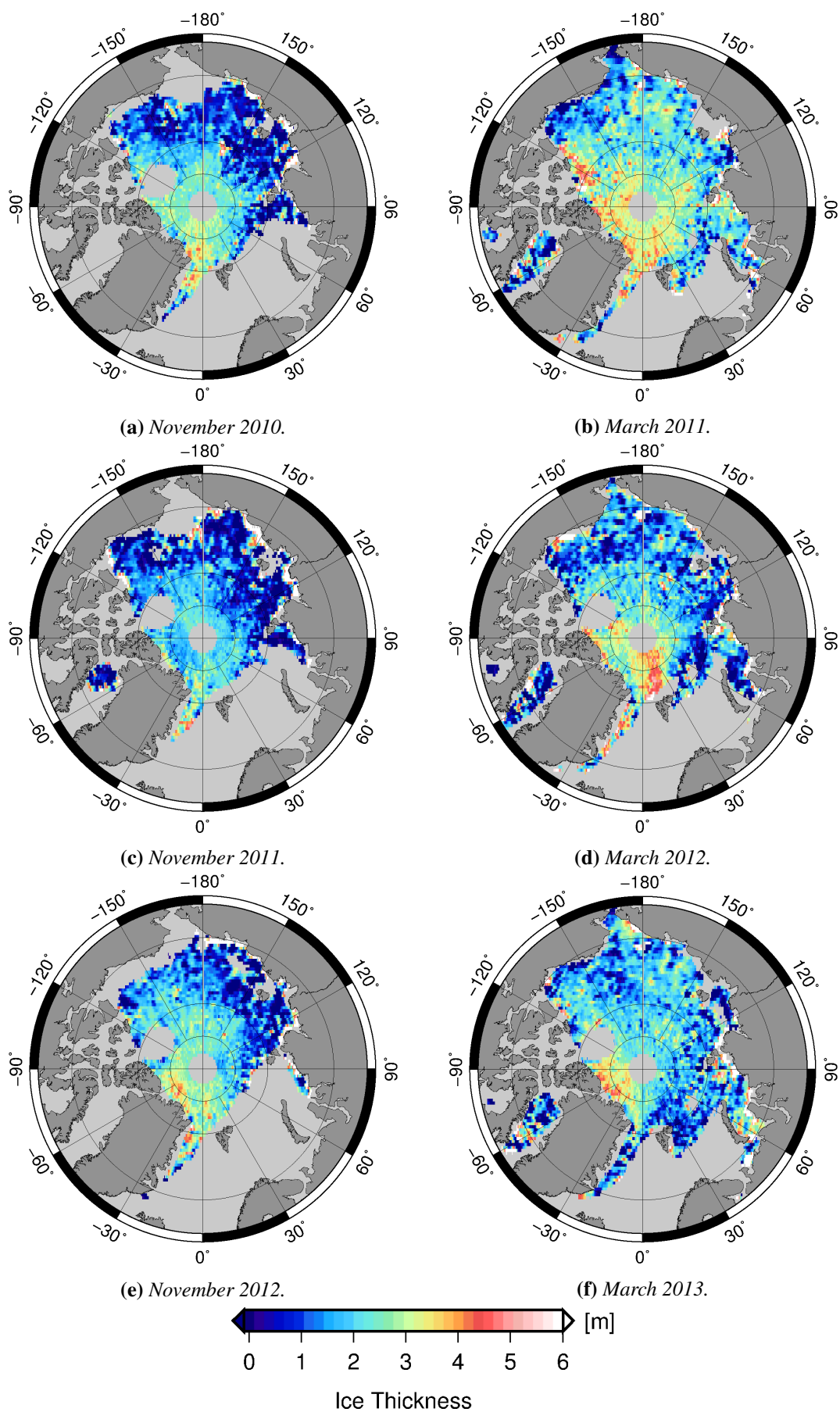


Figure 11.4.1: Sea ice thickness distributions from CryoSat based on the WAT method.

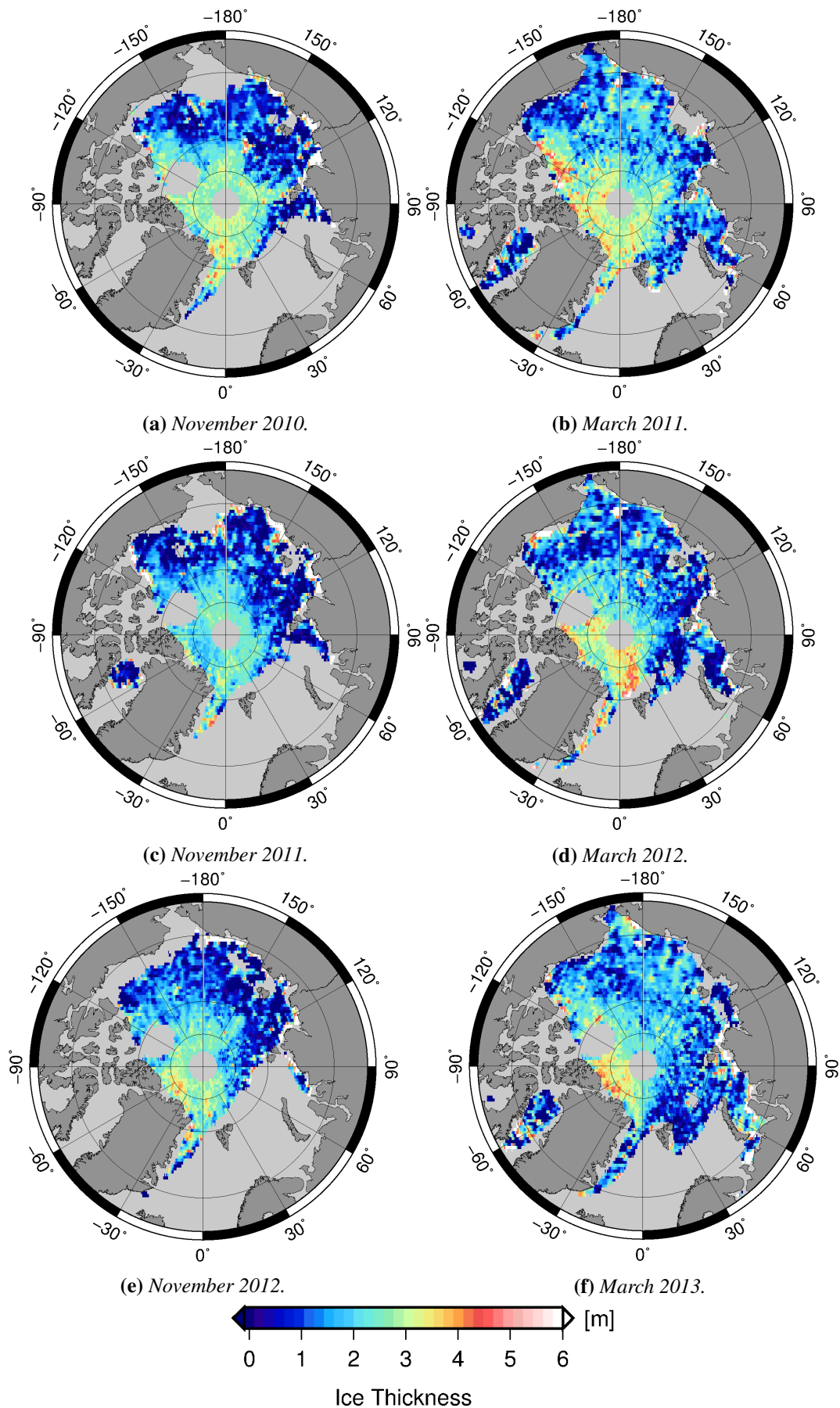


Figure 11.4.2: Sea ice thickness distributions from CryoSat based on the ALT method.

has a second mode around 1.5 m. The significance of these distributions are discussed in Section 11.6.

Generally, the November mean thickness is larger for ALT than for WAT, and the March mean thicknesses are larger for WAT than for ALT. There is thicker first-year and multi-year ice in March than in November, and the modal first-year ice is 2 cm larger for WAT than for ALT. There is between 1-10 cm thicker multi-year ice in WAT than in ALT in November and March, respectively. The multi-year ice cover are larger in March than in November, and 7-10 cm thicker in ALT than in WAT in November, and there is a -3 to 2 cm difference in March between WAT and ALT.

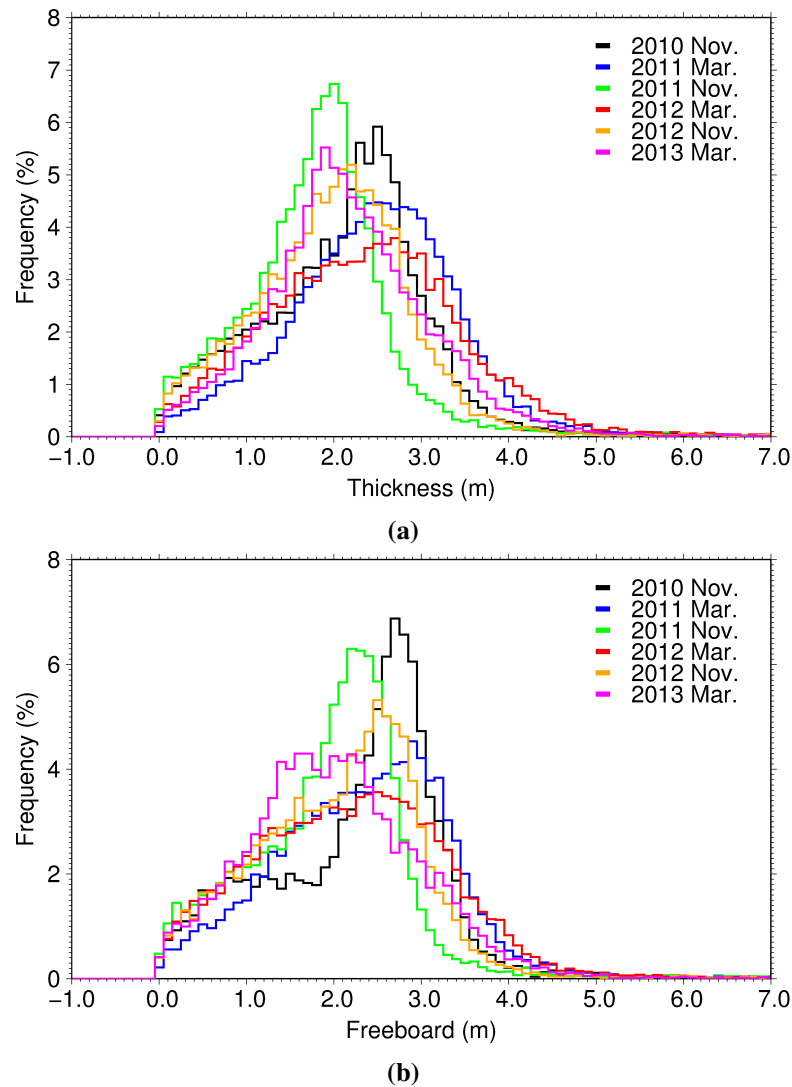


Figure 11.4.3: Sea ice thickness probability distributions from CryoSat. (a) is from WAT and (b) is from ALT.

11.5 Sea Ice Trends

In this section the annual and interannual variations in the data are discussed and perspectives to other studies are drawn. The ice conditions for each month within the study are described and compared with observations from other studies.

The available CryoSat record is short in the sense of making any independent remarks about the annual sea ice thickness trends, nevertheless this is attempted. The CryoSat record should be seen as an extension to the existing sea ice records from ERS-1 and -2 and ICESat, and to bridge the gap to the up-coming missions ICESat-2 and Sentinel-3. ICESat-2 and CryoSat comparisons will be very valuable with combining laser and radar altimetry, and combining Sentinel-3 and CryoSat will archive at more accurate sea ice cover over thin ice areas where Sentinel-3 will have its advantage.

11.5.1 Annual Freeboard Trends

The best linear fit to the freeboard heights is found by a least square fit, and the uncertainty of the total trend is calculated assuming the same uncertainty for each freeboard measurement (Appendix B.3). For the total mean freeboard thickness, a thinning of 1.5 ± 0.9 cm/year is observed (Fig. 11.5.1). The November and March trends are -1.5 and -1.7 cm/year, respectively. The trends are only based on three observations, which are statistically insignificant, but because we are dealing with a geophysical phenomenon and know the trends from other studies, this can be a signal or warning if this study is showing the right results or not. Therefore, no uncertainty is calculated for these values. Table 11.5.1 summarizes the results for November, March and the total freeboard thickness trends.

The March sea ice freeboard decrease from 2011 to 2013 is 7.6%, whereas the November decrease is 14.8%. To the author's knowledge, there is not yet published any freeboard trends from CryoSat data from the Arctic Ocean. Here, it is right to mention that both Laxon et al. [2013] and Kaleschke and Rickert [2013] of course use the CryoSat freeboard to calculate their

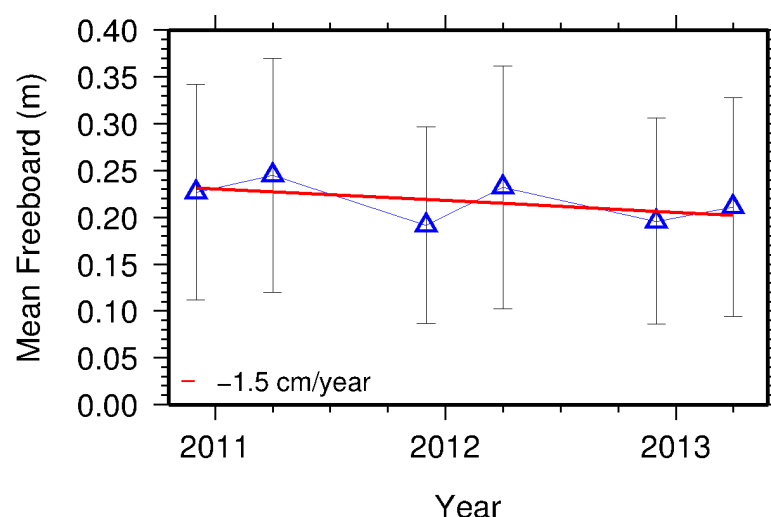


Figure 11.5.1: Mean sea ice freeboard trends from the six study months from November 2010 to March 2013. The error bars in the figure are the standard deviation. The total trend is -1.5 ± 0.9 cm/year.

	November	March	Total
Trend (cm/year)	−1.5	−1.7	−1.5
Change (%)	14.8	7.6	-

Table 11.5.1: Sea ice freeboard trends and percentage change for November, March and total trend from November 2010 to March 2013.

sea ice thicknesses. Just before the thesis deadline the Alfred Wegener Institute (AWI) for polar research announced their version a L2 CryoSat Arctic freeboard and thickness dataset available at <http://meereisportal.de>.

There exist several other studies from, e.g. ICESat. Keep in mind that the time period for ICESat is 2003–2008, while the CryoSat record is from 2010 to present. The March trend of -1.7 cm/year corresponds well with a study based on ICESat results from Farrell et al. [2009], who find a decrease of 1.6 and 1.8 cm/year for October/November and February/March, respectively. However, this study includes the ice and the snow freeboard. The ICESat freeboard varies from 28.3 to 40 cm in spring and from 21.6 to 29.7 cm in autumn. They also find an accelerated trend in the residual freeboard from 2007 considering the extreme 2007 summer melt year.

For the same period and with the same data Kwok et al. [2009] find a spring (February–March) trend of -2.2 cm/year in the period from 2003 to 2008. They also estimate a trend in the autumn freeboard of -2.3 cm/year. The trends are larger than the trends found in this study.

Skourup [2009] also use ICESat data and find a 27% or 9.5 cm decrease in autumn and a 16% or 6 cm decrease in spring over a five year period. This study also included the snow freeboard.

11.5.2 Annual Thickness Trends

A yearly trend map is shown for the mean sea ice thickness studies in Fig. 11.5.2(a). The blue marks are from WAT and the red marks from ALT. In this figure, the total ice thickness (triangles) is shown together with the first-year ice (squares) and the multi-year ice (diamonds) thicknesses. The overall trends for WAT and ALT are similar.

The total annual thickness trend is -5.8 ± 3.0 and -11.5 ± 5.8 cm/year for WAT and ALT, respectively. The autumn and spring trends are again carried out, based on only three mean thickness estimates. The total mean thickness trends are -15.7 and -16.9 cm/year for WAT and ALT, respectively. First-year ice trends of 1.3 cm/year for WAT and -3.3 cm/year for ALT are found, and for multi-year ice the trends are -10.1 and -12.6 cm/year for WAT and ALT, respectively. A summary of the ice thickness trends are written in Table 11.5.2.

Laxon et al. [2013] find that in the period from 2003 to 2008 (ICESat data) and again from 2010 to 2012 (CryoSat data), an average volume loss of $500 \text{ km}^3/\text{year}$ equivalent to a 7.5 cm/year decrease in thickness and an average autumn volume decrease of about $800 \text{ km}^3/\text{year}$, which was 60% higher than the PIOMAS volume loss. The yearly trend found in Laxon et al. [2013] is in between the values found in this study with the two different methods, but we also have to keep in mind the different time series.

In Kaleschke and Rickert [2013] they combine CryoSat and SMOS data from March 2011, 2012, and 2013, and find trend of -7 cm/year in the mean sea ice thickness, similar to the total

	Total (cm/year)	FY (cm/year)	MY (cm/year)
	Autumn		
WAT	−8.1	7.9	−3.0
ALT	−11.6	7.6	−4.5
	Spring		
WAT	−15.7	1.3	−10.1
ALT	−16.9	−3.3	−12.6

Table 11.5.2: Ice thickness trends for autumn (November 2010 to November 2012) and spring (March 2011 to March 2013). The total annual thickness trends are -5.8 ± 3.0 cm/year and -11.5 ± 5.8 cm/year for WAT and ALT, respectively.

trend found in Laxon et al. [2013]. This is lower than the spring trends found in this study.

The sea ice thickness trend is also measured from the ERS-1 and -2 satellites covering an eight year period from 1993 to 2001. A mean winter thickness of 2.73 m was found from the geographically sparse coverage to 81.5°N [Laxon et al., 2003].

Giles et al. [2008] used Envisat data between winter 2002/2003 and 2007/2008 to estimate Arctic sea ice thinning. They found a reduction of the total thickness of 0.26 m to the six year average corresponding to a trend of -4.3 cm/year.

The sea ice cover has in recent years retreated with an accelerated speed [Comiso et al., 2008; Stroeve et al., 2012]. The results in this study may be a result of this, however it is difficult to make any final conclusions with the very short data record.

Simulated sea ice thicknesses from PIOMAS are shown in Fig. 11.5.3, where March and November are marked with a light blue color. The modeled data show a similar thickness trend in March 2012 and 2013 with 2013 being slightly lower, while 2011 is about 10 cm thicker. In this study the difference from March 2011/2012 is 10 cm, while in 2012/13 it is 20 cm. The

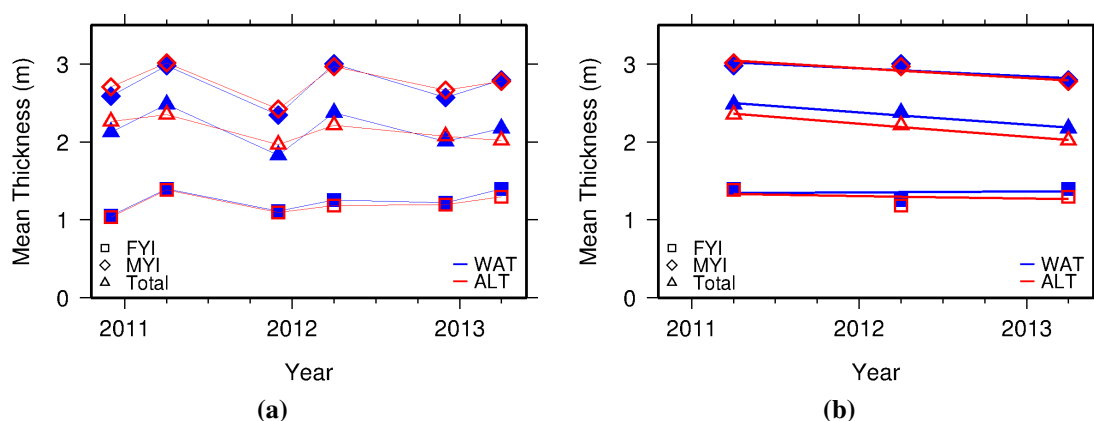


Figure 11.5.2: Sea ice thickness trends for WAT (blue) and ALT (red). (a) all data (b) for autumn only. Triangles are the total mean thickness, the squares are the mean first-year ice thickness, and the diamonds are the mean multi-year ice thickness. The straight lines in (b) are the fitted trends summarized in Table 11.5.2.

thicknesses are in the interval of 1.6 to 1.8 m. For November, the model finds a thickness from 2012 more than 10 cm lower than in 2010 and 2011 with an interval of about 1.05 to 1.2 m. In this study the November 2010/2011 change is 30 cm, whereas the 2011/2012 is 17 cm, which is quit high compared with the PIOMAS model. Another thing to notice in the PIOMAS figure (Fig. 11.5.3) is the large difference in growth from the beginning to the end of month. This will be discussed in the next section.

11.5.3 Interannual Variation

In Fig. 11.5.1 an interannual variation of the sea ice mean freeboard height is also seen with lower mean freeboard heights in autumn after a whole summer's melt and higher thicknesses in spring after a whole winter's growth. The difference in freeboard growth from each season are 1.5, 4.0 and 2.5 cm, and from March to November, over the melt season, the differences are -5.3 and -3.6 cm.

The seasonal trend is also seen in the mean thickness trend (Fig. 11.5.2(a)), except for November 2012 to March 2013 in the ALT thickness. Furthermore, the negative trend is much higher in spring than in autumn (Table 11.5.2), as seen in the sea ice extent (Fig. 3.2.1).

The ice extent is not linearly correlated with the ice thickness, however clearly connected (Section 3.3). A sea ice extent graph from November is shown in Appendix E.3, the March extent is shown in Fig. 3.2.1(b) in Section 3.2, and for interannual variation see Fig. 3.2.3 in Section 3.2.1. These graphs are used in the following together with meteorological and sea ice extent information gathered with courtesy from NSIDC.

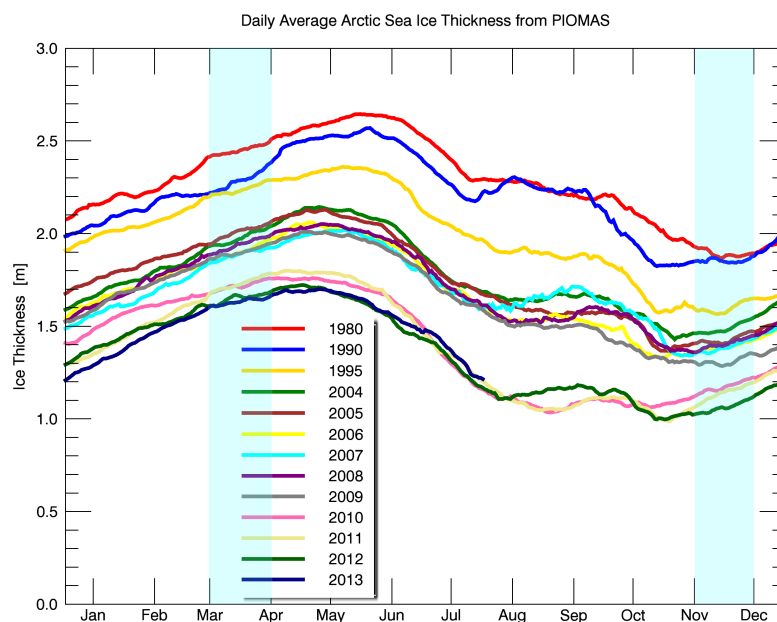


Figure 11.5.3: Average Arctic sea ice thickness over the ice-covered regions from PIOMAS. Adapted from Polar Science Center, University of Washington.

November 2010

November 2010 was marked with a very low November ice extent (Appendix E.3), due to local weather systems giving rise to local ice free areas. This month is recorded as the second lowest November sea ice extent since the start of the satellite era, only exceeded by November 2006.

In this study, the mean freeboard height was 22.7 cm, which was observed as the highest freeboard in the record, but the freeboard height (and thickness) of the first-year ice was low indicating slowly growing ice.

March 2011

In the following March 2011, the sea ice extent was also observed as the second lowest in the satellite era. Notice how low the sea ice extent is compared to the extent in 2012 and 2013 (Fig. 3.2.1(b) in Section 3.2). Temperatures were slightly above average, and the thick ice had increased slightly over the last year. The AO-index was positive, tending to favor ice growth. This month had the thickest mean thickness, first-, and multi-year ice.

November 2011

There was a very strong low pressure system in the Arctic, starting early November 2011, causing a slowdown in the sea ice growth. The AO-index was positive and the Beaufort Gyre weak. Remember, a weak Beaufort Gyre increases the ice transport out of the Arctic. The air temperatures in the autumn 2011 were warmer than usual, stretching into November. The higher air temperatures were found over the Kara and Barents seas, the east Greenland Sea and the Canadian Archipelago. These areas were also the regions with below-average ice extent.

In this study, the November 2011 has the lowest thickness in the record, which does not match the ice extent pattern for this month, which was the largest extent for the period (Appendix E.3). This could be due to an increase in new ice, which may not be picked up properly by CryoSat. In both the freeboard (Fig. 11.3.2) and the thickness elevation maps (Fig. 11.4.1 and 11.4.2) there is very little multi-year ice north of Greenland in November 2011. This may be a problem arising from the lead discrimination, where few leads are observed in this region. In Fig. E.2.1(c) in Appendix E.2, the number of observations of each block are shown and there appear to be less than 25 observations in the blocks in this region. The probability distributions from this month (green curve) support this speculation by a very sharp trailing edge, which indicates less multi-year ice compared to the other distributions. This problem has to be investigated in more details.

March 2012

Even though 2012 was an extreme summer melt year, the March 2012 sea ice extent was larger than in 2011 and 2013. Ice age data (Fig. 3.3.1, Section 3.3) indicates that despite the larger extent compared to recent years, the winter sea ice continues to be dominated by younger and thinner sea ice.

Following the thicknesses derived from this study, the multi-year ice has grown 66 cm (WAT) or 55 cm (ALT) since November, which is the largest multi-year ice growth in the study, and the same time the smallest first-year ice growth (14 and 9 cm for WAT and ALT, respectively).

The sea ice maps for March 2012 (Fig. 11.3.2(d), 11.4.1(d) and 11.4.2(d)) have unusually thick sea ice north of Svalbard and areas with lower ice northeast of Greenland. This pattern is also seen in Kaleschke and Rickert [2013]. The probability distributions from March 2011 (red curve) have a lower precision (the mode is less frequent) compared to the other distribution due to a larger spread of data.

November 2012

As described in Section 3.1.1 the sea ice was affected by a strong storm in August 2012, which caused the ice to drift away, however in autumn the weather conditions were favorable for ice growth and it actually grew faster than usual. The summer of 2012 was an extreme melt year with the lowest sea ice extent ever recorded. Therefore, a very low sea ice freeboard was expected in November 2012 after the melt season, but as seen in data the difference from March to November 2012 was not that large. Following NSIDC, the ice growth in November 2012 was faster than normal, due to a high pressure system over the Barents Sea and strong winds from the south. Whether this is an error in data or whether this is due to the relatively high sea ice extent in these months is presently unknown, however one thing to keep in mind is that CryoSat do not pickup the very thin new ice because of its specular surface, and thus it will probably detect the thin ice as leads.

March 2013

Following the analysis from this study there was not much growth in the sea ice from autumn 2012 to spring 2013, even though the ice extent has expanded since the big summer melt event in 2012. ALT shows a too low March 2013 thickness, it is even lower than November 2012, which is not realistic, and thus has to be investigated in further details. The problem does not arise for the separate ice type thicknesses. This may be due to the problem with the November 2012 data described above.

Following NSIDC, the level of multi-year ice in March 2013 remains extremely low. The very strong Beaufort Gyre observed this year actually caused the ice to break up all over the Beaufort Sea, which normally is a very compact ice cover. At the same time more ice is observed at the Siberian coast. This is visible in the sea ice maps comparing March 2012 and March 2013 ((d) and (f) in Fig. 11.3.2, 11.4.1 and 11.4.2). Furthermore, the distribution of leads in the Arctic Ocean (Fig. 11.1.2) clearly shows a larger amount of leads in 2013 than in the previous months (Appendix E.2). The difference between the 2013 and 2012 thicknesses are displayed in Fig. 11.5.4 from the PIOMAS model and shows how the first-year ice in the Russian Arctic has gained thickness, while areas north of Greenland, in the Beaufort Sea, and in the Chukchi Sea have thinned. This is the opposite of what is normally seen at this time of year, but corresponding well with the increase observed in this study for the first-year ice in this study from 2012 to 2013.

11.6 Further Discussions and Enhancements

In this study a mean freeboard height between 24.5 and 19.2 cm was found. Kwok et al. [2009] derived the mean freeboard from the ICESat record (2003-2008) to 40.2 cm in October/November and 42.5 cm in February/March. Farrell et al. [2009] found values between 25 and 40 cm

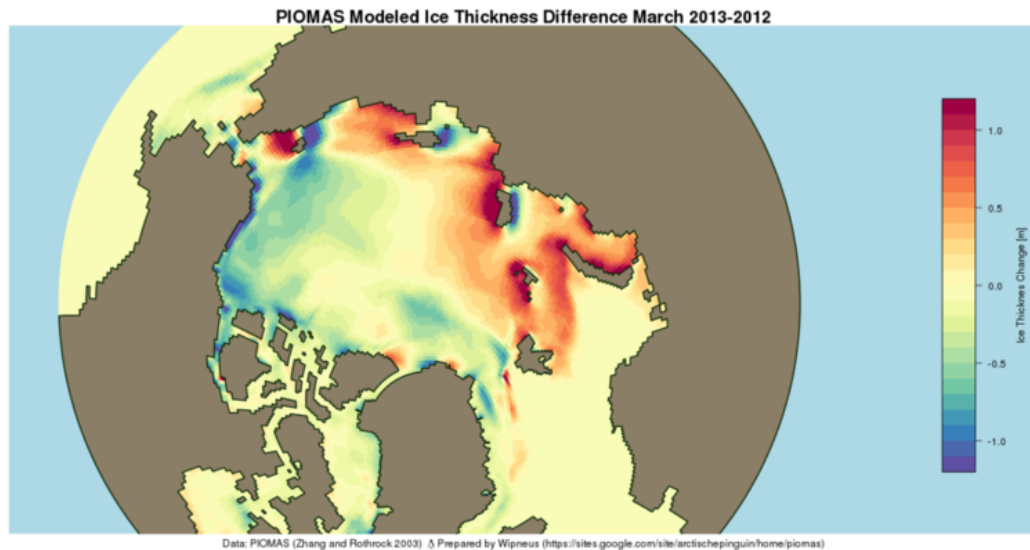


Figure 11.5.4: Differences in the sea ice thicknesses between 2013 and 2012 from the PIOMAS model. Credit: Polar Science Center, University of Washington.

from the same data. Skourup [2009] also used ICESat to calculate basin wide mean freeboard height and found values between 22.4 to 37.6 cm in the five year period.

All the ICESat studies are measuring a freeboard with both ice and snow layer included. Kwok et al. [2009] also measure a mean snow depth from the period, and this is 24 cm in the fall and 30 cm in spring. Even considering a snow layer the freeboard heights, in this study seem too large.

The mean thickness in this study is also thicker than the unpublished results from Kaleschke and Rickert [2013]. They combine CryoSat and SMOS data for March 2011, 2012, and 2013, with a mean thickness of between 2.2 to 1.8 in the period. Kwok et al. [2009] find a mean thickness in February/March of 2.9 m over the ICESat record and a October/November mean thickness of 2.6 m.

The results may be biased by the missing data in the Wingham box. This is typically an area with thick multi-year ice and would cause lower than normal mean freeboard/thicknesses in this study. Another bias arises when excluding negative freeboard heights and freeboard values over 1 m, but on the other hand this will also exclude elevations that are retracked wrongly if waveforms are corrupted before the first return.

There are some issues regarding evaluating ice thicknesses of first- and multi-year ice separately. Firstly, the ice type model has to be good. Comparing the OSI SAF model to other available datasets we see quite large differences, resulting in errors in the thickness distribution. Secondly, the ice type model is a snapshot represented by one day. Thus, distribution of ice types can vary during the month and the same applies for the ice edge, whereas the thickness data span a full month. To do it more correctly, the CryoSat data should have been evaluated for each day to the OSI SAF ice type model. Though an issue would then be the occurrence of huge unrealistic variations from day to day, and in some occurrences multi-year ice was located in areas normally not containing multi-year ice.

The difference in WAT and ALT for the annual trend for the period between autumn 2010

to spring 2013 is quite large, but it shows how sensitive the thickness retrieval is to the method used.

For the November months there is a large difference in the ice extent in the beginning of the month and in the end. This is causing a large uncertainty especially in the autumn distributions. The right thing to do would have been to evaluate the ice edge location for every day through out the month. As stated in the beginning of this section it would have been more appropriate to use September or October as the fall month. Comparing the ice extent from September (Fig. 3.2.1(a)) with November (Appendix E.3) it is clear how different a September and November extent can be with November being much more stable than September.

In the freeboard and thickness distributions in Fig. 11.3.3 and 11.4.3, the modal freeboard becomes lower with time corresponding to a sea ice thinning. In autumn there is not the same picture, this is caused by the November 2011 data being clearly underestimated. Also looking at the shape of the distribution (green curve) there is no slow decreasing trailing edge, which clearly is a signal of missing multi-year ice.

There are some noise in data. Thick multi-year ice is not expected in the Chukchi Sea or in the Russian Arctic. This is mainly boundary problems, due to open water, islands, or land, however it is also seen in Fig. 11.4.1(a) and 11.4.2(a) in the central Arctic e.g. around longitude 150° and 80° latitude. The problems could maybe have been avoided by making a cross-over analysis for the lead values, where elevations in crossing satellite tracks are compared.

In situations where the DT changes dramatically during the month a freeboard retrieval of every single track could have been advantageous, like the method used for retrieving freeboard in Rose et al. [2013b]. Kurtz et al. [2008] showed by comparing ICESat and airborne data that a method similar to the one used in this study performs better over areas with thicker ice.

Comparing the thickness distributions and the resulting sea ice thickness trends from WAT and ALT, WAT seems to perform the best. It is known that the snow depths used in WAT are overestimated in low latitudes, and that the ALT model perform best in the Russian Arctic. This can be seen in Fig. 11.5.2(a), where there seems to be problems with ALT in multi-year ice areas, which is as expected [Alexandrov et al., 2010].

Conclusion

In this Ph.D study radar altimetry data from CryoSat are processed with a threshold retracker. The results over leads show similar results as with the Gaussian fit retracker, which is the most frequently used method.

Two study areas; one in the Lincoln Sea with primarily multi-year ice and one north of Svalbard, with primarily first-year ice, are used to validate the retracked CryoSat observations. Laser altimetry data from the CryoVEx campaign and from NASA's OIB are averaged to the CryoSat ground resolution. They are corrected for ice drift, and show in relation to each other, a very strong correlation. There was not observed drift between the two datasets in the first part of the track. The CryoSat data are also corrected for drift by a linear interpolation in time, and the correlation was acceptable for such different datasets, but the drift may be error-prone, and has to be investigated in more details.

The CryoSat data were found to be very sensitive to specular returns (leads) off-nadir. Data are filtered based on a pulse peakiness criteria [Armitage and Davidson, 2013], which resulted in a rejection of more than 60% of the measurements. Removing these off-ranging elevations improved the correlation, and freeboard between the laser scanner datasets and CryoSat agreed when considering a snow layer. From this, it was also concluded, that CryoSat performs best in areas with thicker ice, and fewer leads.

Leads are used to form the local SSH, and is crucial in the freeboard retrieval. Two lead detection algorithms were developed during the studies, described in Rose et al. [2013b] and in Section 10.3. The SSH can also be established from GPS measurements on the sea ice north of Greenland, while knowing the geophysical parameters. This was shown in [Rose et al., 2013c], where also the ocean tides were derived from the GPS measurements and compared to the Arctic tide model AOTIM-5 [Padman and Erofeeva, 2004]. The tide model and the GPS measurements showed good correlation in the Arctic Ocean north of Greenland, and less good in the fjord and in coastal areas, due to more complex tides and lack of ocean tide information.

The Greenland fjords exchange freshwater between the glaciers in the fjords system and the ocean. This has an impact on the global sea-level and ocean salinity, circulation, and the local echo system. In Rose et al. [2013d], we study “a snapshot” of the mass loss from the glaciers and sea ice located in the inner fjord. We find 1.70 ± 1.26 GT ice in the fjord May, 27 2012 corresponding to 38% of the yearly ice flux, and considering the time of year, this corresponds well with other studies [Rignot and Kanagaratnam, 2006; Mortensen et al., 2013].

In a preliminary study the CryoSat observations are converted to freeboard heights and the annual and interannual variations in the sea ice cover for the whole Arctic region were estimated and discussed for the CryoSat record between 2010 to 2013. In the very short record a mean thinning of 1.5 cm/year in the Arctic sea ice freeboard cover was found.

For the same data two methods for retrieving sea ice thicknesses were applied, and the potential of large uncertainties in the thickness retrieval were stressed. Both methods were based on an assumption that sea ice is in hydrostatic equilibrium with water. The first method used snow depth loading from Warren et al. [1999] climatology, but only half of the snow loading over first-year ice was applied [Kurtz and Farrell, 2011]. In the second method an imperial relationship was used from Alexandrov et al. [2010] separating first- and multi-year ice, where the snow loading is included. The methods performed well and a thinning in the thickness in autumn was found to be in the range 8.1–11.6 cm/year and in spring the thinning were 15.7–16.9 cm/year. There were found a problem with the retrieved freeboard heights and thickness estimates in November 2011 and in the ALT method for March 2013, which of course influenced the trends.

12.1 Future Work

During this study several ideas for improving the work and other interesting topics for future work have emerged. In the following some of these ideas will be outlined.

- Discriminate between open leads/refrozen leads and leads with snow on top. To make sure to derive the true SSH; open leads are the true SSH, refrozen and refrozen leads with snow on top bias the SSH. This will be a study of the peak power, pulse peakiness and or the beam parameters from CryoSat, where comparisons to other data e.g. airborne or satellite imagery. The surrounding sea ice may also influence the power, and may be taking into account.
- Look more in depth into the rejection criteria from filtering CryoSat elevations, described in Section 10.6. So far the Laxon et al. [2013] and Armitage and Davidson [2013] criteria are used, but this can maybe be tuned, especially for areas with thin ice and many leads. This was visible in Section 11.1.1, where the distribution of retracking gates had a bimodal distribution.
- Testing the geophysical corrections available in the CryoSat product, and applying a dynamic topography model to the data. It would be obvious to start by looking at the ocean tide, because it gives a large contribution (meter-level), and because several studies showed, that AOTIM-5 performs better in the Arctic Ocean than FES2004 which is used in the CryoSat product.
- Make a study of surface and volume scattering of the SAR altimeter waveforms. Is it possible to discriminate the waveforms with volume scattering to discriminate first-, multi-year ice and ridges? Large volume scattering, which are seen for rough surfaces are indicated by high backscatter.
- An other interesting study of the CryoSat waveforms would be to look at the preferential sampling error as done in Tonboe et al. [2010] for a simple waveform model. A further

development would be to establish a more advanced SAR waveform model, and study the waveform characteristics.

- Develop a retracker for the CryoSat SARin mode to fill out the gap in the Arctic Ocean, and furthermore use the method developed in [Rose et al. \[2013d\]](#) to study the glaciers in the Godthåbsfjord with CryoSat SARin, and validate the findings.
- Study the averaging of laser altimeter data to the CryoSat ground resolution in more details. Are there other sampling methods, that perform better compared with the satellite data? and look at the sampling independent on the satellite sampling.
- Study the ascending and descending CryoSat satellite tracks to look for a possible bias.

The results in this study show how the Arctic sea ice cover has encountered large changes in recent years. CryoSat data were validated and the possibility of estimating sea ice freeboard and thickness from the satellite were demonstrated. The short CryoSat record in this study agree with recent studies with a continuing thinning of the mean sea ice in all seasons.

This study contribute to a better understanding of the CryoSat data, which in turn will improve the accuracy of cryosphere observations. The CryoSat mission will together with future satellite missions provide a more accurate picture of the ice conditions and contribute to a deeper knowledge into the inherent errors, and in turn improve the numerical climate models.

Bibliography

- Aagaard, K. and Carmack, E. (1989). The role of sea ice and other fresh water in the Arctic circulation. *J. Geophys. Res.-Oceans*, 94(C10):14485–14498.
- Alexandrov, V., Sandven, S., Wahlin, J., and Johannessen, O. (2010). The relation between sea ice thickness and freeboard in the Arctic. *The Cryosphere*, 4:641–661.
- Andersen, O. B. (2010). The DTU10 Gravity field and Mean sea surface. In *Second international symposium of the gravity field of the Earth (IGFS2)*. Fairbanks, Alaska.
- Armitage, T. W. K. and Davidson, M. W. J. (2013). Using the Interferometric Capabilities of the ESA CryoSat-2 Mission to Improve the Accuracy of Sea Ice Freeboard Retrievals. *IEEE T. Geosci. Remote*, in press:1–8.
- Bamber, J. L. and Kwok, R. (2004). Remote-sensing techniques. In Bamber, J. L. and Payne, A. J., editors, *Mass balance of the cryosphere: observations and modelling of contemporary and future changes*, pages 337–366. Cambridge University Press.
- Beaven, S. G., Lockhart, G. L., Gogineni, S. P., Hossetnmostafa, A. R., Jezek, K., Gow, A. J., Perovich, D. K., Fung, A. K., and Tjuatja, S. (1995). Laboratory measurements of radar backscatter from bare and snow-covered saline ice sheets. *Int. J. Remote Sens.*, 16:851–876.
- Brown, G. (1977). The average impulse response of a rough surface and its applications. *IEEE Trans. Antennas Propag.*, 25(1):67–74.
- Cavalieri, D., Crawford, J., Drinkwater, M., Eppler, D., Farmer, L., Jentz, R., and Wackerman, C. (1991). Aircraft active and passive microwave validation of sea ice concentration from the Defense Meteorological Satellite Program Special Sensor Microwave Imager. *J. Geophys. Res.-Oceans*, 96(C12):21989–22008.
- Cavalieri, D. J., Gloersen, P., and Campbell, W. J. (1984). Determination of sea ice parameters with the nimbus 7 smmr. *J. Geophys. Res.*, 89(D4):5355–5369.
- Comiso, J. (1990). Arctic multiyear ice classification and summer ice cover using passive microwave satellite data. *J. Geophys. Res.*, 95(C8):13411–13.
- Comiso, J., Parkinson, C., Gersten, R., and Stock, L. (2008). Accelerated decline in the Arctic sea ice cover. *Geophys. Res. Lett.*, 35(1):L01703.

- Comiso, J., Wadhams, P., Krabill, W., Swift, R., Crawford, J., and Tucker III, W. (1991). Top/bottom multisensor remote sensing of Arctic sea ice. *J. Geophys. Res.*, 96(C2):2693–2709.
- Comiso, J. C. (1995). *SSM/I sea ice concentrations using the bootstrap algorithm*, volume 1380. National Aeronautics and Space Administration, Goddard Space Flight Center.
- Connor, L., Farrell, S. L., McAdoo, D. C., Krabill, W. B., and Manizade, S. (2013). Validating ICESat Over Thick Sea Ice in the Northern Canada Basin. *IEEE T. Geosci. Remote*, 51(4):2188–2200.
- Connor, L. N., Laxon, S. W., Ridout, A. L., Krabill, W. B., and McAdoo, D. C. (2009). Comparison of Envisat radar and airborne laser altimeter measurements over Arctic sea ice. *Remote Sens. of Environ.*, 113(3):563–570.
- Curry, J. A., Schramm, J. L., and Ebert, E. E. (1995). Sea ice-albedo climate feedback mechanism. *J. Climate*, 8(2):240–247.
- Davis, C. (2002). A robust threshold retracking algorithm for measuring ice-sheet surface elevation change from satellite radar altimeters. *IEEE Trans. Geosci. Remote Sens.*, 35(4):974–979.
- Dean, S. and Illowsky, B. (2012). Descriptive Statistics: Skewness and the Mean, Median, and Mode. Connexions Web site.
- Deng, X. (2003). *Improvement of Geodetic Parameter Estimation in Coastal Regions from Satellite Radar Altimetry*. PhD thesis, Curtin University of Technology.
- Dijkstra, H. A. (2008). Arctic Ocean Circulation. In *Dynamical Oceanography*, pages 351–374. Springer.
- DMI (1930). *Nautisk-Meteorologisk Aarbog*. Danish Meteorological Institute.
- Dominguez, R. (2012). IceBridge DMS L1B Geolocated and Orthorectified Images, [2012.04.02].
- Eastwood, S., Breivik, L., Godø, Ø., Lavergne, T., Lind, M., Porcires, M., and Schyberg, H. Tonboe, R. (2012). *Sea Ice – Product Manual*. OSI SAF, 3.8 edition.
- Ekman, M. (1989). Impacts of geodynamic phenomena on systems for height and gravity. *J. Geod.*, 63(3):281–296.
- ESA (2003). CryoSat - Science Report. SP-1272, European Space Agency. March 2003.
- ESA (2007a). *ASAR Product Handbook*. February.
- ESA (2007b). CryoSat Mission and Data Description. CS-RP-ESA-SY-0059 3, ESTEC, Noordwijk, The Netherlands.
- ESA (2011a). CRYOSAT Ground Segment, Products Specification Format. Technical Report CS-RS-ACS-GS-5106, ESA. Instrument Processing Facility L1b, Issue: 4.9.

- ESA (2011b). Observing the Earth, ERS Overview. ESA Earthnet Online.
- ESA (2013). Observing the Earth, Envisat Overview. ESA Earthnet Online.
- ESA and UCL (2013a). *CryoSat Product Handbook*. ESRIN - ESA and Mullard Space Science Laboratory - University College London, April 2013 edition. Available at: <http://earth.esa.int/cryosat>.
- ESA and UCL (2013b). *CryoSat Product Handbook*. Technical report, ESRIN - ESA and Mullard Space Science Laboratory - University College London.
- European Space Agency (2010). ESA - Living Planet Programme - CryoSat-2. <http://www.esa.int/esaLP/LPcryosat.html>.
- Farrell, S., Kurtz, N., Connor, L., Elder, B., Leuschen, C., Markus, T., McAdoo, D., Panzer, B., Richter-Menge, J., and Sonntag, J. (2012). A first assessment of IceBridge snow and ice thickness data over Arctic sea ice. *IEEE T Geosci Remote*, 50(6):2098–2111.
- Farrell, S. L., Laxon, S. W., McAdoo, D. C., Yi, D., and Zwally, H. J. (2009). Five years of arctic sea ice freeboard measurements from the ice, cloud and land elevation satellite. *J. Geophys. Res.: Oceans (1978–2012)*, 114(C4).
- Fetterer, F. M., Drinkwater, M. R., Jezek, K. C., Laxon, S. W., and Onstott, R. G. (1992). Sea ice altimetry. In Carsey, F. D., editor, *Microwave remote sensing of sea ice*.
- Flato, G. M. (2004). Sea-ice modelling. In Bamber, J. L. and Payne, A. J., editors, *Mass balance of the cryosphere: observations and modelling of contemporary and future changes*, pages 367–392. Cambridge University Press.
- Forsberg, R. and Skourup, H. (2005). Arctic Ocean gravity, geoid and sea-ice freeboard heights from ICESat and GRACE. *Geophys. Res. Lett.*, 32(21).
- Forsberg, R., Skourup, H., Andersen, O., Knudsen, P., Laxon, S. W., Ridout, A., Braun, A., Johannessen, J., Tscherning, C. C., and Arabelos, D. (2006). Arctic Ocean Geoid, Ice Thickness and Mean Sea Level - The ARCGICE Project. In *Proceedings ESA workshop "15 years of progress in radar altimetry"*, Venice.
- Forsberg, R., Skourup, H., Andersen, O. B., Knudsen, P., Laxon, S. W., Ridout, A., Johannessen, J., Siegismund, F., Drange, H., Tscherning, C. C., Arabelos, D., Braun, A., and Renganathan, V. (2007). Combination of Spaceborne, Airborne and In-Situ Gravity Measurements in Support of Arctic Sea Ice Thickness Mapping. Technical report no 7, Danish National Space Center.
- Forsstrom, S., Gerland, S., and Pedersen, C. A. (2011). Thickness and density of snow-covered sea ice and hydrostatic equilibrium assumption from in situ measurements in Fram Strait, the Barents Sea and the Svalbard coast. *Ann. Glaciol.*, 52(57):261–270.
- Fowler, C., Emery, W., and Maslanik, J. (2004). Satellite-derived evolution of Arctic sea ice age: October 1978 to March 2003. *IEEE Geosci. Remote S.*, 1(2):71–74.

- Fu, L. and Cazenave, A. (2001). *Satellite altimetry and earth sciences: A handbook of techniques and applications*. Academic Press.
- Gao, G. X., Heng, L., and Walter, T. and Enge, P. (2012). Breaking the ice: Navigation in the arctic. In *Global Navigation Satellite Systems: Report of a Joint Workshop of the National Academy of Engineering and the Chinese Academy of Engineering*, page 229. National Academies Press.
- Giles, K. and Hvidegaard, S. (2006). Comparison of space borne radar altimetry and airborne laser altimetry over sea ice in the Fram Strait. *Int. J. Remote Sens.*, 27(15):3105–3113.
- Giles, K., Laxon, S., and Ridout, A. (2008). Circumpolar thinning of Arctic sea ice following the 2007 record ice extent minimum. *Geophys. Res. Lett.*, 35(22):L22502.
- Giles, K., Laxon, S., Wingham, D., Wallis, D., Krabill, W., Leuschen, C., McAdoo, D., Manizade, S., and Raney, R. (2007). Combined airborne laser and radar altimeter measurements over the Fram Strait in May 2002. *Remote Sens. Environ.*, 111(2-3):182–194.
- Giles, K. A., Laxon, S. W., Ridout, A. L., Wingham, D. J., and Bacon, S. (2012). Western Arctic Ocean freshwater storage increased by wind-driven spin-up of the Beaufort Gyre. *Nat. Geosci.*, NGE01379:1–4.
- Gregorius, T. (1996). Gipsy-oasis ii: how it works. *Department of Geomatics, University of Newcastle upon Tyne*, 109.
- Haas, C. et al. (2010a). Dynamics versus thermodynamics: The sea ice thickness distribution. In Thomas, D. and S., D. G., editors, *Sea Ice*, pages 82–111. John Wiley and Sons.
- Haas, C., Gerland, S., Eicken, H., and Miller, H. (1997). Comparison of sea-ice thickness measurements under summer and winter conditions in the Arctic using a small electromagnetic induction device. *Geophysics*, 62(3):749–757.
- Haas, C., Hendricks, S., Eicken, H., and Herber, A. (2010b). Synoptic airborne thickness surveys reveal state of Arctic sea ice cover. *Geophys. Res. Lett.*, 37(9).
- Haas, C., Pfaffling, A., Hendricks, S., Rabenstein, ., Etienne, J., and Rigor, I. (2008). Reduced ice thickness in Arctic Transpolar Drift favors rapid ice retreat. *Geophys. Res. Lett.*, 35(17).
- Hallikainen, M. (1992). Review of the microwave dielectric and extinction properties of sea ice and snow. In *Geoscience and Remote Sensing Symposium, 1992. IGARSS'92. International*, volume 2, pages 961–965. IEEE.
- Herring, T., King, R., and McClusky, S. (2008). Introduction to gamit/globk. *Mass Inst. of Technol., Cambridge*.
- Hofmann-Wellenhof, B., Lichtenegger, H., and Wasle, E. (2008). *Gnss: Global Navigation Satellite Systems: Gps, Glonass, Galileo, and More*. Springer.
- Holland, M. M. and Bitz, C. M. (2003). Polar amplification of climate change in coupled models. *Clim. Dynam.*, 21(3-4):221–232.

- Hugentobler, U., Schär, S., Fridez, P., and Beutler, E. (2001). *Bernese GPS Software: Version 4.2*. University of Berne.
- Jakobsson, M., Mayer, L., Coakley, B., Dowdeswell, J. A., Forbes, ., Fridman, B., Hodnesdal, H., Noormets, R., Pedersen, R., Rebesco, M., et al. (2012). The international bathymetric chart of the arctic ocean (ibcao) version 3.0. *Geophys. Res. Lett.*, 39(12).
- Jensen, A. B. and Sicard, J. (2010). Challenges for Positioning and Navigation in the Arctic. *Coordinates*, 6:10–13.
- Johannessen, O. M., Bengtsson, L., Miles, M. W., Kuzmina, S. I., Semenov, V. A., Alekseev, G. V., Nagurnyi, A. P., Zakharov, V. F., Bobylev, L. P., Pettersson, . H., et al. (2004). Arctic climate change: Observed and modelled temperature and sea-ice variability. *Tellus A*, 56(4):328–341.
- Kaleschke, L. and Rickert, R. (2013). Sea Ice Outlook 2013 - Sea Ice Thickness from CryoSat-2 and SMOS. www.arcus.org.
- Kaplan, E. D. and Hegarty, C. J. (2006). *Understanding GPS: principles and applications*. Artech House Publishers.
- Kedar, S., Hajj, G., Wilson, B., and Heflin, M. (2003). The effect of the second order GPS ionospheric correction on receiver positions. *Geophys. Res. Lett.*, 30(16):1829.
- Kenyon, S., Forsberg, R., and Coakley, B. (2008). New Gravity Field for the Arctic. *Eos Trans. AGU*, 89:32.
- Khan, S., Wahr, J., Leuliette, E., van Dam, T., Larson, K. M., and Francis, O. (2008). Geodetic measurements of postglacial adjustments in Greenland. *J Geophys Res-Sol Ea*, 113(B2).
- Khan, S. A., Wahr, J., Bevis, M., Velicogna, I., and Kendrick, E. (2010). Spread of ice mass loss into northwest Greenland observed by GRACE and GPS. *Geophys. Res. Lett.*, 37(6).
- Knudsen, P., Andersen, O. B., and Tscherning, C. C. (1992). Altimetric gravity anomalies in the Norwegian-Greenland Sea-Preliminary results from the ERS-1 35 days repeat mission. *Geophys. Res. Lett.*, 19(17):1795–1798.
- Krabill, W. B. (2012). IceBridge Narrow Swath ATM L1B Qfit Elevation and Return Strength [2012.04.12]. Digital media.
- Kurtz, N. T. and Farrell, S. L. (2011). Large-scale surveys of snow depth on Arctic sea ice from Operation IceBridge. *Geophys. Res. Lett.*, 38(20).
- Kurtz, N. T., Farrell, S. L., Studinger, M., Galin, N., Harbeck, J. P., Lindsay, R., Onana, V. D., Panzer, B., and Sonntag, J. G. (2013). Sea ice thickness, freeboard, and snow depth products from Operation IceBridge airborne data. *The Cryosphere*, 7:1035–1056.
- Kurtz, N. T., Markus, T., Cavalieri, D. J., Krabill, W., Sonntag, J. G., and Miller, J. (2008). Comparison of ICESat data with airborne laser altimeter measurements over Arctic sea ice. *IEEE T. Geosci. Remote*, 46(7):1913–1924.

- Kwok, R. (2004). Annual cycles of multiyear sea ice coverage of the Arctic Ocean: 1999–2003. *J. Geophys. Res.*, 109(C11):C11004.
- Kwok, R., Cunningham, G., and Yueh, S. (1999). Area balance of the Arctic Ocean perennial ice zone: October 1996 to April 1997. *J. Geophys. Res.: Oceans*, 104(C11):25747–25759.
- Kwok, R., Cunningham, G., Zwally, H., and Yi, D. (2007). Ice, Cloud, and land Elevation Satellite (ICESat) over Arctic sea ice: Retrieval of freeboard. *J. Geophys. Res.*, 112:C12013.
- Kwok, R., Cunningham, G. F., Wensnahan, M., Rigor, I., Zwally, H. J., and Yi, D. (2009). Thinning and volume loss of the Arctic Ocean sea ice cover: 2003–2008. *J. Geophys. Res.-Oceans*, 114(C7).
- Kwok, R., Cunningham, G. F., Zwally, H. J., and Yi, D. (2006). ICESat over Arctic sea ice: Interpretation of altimetric and reflectivity profiles. *J. Geophys. Res.*, 111(C06006).
- Kwok, R., Schweiger, A., Rothrock, D., Pang, S., and Kottmeier, C. (1998). Sea ice motion from satellite passive microwave imagery assessed with ers sar and buoy motions. *J. Geophys. Res.: Oceans*, 103(C4):8191–8214.
- Laxon, S. (1994a). Sea ice altimeter processing scheme at the eodc. *Int. J. Remote Sens.*, 15(4):915–924.
- Laxon, S. (1994b). Sea ice extent mapping using the ers-1 radar altimeter. *EARSeL Adv. Remote Sens.*, 3:112–116.
- Laxon, S., Peacock, N., and Smith, D. (2003). High interannual variability of sea ice thickness in the Arctic region. *Nature*, 425(6961):947–950.
- Laxon, S., Walsh, J. E., Wadhams, P., Johannessen, O. M., and Miles, M. (2004). Sea-ice observations. In Bamber, J. L. and Payne, A. J., editors, *Mass balance of the cryosphere: observations and modelling of contemporary and future changes*, pages 337–366. Cambridge University Press.
- Laxon, S. W., Giles, K. A., Ridout, A. L., Wingham, D. J. and Willatt, R., Cullen, R. T., Kwok, R., Schweiger, A., Zhang, J., Haas, C., et al. (2013). CryoSat-2 estimates of Arctic sea ice thickness and volume. *Geophys. Res. Lett.*, 40:1–6.
- Laxon, S. W. and Rapley, C. G. (1987). Radar altimeter data quality flagging. *Adv. Space Res.*, 7(11):315–318.
- Lindsay, R. and Zhang, J. (2005). The thinning of arctic sea ice, 1988–2003: Have we passed a tipping point? *J. Climate*, 18(22):4879–4894.
- Lindsay, R. W., Zhang, J., Schweiger, A., Steele, M., and Stern, H. (2009). Arctic sea ice retreat in 2007 follows thinning trend. *J. Climate*, 22(1):165–176.
- Mäkinen, J. and Ihde, J. (2008). The permanent tide in height systems. *Observing our Changing Earth*, pages 81–87.

- Markus, T. and Cavalieri, D. J. (2000). An enhancement of the nasa team sea ice algorithm. *IEEE Geosci. Remote S.*, 38(3):1387–1398.
- Markus, T., Stroeve, J. C., and Miller, J. (2009). Recent changes in arctic sea ice melt onset, freezeup, and melt season length. *J. Geophys. Res.-Oceans*, 114(C12).
- Martin, T., Zwally, H., Brenner, A., and Bindshadler, R. (1983). Analysis and retracking of continental ice sheet radar altimeter waveforms. *J. Geophys. Res.*, 88(C3):1608–1616.
- Maslanik, J. A., Fowler, C., Stroeve, J., Drobot, S., Zwally, J., Yi, D., and Emery, W. (2007). A younger, thinner arctic ice cover: Increased potential for rapid, extensive sea-ice loss. *Geophys. Res. Lett.*, 34(24).
- Misra, P. and Enge, P. (2011). *Global Positioning System: Signals, Measurements and GPS*. Ganga-Jamuna Press (available through Navtech), 2 edition.
- Mortensen, J., Bendtsen, J., Motyka, R., Lennert, K., Truffer, M., Fahnestock, M., and Rysgaard, S. (2013). On the seasonal freshwater stratification in the proximity of fast-flowing tidewater outlet glaciers in a sub-Arctic sill fjord. *J. Geophys. Res.-Oceans*, 118:1385–1395.
- National Geospatial-intelligence Agency (2013). EGM2008 - WGS 84 Version. April 29, 2013. http://earth-info.nga.mil/GandG/wgs84/gravitymod/egm2008/egm08_wgs84.html.
- Nghiem, S. V., Rigor, I. G., Perovich, D. K., Clemente-Colón, P., Weatherly, J. W., and Neumann, G. (2007). Rapid reduction of Arctic perennial sea ice. *Geophys. Res. Lett.*, 34(19).
- Olynik, M., Petovello, M., Cannon, M., and Lachapelle, G. (2002). Temporal variability of gps error sources and their effect on relative positioning accuracy. *Proceedings of the Institute of Navigation NTM 2002*.
- Overland, J. E. and Wang, M. (2013). When will the summer arctic be nearly sea ice free? *Geophys. Res. Lett.*
- Padman, L. and Erofeeva, S. (2004). A barotropic inverse tidal model for the Arctic Ocean. *Geophys. Res. Lett.*, 31(2):L02303.
- Parkinson, C. L. and Comiso, J. C. (2013). On the 2012 record low Arctic sea ice cover: Combined impact of preconditioning and an August storm. *Geophys. Res. Lett.*, pages 1–6.
- Pavlis, N., Holmes, S., Kenyon, S., and Factor, J. (2008). An earth gravitational model to degree 2160: Egm2008. *EGU General Assembly*, pages 13–18.
- Pavlov, V. K. (1998). Circulation in ice-covered waters. In *Physics of ice-covered waters*, volume Vol 2. Helsinki University Printing House.
- Peacock, N. and Laxon, S. (2004). Sea surface height determination in the Arctic Ocean from ERS altimetry. *J. Geophys. Res.*, 109(C7).
- Penna, N., King, M., and Stewart, M. (2007). GPS height time series: Short-period origins of spurious long-period signals. *J. Geophys. Res.*, 112(B2):B02402.

- Perovich, D., Meier, W., Tschudi, M., Gerland, S., and Richter-Menge, J. (2012). Sea Ice in Arctic Report Card: Update for 2012. http://www.arctic.noaa.gov/reportcard/sea_ice.html.
- Perovich, D. K., Light, B., Eicken, H., Jones, K. F., and Runciman, K. and Nghiem, S. V. (2007). Increasing solar heating of the Arctic Ocean and adjacent seas, 1979–2005: Attribution and role in the ice-albedo feedback. *Geophys. Res. Lett.*, 34(19).
- Perovich, D. K., Richter-Menge, J. A., Jones, K. F., and Light, B. (2008). Sunlight, water, and ice: Extreme arctic sea ice melt during the summer of 2007. *Geophys. Res. Lett.*, 35(11).
- Proshutinsky, A. Y. and Johnson, M. A. (1997). Two circulation regimes of the wind-driven arctic ocean. *Journal of Geophysical Research: Oceans*, 102(C6):12493–12514.
- Rampal, P., Weiss, J., and Marsan, D. (2009). Positive trend in the mean speed and deformation rate of arctic sea ice, 1979–2007. *J. Geophys. Res.-Oceans*, 114(C5).
- Raney, R. K. (1998). The delay/Doppler radar altimeter. *IEEE Geosci. Remote S.*, 36(5):1578–1588.
- Rapp, R., Nerem, R., Shum, C., Klosko, S., and Williamson, R. (1991). Consideration of permanent tidal deformation in the orbit determination and data analysis for the TOPEX/POSEIDON mission. NASA Technical Memorandum 100775.
- Renganathan, V. (2010). *Arctic Sea Ice Freeboard Heights from Satellite Altimetry*. Phd thesis, University of Calgary.
- Resti, A., Benveniste, J., Roca, M., Levrini, G., and Johannessen, J. (1999). The envisat radar altimeter system (ra-2). *ESA bulletin*, 98:94–101.
- Rignot, E. and Kanagaratnam, P. (2006). Changes in the velocity structure of the greenland ice sheet. *Science*, 311(5763):986–990.
- Rigor, I. G. and Wallace, J. M. (2004). Variations in the age of arctic sea-ice and summer sea-ice extent. *Geophys. Res. Lett.*, 31(9).
- Rigor, I. G., Wallace, J. M., and Colony, R. L. (2002). Response of sea ice to the Arctic Oscillation. *J. Climate*, 15(18):2648–2663.
- Rivas, M. B., Maslanik, J. A., and Axelrad, P. (2010). Bistatic scattering of GPS signals off Arctic sea ice. *IEEE T. Geosci. Remote*, 48(3):1548–1553.
- Rose, S., Conner, L. N., Farrell, S. L., Forsberg, R., Newman, T., Pedersen, L. T. Smith, W. H. F., Skorup, H., and Stenseng, L. (2013a). A Comparative Analysis of the Sea Ice Freeboard from CryoSat, CryoVEx and IceBridge. In *CryoSat Third User Workshop*. ESA.
- Rose, S., Conner, L. N., Farrell, S. L., Forsberg, R., Newman, T., Smith, W. H. F., and Skorup, H. (2013b). A Sea Ice Freeboard Analysis from CryoSat, CryoVEx and IceBridge over First- and Multi-year Ice Areas. *IEEE T. Geosci. Remote*, Rejected, with resubmission after major revision:1–13.

- Rose, S., Skourup, H., and Forsberg, R. (2013c). Arctic Tides from GPS on Sea-ice. *J. Geodyn.*, 63:45–53.
- Rose, S. K., Forsberg, R., Hvidegaard, S. M., Nielsen, K., Pedersen, L. T., Simonsen, S. B., and Sørensen, L. S. S. (2013d). Ice mélange volume estimates from LiDAR - A snapshot of ice discharge in the inner Godthåbsfjord, Greenland. *J. Glaciol.*, Submitted.
- Rose, S. K., Stenseng, L., Skourup, H., Pedersen, L. T., and Forsberg, R. (2011). Initial results of CryoSat-2 data from the Arctic. In *CryoSat Validation Workshop 2011*, volume SP-693. ESA.
- Rothrock, D., Yu, Y., and Maykut, G. (1999). Thinning of the Arctic sea-ice cover. *Geophys. Res. Lett.*, 26(23):3469–3472.
- Rouse, J. W. (1969). Arctic ice type identification by radar. *Proceedings of the IEEE*, 57(4):605–611.
- Saastamoinen, J. (1972). Atmospheric correction for the troposphere and stratosphere in radio ranging satellites. *Geoph. Monog. Series*, 15:247–251.
- Schutz, B., Zwally, H., Shuman, C., Hancock, D., and DiMarzio, J. (2005). Overview of the ICESat mission. *Geophys. Res. Lett.*, 32(21):L21S01.
- Seeber, G. (2003). *Satellite Geodesy*. de Gruyter, 2nd edition.
- Serreze, M., Holland, M., and Stroeve, J. (2007). Perspectives on the Arctic’s shrinking sea-ice cover. *Science*, 315(5818):1533–1536.
- Serreze, M. C., Barrett, A. P., Slater, A. G., Woodgate, R. A., Aagaard, K., Lammers, R. B., Steele, ., Moritz, R., Meredith, M., and Lee, C. M. (2006). The large-scale freshwater cycle of the Arctic. *J. Geophys. Res.: Oceans*, 111(C11).
- Skourup, H. (2009). *A study of Arctic sea ice freeboard heights, gravity anomalies and dynamic topography from ICESat measurements*. Ph.d. thesis, University of Copenhagen.
- Skourup, H., Barletta, V., Einarsson, I., Forsberg, R., Haas, C., Helm, V., Hendricks, S., Hvidegaard, S. M., and Sørensen, L. S. (2013a). *ESA CryoVEx 2011, Airborne field campaign with ASIRAS radar, EM induction sounder and laser scanner*. National Space Institute (DTU Space). Tech. report.
- Skourup, H., Einarsson, I., Forsberg, R., Hvidegaard, S. M., Nilsson, J., and Olesen, A. (2013b). *ESA CryoVEx 2012 - Airborne field campaign, Data Acquisition Report*. National Space Institute (DTU Space). TEch. report.
- Skourup, H. and Forsberg, R. (2008). Geoid, sea-level and vertical datum of the Arctic—Improved by ICESat and GRACE. *Geomatica*, 62:287–298.
- Smith, D. M. (1998). Recent increase in the length of the melt season of perennial Arctic sea ice. *Geophys. Res. Lett.*, 25(5):655–658.

- Smith, S. D., Muench, R. D., and Pease, C. H. (1990). Polynyas and leads: An overview of physical processes and environment. *J. Geophys. Res.-Oceans*, 95(C6):9461–9479.
- Spada, G., Ruggieri, G., Sørensen, L. S., Nielsen, K., Melini, D., and Colleoni, F. (2012). Greenland uplift and regional sea level changes from ICESat observations and GIA modelling. *Geophys. J. Int.*, 189(3):1457–1474.
- Spren, G., Kwok, R., and Menemenlis, D. (2011). Trends in arctic sea ice drift and role of wind forcing: 1992–2009. *Geophys. Res. Lett.*, 38(19).
- Stenseng, L. and Andersen, O. B. (2012). Preliminary gravity recovery from CryoSat-2 data in the Baffin Bay. *Adv. in Space Res.*, 50(8):1158–1163.
- Stroeve, J., Holland, M., Meier, W., Scambos, T., and Serreze, M. (2007). Arctic sea ice decline: Faster than forecast. *Geophys. Res. Lett.*, 34(9):9501.
- Stroeve, J., Serreze, M., Holland, M., Kay, J., Malanik, J., and Barrett, A. (2012). The Arctic's rapidly shrinking sea ice cover: a research synthesis. *Climatic change*, 110(3):1005–1027.
- Stroeve, J. C., Maslanik, J., Serreze, M. C., Rigor, I., Meier, W., and Fowler, C. (2011). Sea ice response to an extreme negative phase of the Arctic Oscillation during winter 2009/2010. *Geophys. Res. Lett.*, 38:L02502.
- Taylor, J. R. (1997). *An introduction to error analysis: the study of uncertainties in physical measurements*. University science books, 2nd edition edition.
- Thompson, D. W. and Wallace, J. M. (1998). The Arctic Oscillation signature in the wintertime geopotential height and temperature fields. *Geophys. Res. Lett.*, 25(9):1297–1300.
- Tonboe, R., Andersen, S., and Pedersen, L. (2006). Simulation of the Ku-band Radar altimeter sea ice effective scattering surface. *IEEE Geosci. Remote S.*, 3(2):237–240.
- Tonboe, R., Pedersen, L., and Haas, C. (2010). Simulation of the satellite radar altimeter sea ice thickness retrieval uncertainty. *Can. J. Remote Sens.*, 36(1):55–67.
- Torge, W. (2001). *Geodesy*. Walter de Gruyter, 3rd edition edition.
- Ulaby, F., Moore, R., and Fung, A. (1986). *Microwave Remote Sensing Active and Passive Vol. 3: From theory to Applications*. Artech House.
- Van Dam, T. and Wahr, J. (1998). Modeling environment loading effects: a review. *Physics and Chemistry of the Earth*, 23(9):1077–1087.
- Wadhams, P. (1997). Ice thickness in the arctic ocean: The statistical reliability of experimental data. *J. Geophys. Res.-Oceans*, 102(C13):27951–27959.
- Wadhams, P. (2013). Diminishing sea-ice extent and thickness in the arctic ocean. In for Peace, N. S. and Series, S., editors, *Environmental Security in the Arctic Ocean*, C: Enviromental Security, pages 15–30. Springer.
- Wadhams, P. and Davis, N. R. (2000). Further evidence of ice thinning in the arctic ocean. *Geophys. Res. Lett.*, 27(24):3973–3975.

- Wadhams, P., Tucker III, W., Krabill, W., Swift, R., Comiso, J., and Davis, N. (1992). Relationship between sea ice freeboard and draft in the Arctic Basin, and implications for ice thickness monitoring. *J. Geophys. Res.*, 97(C12):20325.
- Walsh, E. J., Uliana, E. A., and Yaplee, B. S. (1978). Ocean wave heights measured by a high resolution pulse-limited radar altimeter. *Boundary-Layer Meteorology*, 13(1-4):263–276.
- Wang, M. and Overland, J. E. (2012). A sea ice free summer Arctic within 30 years: An update from CMIP5 models. *Geophysical Research Letters*, 39(18).
- Warren, S. G., Rigor, I. G., Untersteiner, N., Radionov, V. F., Bryazgin, N. N., Aleksandrov, Y. I., and Colony, R. (1999). Snow depth on Arctic sea ice. *J. Climate*, 12(6):1814–1829.
- Willatt, R., Laxon, S., Giles, K., Cullen, R., Haas, C., and Helm, V. (2011). Ku-band radar penetration into snow cover on Arctic sea ice using airborne data. *Ann. Glacial.*, 52(57):197–205.
- Willatt, R. C., Giles, K. A., Laxon, S. W., Stone-Drake, L., and Worby, A. P. (2010). Field investigations of Ku-band radar penetration into snow cover on Antarctic sea ice. *IEEE Trans. Geosci. Remote Sens.*, 48(1):365–372.
- Wingham, D., Francis, C., Baker, S., Bouzinac, C., Brockley, D., Cullen, R., de Chateau-Thierry, P., Laxon, S., Mallow, U., Mavrocordatos, C., et al. (2006). CryoSat: A mission to determine the fluctuations in Earth's land and marine ice fields. *Adv. Space Res.*, 37(4):841–871.
- Wingham, D., Rapley, C., and Griffiths, H. (1986). New techniques in satellite altimeter tracking systems. In *ESA Proceedings of the 1986 International Geoscience and Remote Sensing Symposium (IGARSS'86) on Remote Sensing: Today's Solutions for Tomorrow's Information Needs*, volume 3.
- World Meteorological Organization (1970). *WMO Sea-ice nomenclature*. World Meteorological Organization. No. 259, TP 145.
- Xu, G. and Knudsen, P. (2000). Earth tide effects on kinematic/static GPS positioning in Denmark and Greenland. *Phys. Chem. Earth, Part A*, 25(4):409–414.
- Zhang, J. and Rothrock, D. A. (2003). Modeling global sea ice with a thickness and enthalpy distribution model in generalized curvilinear coordinates. *Mon. Weather Rev.*, 131(5):681–697.
- Zhang, X. (2005). Precise Point Positioning Evaluation and Airborne Lidar Calibration. Technical Report 4, Danish National Space Center.
- Zwally, H. J., Abdalati, W., Herring, T., Larson, K., Saba, J., and Steffen, K. (2002). Surface melt-induced acceleration of greenland ice-sheet flow. *Science*, 297(5579):218–222.
- Zwally, H. J., Yi, D., Kwok, R., and Zhao, Y. (2008). ICESat measurements of sea ice freeboard and estimates of sea ice thickness in the Weddell Sea. *J. Geophys. Res.-Oceans*, 113(C2).

- Zygmuntowska, M., Khvorostovsky, K., Helm, V., and Sandven, S. (2013). Waveform classification of airborne synthetic aperture radar altimeter over arctic sea ice. *The Cryosphere*, 7(4):1315–1324.

Appendices

Snow Depths from Warren's Climatology

Even though the snow depths from [Warren et al. \[1999\]](#) climatology is the most widely used snow model from the Arctic, it is to the author's knowledge not available online, nor a thorough description how to apply the model is available. Therefore, in this section the model implementation is described in details. This work is done in cooperation with Gabriel Strykowski, DTU Space.

From Warrens paper a two dimensional quadratic equation $H = H_0 + Ax + By + Cxy + Dx^2 + Ey^2$ is given together with table values (A - E) for each month to be inserted in the equation. x and y are given as degrees of arc and define a curvilinear grid. The grid has its origin at the North Pole, and x is positive along the Greenwich meridian, and y is positive along 90°E .

Any point on the surface of a sphere can be described by a set of Warrens curvilinear coordinates (x, y) using formulas of spherical triangle trigonometry in which the sides of a spherical right triangle are arcs of great circles. In Fig. [A.0.1](#), the triangles are depicted when looking down at the North Pole. First, we define a geodetic coordinate system with ellipsoidal latitude φ from 60° to 90° and longitude λ from -180° to 180° . Implicitly it is assumed, that the surface of the ellipsoid is projected on the surface of the standard sphere along the ellipsoidal normal. While converting from the ellipsoidal geodetic coordinate system to the geocentric spherical coordinate system

$$\begin{pmatrix} \varphi \\ \lambda \end{pmatrix}_{a,b} \rightsquigarrow \begin{pmatrix} \bar{\varphi} \\ \lambda \end{pmatrix} \rightsquigarrow \begin{pmatrix} x \\ y \end{pmatrix} \quad (\text{A.0.1})$$

where ρ is the distance from the center to the surface, λ is the longitude and φ the ellipsoidal latitude, and $\bar{\varphi}$ the geocentric is only different by the geocentric latitude $\bar{\varphi}$. From [Torge \[2001\]](#) a series expansion gives the difference between the angles, and the approximated transformation becomes

$$\bar{\varphi} = -\varphi - 2\beta \quad \text{where} \quad \tan \beta = \frac{b}{a} \tan \varphi . \quad (\text{A.0.2})$$

β is the reduced latitude, and a and b are the semimajor and semiminor axes, respectively, here

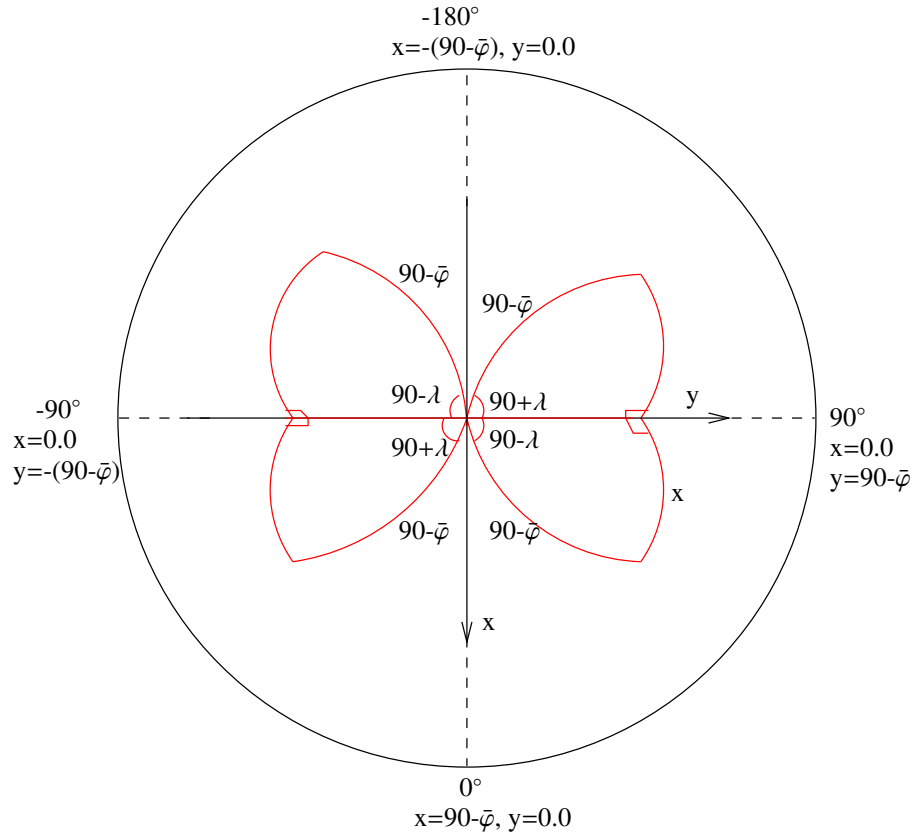


Figure A.0.1: Sketch of the coordinate system and the astronomical right triangle formed from the great axes x and y from Warren's snow model.

given by the WGS84 system. The angles in the four triangles in Fig. A.0.1 varies depending on the position on the sphere. The arc length x and y are found from the sine and cosine relations for a spherical triangle, where the singularities are also shown in the figure. From Eq. (A.0.1)

$$x = x(\varphi, \lambda) , \quad (\text{A.0.3})$$

$$y = y(\varphi, \lambda) \quad (\text{A.0.4})$$

and thus

$$H = H(x, y) = H(\varphi, \lambda) . \quad (\text{A.0.5})$$

Fig. A.0.2 is yielding the model results from September to December and Fig. A.0.3 from January to March. The mean snow depth from March is 32.4 cm with a RMS error of 9.4 cm and from mean September snow depth is 11.2 cm with a RMS error of 7.8 cm. The reliability of the model decreases with decreasing latitude, and negative values are set to zero.

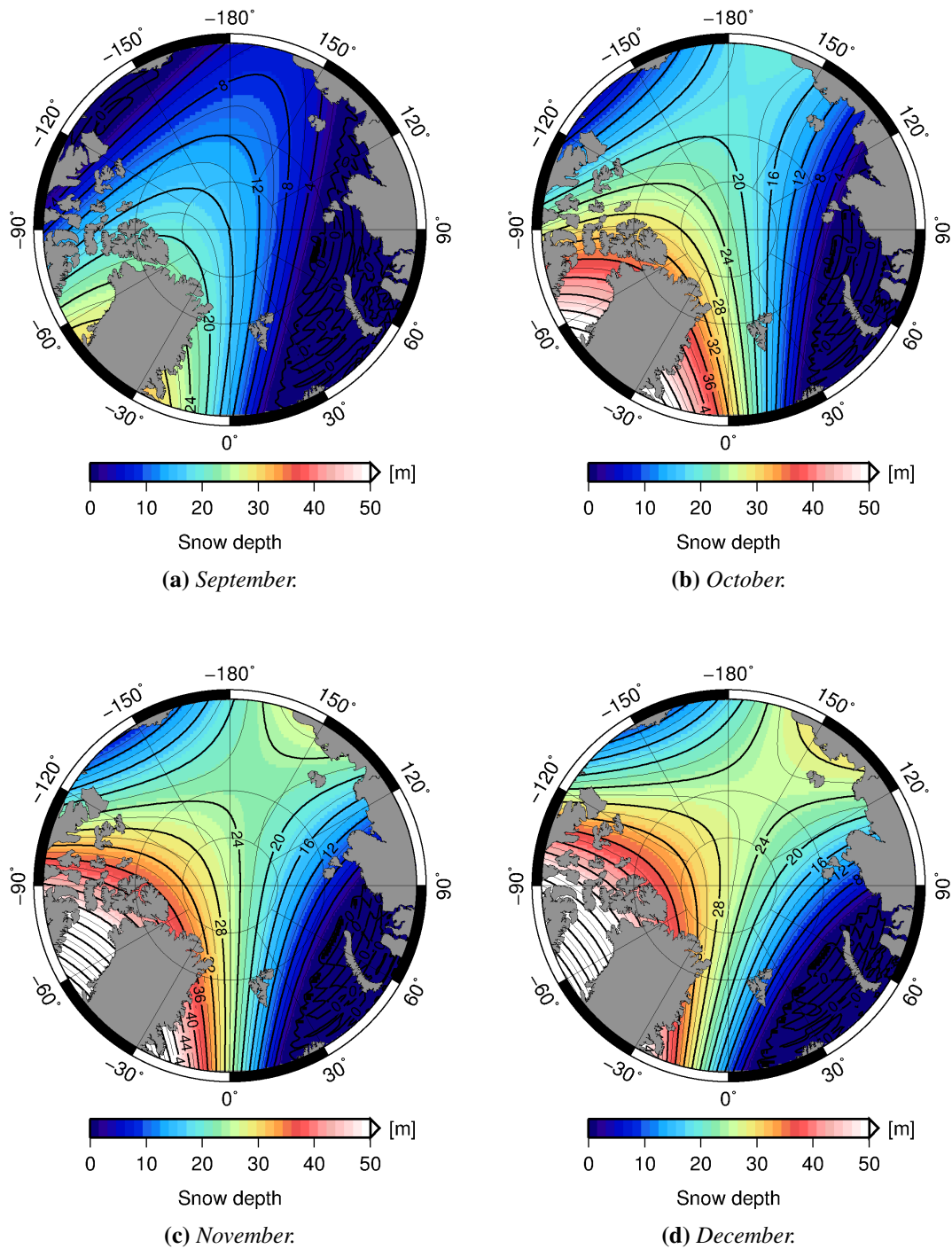


Figure A.0.2: Snow depths from *Warren et al. [1999]* climatology from September to December.

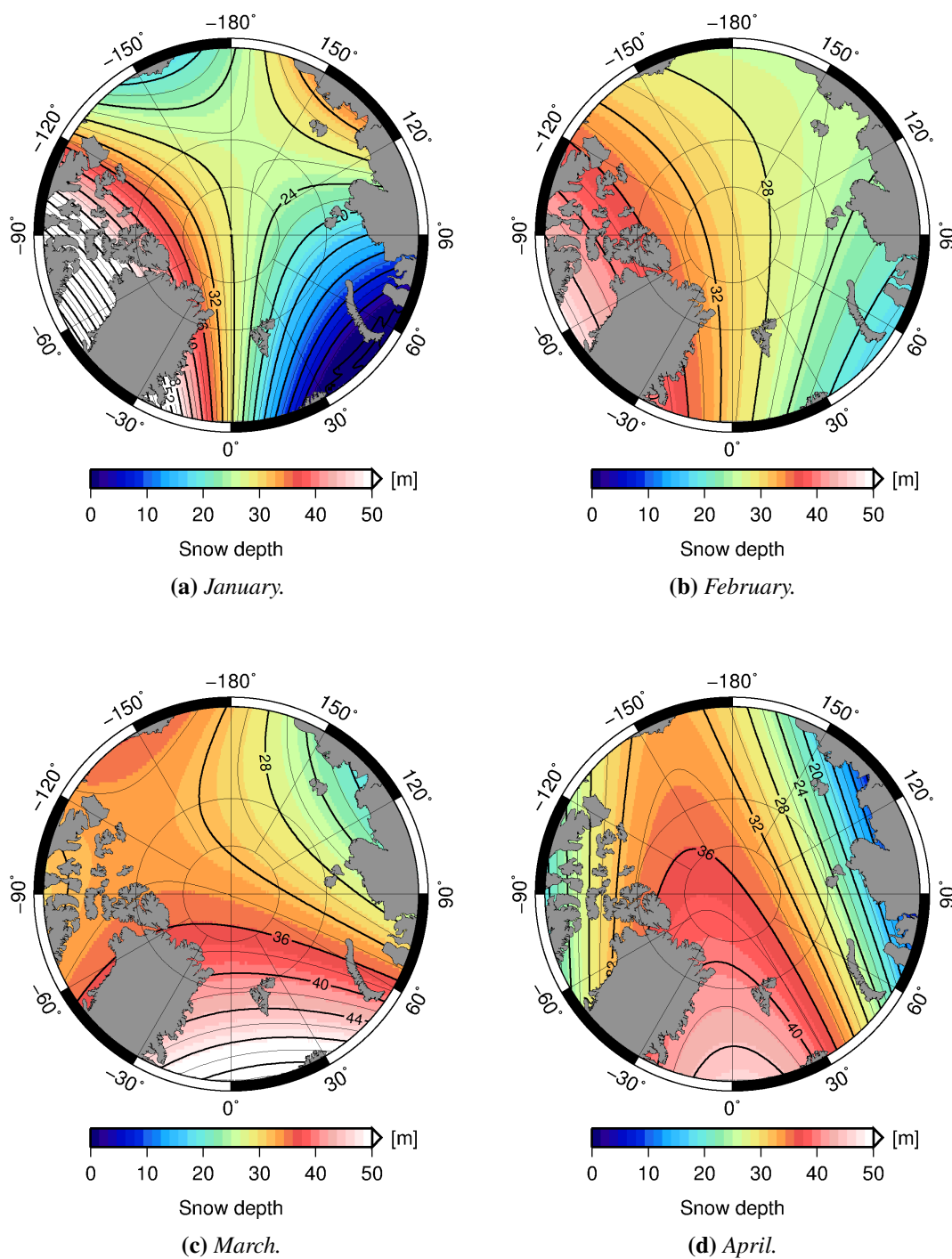


Figure A.0.3: Snow depths from Warren *et al.* [1999] climatology from January to April

Appendix B

Statistics

B.1 Standard Deviation of the Mean

The normal approach for determine the freeboard error Eq. 8.1.4 in Section 8.1.1, with many measurements are to use the regular expression of the standard deviation of the mean given by

$$\sigma_{\overline{fb}} = \frac{\sigma_{fb}}{\sqrt{N}} , \quad (B.1.1)$$

where σ_{fb} is the standard deviation of the measurements and N is the number of measurements. From this equation it is obvious that raising the number of measurements will lower the freeboard error. The error include uncertainties of the geophysical corrections (Section 7).

B.2 A Skew Distribution

The skewness of the distribution is in this thesis defined following the definition in [Dean and Illowsky \[2012\]](#), where a negative skew is defined as: The left tail is longer, and the mass of the distribution is concentrated on the right of the figure. It has relatively few low values. The distribution is said to be left-skewed. Likewise is the positive skewed distribution defines: The right tail is longer, and the mass of the distribution is concentrated on the left of the figure. It has relatively few high values. The distribution is said to be right-skewed. The skew is not necessarily connected to the mean and the median relationship.

B.3 Uncertainty in the Slope

In Section 11.5 the sea ice freeboard and thickness trends are calculated, and for the total trend (six observations) the uncertainty is given.

The linear slope is calculated by a least-squares fit, by the linear relation: $y = ax + b$. Neglecting the uncertainty in x , the uncertainty of the slope a is given by:

$$\sigma_a = \sigma_y \sqrt{\frac{N}{N \sum x^2 - (\sum x)^2}} , \quad (\text{B.3.1})$$

where N is the number of measurements, and σ_y is the uncertainty in y_1, y_2, \dots, y_N :

$$\sqrt{\frac{1}{N-2} \sum_{i=1}^N (y_i - ax_i - b)^2} , \quad (\text{B.3.2})$$

[Taylor, 1997].

Appendix C

Averaging Airborne Data

C.1 Scatter Plots

The Following figures show the results of the comparison of averaged airborne laser scanner (here ATM) and CryoSat elevations. The red curve shows the linear correlation calculated from a robust least square fit. Fig. C.1.1 show the ATM averaging with no interpolation, Fig C.1.2 show the averaged results from the surface method, and Fig. C.1.3 show the results from the nearest neighborhood search. The results are described in Section 10.2.

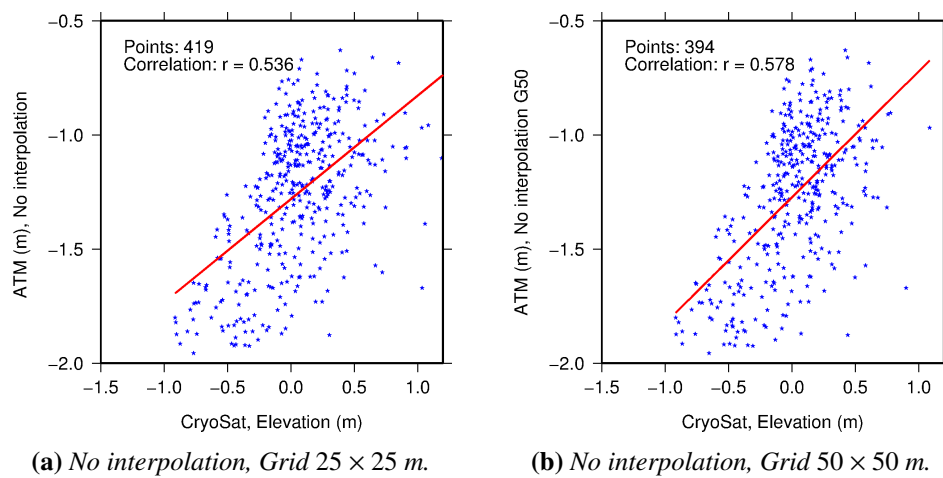


Figure C.1.1: Scatter plots of ATM versus CryoSat. ATM is averaged with the non-interpolation method.

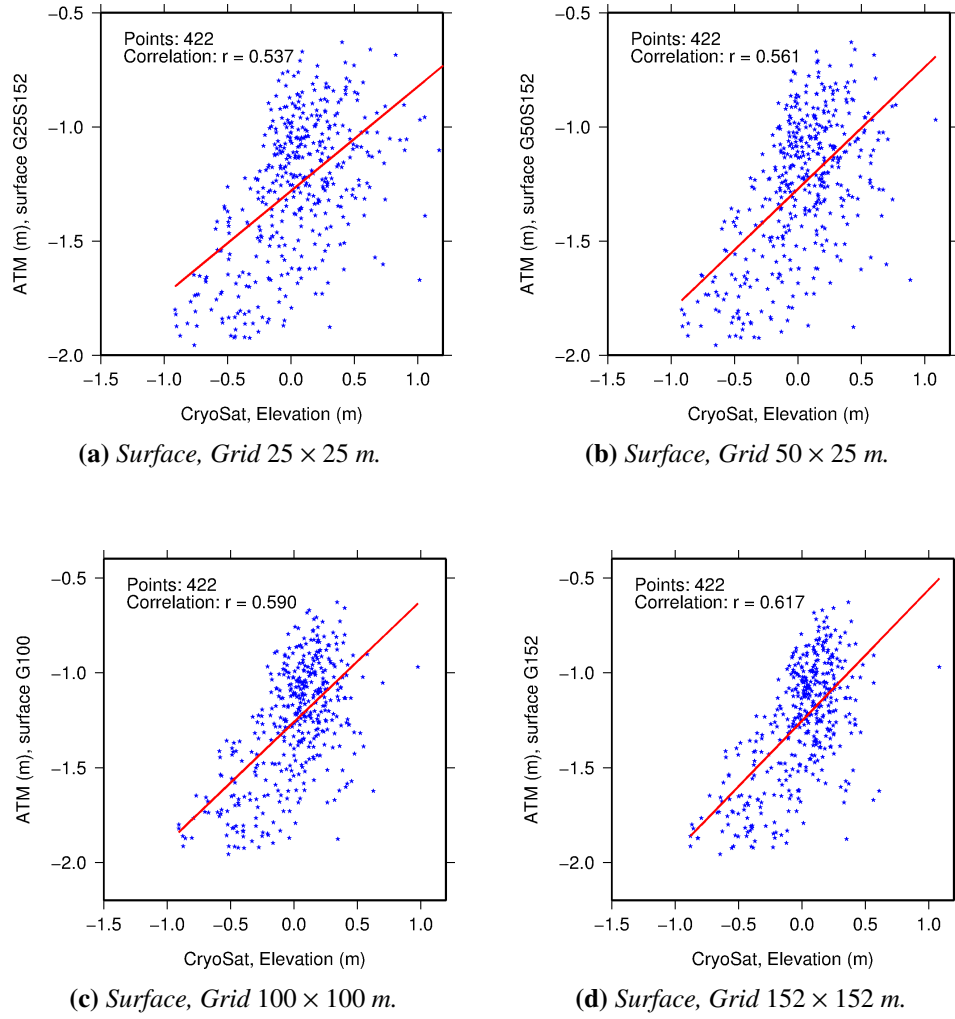
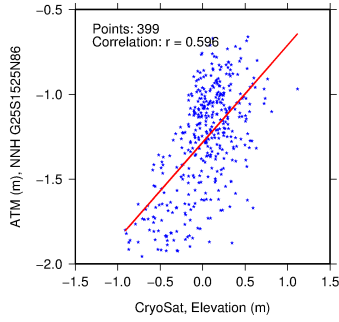
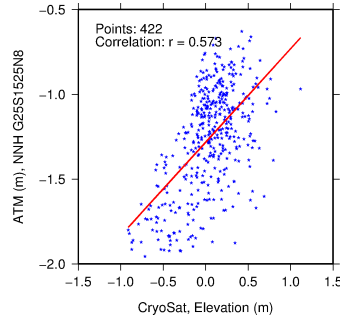


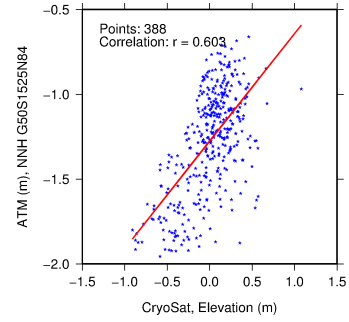
Figure C.1.2: Scatter plots of ATM versus CryoSat. ATM is averaged with the surface method.



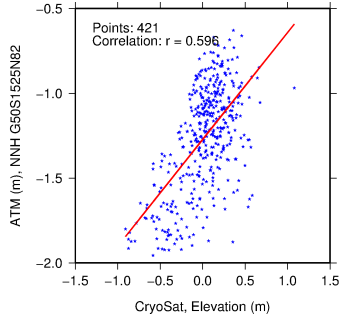
(a) Near neighbor, Grid 25×25 m, No. sectors 8/6.



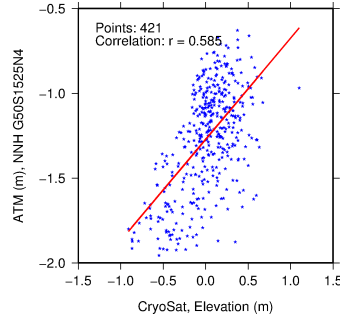
(b) Near neighbor, Grid 25×25 m, No. sectors 8/1.



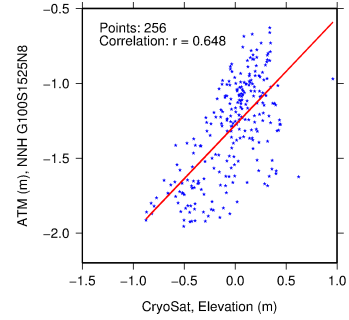
(c) Near neighbor, Grid 50×50 m, No. sectors 8/4.



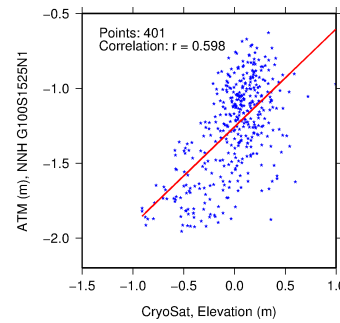
(d) Near neighbor, Grid 50×50 m, No. sectors 8/2.



(e) Near neighbor, Grid 50×50 m, No. sectors 4/1.



(f) Near neighbor, Grid 100×100 m, No. sectors 8/1.



(g) Near neighbor, Grid 100×100 m, No. sectors 1/1.

Figure C.1.3: Scatter plots of ATM versus CryoSat. ATM is averaged with the nearest neighbor method, the search radius is in all cases 152.5 m.

Appendix D

CryoSat Elevation Analysis

D.1 Ice Drift

This appendix show results from Section 10.4.

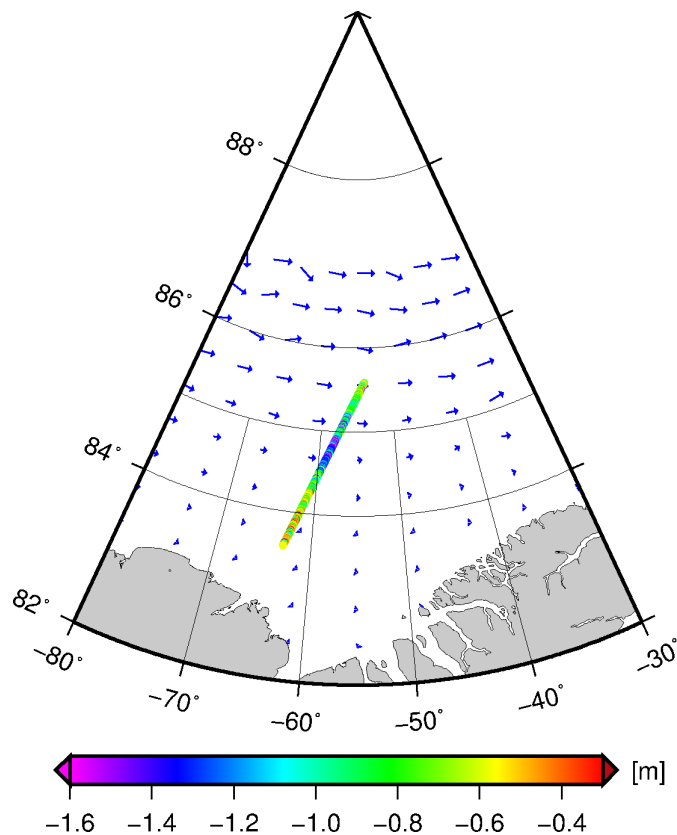


Figure D.1.1: Ice drift in the period between IceBridge and CryoSat overflights. Generated from ASAR images. The arrow length indicates the size of the drift given in km. CryoSat elevation in study area is also shown in the plot.

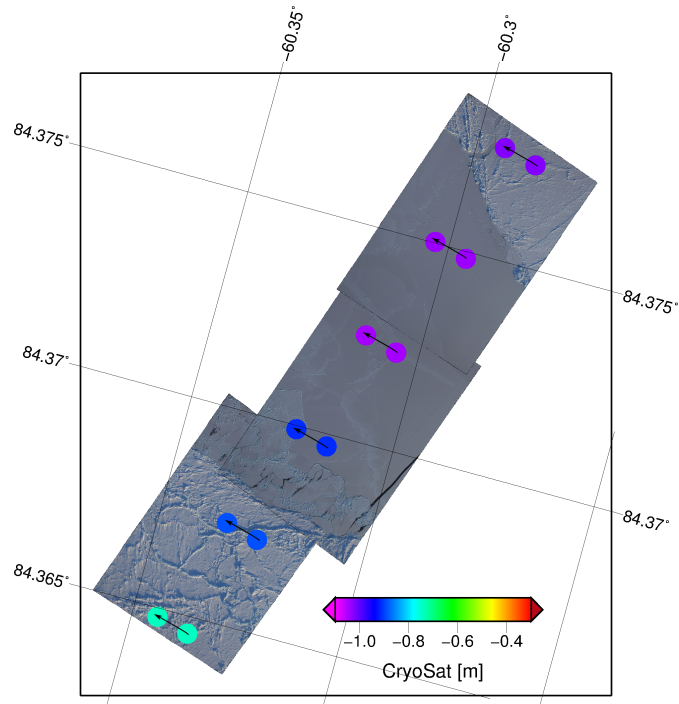


Figure D.1.2: *CryoSat drift based on ASAR drift vectors.*

D.2 CryoSat Elevations over Leads

In Section 10.5 CryoSat elevations are described in details in a small track (see ASAR image Fig. D.2.1) of orbit 10520 April 2, 2012. The leads not described in the section are shown here in Fig. D.2.2, Fig. D.2.3, Fig. D.2.4, Fig. D.2.5 and Fig. D.2.6. The CryoSat elevations are corrected for drift corresponding to the ASAR drift vectors.

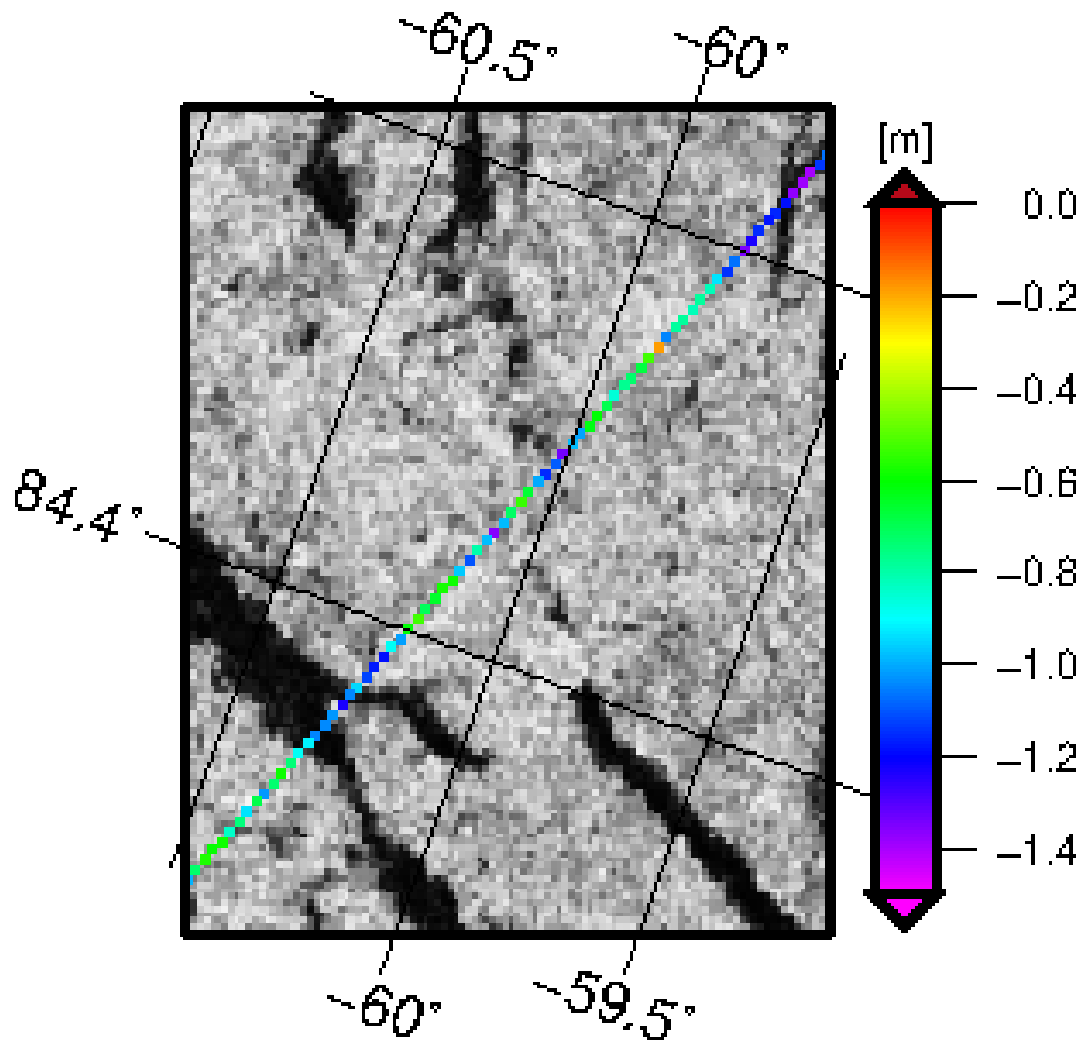


Figure D.2.1: CryoSat elevations are overlaid a zoom of a ASAR image from April 2, 2012 17:51.

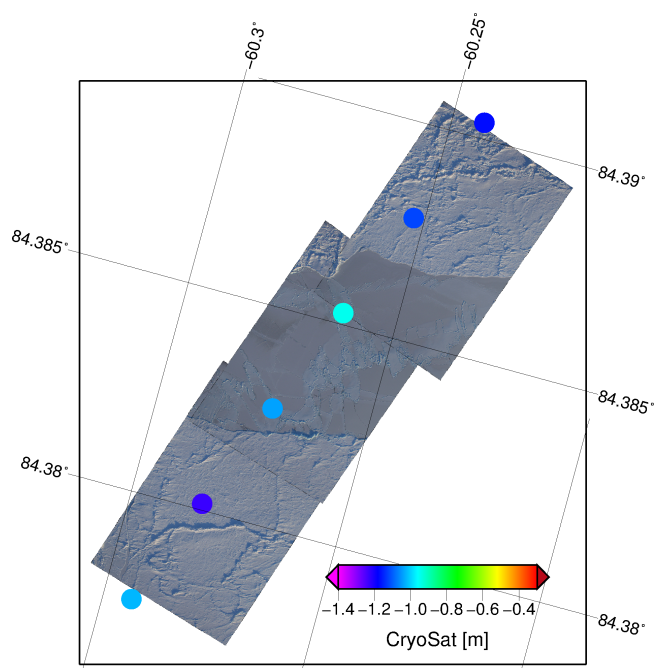


Figure D.2.2: CryoSat elevations on top of DMS images from April 2, 2012 at 12:42:17, 12:42:21, 12:42:24 o'clock. The lead is refrozen and with snow on top, there is also ridges and fractures in the lead.

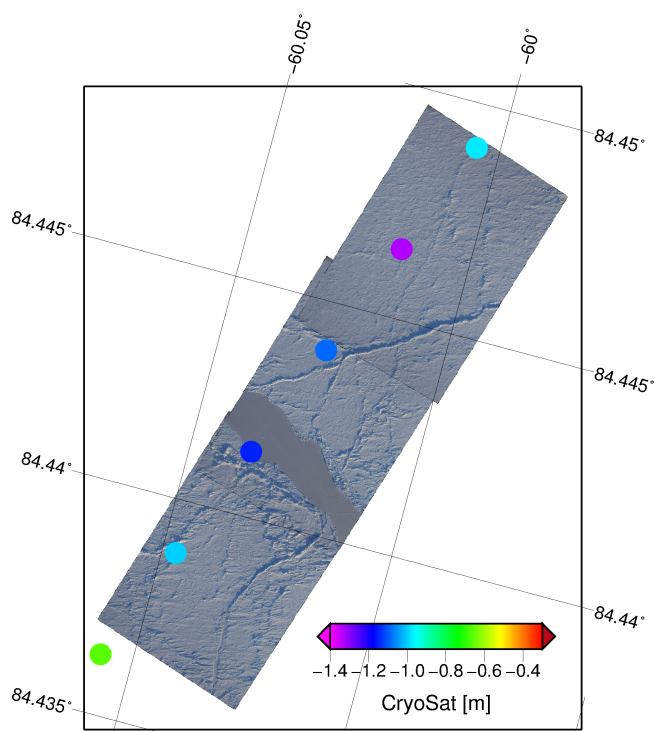


Figure D.2.3: CryoSat elevations on top of DMS images from April 2, 2012 at 12:43:15, 12:43:18 and 12:43:22 o'clock. The lead is a small refrozen lead with a smooth snow layer.

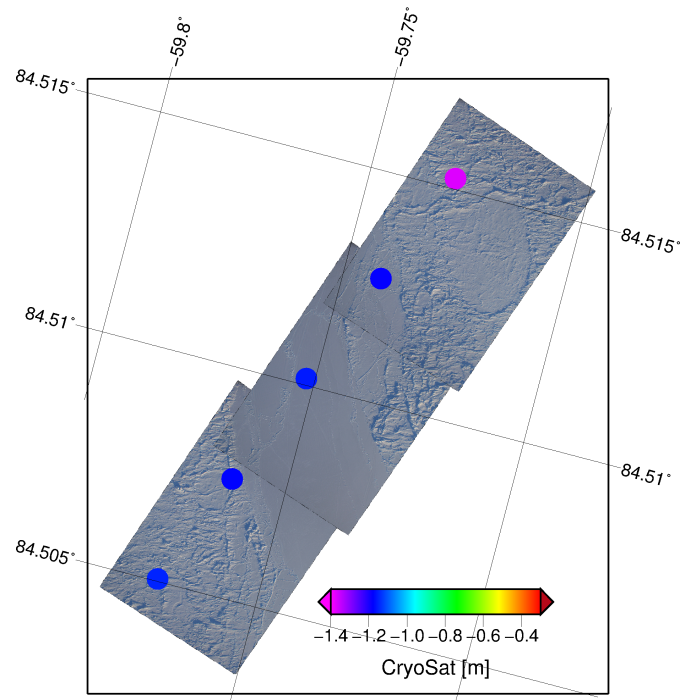


Figure D.2.4: CryoSat elevations on top of DMS images from April 2, 2012 at 12:44:21, 12:44:24 and 12:44:28. Refrozen lead with snow and ridges.

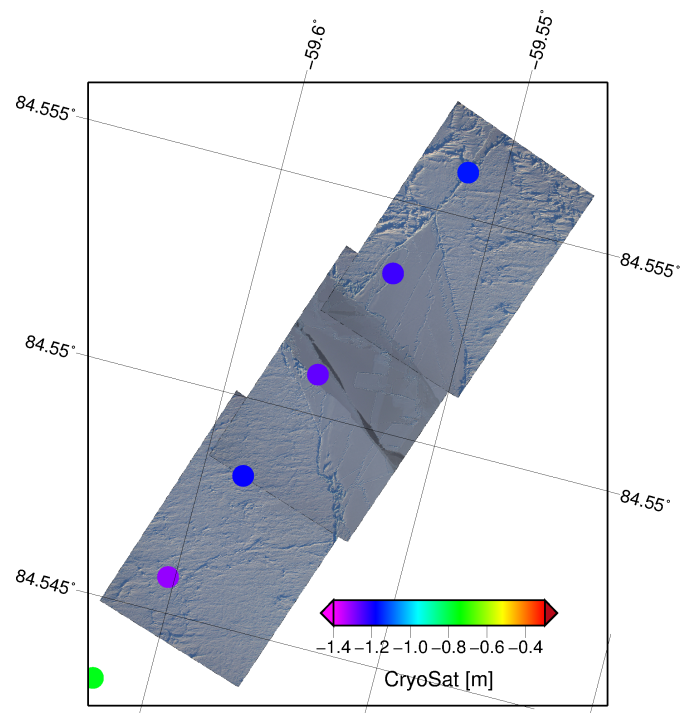


Figure D.2.5: CryoSat elevations on top of DMS images from April 2, 2012 at 12:45:00, 12:45:04 and 12:45:07. Most of the lead is refrozen with snow layer and ridges, but the lead also has a crack with thin refrozen ice.

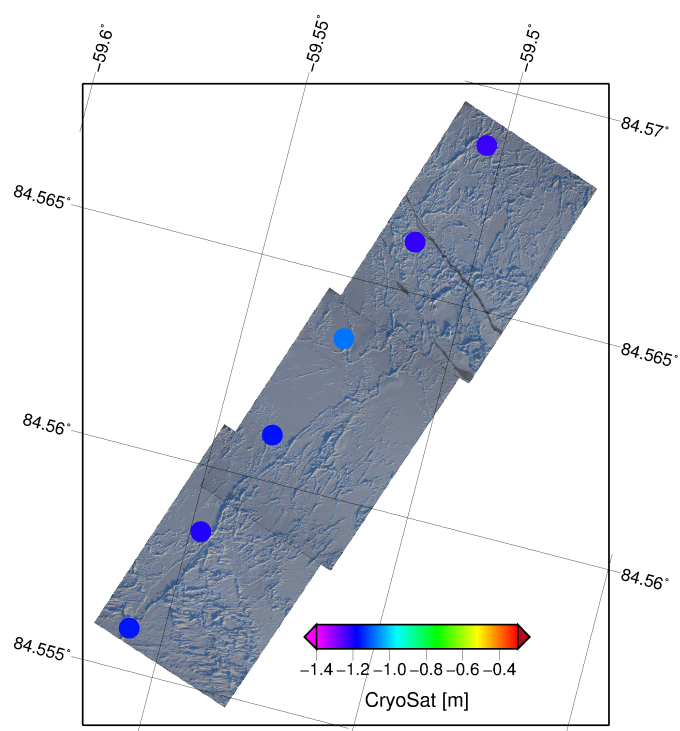


Figure D.2.6: CryoSat elevations on top of DMS images from April 2, 2012 at 12:45:11, 12:45:15 and 12:45:19. This is an area with many small fractures, and what seems to be old leads.

Sea Ice Map from CryoSat

E.1 Retracking Gate

The retracking gate described in Section 11.1.1 for leads only in Fig. E.1.1(a), and for ice floes Fig. E.1.1(b).

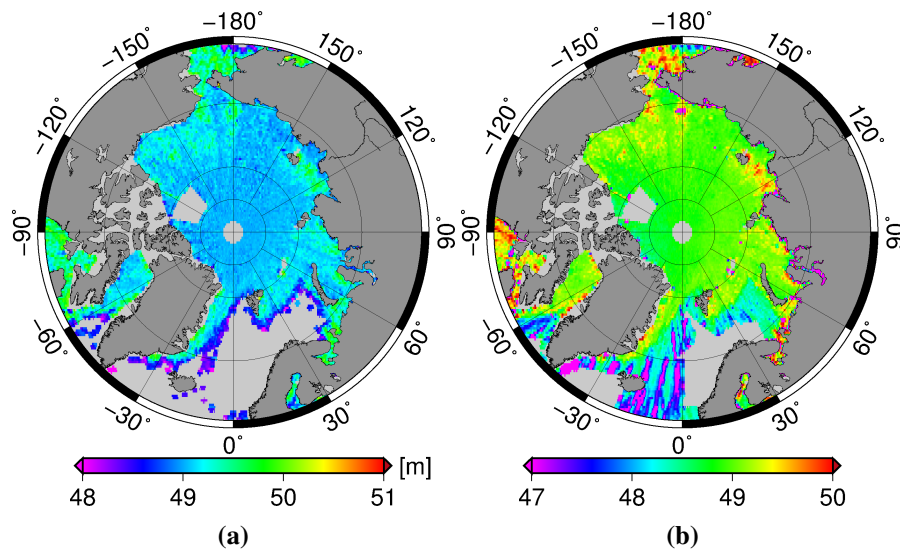


Figure E.1.1: Map of (a) retracking gate of leads and (b) floes in the CryoSat SAR data from March 2013, after the first filtering step.

E.2 Number of Points in Grid

The next two figures show the number of points in each grid cell for leads (Fig. E.2.1) and for all data in Fig. E.2.2. Notice the different color scales. These figures are described in Section 11.1.2.

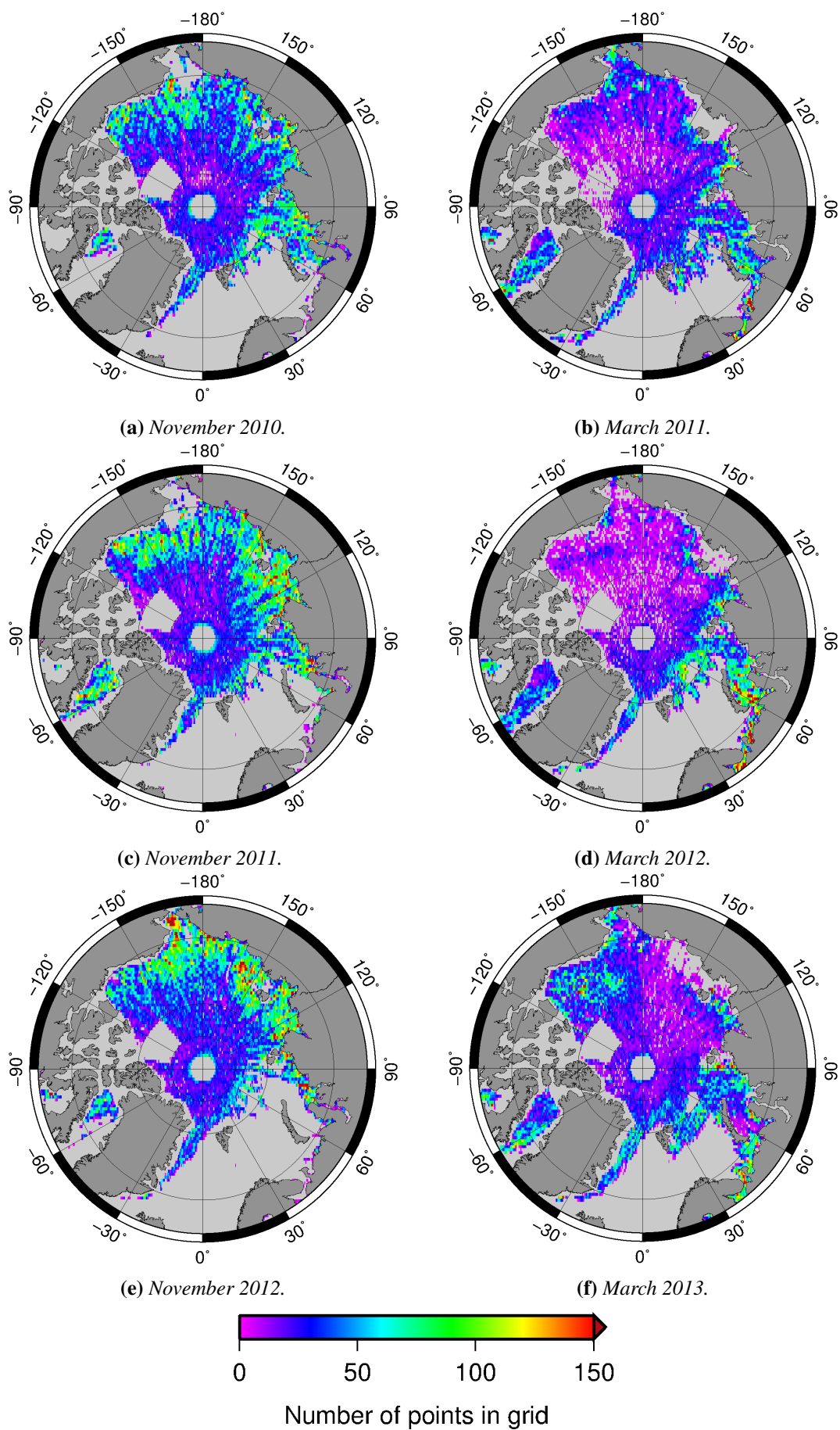
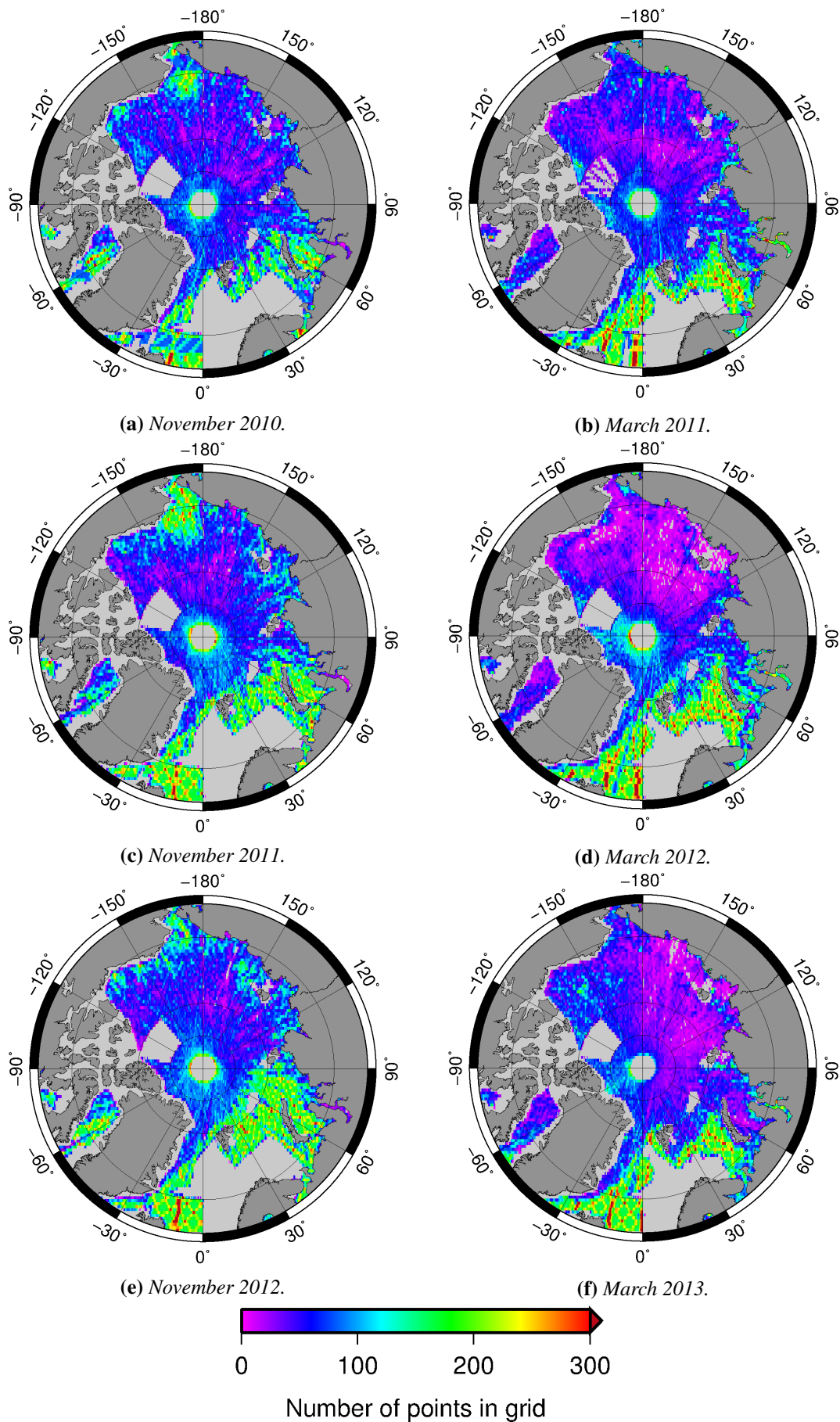


Figure E.2.1: Number of points in each lead grid cell.

**Figure E.2.2:** Number of total points in each grid cell.

E.3 Ice Conditions

The figures below are a supplementary to Section 11.5.3.

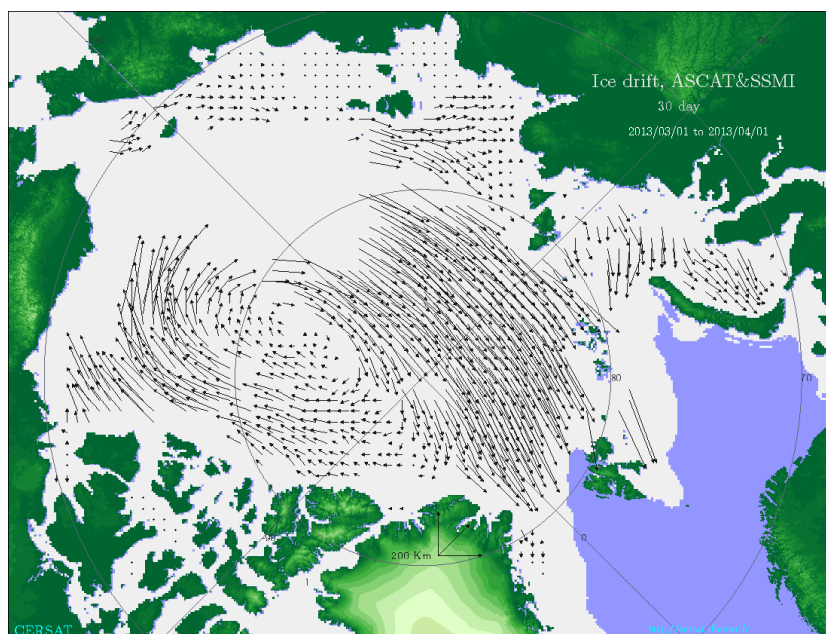


Figure E.3.1: Drift pattern in the Arctic Ocean from March 2013. With courtesy: IFREMER (French Institute for Exploration of the Sea).

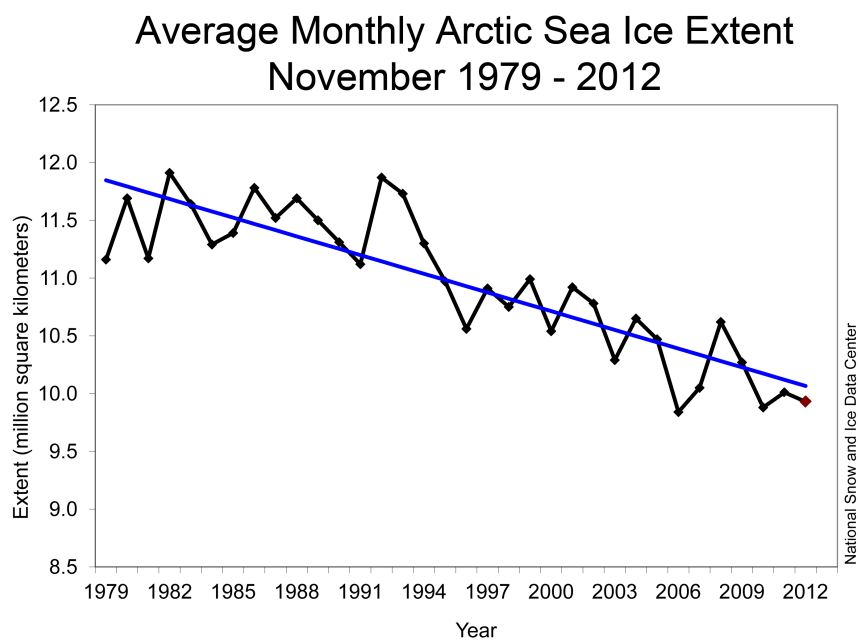


Figure E.3.2: Average sea ice extent for November. Credit: NSIDC.

E.4 Ice Edge Detection Maps

Data are described in Section 5.3 and used in Section 11.3.1.

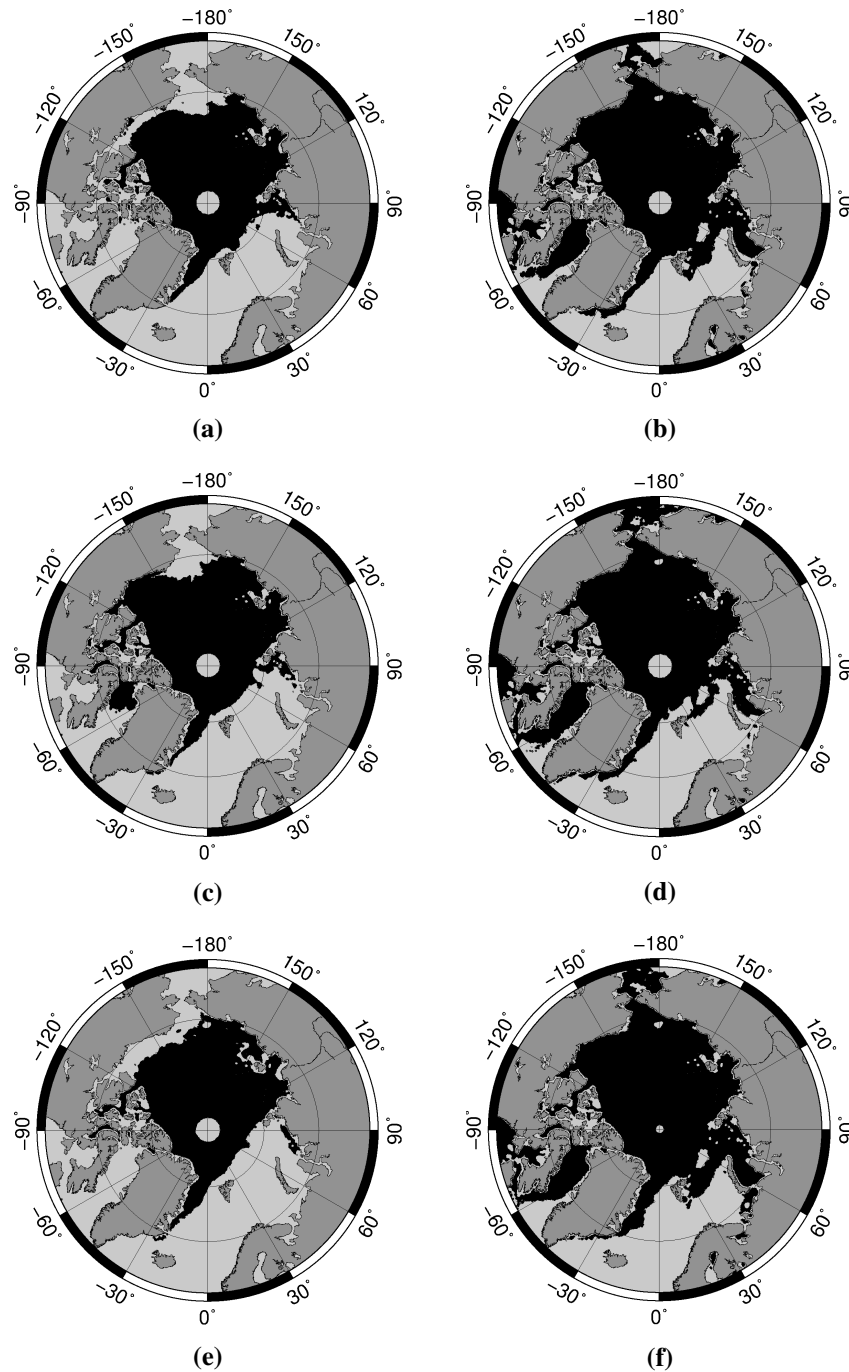


Figure E.4.1: The black color show the sea ice edge for (a) November, 1 2010, (b) March, 15 2011, and (c) November, 6 2011, (d) March, 17 2012, (e) November, 3 2012, (f) March, 15 2013. Data are from the Norwegian Meteorological Service OSI SAF system.

E.5 Ice Type Detection Maps

Data are described in Section 5.3, and used in Section 11.4.

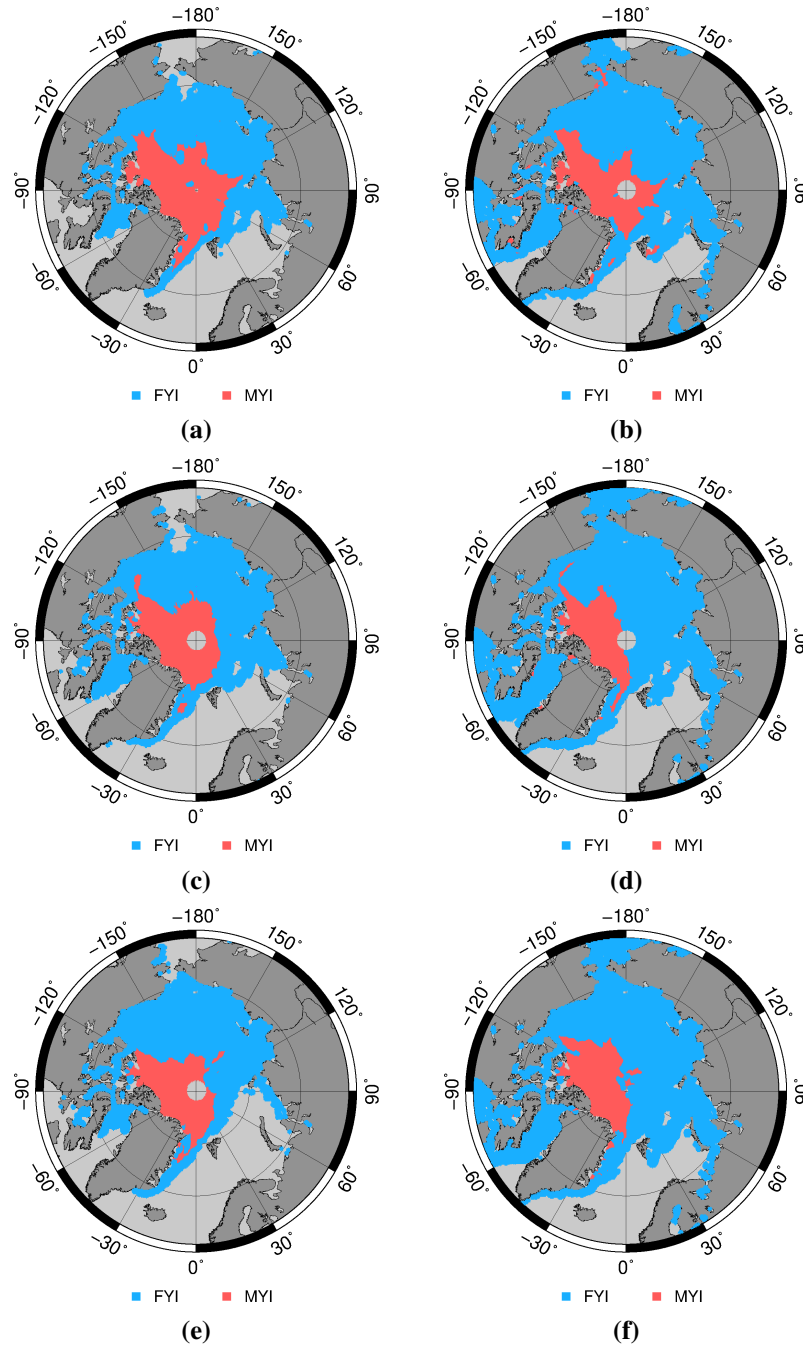
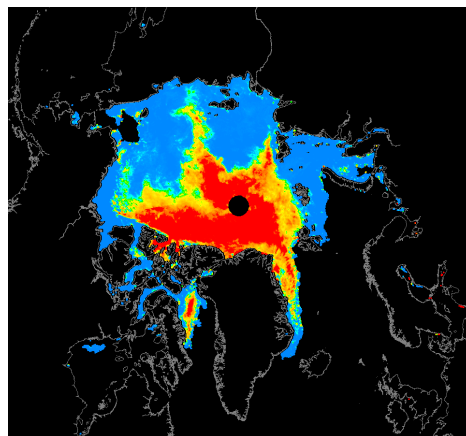
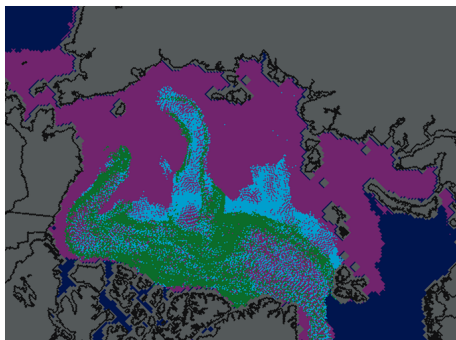


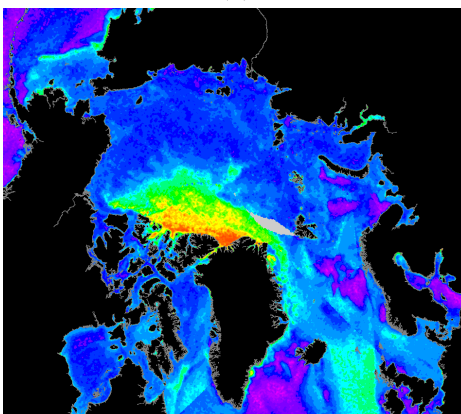
Figure E.5.1: Sea ice types; multi-year ice (MYI) is blue and first-year (FYI) ice is red. (a) November, 14 2010, (b) March, 2 2011, and (c) November, 17 2011, (d) March, 2 2012, (e) November, 15 2012, (f) March, 3 2013. Data are from the Norwegian Meteorological Service OSI SAF system. Multi-year ice (MYI) is blue and first-year (FYI) ice is red.



(a)



(b)



(c)

Figure E.5.2: Multi-year ice cover from (a) AMSR November, 30 2010, (b) mean sea ice age for March 2011, credit: NSIDC and (c) multi-year ice coverage from OSCAT on March 16, 2013.

Appendix **F**

Scientific Papers

F.1 Initial Results of CryoSat-2 Data from the Arctic

INITIAL RESULTS OF CRYOSAT-2 DATA FROM THE ARCTIC

Stine Kildegaard Poulsen^{1*}, Lars Stenseng², Henriette Skourup¹, Leif Toudal Pedersen³, Rene Forsberg¹, and Louise Sandberg Sørensen¹

¹Div. of Geodynamics, DTU Space, National Space Institute, Juliane Maries Vej 30, 2100 Copenhagen, Denmark.

²Div. of Geodesy, DTU Space, National Space Institute, Juliane Maries Vej 30, 2100 Copenhagen, Denmark.

³Danish Meteorological Institute, Lyngbyvej 100, 2100 Copenhagen, Denmark.

*stine@space.dtu.dk

ABSTRACT

We examine SAR L1b data from the commissioning phase, currently available for the calibration and validation teams. We use CryoSat-2 data to detect leads in the sea-ice in an area north of Svalbard. Furthermore, we classify the sea-ice from computed freeboard values, and evaluate the coherence between the SAR backscatter and the CryoSat-2 data. The surface elevation is extracted from an 80% threshold retracker and a five parameter β -retracker, and this is given with respect to the DTU10 Mean Sea Surface model (MSS). The results are compared with an Envisat ASAR image, and we show that there is a strong correspondence between the freeboard heights and the leads visible in the ASAR image.

Key words: CryoSat-2, sea-ice, freeboard, leads, retracking, Envisat ASAR.

1. INTRODUCTION

CryoSat-2 is aimed at observing changes in the Earth's cryosphere, i.e. changes in the ice- and snow-covered parts of the Earth. The satellite was launched on 8 April 2010, it has an inclination angle of 92° and a mean altitude of 717 km. CryoSat-2 is carrying the SIRAL instrument, which is a radar altimeter, able to measure in SAR mode over sea-ice, interferometric mode (SARin) over rapidly varying topographic features on the ice sheet margins, and low-resolution mode (LRM) over the interior of the ice sheet and over ocean.

Due to large errors in the sea-ice freeboard determination from satellite altimetry [1, 2, 3, 4], validation of the satellite data is necessary.

1.1. CryoVEx

DTU Space is part of the CryoSat Calibration and Validation team (CryoVEx), the object of which is to provide

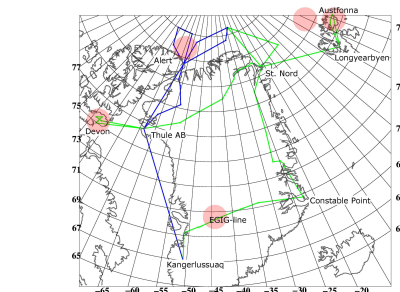


Figure 1. CryoVEx 2011 main sites (red dots). The work will be carried out during April and early May. The green and blue lines are the planned flying routes.

vide pre-launch and post-launch reference datasets for CryoSat-2. We undertake measurements of ice sheet elevations and sea-ice thicknesses, and make ice profiles from the measurements. The CryoVEx campaign is in particular aimed at understanding miscellaneous sources of error: snow loading, ice density, radar penetration, preferential sampling and various freeboard measurement errors. CryoVEx is a joint effort of ESA, DTU Space and other European and Canadian research groups.

Extensive validation campaigns to gather a multitude of ground truth measurements were carried out in the Arctic, prior to the launch of the first CryoSat mission and is now continuing for CryoSat-2. The campaigns consist of airborne radar and laser altimetry, EM sounding, and in-situ observations. The CryoVEx 2011 Arctic campaign will be carried out during April and early May, see [5]. Underflights of CryoSat will be performed together with overflights of ground teams performing in-situ measurements. The main sites are shown in red in Figure 1, and are covering sea-ice near Alert, and north of Svalbard (coordinated with RV Lance cruise), and continental ice at the EGIG line in central Greenland, Devon Ice Cap in Canada, and Austfonna on Svalbard. The airborne surveying will be carried out from a Twin Otter carrying radar and laser altimeters observing the surface elevation,

and with the German Polar 5 (DC3) using EM sounding to measure the total sea ice thickness.

1.2. Retracking

Retracking of altimetry data is performed by estimating the departure of the waveforms leading edge from the altimeter tracking gate, and correcting the satellite range measurement accordingly. The shape of the return radar echo must be analyzed more thoroughly. The shape of the returned radar echo is a combination of the range to the different illuminated reflectors, their scattering properties and their position within the antenna beam pattern. The complexity of the returned echo is therefore related to the complexity of the entire illuminated surface. Finally, the return echo is affected by thermal and speckle noise as well as the impulse response of the radar.

There exist two methods of waveform retracking; physical and empirical methods. The physically-based retracers are computed from physical models, the knowledge of microwave scattering at nadir. They often include the Brown-type waveforms as a convolution of the average impulse response from a flat surface, the surface elevation probability density function of specular points within the altimeter footprint, and the radar system point target response. The method is described in more details in [6]. This type of retracking is often more comprehensive than the empirical methods. Furthermore, the Brown-model does not deal properly with the geometry of ice surfaces, [7]. The empirical methods can be divided into statistical based properties and those based on fitting empirical functions to the waveform. The offset centre of gravity (OCOG) retracking is of the statistical kind, developed by [8], and it is a simple, robust method which is easy to implement. In short, the principle of the OCOG retracker is to define a rectangle about the centre of gravity of the waveform, calculate the amplitude and the width of the waveform. The resulting output is the position of the leading edge. The threshold retracker was first developed by [9], initially intended for measuring ice-sheet elevations. The position of the leading edge of the return waveform is derived by locating the first range bin to exceed a percentage of the maximum waveform amplitude. This can be achieved by the OCOG amplitude. For complex waveforms the OCOG and the threshold retracker cannot determine the surface ranging gate properly. This is improved by [10, 11]. The β -retracker, developed by [12], is a fitting algorithm given with 5- or 9-parameter functional form of the returned power, to fit single or double-ramped waveforms, respectively. The Ice Altimetry Group at NASA's Goddard Space Flight Centre (GSFC) has developed a series of retracing algorithms for ice-sheet and sea-ice waveforms based upon this method. An empirical CryoSat retracker built to replicate the theoretical model of a multilooking SAR altimeter echo is developed by [13] and simplified by [3].

In this paper, we present initial results of lead detection in sea-ice from CryoSat-2 commissioning phase L1b SAR

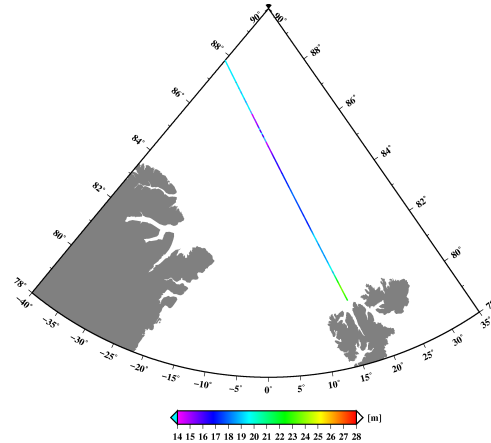


Figure 3. Location map of CryoSat-2 track used in this study from the 10th of October 2010. The height is given directly from the threshold retracker, without reference to DTU10 MSS.

data. Data are retracked with an 80% threshold retracker and a five parameter β -retracker. The threshold retracker showed the best results. Furthermore, freeboard values are calculated by comparison to an interpolation of the DTU10 Mean Sea Surface (MSS) model [14], described in connection with CryoSat-2 in [15]. The results are compared with an Envisat ASAR image, which shows good agreement with the CryoSat-2 track.

2. METHODS

In this study, SAR L1b CryoSat-2 data from the October 10th, 2010, starting at 19:08:00 UTC, was used. The ascending track was located north of Svalbard. We have picked out data from echo number 1300 to 1800, which was without too much noise. The beginning of the whole track, is shown in Figure 3.

We used both an 80% threshold retracker, where the position of the leading edge was determined with an OCOG retracker, and a five parameter β -retracker, see more in [16].

The elevation is given with respect to the DTU10 MSS model [14], which includes the mean dynamic topography and the geoid. Furthermore, we have used a lowest level least square collocation filtering procedure [17] to detect the local sea surface heights from the altimetry.

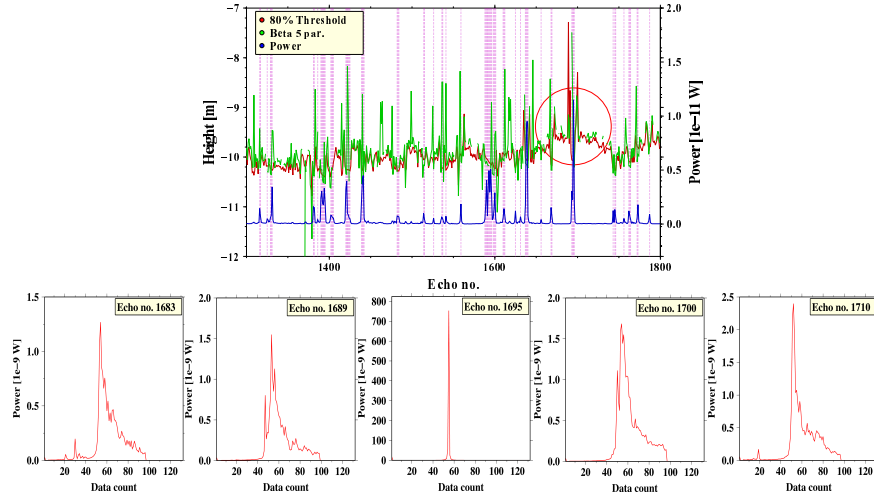


Figure 2. Top: The height plotted against the echo number computed from the 80% threshold retracker (red), the five parameter β -retracker (green), and the power (blue). The red horizontal lines indicate areas where the power strikes out and an open lead could occur. Bottom: Power waveforms showing rough ice (echo 1683), very rough ice (echo 1689), very smooth surface i.e. water (echo 1695), very rough ice or a wet snow layer over the ice is present (echo 1700) and rough ice (echo 1710), properly multi-year ice.

3. SEA-ICE NORTH OF SVALBARD, FALL 2010

In Figure 2, the resulting elevations from the retracked sea-ice elevation from CryoSat-2 data with respect to DTU10 MSS, are shown in the top. The red curve is the results from the 80% threshold retracker, and the green curve is from the five parameter β -retracker. The mean elevation of the threshold and the β -retracker are -10.16 m and -9.78 m, respectively, with a standard deviation of 0.96 m and 18.44 m, respectively.

It is clear, that the threshold retracker is less noisy and therefore, this is chosen in the further analysis. The β -retracker needs more constrains, to be reliable. The blue curve shows the power as a function of the echo, and the red horizontal lines indicates high power echoes, i.e. area with the possibility to detect leads. High power could resemble high backscatter and a smooth surface, e.g. slack water (here open lead), or new ice. There is no characteristic lower level in the elevations, as we would have expected. This is due to strong noise in the data. The figure shows a large offset in the retracking height of about -10 m. This could be due to instrument delays, wrong geophysical corrections in the datafile and/or errors in the supplied corrections.

The five power waveforms plotted in the bottom of Figure 2, correspond to echoes plotted in the red circle in Figure 2 and 4. A clear difference in the waveforms, corresponding to the varying surface is seen. The first and the last waveforms look similar to a conventional waveform over

a rough surface. The maximum power is lower here, than in the waveform in the middle, and the trailing edge decreases relatively sharply, which indicates that the surface is over open water. The high spiked waveform in the middle of the figure, is most likely a return from a very smooth surface. It could be a lead, where the water is quiet in between the ice floes. The second and forth waveforms, are waveforms from a more complex surface, showing returns from more than one surface.

Figure 4, shows an Envisat ASAR 100 resolution image from October 10, at 19:17 UTC. Based on the knowledge of the ice conditions in this region before summer, and the derived freeboard heights of 0.1 to 1.1 m, we assume the ice is multi-year ice, measuring 1.5 - 3 m in thickness. The CryoSat-2 track is delayed nine minutes compared to the image, i.e. assuming no movements in the ice. The height is extracted from the 80% retracker, and interpolated to the local sea surface. There is a clear correspondence between the freeboard heights and the leads visible in the ASAR image as black features. Furthermore, the freeboard is large around the leads, probably resembling pressure ridges. See the marked areas in Figure 4.

4. CONCLUSION AND OUTLOOK

The SAR CryoSat-2 track was compared with an Envisat ASAR image, and it showed good agreement. It was possible to detect leads, and they were verified by waveforms around the lead. This work will be improved

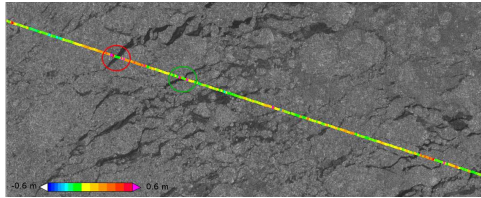


Figure 4. Freeboard calculated from the CryoSat-2 line plotted on an Envisat ASAR 100 m resolution image from October 10 at 19:17 UTC.

with more investigation into data after the commissioning phase, and further enhancements of the retracking procedure will be undertaken. Finally, we will need validation of the satellite data, to rely on the results. This will be achieved after the 2011 CryoVEX campaign.

5. ACKNOWLEDGMENTS

The authors would like to thank ESA and the CVRT team for the huge efforts

REFERENCES

- [1] DA Rothrock. Ice thickness distribution-measurement and theory. *The geophysics of sea ice*, pages 551–575, 1986.
- [2] P. Wadhams, WB Tucker III, WB Krabill, RN Swift, JC Comiso, and NR Davis. Relationship between sea ice freeboard and draft in the Arctic Basin, and implications for ice thickness monitoring. *Journal of Geophysical Research*, 97(C12):20325, 1992.
- [3] KA Giles, SW Laxon, DJ Wingham, DW Wallis, WB Krabill, CJ Leuschen, D. McAdoo, SS Manizade, and RK Raney. Combined airborne laser and radar altimeter measurements over the Fram Strait in May 2002. *Remote Sensing of Environment*, 111(2-3):182–194, 2007.
- [4] RT Tonboe, LT Pedersen, and C. Haas. Simulation of the satellite radar altimeter sea ice thickness retrieval uncertainty. *Can. J. Remote Sensing*, 36(1):55–67, 2010.
- [5] H. Skourup, S. Hanson, S. M. Hvidegaard, R. Forsberg, S. K. Poulsen, E. M. Morris, L. S. Sørensen, and L. Stenseng. Airborne Campaigns for CryoSat prelaunch calibration and validation. In *ESA CryoSat Validation Workshop*, February 1-3 2011.
- [6] G. Brown. The average impulse response of a rough surface and its applications. *Antennas and Propagation, IEEE Transactions on*, 25(1):67–74, 1977.
- [7] X. Deng. *Improvement of Geodetic Parameter Estimation in Coastal Regions from Satellite Radar Altimetry*. PhD thesis, Curtin University of Technology, 2003.
- [8] DJ Wingham, CG Rapley, and H. Griffiths. New techniques in satellite altimeter tracking systems. In *ESA Proceedings of the 1986 International Geoscience and Remote Sensing Symposium (IGARSS'86) on Remote Sensing: Today's Solutions for Tomorrow's Information Needs*, volume 3, 1986.
- [9] CH Davis. A robust threshold retracking algorithm for measuring ice-sheet surface elevation change from satellite radar altimeters. *Geoscience and Remote Sensing, IEEE Transactions on*, 35(4):974–979, 2002.
- [10] C. Hwang, J. Guo, X. Deng, H.Y. Hsu, and Y. Liu. Coastal gravity anomalies from retracked Geosat/GM altimetry: improvement, limitation and the role of airborne gravity data. *Journal of Geodesy*, 80(4):204–216, 2006.
- [11] L. Bao, Y. Lu, and Y. Wang. Improved retracking algorithm for oceanic altimeter waveforms. *Progress in Natural Science*, 19(2):195–203, 2009.
- [12] T.V. Martin, H.J. Zwally, A.C. Brenner, and R.A. Bindshadler. Analysis and retracking of continental ice sheet radar altimeter waveforms. *Journal of Geophysical Research*, 88(C3):1608–1616, 1983.
- [13] DJ Wingham, CR Francis, S. Baker, C. Bouzinac, D. Brockley, R. Cullen, P. de Chateau-Thierry, SW Laxon, U. Mallow, C. Mavrocordatos, et al. CryoSat: A mission to determine the fluctuations in Earth's land and marine ice fields. *Advances in Space Research*, 37(4):841–871, 2006.
- [14] O. B. Andersen and P. Knudsen. The DTU10 global Mean sea surface and Bathymetry. In *Geophysical Research Abstract*, volume 10. European Geophysical Union, 2008.
- [15] O. B. Andersen and P. Knudsen. The DTU10 Mean Sea Surface for and with CryoSat-2. In *ESA CryoSat Validation Workshop*, February 1-3 2011.
- [16] L. Stenseng and O. B. Andersen. First Results of Recovery of Short Wavelength Gravity Field Signals from CryoSat-2 Data. In *ESA CryoSat Validation Workshop*, February 1-3 2011.
- [17] Henriette Skourup. *A study of Arctic sea ice freeboard heights, gravity anomalies and dynamic topography from ICESat measurements*. PhD thesis, University of Copenhagen, 2009.

F.2 Arctic Tides from GPS on sea ice



Arctic tides from GPS on sea-ice

S.K. Rose*, H. Skourup, R. Forsberg

Geodynamics Department, DTU Space National Space Institute, Juliane Maries Vej 30, 2100 Copenhagen, Denmark

ARTICLE INFO

Article history:

Received 29 February 2012

Received in revised form 24 August 2012

Accepted 14 September 2012

Available online 24 September 2012

Keywords:

Tides

GPS

GPS buoy

AOTIM-5

Tide model

Reference systems

North of Greenland

ABSTRACT

The presence of sea-ice in the Arctic Ocean plays a significant role in the Arctic climate. Sea-ice dampens the ocean tide amplitude with the result that global tidal models perform less accurately in the polar regions. This paper presents, a kinematic processing of global positioning system (GPS) placed on sea-ice, at six different sites north of Greenland for the preliminary study of sea surface height (SSH), and tidal analysis to improve tide models in the Central Arctic. The GPS measurements are compared with the Arctic tide model AOTIM-5, which assimilates tide-gauges and altimetry data. The results show coherence between the GPS buoy measurements, and the tide model. Furthermore, we have proved that the reference ellipsoid of WGS84, can be interpolated to the tidal defined zero level by applying geophysical corrections to the GPS data.

© 2012 Elsevier Ltd. All rights reserved.

1. Introduction

Satellite altimetry is the most widely used method for mapping the ocean tides. The satellite most used for this purpose is TOPEX/Poseidon (T/P), and from these data many global tidal models are computed in the satellite sampling area. T/P measures sea-level of the ice-free ocean to an accuracy of 3.3 cm (Andersen et al., 1995; Shum et al., 1997). In the polar regions, satellite altimetry data are very limited due to the satellite's latitude range. T/P has a turning latitude of $\sim 66^\circ$ while other radar altimetry satellites, such as GEOSAT and ERS-1/2, have higher turning latitudes of $\sim 72^\circ$ and $\sim 82^\circ$, respectively, but these satellites do not directly provide high-quality data when sea-ice is present, and due to pure orbit determinations, the tidal harmonics cannot be resolved well enough (Smith et al., 2000).

It is difficult to measure the ocean tides in the Arctic due to the lack of satellite data and geographically sparse bathymetric and tide gauge data (Ray et al., 2001). Furthermore, sea-ice dampens the ocean tide amplitude, which leads to phase lag in the cotidal amplitude and changes the dynamics of ocean tides and currents (Prinsenber, 1988; Kowalik and Proshutinsky, 1994; Padman and Erofeeva, 2004; Forsberg et al., 2007). In Forsberg et al. (2007) it is shown how the annual cycles in sea-ice and ocean tide constituents correlate negative, and how the global tide models do not respond

on the presence of sea-ice. Following Kowalik and Proshutinsky (1994), the presence of sea-ice cover changes the ocean tidal amplitude by up to 3%, and the phase up to 1 h. Locally this change can be much higher, especially in shallow water. In a study (Prinsenber, 1988), from the western Hudson Bay, it was shown, that the off-shore tidal currents were affected as much as the inshore tidal heights. The diurnal bands were ambiguous, but the semi-diurnal band components were reduced by up to 40%, and occurred earlier during the ice season, where the phase advanced by more than 20 min. In the DTU report (Forsberg et al., 2007), they conclude that the tidal constituents in the Arctic Ocean, is unstable due to seasonal changes and changing ice cover.

There are several tide models available for the Arctic Ocean (e.g. CSR (Eanes and Ray, 1996), FES (Lyard et al., 2006), GOT (Ray, 1999), TOPX (Egbert et al., 1994; Egbert and Erofeeva, 2002), AOTIM-5 (Padman and Erofeeva, 2004), etc.), but none of these models assimilate altimetry data over sea-ice or consider ice-ocean interaction, such as friction (King and Padman, 2005).

In this study, the choice fell at the Arctic Ocean Tidal Inverse Model (AOTIM-5) by Padman and Erofeeva (2004), based on an assessment of the Arctic Ocean tide models by Forsberg et al. (2007), where various tide models were compared with the annual sea-ice cover.

Tidal observations on floating ice from GPS receivers, were carried out in Antarctica (Aoki et al., 2000; King et al., 2000; King and Aoki, 2003). The later study made a tidal harmonic analysis and compared GPS precise point positioning (PPP), with bottom pressure gauge (BPG) observations on floating ice. The vertical difference between GPS and BPG varied with the sea-ice season,

* Corresponding author. Tel.: +45 45259737.

E-mail addresses: stine@space.dtu.dk (S.K. Rose), hsk@space.dtu.dk (H. Skourup), rf@space.dtu.dk (R. Forsberg).

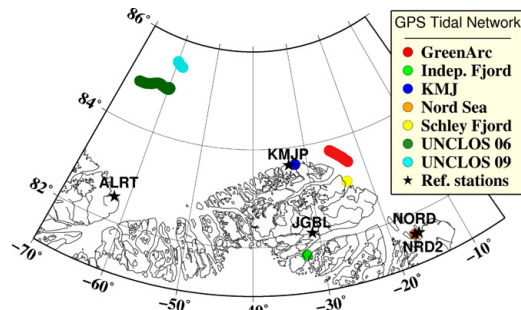


Fig. 1. Location of GPS receivers in the tidal network and their drift. The black stars represent the GPS reference stations Alert (ALRT), Kap Morris Jessup (KMJP), Jørgen Bjørnlund Fjord (JGBL), Station Nord (NORD) and the DTU Space deployed reference station named NRD2.

having a maximum separation in November by 50 cm. Aoki et al. (2000), found a 2 cm accuracy to the sea level variation compared with video monitoring, and a 17.7 cm offset. Comparison of GPS buoys and radar altimetry (from ERS-2) in the Mediterranean Sea, gave a bias in the SSH of 11 cm (Cardellach et al., 2000).

In this paper, we present a kinematic baseline processing of GPS receivers placed on sea-ice, north of Greenland, with differential processing directly to obtain the tidal zero level. Geophysical parameters are applied to the GPS heights to give the SSH, and to compare data to the AOTIM-5 tide model. The differences between the observed tides and the tide model are analyzed. We make an estimate of the contributing geophysical parameters to validate the zero heights. We find, that the GPS data correlate very well with the AOTIM-5 tidal model, and we interpolate by geophysical parameter corrections to the zero height by an offset of 3–52 cm.

This work was carried out as a test study for the ongoing SATICE project, where a long-term tidal network of GPS buoys will be deployed in the Arctic Ocean north of Greenland and northeast of Canada.

2. Methods

In the period from 20 March to 1 May 2009, a GPS network with six receivers was established north of Greenland on drifting sea-ice and on fast ice close to the coast. The locations are shown in Fig. 1, together with a corresponding measurement from a 2006 campaign.

The drifting ice stations were aircraft supported camps for joint Danish–Canadian UNCLOS project in 2006 and 2009 (the two sites north of Alert), and from an interdisciplinary ice camp GreenArc in 2009 (camp north of Greenland), funded as part of the Danish IPY program. The GreenArc camp ice floe broke up early during deployment, and later equipments were rescued by a helicopter operation from Schley Fjord, giving rise to breaks in the GPS data, see Table 1.

The GPS units were Javad and Novatel card receivers provided by DTU Space and the Catalanian Space Institute, respectively. The Spanish instrument in the GreenArc site was a prototype for the future SATICE GPS buoys. The instruments were powered by batteries and solar panels. Due to solar panel and battery failure, no data was recorded from the Schley Fjord station. Table 1 shows information about the stations deployed combined with the GPS units used.

Table 1

Tidal GPS units deployed. The table contains the site name, GPS unit, period of operation and failure (including bad data records, skipped data, and when no data was recorded at all). The UNCLOS 06 data, were collected in 2006, the remaining data sets were collected in 2009.

Site	Unit	Period	Failures
GreenArc	CSIC	23 April–1 May	27–30 April
Independence Fjord	Javad	25–30 April	
KMJ	Javad	19–27 April	20, 24–26 April
Nord Sea	Javad	21–26 April	
Schley Fjord	Javad	28–29 April	No data
UNCLOS 06	Javad	8–28 April	
UNCLOS 09	Javad	5–16 April	7 April

2.1. GPS processing

General accuracies in the GPS coordinates depend on the baseline length, receiver type, field procedure and data quality, i.e. cycle slips, ionospheric activity, and multipath. Application of GPS in the Arctic region is challenging because of the satellite constellations, which are not evenly distributed over the sky as in other regions. The dilution of precision (DOP) is a measure of the robustness of the GPS constellation geometry at each epoch. One of the concerns in the Arctic, is the low satellite elevations, which results in a poor vertical DOP (VDOP). In general, for the GPS signal in the Arctic, this results in longer travel time through the atmosphere. An other source of inaccuracy is the reduced speed of the signal propagation in the troposphere and ionosphere, and the refraction of the propagation in the troposphere (Misra and Enge, 2011). The ionospheric activity in polar regions are primarily associated with geomagnetic storms, coronal mass ejections and coronal holes (Skone, 1998). The first order ionospheric effect is the largest, but can be eliminated using differential GPS (DGPS). Normally when processing DGPS in short baselines <100 km the measurement errors, that occur at each station, are very similar, and they cancel each other out when the differences between the observations are taken. According to Bassiri and Hajj (1993), the second and third order residual effects can in worst case scenario reach up to 20 cm (at zenith) depending on the time, day of year, solar activity, and DOP. The error is getting larger with lower elevation angles. The tropospheric delay is divided into a wet and a dry component, the dry component has a residual error of a few millimeters (at zenith), and the wet component is latitude dependent going from few centimeters in dry areas (i.e. Arctic) to 35 cm in humid regions. Again the error increases with low elevation satellites (Bevis et al., 1992).

Several studies Bakry El-Arini et al. (1994), Chang and Lin (1999), Waypoint Consulting (2005) shows how the achievable accuracy is dependent on the baseline length. Therefore, using longer baselines the atmospheric delay has to be included. The errors from satellite position and the selective availability are negligible using satellite clock model and precise ephemeris (Misra and Enge, 2011). Airborne surveys from the Arctic with intermediate baselines (100–300 km), shows an elevation accuracy in DGPS of 5 cm (Brock et al., 2002), 10 cm (Hvidegaard et al., 2009), and with PPP over the North Atlantic shows an accuracy of 10 cm but 30 cm over sea-ice covered regions (Zhang and Forsberg, 2007).

2.1.1. Validating and comparing processing software

All data were differential processed using the kinematic baseline processor Waypoint GrafNav 8.20 from Novatel. To verify this choice, we have compared the differential solution with GrafNav's PPP solutions, with TRACK differential processing and with Automated Precision Positioning Service (APPS). We made two tests between permanent GPS stations. The first station was at the Danish military base, Station Nord (NORD), which was processed differential with the UNAVCO GNET site Kap Morris Jessup (KMJP), as a

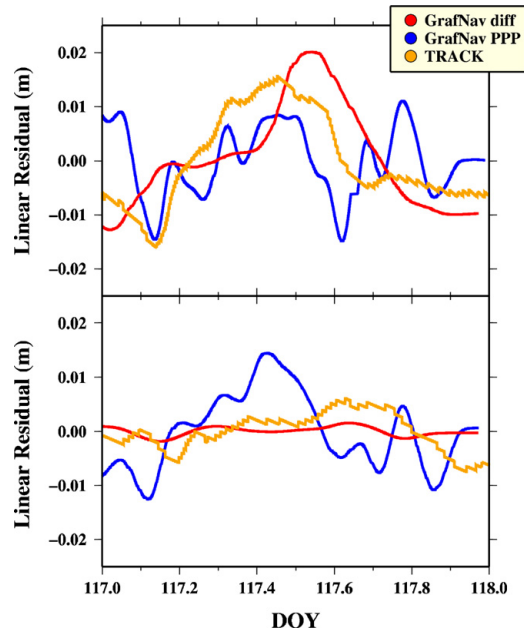


Fig. 2. Linear residual of the ellipsoidal height from two permanent GPS stations in the research area, KMJP and NORD, showed by three processing methods as a fraction of DOY 117 (17 April, 2009). The top figure shows station NORD, which in the *GrafNav diff* and the *TRACK* solutions with KMJP as the reference base station, together with the *GrafNav PPP* solution. The bottom figure shows the result of processing station KMJP, with JGBL being the reference base station for the differential processing. (For interpretation of the references to color in this figure legend, the reader is referred to the web version of this article.)

reference base station. The baseline length was 329 km. The second was at KMJP with Jørgen Bjørnlund Fjord (JGBL) as a reference, the baseline length was 163 km. These baselines are considered to be medium to long. The results are depicted in Fig. 2. According to the *GrafNav* manual, the dual frequency accuracy for distances longer than 35 km is 10 cm + 2 PPM, which in a 100 km baseline corresponds to an accuracy of 30 cm. Following Hvidegaard et al. (2009), the experience of using *GrafNav* was much better than claimed. They found an accuracy of 10 cm in the Arctic, with baselines of several hundred kilometers. This technical report from Waypoint (Roesler, 2000), also gives better results with an average relative error on the vertical of 0.217 PPM with baselines longer than 1000 km.

The software *TRACK*, developed by Massachusetts Institute of Technology (MIT), is part of the *GAMIT* kinematic GPS processing module. The data (yellow curve) were processed with the ionospheric-free combination solution (LC) with a random walk variance of position and atmospheric delay of 10^{-4} m/ \sqrt{s} and 10^{-2} m/ \sqrt{s} , respectively. The time interval used was 30 s.

The *GrafNav* differential solution (red curve) was processed with a dual frequency carrier phase in a 30 s interval. There was applied a L2 ionospheric correction, a tropospheric correction with an error state of 5×10^{-10} m²/s processed, and a base position treatment in PPP.

The *GrafNav* PPP solution (blue curve) was processed with dual frequency carrier PPP processing mode. Processing the absolute error in PPP, must be accounted for, and this is done by modeling

Table 2

GPS processing information. From left to right: GPS site, reference station, maximum baseline between GPS site and reference station in km, mean standard deviation, $\bar{\sigma}_m$ for the ellipsoidal height in cm, and the PDOP.

Site	Ref. station	Baseline (km)	$\bar{\sigma}_m$ (cm)	PDOP
GreenArc	KMJP	112	17.89	2.30
Independence Fjord	JGBL	52	7.66	1.88
KMJ	KMJP	14	7.52	2.05
Nord Sea	NRD2	1	7.29	2.04
UNCLOS 06	ALRT	277	37.56	2.12
UNCLOS 09	ALRT	340	13.92	2.14

the tropospheric zenith delay as a state in the Kalman filter. Both *GrafNav* solutions were alternated with precise ephemeris files.

The APPS is an automated precise positioning service of the global differential GPS system from NASA's Jet Propulsion Laboratory. Data were modeled kinematic with dual frequency measurements in a 30 s interval. The L1 carrier was modeled with C/A code. Data were unusable and therefore not included in the figure.

We have checked for multipath, but did not find any signals to be concerned about. In the processing, the coordinate of the reference stations, were constrained by solutions of AUSPOS, an online GPS processing service provided by Geoscience Australia. When using the coordinate of the International GNSS Service (IGS) stations network log file or the RINEX header as a constraint coordinate, we got a difference in the vertical of about 5 cm to the AUSPOS solution. Overall we conclude, that the differential *GrafNav* software is capable of computing vertical solutions at the 5 cm level, and therefore useful for tidal measurements.

2.1.2. GPS data in the study area

The GreenArc and the KMJ sites were processed with the KMJP site as a reference station. The site Independence Fjord, was processed with the permanent GPS station JGBL as a reference. Nord Sea with NRD2, and UNCLOS 06 and 09 with ALRT as a reference. NRD2 is a stationary reference GPS station placed by DTU Space near Station Nord. This is summarized in Table 2, together with the maximum baseline length, mean standard deviation and PDOP. The reference stations geographical location are shown in Fig. 1 as black stars. Most of the GPS receivers were sampling data at 5-s intervals, however, the GreenArc data were sampled every second, and the UNCLOS 06 every 10 s.

The GreenArc and the UNCLOS camps moved substantial distances (Fig. 1). For GreenArc we have only included the first 5 days due to a large gap in data, during which the site moved 48 km Southeast. UNCLOS 09 moved 16 km Southeast, and UNCLOS 06 moved as much as 71 km Southeast.

The GPS data were processed with respect to the geodetic datum ITRF05, in intervals due to the base stations, i.e. in 30 s intervals for all sites except Nord Sea, which was processed with a 10 s interval. All data was processed with dual-frequency carrier phase, processed forward and backwards. The satellite elevation cut-off angles were set between 7.75° and 10°. We were correcting for the ionospheric delay using a ionosphere free model in a linear combination of L1 and L2 carrier phase measurements, which provided an estimate of the carrier phase observation, on one frequency, with the effects of the ionosphere removed. The tropospheric delay was corrected in two steps. First, a PPP solution was processed to solve for zenith path delay at the base station. The base station was kept fixed. Second, a tropospheric error state was added to the Kalman filter with spectral density of 5×10^{10} m²/s. We were using a strict *AdVance™* RTK (ARTK) integer ambiguity resolution, which controlled how easily the Kalman filter accepted integer fixes generated by ARTK. The height was given with respect to the reference ellipsoid associated with WGS84.

2.2. Sea surface height and reference system

The SSH (h_{SSH}) was measured directly by GPS (h) with respect to a reference ellipsoid (Section 2.1.2). In terms of ellipsoidal height (h), SSH is expressed as

$$h_{SSH} = h - h_{AH} - h_{FB}, \quad (1)$$

where h_{AH} is the GPS antenna height over the sea-ice, and h_{FB} is the sea-ice freeboard, defined as the part of the sea-ice above the sea surface. The SSH can also be expressed by various geophysical parameters;

$$h_{SSH} = N + h_{tides} + h_{DT} + h_{IBE} + h_{errors}. \quad (2)$$

The parameters are: the geoid (N), the tides (h_{tides}), the dynamic topography (h_{DT}), the inverse barometric effect (h_{IBE}) caused by atmospheric loading, and height corrections (h_{errors}) from instrument and model inaccuracies.

Tides are not defined in a geodetic reference frame, but to an averaged zero sea level without any explicit reference frame. We expect the GPS tidal observations to be biased by about 71 cm in the study area relative to the actual mean SSH, because the reference ellipsoid of the WGS84 system refers to an Earth ellipsoid larger than the “best” mean Earth ellipsoid (as approximated by the T/P ellipsoid) (Pavlis et al., 2008). This bias is added to Eq. (1).

2.3. Geophysical parameter corrections

The antenna and freeboard heights were measured during the respective campaigns. In this section, only the computed geophysical corrections, given in Eq. (2) are described. The tidal term h_{tides} , includes the ocean tide, the load tide, the earth tide, and the permanent tide correction. The pole and the air tides are ignored in this study.

2.3.1. Geoid

The geoid height was interpolated from the Earth Gravitational Model 2008 (EGM08), released by the National Geospatial-Intelligence Agency (NGA) EGM Development Team (Pavlis et al., 2008). We have used the reference ellipsoid of WGS84 version in a 1 min \times 1 min grid, consistent with GPS.

The EGM08 geoid is a global model derived from different gravity studies. In the Arctic, data are adapted from the Arctic Gravity Project (ArcGP), where the geoid has an estimated accuracy of 10 cm in the open basin and better than 20 cm in coastal regions and narrow fjord systems (Forsberg et al., 2006; Kenyon et al., 2008).

2.3.2. Ocean tide

The ocean tide is responsible for more than 80% of the total signal, and therefore the amplitude of the ocean tide, is the dominant factor in temporal variations of the SSH.

The tide model used in this study was AOTIM-5 by Padman and Erofeeva (2004). The model is divided into seven domains; the area of this study is located in Domain Five, the Canadian Arctic Archipelago.

In the tide model, eight constituents were included: M_2 , S_2 , N_2 , K_2 , K_1 , O_1 , P_1 , Q_1 . Furthermore, when making the tide predictions, a load tide correction was made, resulting in the vertical component of the tides being calculated to the geodetic SSH, datum (zero). Corrections were also made for minor constituents.

2.3.3. Solid earth tide

The solid earth tide or body tide is the deformation of ocean and land, only dependent on the temporal gravitational forces of the Moon, Sun and other external objects. Solid earth tides are not mentioned in the GrafNav documentation, but from personal

communication, we have discovered, that the DGPS solution does not include a solid earth tide correction, due to the assumption, that the tidal effect cancels out doing the differential process or is negligible, except in extremely long baselines. Xu and Knudsen (2000) and many others claim, that the vertical GPS height should be corrected for solid earth tides. Therefore, we have redrawn the Cartwright–Edden solid earth tides (Cartwright and Tayler, 1971; Cartwright and Edden, 1973) from the measurements. In the study area the correction is in the order of 5 cm.

2.3.4. Permanent tide

The permanent tide is lower in the polar areas due to the position of the Sun and the Moon. From Eqs. (1) and (2), it is clear that h and N have to be computed within the same tide reference system. The geoid is referenced to the tide-free geoid, the mean-tide geoid, or the zero-tide geoid. The tide-free geoid is given for a tide-free Earth with all effects of the Sun and the Moon redrawn. The mean-tide geoid would exist if no permanent tidal effects were removed. The zero-tide geoid is the surface without the permanent tidal effects, but with the effects related to the elastic deformation of the Earth kept constant. Determination of the geoid is complicated by the constant deformation due to the attraction of the Sun and the Moon. These permanent tidal effects can lead to inconsistent definitions of geoid and GPS reference ellipsoid, and this can result in large errors (Ekman, 1989; Lemoine et al., 1998). The GPS data in this study was processed in a tide-free reference frame, the same system as the EGM08 WGS84 geoid version used.

Normally, for determination of SSH in satellite altimetry, the mean-tide system is used. Poutanen et al. (1996) states, that the mean-tide system should be used, because in long-term equilibrium the mean-tide is the shape of the SSH. Using the mean-tide crust as a reference, the height of the tide-free crust is given as

$$h_f = \gamma \frac{W_2}{g}, \quad (3)$$

with the tilt factor $\gamma = 0.609$, which is a function of the Love numbers. W_2 is the second order tidal potential, g the acceleration of gravity, and ϕ is the geodetic latitude (Ekman, 1989; Mäkinen and Ihde, 2008). This correction lead to a 11 cm offset in the study area.

2.3.5. Dynamic topography

The sea surface varies due to density changes in the oceans affiliated with horizontal pressure gradients. The large-scale oceanic flows are nearly in geostrophic balance (the horizontal pressure gradient force and the Coriolis force), and the dynamic topography (DT) is close to an estimate of the large-scale ocean circulation. Globally, the amplitude of DT relative to the geoid is in the order of 2.5 m (Fu and Cazenave, 2001). In the Arctic Ocean, the amplitude is about 1 m, with minimum located south of Greenland and maximum in the Canadian basin, caused by the anticyclonic Beaufort Gyre (Forsberg et al., 2007). The dynamic topography data are obtained from PIOMAS coupled ice-ocean model by Zhang and Rothrock (2003).

The DT are plotted as a mean for April 2009 only (Fig. 3). The values at the GPS sites, are varying from 56.1 to 61.9 cm.

2.3.6. Atmospheric pressure loading

Atmospheric loading exerts a pressure force on the SSH. As the ocean compressibility is small, the spatial and temporal atmospheric pressure variations are compensated by changes in the SSH. This response is known as the inverse barometer effect (IBE).

The height (h_a) corrections originating from the inverse barometer effect is given by:

$$h_a = \frac{1}{\rho_w g} (p_0 - \bar{p}) = \alpha (p_0 - \bar{p}), \quad (4)$$

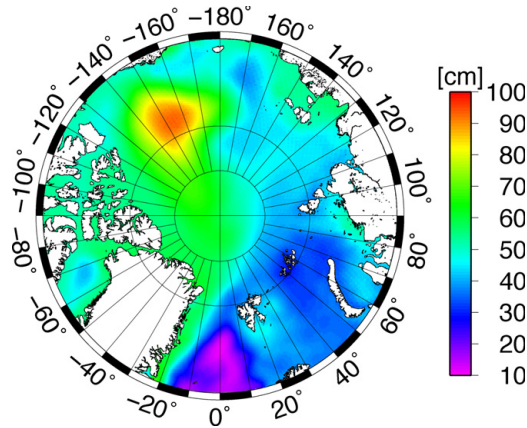


Fig. 3. Mean dynamic topography in the Arctic, April 2009, computed from Zhang and Rothrock (2003).

where g is the standard gravity acceleration ($g=980.6\text{ cm/s}^2$), ρ_w the density of the ocean, p_0 the atmospheric pressure at sea level and \bar{p} is the mean pressure of the atmosphere over the ocean, taken at sea level. \bar{p} is 1011.1 mbar for a standard atmosphere over the ocean domain (Vignudelli et al., 2010). The proportionality constant α is taken to be -1.12 cm/mbar based on work done by repeated ICESat tracks in the Arctic by Kwok et al. (2006).

The sea level pressure (p_0) fields are obtained by linear interpolation of 6-hourly NCEP/NCAR reanalysis products, provided by the NOAA-ESRL PSD Climate Diagnostics Center Branch, Boulder Colorado.

3. Results

In Table 2, the results of the GPS processing is summarized. The mean standard deviation, σ_h , of the vertical distance is displayed together with the PDOP. The standard deviation is between 7.29 cm at Nord Sea to 37.56 cm at the UNCLOS 06 site, and the PDOP is 1.88–2.30, with Independence Fjord having the best PDOP

Table 3

Standard deviation σ and RMS of the vertical height before (uf), after the geophysical corrections (geocor), and the filter (f) are applied.

Site	σ_{uf} (m)	RMS _{uf} (m)	σ_{geocor} (m)	RMS _{geocor} (m)	σ_f (m)	RMS _f (m)
GreenArc	0.444	28.281	0.107	0.326	0.102	0.322
Independence Fjord	0.156	32.175	0.121	0.738	0.112	0.734
KMJ	0.047	27.237	0.046	0.404	0.037	0.404
Nord Sea	0.097	29.541	0.095	0.114	0.089	0.108
UNCLOS 06	0.162	20.888	0.087	0.426	0.079	0.423
UNCLOS 09	0.088	22.604	0.083	0.087	0.075	0.081

Table 4

Mean ellipsoidal height \bar{h} , and geophysical parameter corrections as given in Eqs. (1) and (2). \bar{N} is the mean EGM08 geoid, h_{AH} is the antenna height, h_{FB} is the freeboard of the sea-ice, where the GPS site was located. h_{DT} is the dynamic topography, h_{IBE} is the inverse barometric effect, h_{etide} the solid earth tides, and h_{perm} is the permanent tide correction. The expected uncertainty of the data are also written in the table.

Site	\bar{h} (m)	\bar{N} (m)	h_{AH} (cm)	h_{FB} (cm)	h_{DT} (cm)	h_{IBE} (cm)	h_{etide} (cm)	h_{perm} (cm)
GreenArc	28.28	28.21	50	20	59.5	-7.05 to -1.25	-5.58 to 1.03	-11.86
Independence Fjord	31.17	32.59	15	20	60.4	-10.72 to 10.41	-5.77 to 8.33	-11.71
KMJ	27.24	27.39	14	20	58.5	-8.21 to -0.050	-3.99 to 5.55	-11.86
Nord Sea	29.24	28.94	96	Negative	61.9	-9.27 to -0.610	-5.77 to 4.07	-11.70
UNCLOS 06	20.89	20.98	46	16	56.1	-15.37 to 20.63	-5.43 to 6.81	-11.97
UNCLOS 09	22.60	21.79	65	50	58.3	-25.29 to 1.37	-2.17 to 3.28	-11.97
Uncertainty	0.05	0.15	0.1	1–3	20	5	–	–

Table 5

Mean values of SSH from Eqs. (1) and (2), the difference between the two SSH values (h_{error}).

Site	Eq. (1) (m)	Eq. (2) (m)	h_{error} (SSH) (m)
GreenArc	28.29	28.60	0.31
Independence Fjord	32.54	33.06	0.52
KMJ	27.40	27.80	0.19
Nord Sea	29.29	29.35	0.06
UNCLOS 06	20.98	21.40	0.42
UNCLOS 09	22.16	22.13	0.03

and GreenArc the worst, however all the PDOP values are within an acceptable level.

We have filtered out the noise of the GPS data. The filter applied consisted of two parts; a coarse linear filter to eliminate strongly deviating points, and a low-pass RC filter with a time constant between 10 and 25 s, and zero phase applied forwards and backwards.

The uncertainties of the height (Table 3), are given as the standard deviation (σ), and the root mean square (RMS) of the data before the geophysical parameter corrections (uf) were applied, after the corrections (geocor), and after the final filtering (f). The uncertainties decreases after each step as expected.

3.1. Sea surface height and geophysical parameters

We have determined the geophysical parameter corrections (Section 2.2). All the various heights and corrections are written in Table 4. The ellipsoidal and geoid heights are given as mean values. The table also contains the expected uncertainties of the corrections.

The SSH given by Eqs. (1) and (2), were calculated together with the difference between the two SSH values h_{error} (Table 5). Also these values are mean values of the corrections, and the AOTIM-5 tidal model prediction. h_{error} are in the range of 3–52 cm.

3.2. GPS versus AOTIM-5 tides

The ocean tide (including the load tide) is extracted from Eqs. (1) and (2), where load tide is included, because the GPS is not held to the seabed. The resulting GPS tidal heights in m for the six functional sites, are given as a fraction of Day Of Year (DOY),

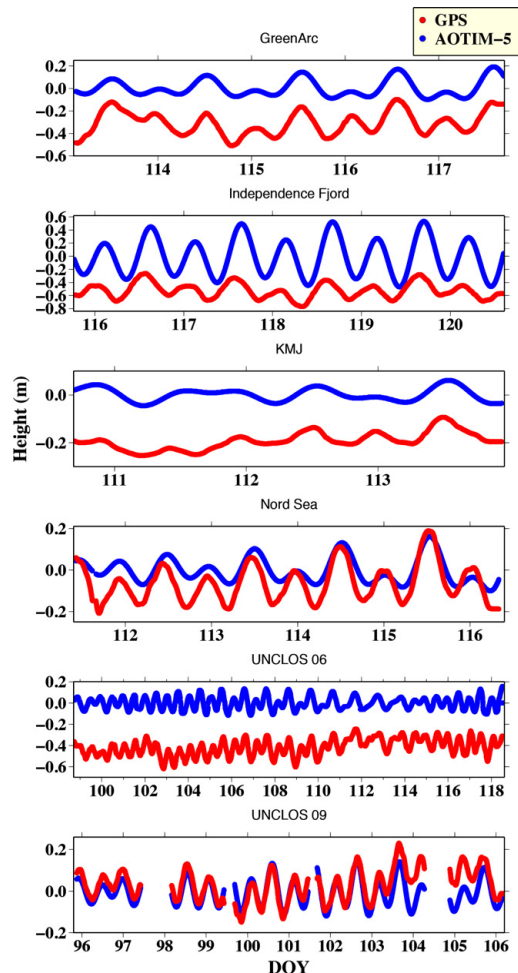


Fig. 4. The ocean and load tides from the geophysical parameter corrected GPS data (red) plotted against the AOTIM-5 tide model (blue) for the six GPS sites; GreenArc, Independence Fjord, KMJ, Nord Sea, UNCLOS 06 and 09. (For interpretation of the references to color in this figure legend, the reader is referred to the web version of this article.)

and shown in Fig. 4 (red), and plotted together with the predicted vertical component of the tides from AOTIM-5 (blue).

Tidal analysis of the GPS tides was accomplished through the use of a least squares harmonic analysis routine *t_tide* from Pawlowicz et al. (2002). To separate various periods, the Rayleigh criterion, which is a function of the frequency of neighboring constituents and record length, must be applied. In Table 6, the amplitude and phase of the constituents are written. The error is calculated by a linearized analysis described in more details in Pawlowicz et al. (2002). The routine also gave various minor constituents, but they were too small compared with the error of the larger constituents, to be accounted for in this analysis. In UNCLOS 09, it was necessary to divide data in five pieces, and afterwards average the pieces, due to large gaps in the data. The tidal analysis is carried out, before the filtering of data is applied, to make sure no extra dampening or phase changes have occurred. The nine primary tidal constituents

Table 6
Amplitudes, phases and their error of the largest tidal constituents, of the six GPS sites, fulfilling the Rayleigh criteria.

	Constituents	Amplitude (cm)	Phase (°)
GreenArc	K1	7.04 ± 3.31	-39.6 ± 27.0
	M2	9.94 ± 0.71	5.5 ± 4.1
	M3	0.31 ± 0.56	-141.7 ± 102.6
	M4	0.20 ± 0.25	0.8 ± 71.7
IP	K1	7.88 ± 1.66	1.1 ± 12.0
	M2	13.77 ± 0.77	-25.9 ± 3.2
	M3	0.26 ± 0.30	-176.1 ± 64.0
	M4	0.54 ± 0.30	76.1 ± 31.6
KMJ	K ₁	1.24 ± 0.17	-24.5 ± 7.8
	M ₂	2.77 ± 0.17	27.6 ± 3.5
	M ₃	0.23 ± 0.17	47.8 ± 42.4
	M ₄	0.66 ± 0.29	41.8 ± 25.4
Nord Sea	K ₁	5.65 ± 1.42	-70.9 ± 14.4
	M ₂	10.22 ± 0.99	-30.9 ± 5.6
	M ₃	0.53 ± 0.33	152.9 ± 35.8
	M ₄	0.13 ± 0.09	123.7 ± 40.4
UNCLOS 06	MSF	3.99 ± 0.55	-130.8 ± 7.9
	O ₁	2.84 ± 0.55	-81.0 ± 11.1
	K ₁	3.81 ± 0.55	-66.3 ± 8.3
	M ₂	5.28 ± 0.92	-15.9 ± 10.0
	S ₂	3.19 ± 0.92	84.6 ± 16.5
	M ₃	0.44 ± 0.29	123.4 ± 38.2
UNCLOS 09	M ₄	0.20 ± 0.23	-74.0 ± 67.5
	M ₆	0.27 ± 0.14	111.8 ± 30.5
	K ₁	3.93 ± 0.74	-107.3 ± 9.8
	M ₂	7.89 ± 0.41	49.5 ± 3.2
	M ₃	0.86 ± 0.41	138.2 ± 29.4
	M ₄	0.83 ± 0.41	138.8 ± 36.1

from AOTIM-5 are extracted by Padman and Erofeeva (2004), and averaged (Table 7).

Fig. 5 are showing the M₂ amplitude (a) and the M₂ phase (b). The M₂ amplitude difference between AOTIM-5 and the GPS are for GreenArc (46%), Independence Fjord (303%), KMJ (27%), Nord Sea (31%), UNCLOS 06 (14%) and UNCLOS 09 (83%). The M₂ phase differences are: GreenArc (20 min), Independence Fjord (19 h), KMJ (1 h), Nord Sea (21 h), UNCLOS 06 (20 h) and UNCLOS 09 (31 min). Combining the amplitude and phase at each site, gives a root sum of squares (RSS) of 3.2 cm (GreenArc), 30.4 cm (Independence Fjord), 1.71 cm (KMJ), 5.8 cm (Nord Sea), 5.5 cm (UNCLOS 06), and 2.3 cm (UNCLOS 09).

4. Discussion

The computed vertical component of the ocean and load tides from the GPS sites, and the tidal model AOTIM-5, show strong coherence (Fig. 4). The offset between the two generated tides are 3–52 cm in the vertical height, corresponding well with the 2–50 cm offset found in various studies (Section 1). The offset is due to uncertainties and errors in the GPS processing, and the applied geophysical parameter corrections. The GPS data at the GreenArc site (before filtering) was relatively noisy. This could be due to stress and strain in the sea-ice on which the GPS receiver was located. Later the stress and strain caused the ice to break up. There is clearly a phase shift in the results from Independence Fjord, KMJ and Nord Sea compared with AOTIM-5, where the maximum amplitude arrives before the AOTIM-5 model. In NORD SEA and UNCLOS 06, there were clearly visible cycle slips in the data, occurring in Day 111 and end of DOY 102, respectively.

GPS error sources can be grouped into three sets based on their nature; satellite-based, propagation-based, and receiver- or user-based. In the GPS processing, lowering the elevation mask,

Table 7
Amplitude and phases of the nine primary tidal constituents of AOTIM-5, at the GPS sites.

	Constituents	Amplitude (cm)	Phase (°)
GreenArc	K ₁	6.11	8.8
	M ₂	6.80	10.5
	S ₂	2.51	80.2
	N ₂	2.26	−87.1
	K ₂	0.50	7.7
	O ₁	3.70	−10.4
	P ₁	1.76	6.3
	Q ₁	0.60	−11.2
IP	K ₁	7.20	54.4
	M ₂	31.40	47.4
	S ₂	14.40	115.4
	N ₂	9.30	−58.5
	K ₂	3.00	35.1
	O ₁	4.90	32.2
	P ₁	2.30	49.5
	Q ₁	0.80	31.0
KMJ	K ₁	6.30	16.8
	M ₂	3.80	10.2
	S ₂	1.70	99.4
	N ₂	1.40	−89.9
	K ₂	0.20	29.4
	O ₁	4.00	−5.2
	P ₁	1.70	13.0
	Q ₁	0.60	−11.5
Nord Sea	K ₁	6.60	13.0
	M ₂	7.80	3.2
	S ₂	2.70	66.6
	N ₂	2.70	−97.1
	K ₂	0.70	−13.8
	O ₁	4.00	−1.7
	P ₁	1.90	12.7
	Q ₁	0.70	−3.1
UNCLOS 06	K ₁	4.42	5.0
	M ₂	6.15	40.9
	S ₂	3.30	100.9
	N ₂	1.24	−48.0
	K ₂	0.63	82.6
	O ₁	2.46	−25.0
	P ₁	1.24	1.0
	Q ₁	0.30	−14.8
UNCLOS 09	K ₁	4.00	8.8
	M ₂	5.80	41.6
	S ₂	3.00	102.4
	N ₂	1.30	−49.0
	K ₂	0.60	78.0
	O ₁	2.47	−9.8
	P ₁	1.19	6.0
	Q ₁	0.40	−9.0

will allow more satellites and strengthen the geometry, but tropospheric and ionospheric errors increase at lower satellite elevations. Comparing h_{error} (Table 5), and the baseline length (Table 2), it is not possible to see if the baseline length plays a role in the vertical offset observed between the model and the GPS tides. The sites with small baselines (Nord Sea and KMJ), are showing small offsets, but contrary the GreenArc site, with the largest baseline, has the smallest offset. With so many corrections and therefore error sources, it is impossible to say, if the baseline played a role in the vertical height determination. Chang and Lin (1999) have done a study in medium range baselines, which turned out to improve the RMS by 35% in the vertical using multi-reference stations.

The amplitude of the GPS data were expected to be dampened up to 40%, and having a phase change up to 1 h, compared to the AOTIM-5 tide model, due to the ice dampening of the ocean (Section 1). The semi-diurnal M_2 is by far the most dominating constituent (79%). Following Prinsenberg (1988), the semi-diurnal tides are

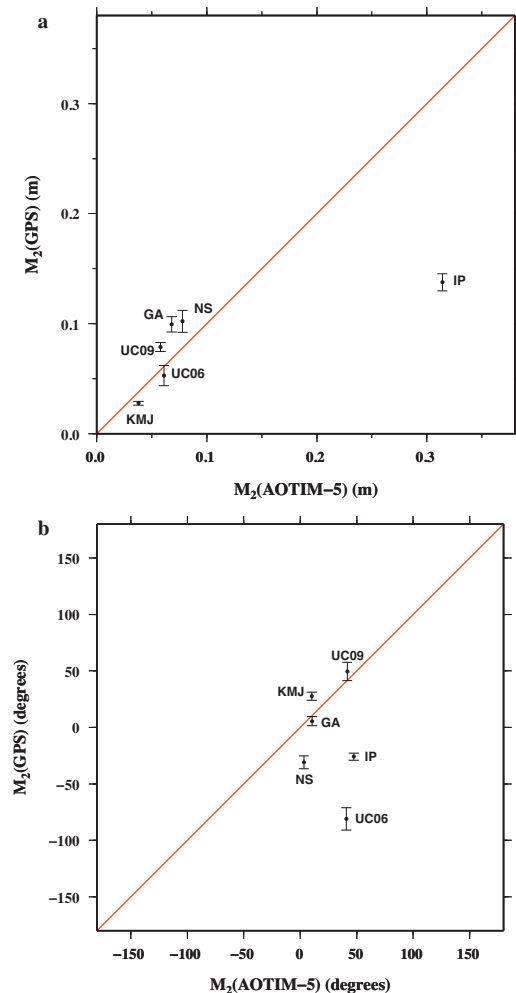


Fig. 5. (a) M_2 amplitudes, and (b) M_2 phases of GPS tides plotted against AOTIM-5 from the six sites GreenArc (GA), Independence Fjord (IP), KMJ, Nord Sea (NS), UNCLOS (UC) 06 and 09.

most affected by the ice dampening. From Fig. 5a, it is very clear how well the GPS and the AOTIM-5 tide amplitudes cohere, disregarding the Independence Fjord site. The GreenArc, Nord Sea and UNCLOS 09 site amplitudes are some what larger than the model. For the GreenArc and Nord Sea sites, that is probably due to coastal effects. The results from UNCLOS 09 relied on five very short time series, which is inadequate for making a trustworthy harmonic analysis. There are no obvious connection between the sites on fast moving ice (GreenArc, UNCLOS 06 and 09), or the sites on steady ice (KMJ, Nord Sea).

The difference of the total amplitudes in Independence Fjord, indicates that AOTIM-5 does not work well in the fjords. This is most likely a result of missing tide information and depth of the ocean floor in the fjord system. Very little is known about the ocean tides in the Independence Fjord. We would expect shallow-water tidal effects and a permanent sea-ice cover. The amplitudes at this

site, given in Table 6 is as expected much higher compared to the sites away from the inner fjord. The amplitude of the shallow-water constituent M_4 , an overtide of M_2 , is not larger in the Independence Fjord site nor has a greater ratio to M_2 compared to the other sites. The difference of the M_2 amplitude of Independence Fjord and Nord Sea is 3.6 cm, i.e. the tide has enhanced by 35% from the start of the fjord to the inner fjord. In the AOTIM-5 model this difference is 23.6 cm corresponding to a 303% enhancement of the M_2 amplitude, which is too much. We would need longer time series to include more constituents in the tidal analysis, e.g. S_2 , the principal solar semi-diurnal signal is only given for UNCLOS 06. We suggest to improve the tide model by a friction model similar to the one done in Kowalik and Proshutinsky (1994), there model failed due to a too high resolution, but this could be overcome with the five km resolution in AOTIM-5. An other suggestion is to make an empirical relationship taking the seasonal variations into account.

This study has also been a validation of the tide model over longer distances, mainly at the GreenArc and the UNCLOS sites, where the sea-ice moved relatively long distances. AOTIM-5 proved to work very well. Naturally, this is only true assuming an accurate geoid.

The GPS data and the tide model are defined with respect to different reference systems. GPS data are processed with respect to WGS84 and the tide model is defined with respect to SSH, where a long time average of modeled elevation at each location is zero, and there are no trends in terms of tidal or periodic sources of SSH. In order to compare the data sets it is very important to reduce the GPS solutions to the same reference system as the tide model or vice versa. We were assuming the T/P reference system, to be the mean SSH, but of course this is not exactly true.

For comparison of GPS heights to SSH and the tide model, we have applied the DT correction to tie data, but note that DT data, refers to a level of no motion in the ocean, and thus are not in a rigorous geodetic reference system. The DT is in general subject to large uncertainties. According to Forsberg et al. (2007), the error could reach up to 20 cm, which could definitely explain the elevation difference between model and data.

There are large uncertainties in the freeboard and the antenna height values due to human error in the in situ measurements. In several cases (GreenArc and UNCLOS 06) it was not possible to find the measured antenna and freeboard height, i.e. the values are estimated from pictures of the GPS station. The negative freeboard at Nord Sea also leads to an error.

5. Conclusion

We have presented a kinematic baseline processing of GPS receivers placed on sea-ice in the Arctic. The SSH is directly computed by GPS measured heights and by geophysical parameter correction. The results show, that it is possible to interpolate the ellipsoidal height from GPS to the vertical tidal defined zero level, with an offset of 3–52 cm. The large offsets were due to errors in the geoid, GPS processing, DT and/or measurement errors in the freeboard and antenna height. Furthermore, we were able to reproduce the ocean and load tide from the six GPS sites, compared with the tide model AOTIM-5. The total amplitude of the GPS tides was dampened due to sea-ice. The tide model AOTIM-5 seems to work well over sea-ice covered areas, but is lacking in fjord systems.

The tidal data of this paper are significant of their kind, they show that the AOTIM-5 tide model works fine in the Arctic Ocean away from the coast, but needs to be improved in fjord systems and close to the coastline. Greater accuracy and longer time series are needed, and hopefully this will be achieved when the SATICE project is realized.

Acknowledgments

We thank Jørgen Skaffte, and the Danish UNCLOS project, for running the GPS stations north of Alert, Pedro Elosegui and Julia de Juan Verger from Institute for Space Sciences, National Council, Barcelona for their hospitality and introduction to TRACK. The authors also acknowledge the discussions and comments by Ole B. Andersen from DTU Space on the tidal analysis, and constructive comments on the submitted manuscript by the reviewer.

References

- Andersen, O., Woodworth, P., Flather, R., 1995. Intercomparison of recent ocean tide models. *Journal of Geophysical Research* 100 (25), 261–325.
- Aoki, S., Ozawa, T., Doi, K., Shibuya, K., 2000. GPS observation of the sea level variation in Lützow-Holm Bay, Antarctica. *Geophysical Research Letters* 27 (15), 2285–2288.
- Bakry El-Arini, M., Conker, R., Albertson, T., Reagan, J., Klobuchar, J., Doherty, P., 1994. Comparison of real-time ionospheric algorithms for a GPS wide-area augmentation system (WAAS). *Navigation* 41 (4), 393–413.
- Bassiri, S., Hajj, G., 1993. Higher-order ionospheric effects on the global positioning system observables and means of modeling them. *AAS* 93–169.
- Bevis, M., Businger, S., Herring, T., Rocken, C., Anthes, R., Ware, R., 1992. GPS meteorology – remote sensing of atmospheric water vapor using the global positioning system. *Journal of Geophysical Research* 97 (D14), 15787–15801.
- Brock, J., Wright, C., Sallenger, A., Krabill, W., Swift, R., 2002. Basis and methods of NASA airborne topographic mapper lidar surveys for coastal studies. *Journal of Coastal Research*, 1–13.
- Cardellach, E., Behrend, D., Ruffini, G., Rius, A., 2000. The use of GPS buoys in the determination of oceanic variables. *Earth Planets Space* 52 (11), 1113–1116.
- Cartwright, D., Edden, A., 1973. Corrected tables of tidal harmonics. *Geophysical Journal of the Royal Astronomical Society* 33 (3), 253–264.
- Cartwright, D., Tayler, R., 1971. New computations of the tide-generating potential. *Geophysical Journal of the Royal Astronomical Society* 23 (1), 45–73.
- Chang, C., Lin, S., 1999. Testing a medium-range DGPS network for the Taiwan area. *Journal of Navigation* 52 (02), 279–288.
- Eanes, R., Ray, R., 1996. The CSR3.0 Global Ocean Tide Model: Diurnal and Semi-diurnal Ocean Tides from TOPEX/POSEIDON Altimetry. Technical Report CRS-TM-96-05. Centre for Space Research, University of Texas, Austin.
- Egbert, G., Bennett, A., Foreman, M., 1994. TOPEX/POSEIDON tides estimated using a global inverse model. *Journal of Geophysical Research* 99 (C12), 24821–24852.
- Egbert, G., Erofeeva, S., 2002. Efficient inverse modeling of barotropic ocean tides. *Journal of Atmospheric and Oceanic Technology* 19 (2), 183–204.
- Ekman, M., 1989. Impacts of geodynamic phenomena on systems for height and gravity. *Journal of Geodesy* 63 (3), 281–296.
- Forsberg, R., Skourup, H., Andersen, O., Knudsen, P., Laxon, S.W., Ridout, A., Braun, A., Johannessen, J., Tscherning, C.C., Arabelos, D., March 2006. Arctic Ocean geoid, ice thickness and mean sea level – the ARCGICE project. In: Proceedings ESA Workshop “15 years of Progress in Radar Altimetry”, Venice.
- Forsberg, R., Skourup, H., Andersen, O.B., Knudsen, P., Laxon, S.W., Ridout, A., Johannessen, J., Siegmund, F., Drange, H., Tscherning, C.C., Arabelos, D., Braun, A., Renganathan, V., 2007. Combination of Spaceborne, Airborne and In-Situ Gravity Measurements in Support of Arctic Sea Ice Thickness Mapping. Technical Report No. 7. Danish National Space Center.
- Fu, L., Cazenave, A., 2001. Satellite Altimetry and Earth Sciences: A Handbook of Techniques and Applications. Academic Press.
- Hvidegaard, S., Forsberg, R., Helm, V., Hendricks, S., Skourup, H., Stenseng, L., Hanson, S., Haas, C., 2009. CRYOVEX 2008-Final Report. DTU Space, Technical Report 2/2009.
- Kenyon, S., Forsberg, R., Coakley, B., 2008. New Gravity Field for the Arctic. *Eos, Transactions, American Geophysical Union* 89, 32.
- King, M., Aoki, S., 2003. Tidal observations on floating ice using a single GPS receiver. *Geophysical Research Letters* 30 (3), 1138.
- King, M., Coleman, R., Morgan, P., 2000. Treatment of horizontal and vertical tidal signals in GPS data: a case study on a floating ice shelf. *Earth Planets Space* 52 (11), 1043–1047.
- King, M., Padman, L., 2005. Accuracy assessment of ocean tide models around Antarctica. *Geophysical Research Letters* 32 (23).
- Kowalik, Z., Proshutinsky, A., 1994. The Arctic Ocean tides. *Geophysica Monograph Series* 85, pp. 137–137.
- Kwok, R., Cunningham, G.F., Zwally, H.J., Yi, D., 2006. ICESat over Arctic sea ice: interpretation of altimetric and reflectivity profiles. *Journal of Geophysical Research* 111 (C06006).
- Lemoine, F., Kenyon, S., Factor, J., Trimmer, R., Pavlis, N., Chinn, D., Cox, C., Klosko, S., Luthcke, S., Torrence, M., et al., 1998. The Development of the Joint NASA GSFC and the National Imagery and Mapping Agency (NIMA) Geopotential Model EGM 96. Tech. Rep. 19980218814. NASA.
- Lyard, F., Lefevre, F., Letellier, T., Francis, O., 2006. Modelling the global ocean tides: modern insights from FES2004. *Ocean Dynamics* 56, 394–415.

- Mäkinen, J., Ihde, J., 2008. The permanent tide in height systems. In: *Observing our Changing Earth*, pp. 81–87.
- Misra, P., Enge, P., 2011. *Global Positioning System: Signals, Measurements and Performance*, 2nd ed. Ganga-Jamuna Press (available through NavtechGPS).
- Padman, L., Erofeeva, S., 2004. A barotropic inverse tidal model for the Arctic Ocean. *Geophysical Research Letters* 31 (2), L02303.
- Pavlis, N., Holmes, S., Kenyon, S., Factor, J., 2008. An earth gravitational model to degree 2160: Egm2008. In: *EGU General Assembly*, pp. 13–18.
- Pawlowicz, R., Beardsley, B., Lentz, S., 2002. Classical tidal harmonic analysis including error estimates in MATLAB using *t.tide*. *Computers & Geosciences* 28 (8), 929–937.
- Poutanen, M., Vermeer, M., Mäkinen, J., 1996. The permanent tide in GPS positioning. *Journal of Geodesy* 70 (8), 499–504.
- Prinsenberg, S., 1988. Damping and phase advance of the tide in western Hudson bay by the annual ice cover. *Journal of Physical Oceanography* 18 (11), 1744–1751.
- Ray, R., 1999. A Global Ocean Tide Model from TOPEX/POSEIDON Altimetry: GOT99. Technical Report NASA Tech. Mem. 209478. Goddard Space Flight Centre.
- Ray, R., Eanes, R., Egbert, G., Pavlis, N., 2001. Error spectrum for the global M2 ocean tide. *Geophysical Research Letters* 28 (1), 21–24.
- Roesler, G., July 2000. 1000KM Baseline Determination in Static and Kinematic Mode. Tech. Report. Waypoint Consulting Inc. Webpage: <http://www.novatel.com.cn/support/knowledge-and-learning/waypoint-software/technical-reports-about-waypoint-software-products-and-their-applications/>
- Shum, C., Woodworth, P., Andersen, O., Egbert, G., Francis, O., King, C., Klosko, S., Le Provost, C., Li, X., Molines, J., et al., 1997. Accuracy assessment of recent ocean tide models. *Journal of Geophysical Research* 102, 25–25.
- Skone, S., 1998. Wide Area Ionosphere Grid Modeling in the Auroral Region. Ph.D. Thesis. The University of Calgary, Calgary, Alberta, Canada, uCGE Reports Number 20123.
- Smith, A., Ambrosius, B., Wakker, K., 2000. Ocean tides from T/P, ERS-1, and GEOSAT, altimetry. *Journal of Geodesy* 74 (5), 399–413.
- Vignudelli, S., Kostianoy, A., Cipollini, P., Benveniste, J., 2010. *Coastal Altimetry*. Springer.
- Waypoint Consulting, September 2005. Kinematic Batch Processing Accuracies of One Data Set at Varying Baseline Distances using CORS Stations in Grafnav Version 7.50. Tech. Report. Webpage: <http://www.novatel.com/support/knowledge-and-learning/waypoint-software/technical-reports-about-waypoint-software-products-and-their-applications>
- Xu, G., Knudsen, P., 2000. Earth tide effects on kinematic/static GPS positioning in Denmark and Greenland. *Physics and Chemistry of the Earth Part A: Solid Earth and Geodesy* 25 (4), 409–414.
- Zhang, J., Rothrock, D.A., 2003. Modeling global sea ice with a thickness and enthalpy distribution model in generalized curvilinear coordinates. *Monthly Weather Review* 131 (5), 681–697.
- Zhang, X., Forsberg, R., 2007. Assessment of long-range kinematic GPS positioning errors by comparison with airborne laser altimetry and satellite altimetry. *Journal of Geodesy* 81 (3), 201–211.

F.3 A Comparative Analysis of the Sea Ice Freeboard From CryoSat, CryoVEx and ICEBridge

A COMPARATIVE ANALYSIS OF THE SEA ICE FREEBOARD FROM CRYOSAT, CRYOVEX AND ICEBRIDGE

Stine Kildegaard Rose¹, Laurence N. Connor², Sinead L. Farrell^{2,3}, René Forsberg¹, Thomas Newman^{2,3}, Leif T. Pedersen⁴, Walter H.F. Smith², Henriette Skourup¹, and Lars Stenseng¹

¹DTU Space - National Space Institute, Technical University of Denmark, Elektrovej, Build. 327-328, Kgs. Lyngby, Denmark.

²NOAA, Laboratory for Satellite Altimetry, College Park, MD., USA

³Earth System Science Interdisciplinary Center, University of Maryland, College Park, MD., USA

⁴Danish Meteorological Institute, Copenhagen, Denmark

ABSTRACT

The CryoSat Validation Experiment (CryoVEx) has been conducted by ESA, to examine the uncertainties in the satellite measurement of e.g. sea ice thickness. In this study, we aim to estimate the sea ice freeboard from CryoSat-2, and compare it with the high-resolution Airborne Laser Scanner (ALS) measurements collected along CryoSat-2 ground tracks from the CryoVEx 2012 campaign, together with NASA's Operation IceBridge data. We will use the CryoSat SAR data level 1b (L1b) to discriminate the leads and from this, estimate the sea ice freeboard. Furthermore, we are looking at the CryoSat level 2 (L2) product, and correcting the extremely off-ranging points.

Key words: Sea Ice; CryoSat; CryoVEx; IceBridge; Freeboard; Retracking.

1. INTRODUCTION

Sea ice is crucial in the understanding of the Earth's climate, and since 1979, where satellites started to monitor the sea ice extend [Comiso et al., 1991], it has been shrinking [Serreze et al., 2007]. CryoSat-2 has now operated in almost three years, and measures more of the Arctic ocean, than ever before due to its high sampling rate and geographical coverage up to 88°N/S. CryoSat-2 is dedicated to monitor cryosphere changes, including changes in the sea ice thickness. The first sea ice thickness map from CryoSat has recently been published by [Laxon et al., 2013] in a peer reviewed journal, and show good results.

In this paper, we focus on two small sea ice patches. The first patch is from the CryoSat track number 10520 from April 2, 2012 in the Lincoln Sea north of Alert, Canada, where we expect multi-year ice. A joined operation was carried out by NASA's IceBridge team, and the DTU

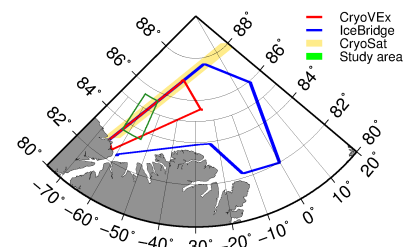


Figure 1: Study area (green box) in the Lincoln Sea.

Space crew to underflew the CryoSat track (Fig. 1).

The second patch is situated north from Svalbard where the CryoSat orbit number 10885 flew on the April 27, 2012 here we expect fast moving first-year ice. In this site, DTU Space underflew the satellite track (Fig. 2).

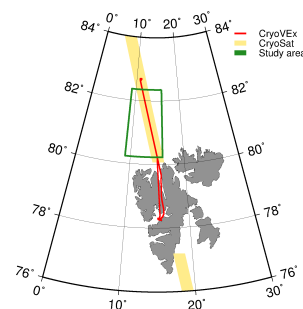


Figure 2: Study area (green box) North from Svalbard.

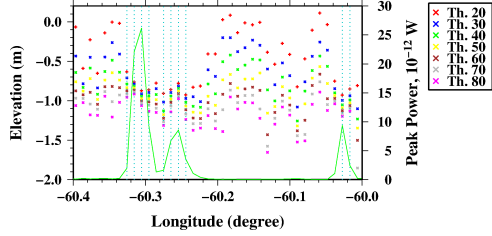


Figure 3: Comparison of various thresholds from 20% to 80% from the first study area. The colored crosses are the various thresholds, the green curve is the peak power, and the blue dots indicate a peak power $> 1.5 \cdot 10^{-12}$ W.

2. DATA PROCESSING

The flights from DTU Space was part of the CryoVEX campaign managed by ESA, and had an Airborne Laser Scanner (ALS) on board. For more details about the scanner see [Skourup et al., 2012]. We use the 5×5 m resolution, because the fine 1×1 resolution was not available, at the time writing.

The NASA's P3 was among other things carrying an Narrow swath Airborne Topographic Mapper (ATM). For more details about the laser scanner see [Krabill, 2012].

For processing CryoSat L1b SAR data, we are using a threshold retracker similar to [Davis, 2002]. We are tracking the first peak above 10% of the maximum peak to avoid picking up the thermal noise. The theoretical threshold of a SAR altimeter is 80%, but this threshold do not assimilate the sea ice conditions, the leads simply do not stand out as a depression in the elevation. There is a large variation of the thresholds (Fig. 3) especially over the ice floes, and less over the leads. Leads have a high peak power, and are indicated in the figure with blue dots. Lowering the threshold decreases the freeboard. After a visual inspection of the various thresholds, we expect a threshold of 40% or 50% to work best over the sea ice region. Which one performing best has to be validated by comparing the freeboard between the airborne campaigns.

To be able to compare the airborne datasets with CryoSat we have applied the same atmospheric and geophysical parameters, and we have resampled the dataset to the CryoSat resolution. All elevations are giving w.r.t. the EGM08 geoid.

In study area I, there was 1 h and 15 m between the OIB and CryoSat overpass, and 2 h between CryoVEX and CryoSat. There has not been observed any remarkable drift. There was 2 h 30 m between the CryoVEX and CryoSat overpass in the second study area, and in this period, there has been a remarkable sea ice drift. Fortunately, CryoVEX made a return in the same path, so data

has been corrected for ice drift.

3. CORRECTING OFF-RANGING L2 DATA

The CryoSat Level 2 (L2) data product looks in a first view very scattered. There are a lot of points off-ranging with elevations up to 23 m off in the study area. When examining these extremely off-ranging points by looking at the corresponding L1b waveform, it occurred to us, that the waveform always contained a small peak followed by a tall peak. They are probably caused by a nearby lead either in the track or off-nadir. The backscatter from a lead is so powerful compared to the backscatter from a snow surface.

We are correcting CryoSat L2 data when a sharp first peak is followed by a sharp second peak (Fig. 4b). Waveform no. 7878 is 2.8 km from the lead. We are using a 80% threshold retracker to track the first and the largest peak, when the largest peak is not the first peak, the difference between the peaks are determined and the elevation difference is added to the L2 height (yellow dots in Fig. 4a). The power return from a lead along track or off-nadir is so power full because of the specular surface, that a lead many kilometers away can effect the signal. It is not always the case, that we can correct the L2 in this matter (e.g. Fig. 4d), the first peak needs to be sharp and isolated. In this case it would have been better to actually track the second peak, or something in between.

Making this correction to the L2 product is not a solution to the product. In the L2 product, the lead (Fig. 4c) is not seen at all. You would need to look into the L2 retracker algorithm to make a better L2 product, but the correction shown here clearly say something about, what is going wrong with the L2 product.

4. FREEBOARD ESTIMATION

The sea ice freeboard is the part of the ice and/or snow over the ocean surface. When talking about laser freeboard the snow is included, and when talking about the radar freeboard, it is the freeboard without snow. The freeboard is estimated by

$$h_{fb} = h - h_{SSH}, \quad (1)$$

where h is the range w.r.t. the geoid, and h_{SSH} is the sea surface height (SSH).

The SSH is determined for all data sets with an updated version of [Hvidegaard and Forsberg, 2002], where the SSH is derived with a collocation method, but here the leads are tied as minimum values. OIB DMS L1B Geolocated and Orthorectified Images [Dominguez, 2012] are examined to verify the minimum values as leads. In determination of the freeboard from CryoSat, we use two

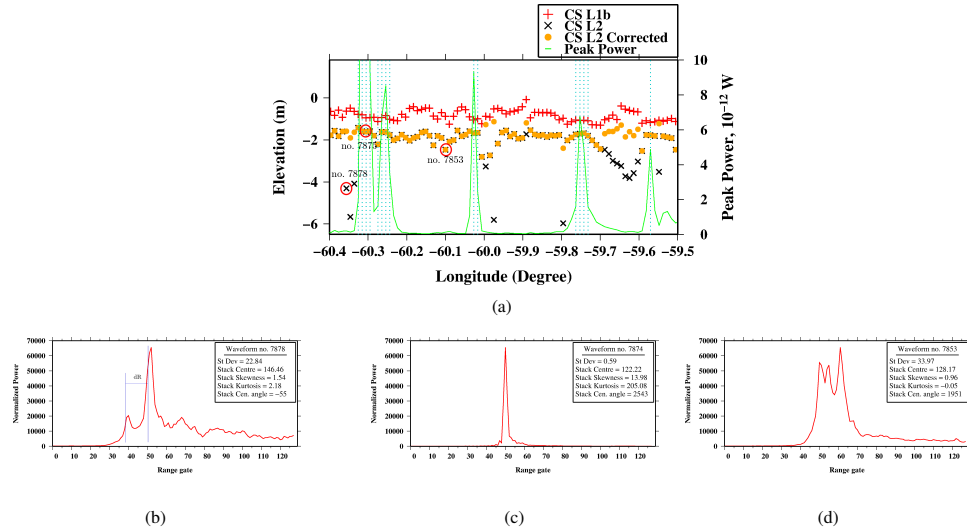


Figure 4: (a) CryoSat (CS) elevations from L1b, L2, L2 corrected and The blue dots indicate peak power $> 10^{-12}W$. The red circles represent the waveforms in (b), (c) and (d). (b) Waveform no. 7878. The blue lines indicate the correction made to the height. This point is 2.8 km from the lead in (c). (d) is an example where the correction algorithm is not working properly.

different methods to determine the minimum values. First we use the peak power from CryoSat to detect the minimum values (M1), and second we use the leads determined from CryoVEx (M2). The two methods agree very well (Fig. 5).

The laser scanner data are measuring from the top of the

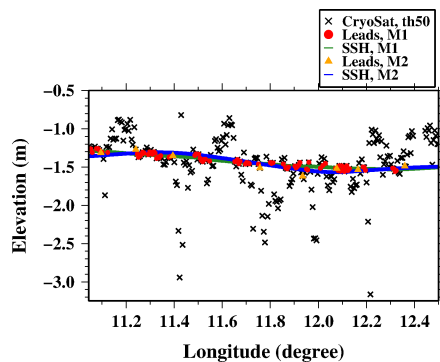


Figure 5: CryoSat elevations w.r.t. EGM08 together with the two SSH's derived from CryoSat peak power (M1), and CryoVEx leads (M2). In this figure the snagging points are not filtered out.

snow, where the radar altimeter on board on CryoSat theoretically is measuring down to the snow/ice interface. This may not be true in practice, but more studies have to be conducted to verify this. OIB is having a snow radar on board, the data were as writing, not available for the 2012 campaign. Fortunately, Kurtz [2012] has developed a OIB quicklook product including snow depths and freeboard values, which we have used in this study for the first study area. We are averaging the snow depth to correspond to the CryoSat resolution, and add it to the elevations to get the laser freeboard. We are assuming the leads to be snow free. Snow will suppress a refrozen lead to a probably more correct SSH, but data are compared to laser scanner data having snow on top, which may lead to an overestimation of the CryoSat freeboard compared with the airborne data. In the second study area, we do not have the OIB snow depth data to rely on. Instead we use a snow depth from Warren et al. [1999] snow model, where a typical snow depth from this area in April is approximately 38 cm. Following OIB snow radar results, [Farrell et al., 2012], half of the snow model should be applied over first-year ice, e.g. we would expect 19 cm of snow in this area.

From the first study area in the Lincoln Sea (730 data points), we retrieve a freeboard from CryoVEx and IceBridge of 42 cm and 49 cm, respectively. The CryoSat freeboard with snow are 51 cm with M1 and 53 cm with M2 with a 40% threshold retracker. With a threshold of 50% we get freeboard values of 45 cm (M1) and 46 cm

(M2).

In the second study area, we evaluate 837 data points. The CryoVEx freeboard is 33 cm. The CryoSat freeboard is 34 cm for M1 with both a threshold of 40% and 50%. M2 retrieved freeboards are 34 cm and 29 cm with 40% and 50%, respectively.

From these values, a threshold of 50% seems to work the best, but here we have to mention the possibility of radar penetration, and the fact, that we made the assumption of leads without snow, which from visual inspections is not true. In none of the data sets, we have removed snagging points. Especially for the study area 2, with first-year ice and lots of leads, this would cause a difference in the freeboard. This makes it difficult to interpret the probability functions which is the reason why we get the same freeboard in M1 for both thresholds.

5. CONCLUSION AND OUTLOOK

We have retrieved the laser freeboard from CryoVEx and IceBridge laser scanner data and CryoSat L1b data with applied snow from an area from April 2, 2012, where we interpret the sea ice as multi-year ice. We found a coherence between the scanner data and freeboard from CryoSat elevations retracked with a 50% threshold retracker. A similar coherence is seen in the second study area, also here the 50% threshold retracker seems to work best, with these preliminary results. We may be overestimating the freeboard, which has to be looked into in more details, and this may cause in another recommendation of thresholds. We are working on removing the snagging from the CryoSat data, to get more reliable results, and to give an uncertainty estimate of the freeboard retrieval.

ACKNOWLEDGMENTS

We would like to acknowledge the DTU and ESA's CryoVEx crew 2012, NASA's IceBridge Arctic 2012 team, the National Snow and Ice Data Center for distribution of IceBridge data, and ESA for providing and processing CryoSat-2 data. Finally we would like to thank Nathan Kurtz for producing the OIB Quicklook product, and making it available.

REFERENCES

- Comiso, J., Wadhams, P., Krabill, W., Swift, R., Crawford, J., and Tucker III, W. (1991). Top/bottom multisensor remote sensing of Arctic sea ice. *J. Geophys. Res.*, 96(C2):2693–2709.
- Davis, C. (2002). A robust threshold retracking algorithm for measuring ice-sheet surface elevation change from satellite radar altimeters. *IEEE Trans. Geosci. Remote Sens.*, 35(4):974–979.
- Dominguez, R. (2012). IceBridge DMS L1B Geolocated and Orthorectified Images, [2012.04.02].
- Farrell, S., Kurtz, N., Connor, L., Elder, B., Leuschen, C., Markus, T., McAdoo, D., Panzer, B., Richter-Menge, J., and Sonntag, J. (2012). A first assessment of IceBridge snow and ice thickness data over Arctic sea ice. *IEEE T Geosci Remote*, 50(6):2098–2111.
- Hvidegaard, S. and Forsberg, R. (2002). Sea-ice thickness from airborne laser altimetry over the Arctic Ocean north of Greenland. *Geophys. Res. Lett.*, 29(20):1952.
- Krabill, W. B. (2012). IceBridge Narrow Swath ATM L1B Qfit Elevation and Return Strength [2012.04.12]. Digital media.
- Kurtz, N. (2012). IceBridge Sea Ice Freeboard, Snow Depth, and Thickness Quick Look. Online.
- Laxon, S. W., Giles, K. A., Ridout, A. L., Wingham, D. J., Willatt, R., Cullen, R., Kwok, R., Schweiger, A., Zhang, J., Haas, C., et al. (2013). CryoSat-2 estimates of Arctic sea ice thickness and volume. *Geoph. Res. Lett.*
- Serreze, M., Holland, M., and Stroeve, J. (2007). Perspectives on the Arctic's shrinking sea-ice cover. *Science*, 315(5818):1533–1536.
- Skourup, H., Einarsson, I., Forsberg, R., Hvidegaard, S. M., Nilsson, J., and Olesen, A. (2012). ESA CryoVEx 2012 - Airborne field campaign, Data Acquisition Report. Technical report, National Space Institute (DTU Space).
- Warren, S. G., Rigor, I. G., Untersteiner, N., Radionov, V. F., Bryazgin, N. N., Aleksandrov, Y. I., and Colony, R. (1999). Snow depth on Arctic sea ice. *J. Climate*, 12(6):1814–1829.

F.4 A sea ice freeboard analysis from CryoSat, CryoVEx and ICE-Bridge over first- and multi-year ice areas

A sea ice freeboard analysis from CryoSat, CryoVEx and ICEBridge over first- and multi-year ice areas

Stine K. Rose, Laurence N. Connor, Sinead

L. Farrell, René Forsberg, Thomas Newman, Walter H. F. Smith, and Henriette Skourup

Abstract—CryoSat has been measuring the sea ice by radar altimetry in the Arctic Ocean since 2010, but there remain uncertainties in the accuracy of its elevation retrievals over sea ice. We present a comparative analysis of CryoSat elevations from two areas with different sea ice conditions. The first study area, with thick multi-year ice, was situated north of Alert, Nunavut, Canada, where the DTU Space - National Space Institute Airborne Laser Scanner and the National Aeronautics and Space Administration Airborne Topographic Mapper, were collecting data in a joint survey underflying CryoSat on April 2, 2012. Thin first-year ice was expected in the second study area north of Svalbard, where DTU Space underflew CryoSat on April 27, 2012. Leads are detected from the CryoSat data, and sea surface height derived from the airborne measurements are exploited to retrieve the CryoSat freeboard. The freeboard is sensitive to the sea surface height. A simple threshold retracker is developed, and we demonstrate how the elevation varies due to the choice of threshold. A threshold of 40% performs best over the sea ice cover. The analysis shows good agreement between the laser and the radar altimetry derived freeboard, when considering a snow layer on top of the radar measurements.

Index Terms—Altimetry, laser radar, sea ice, satellite applications.

I. INTRODUCTION

SEA ice strongly affects the global climate system. To better understand the Arctic sea ice

pack, the ice volume, i.e. sea ice extent and thickness, needs to be determined. The sea ice extent has been monitored since 1979, by passive microwave satellites [1], and has retreated in every decade since [2]. The September satellite record between 1979-2012 shows Arctic sea ice extent retreated by -13.0% per decade [3] relative to the 1979 to 2000 average. Sea ice measurements in the Arctic are now more important than ever before, as recent research shows a more rapid retreat since 1996. Until 2012, the record minimum extent was observed in September 2007 [4]. The retreat in extent occurred much faster than predicted by climate models [5], and based on the 2007 minimum, Wang *et al.* [6] predicted a nearly sea ice free Arctic in September 2037. A new record minimum was observed in 2012 which was 18% lower than in 2007, and 49% lower than the 1979-2000 average [3].

Measuring sea ice thickness is however more difficult to achieve in larger scale, because of the poor accessibility of the sea ice bottom topography, and is further impacted by seasonal variability. Ice thickness can be measured in various ways: In-situ measurements (e.g. [7]), submarine upward looking sonars (ULS) (e.g. [8], [9]), airborne electromagnetic (EM) techniques [7], [10], [11]. All of these methods provide accurate sea ice thickness measurements, but have a very limited spatial coverage. Laxon *et al.* [12], first derived ice thickness from freeboard measured by satellite radar altimeters, carried on ERS-1 and -2, covering eight-years of measurements from 1993-2001. With the Envisat satellite, Giles *et al.* [13] studied sea ice thickness change between winter 2002/2003 and 2007/2008. The Ice and Cloud and Land Elevation Satellite (ICESat) was the first satellite carrying a laser altimeter on board, from which sea ice thickness was derived [14], [15]. Due to the laser altimeter

S. K. Rose, R. Forsberg and H. Shourup are with the Division of Geodynamics, DTU Space - National Space Institute, Technical University of Denmark, Building 327+328, 2800 Kgs. Lyngby, Denmark e-mail: stine@space.dtu.dk.

L. N. Connor and W. H. F. Smith are with the Laboratory for Satellite Altimetry, NOAA, College Park, MD 20740 USA

S. L. Farrell and T. Newman are with the Earth System Science Interdisciplinary Center (ESSIC), University of Maryland, College Park, MD 20740 USA and also with the Laboratory for Satellite Altimetry, NOAA, College Park, MD 20740 USA

Manuscript received July 19, 2013

measurement principal, ICESat returns an echo from the top of the snow layer. Furthermore, it had a extended geographical coverage that stretched to 86°N/S. Launched on 8 April 2010, CryoSat-2 (from now on CryoSat) is dedicated to monitoring the Earth's cryosphere. CryoSat provides the opportunity to measure almost the entire Arctic Ocean due to its high sampling rate and geographical coverage to 88°N/S. The first sea ice thickness mapping and estimate of ice volume from CryoSat was recently released by [16]. CryoSat thickness data was validated with EM ($r = 0.701$), ULS ($r = 0.886$) and National Aeronautics and Space Administration's (NASA) Operation IceBridge (OIB) altimeter ($r = 0.608$) data. Furthermore, the estimated CryoSat thickness was compared with earlier ICESat and Pan-Arctic Ice-Ocean Modelling and Assimilation (PIOMAS) thicknesses. The results confirmed the over all thickness distribution in the Arctic Ocean, and the long-term sea ice volume decrease.

Satellite altimetry provides a better spatial and seasonal coverage than in-situ, ULS, EM and airborne altimetry measurements, but there are more uncertainties associated with the sea ice thickness retrieval. The total ice thickness is derived from the freeboard by assuming the principal of isostasy [1], [17]. In radar altimetry it is commonly assumed that the radar penetrates to the snow-ice interface with cold and dry snow conditions [18]. However, Tonboe *et al.* [19] simulated a pulse-limited space borne radar altimeter and showed, that the snow depth, density and surface roughness influence the radar penetration into the snow and ice. The results demonstrated, that the effective scattering surface depth (horizon to the freeboard) varies as a function of the snow and density properties. This was also verified from field studies [20]. Giles *et al.* [21], derived the contributions of uncertainties in snow depth, snow and ice density and freeboard, on the over all error in the thickness retrieval. Tonboe *et al.* [22] studied retrieval uncertainties by evaluating floe buoyancy and surface penetration of ice thickness by radar altimetry and in-situ measurements, and they showed the importance of also including the radar penetration variability and preferential sampling as error sources.

We present a comparative analysis of CryoSat elevations with NASA's OIB Airborne Topographic Mapper (ATM) laser altimeter data, and/or Airborne Laser Scanner (ALS) operated from the CryoSat

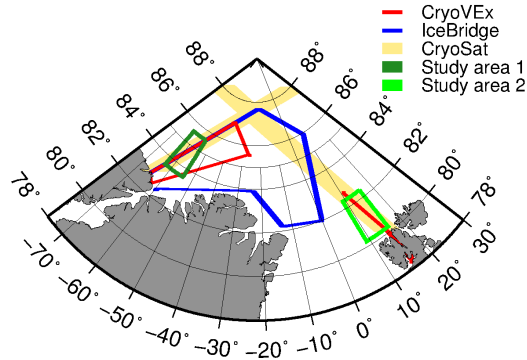


Fig. 1. Study area 1 (dark green box): CryoVEx (red), OIB (blue) flight paths and section of CryoSat (yellow) orbit no. 10520 on April 2, 2012 in the Lincoln Sea north of Alert, Nunavut, Canada. Study area 2 (light green box): CryoVEx (red) flight path and section of CryoSat orbit no. 10885 on April 27, 2012 north from Svalbard.

Calibration and Validation Experiment (CryoVEx) campaign to better understand the CryoSat SAR altimeter measurements.

We find that a threshold retracker of 40% performs best both over multi-year ice and first-year ice. There was a significant drift in the sea ice in the period of investigation, and drift corrections have been applied in both areas. In this paper, we describe five methods to derive the sea surface height (SSH) for the CryoSat freeboard retrieval. The freeboard retrieval shows to be sensible to the SSH determination. We find the CryoSat retrieved freeboards to agree very well with freeboards derived from the ATM and ALS measurements, when considering a snow layer on top of the sea ice.

II. AIRBORNE DATA AND STUDY AREAS

In a joint survey on the April 2, 2012 the NASA P-3 and the Twin Otter operated by the Technical University of Denmark (DTU), DTU Space - National Space Institute completed an underflight of CryoSat orbit number 10520. We concentrate our studies in a 219 km line in the Lincoln Sea (Fig. 1), where we expect multi-year ice and leads due to ice dynamics.

On the April 27, 2012, DTU Space conducted a second CryoSat underflight (orbit no. 10885) north of Svalbard in the Fram Strait (Fig. 1) as part of the CryoVEx campaign. The second study area is a 238 km long line of this track. In this area the sea ice

disappears in the Summer due to melt or drift into the Greenland Sea. Therefore this sea ice is seasonal and regrows in the area every year. This is assumed to be thinner and smoother than the multi-year ice in study area 1.

A. CryoVEx

The CryoVEx campaigns are funded by the European Space Agency (ESA), and aims to understand the sources of error that contribute to the over all ice thickness uncertainty, such as: snow loading, ice density, radar penetration into the snow pack, preferential sampling on snow and ice and freeboard measurement errors. In this study we will focus on data from the ALS instrument. ALS is a Riegl LMS Q-240i type laser scanner operating at a wavelength of 904 nm and with a pulse repetition frequency of 10 kHz. It has a opto-mechanical scan mechanism providing linear and parallel scan lines with a 60° scan angle. In both study areas the Twin Otter flew with an average altitude of about 340 m (1000 feet), yielding a horizontal point resolution of 0.7 m \times 0.7 m at a ground speed of 250 km/hr. The across-track swath corresponds roughly to the altitude of the airplane.

The aircraft location is determined by Global Positioning System (GPS) techniques and the attitude (pitch, roll and heading) recorded by inertial navigation systems (INS). Calibration of the ALS misalignment angles between ALS and INS are estimated by sequential overflights of a building of which the coordinates of its corners are known to high precision. The vertical accuracy of ALS is on the order of 5 - 10 cm depending mainly on the uncertainties in the GPS solutions. Data are provided relative to the WGS-84 reference ellipsoid [23].

B. Operation IceBridge

NASA's OIB mission was initiated to bridge the gap between the ICESat mission and the upcoming ICESat-2 mission. In this study, we will use the OIB Narrow Swath ATM L1B Qfit Elevation and Return Strength dataset [24], the OIB DMS L1B Geolocated and Orthorectified Images [25], and the IceBridge Sea Ice Freeboard, Snow Depth, and Thickness Quick Look product, archived at the National Snow and Ice Data Center (NSIDC) at <http://nsidc.org/data/icebridge/evaluation-products.html>.

The ATM operates at 532 nm with a pulse repetition frequency of 5 kHz. It is a conically scanning device with a 22.5° scan angle. The nominal across-track resolution is 400 m with an average point density of one laser shot per 10 m². The aircraft's attitude was also monitored by an INS. The surface elevation accuracy over sea ice is expected to be better than 10 cm [26], and given relative to the WGS-84 reference ellipsoid [24].

The DMS image resolution varies with aircraft height. The pixel size is about 10 \times 10 cm, at an altitude around 480 m, this results in an image size of about 690 \times 775 m. The imagery is referencing to the EGM2008 geoid.

We use snow thickness estimates provided by the Quick Look data product, because the final sea ice thickness product from the snow radar was not available at the time of writing. We would expect the final product to have a better accuracy. In the Quick Look product the snow thicknesses are provided as averages every 40 m along-track [27].

III. SATELLITE ALTIMETER DATA

The SIRAL instrument on board CryoSat is a Ku-band (13.6 GHz) SAR/interferometric Radar Altimeter. It is capable of operating in one of three modes. The Low Resolution Mode (LRM), a conventional pulse limited radar altimeter, mainly operating over the ice free oceans and on the interior of the large ice caps. The SARin mode, an interferometric mode, taking advantage of the CryoSat's two radar antennas, is usually switched on over ice sheet margins with steep terrain and in coastal zones. In this study we will focus on the Synthetic Aperture Radar (SAR) mode, operating over sea ice covered regions. The radar pulses are passed in bursts of 64 coherent pulses with a pulse repetition frequency of 18.181 kHz. The antenna footprint diameter at the surface is up to 15 km, but the along-track resolution is limited by the Doppler sampling resolution and varies with the satellite altitude. The across-track distance illuminated by the leading edge is around 1.5 km. At an altitude of 750 km, and including the effect of a curved Earth and the beam widening effect, the along-track is approximately 380 m. Each echo in the SAR level 1b (L1b) product consist of 128 pulses corresponding to a vertical window of 30 m. [28], [29]. Here we use the CryoSat L1b 20 Hz data, and the latest product (version B).

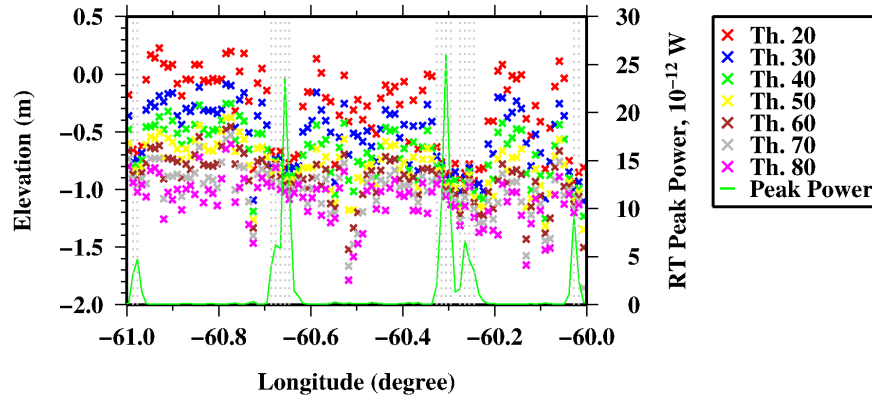


Fig. 2. Comparison of various retracker thresholds (crosses) from 20% to 80% of sea ice elevations with respect to the EGM08 geoid. The green curve is the CryoSat peak power of the retracked peak, and the gray dots, indicate a peak power above $1.5 \cdot 10^{-12}$ W.

IV. DATA PROCESSING

The CryoSat L1b SAR data are processed with a threshold retracker similar to [30]. We track the first peak above 10% of the maximum peak to avoid picking thermal noise. The theoretical threshold of a SAR altimeter is 80%, but this threshold does not account for the sea ice conditions, and the leads do not appear out as a depression in the along-track elevation.

There is a large variation of the various thresholds (Fig. 2) especially over the ice floes, and less over the leads. Leads are associated with a high peak power, and are indicated in the figure with gray dots.

From the figure we find that lowering the threshold decreases the freeboard due to the smaller separation between lead and ice floe elevations. By definition, lowering the threshold will track the waveform leading edge earlier and, therefore, will slow the rise of the ice-type waveforms compared to the fast rise of the lead-type waveforms, yielding a larger separation with a lower retracking threshold.

After a visual inspection of the various thresholds, we expect a threshold of 40% or 50% to work best over the sea ice region. To accurately assess which threshold retracker performs best, we validate them by comparing the CryoSat derived freeboard to coincident data from the airborne campaigns.

Around the leads, we also observe non-lead points with too low elevations. These are due to the so called “snagging” effect [31], where the altimeter locks on the lead (because of the high return power

from the lead) both approaching and once the lead is passed. SIRAL is also sensitive to even small signals from specular surfaces laying off-nadir, due to its large footprint. In this study, we have not attempted to remove any off-ranging elevations. Further investigation is required to separate out true surface elevations from off-ranging snagging effects.

To conduct the comparisons, we have applied the same corrections (inverse barometric effect, ocean tide, long periodic equilibrium ocean tide, ocean loading tide and geocentric polar tide) to the CryoSat and the airborne data sets. For CryoSat we have also applied the ionospheric and the dry and wet tropospheric correction, together with the window delay and the retracking correction (here the difference between the retracking point and the center of the range window). All elevations are given with respect to the EGM08 geoid, and all the corrections are acquired from the CryoSat L1b product.

A. Sea ice drift

In study area 1, 60 to 90 minutes elapsed between the OIB and the CryoSat acquisitions, and 75 to 135 minutes between the CryoVEx and CryoSat acquisitions. There was no ice drift in the first part of the track, but ice drift is observed in the last part of the track starting from about 84.853°N latitude. The drift correction is described below.

There was 150 minutes between the CryoVEX and CryoSat overflights in the second study area,

and in this period, there has been a significant sea ice drift. Ice drift correction were made for both study areas as described below. A failure to correct for the ice motion could be expected to significantly change the results.

1) *Study area 1: Lincoln Sea:* We adjusted the CryoVEx and CryoSat data to the OIB time frame to take advantage of both the ATM and the DMS data sets. In the first study area we have two laser scanner data sets, and 17 identical features in the ATM and ALS data sets are detected and used in determining the drift offset.

A drift vector (distance and bearing) was calculated for each point, and new ALS coordinates were calculated. The coordinate transfer was double checked by plotting ALS on top of OIB DMS images to check the alignments. From the 17 drift vectors, four drift patterns were found in study area 1. This resulted in four relationships in drift as a function of time difference between ALS and ATM. (Fig. 3). Most of the drift relationships were linear, but in one case we got a nonlinear bearing calculation (green curve). In another case (UTC: 13.3 hours), no relationship correlated with the drift. This was close to a data gap in the ALS due to laser operations. During this period the ice drift is changes, i.e. we could not find the place, where the change initiated. We therefore assumed a constant drift in the area (0.002° latitude). In study area 1, the CryoVEx coordinates have moved between 34 m to 108 m with a bearing of 254° to 21° , where the movement was in the direction from north-northeast to west-southwest.

Two cases of ice drift are shown in Fig. 4. On the left-hand side the ALS data are depicted on

top of three DMS images, and on the right-hand side the corrected ALS data are depicted. Fig. 4(a)-(b) shows the time, where the ice starts to move. The DMS imagery measures 1326×1582 m. In the first part of the track (up to 84.853° N), the ALS and ATM data were aligning very nicely. This is visible in the bottom left corner (Fig. 4(a)) east from the open lead (black feature in the image, where ALS is matching the features in the DMS image. Going north from this lead, the sea ice encounter a significant distortion, and we see changes in the sea ice surface between the two flight overpasses.

A large change in the drift direction and speed around 13.43 hours is seen (Fig. 3). This happens within few meters. The sea ice is moving in different directions on both sides of the lead, i.e. the lead is becoming wider. Visible in Fig. 4(c)-(d). These images measures 1277×1589 m.

The ice movement in the time between CryoSat and OIB, is calculated by a new set of drift vectors from old and new ALS coordinates. CryoSat overflow the area before IceBridge and CryoVEx, and we assume the drift direction is constant, and the distance is linear in time. The CryoSat drift is in opposite direction than the drift from ALS with respect to ATM. This drift vector set is in the same sampling rate as ALS data, and therefore we need to resample the drift vectors to the CryoSat sampling rate. The time ratio of the time difference between CryoSat and IceBridge and CryoVEx and IceBridge, is determined for each point, and thereafter the new CryoSat coordinates are determined. We have rejected six CryoSat and ATM elevations during the ALS data gap. The CryoSat coordinates moves between 97 - 290 m and with a bearing varying of

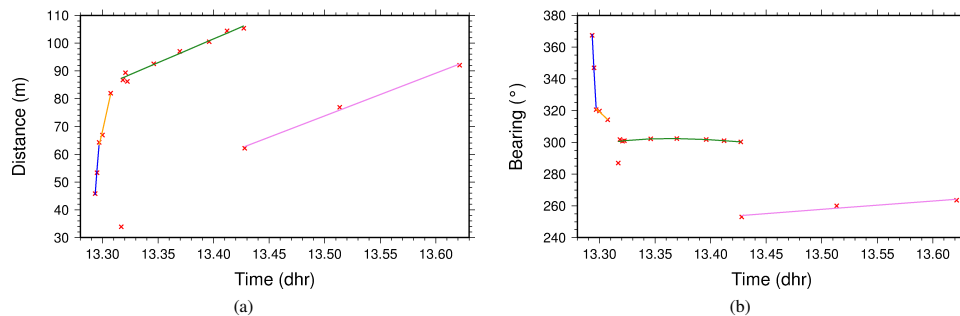


Fig. 3. Sea ice drift of ALS w.r.t ATM. (a) distance and (b) bearing, where $0^\circ = 360^\circ$ is North. The time is in decimal hours (dhr) UTC.

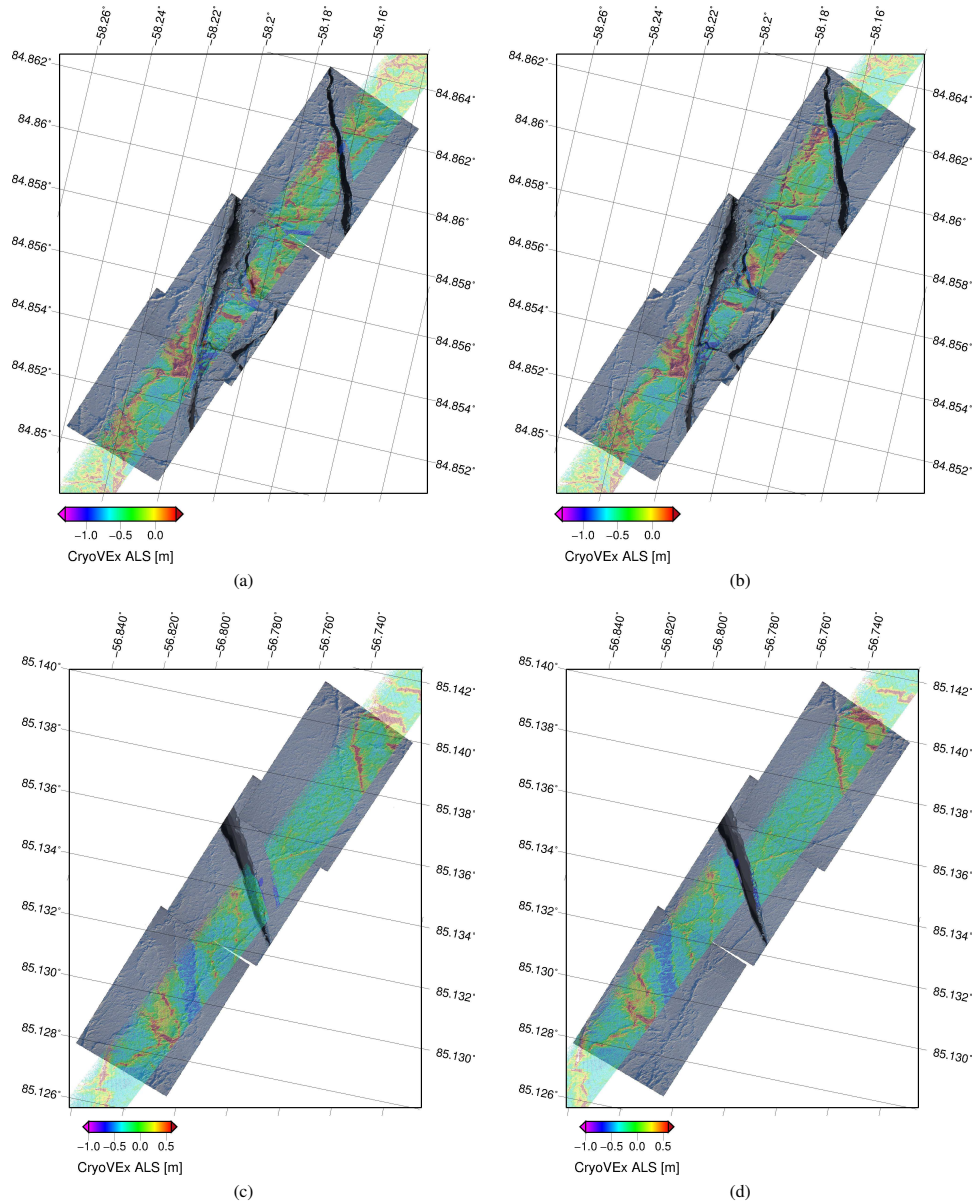


Fig. 4. Sea ice drift examples: (a)-(c) show CryoVEx elevations with respect to EGM08 before drift correction is applied. The data are shown on top of three DMS images. (b)-(d) show the data after the drift correction is applied. (a)-(b) the sea ice drift begins. Southeast from the lower open lead (black feature), there is no drift between ALS and ATM, Northwest from the lead, the sea ice starts to drift. The image dimension is 1326×1582 m. (c)-(d) large change in drift direction and speed. The sea ice is significantly changing direction and speed. This can also be observed in Fig. 3 near 13.3 hours. The image dimension is 1277×1589 m.

254 - 353° moving in the direction north-northwest.

2) *Study area 2: North from Svalbard:* In study area 2, CryoVEx made a return in the same track, so the ice drift correction is made by comparing the outbound and inbound ALS swath. We use the outbound data for the comparison, and the inbound for calculating the drift.

We see large changes in the sea ice between the two overflights, e.g. leads are getting larger from one track to another, and new leads are opening. In some areas it was not even possible to find matching features. We have used a linear relationship based on eight coordinates to calculate the drift between the two CryoVEx overflights.

As for study area 1, it is assumed, that the ice drift direction has remained the same, and the drift distance is linear in time. There is between 52 m and 1 h 53 m between the outbound CryoVEx and the CryoSat overflight of the area. In between the CryoSat and the CryoVEx outbound overflights, the sea ice moves a distance of 248 - 1220 m with a bearing of 339 - 342°, corresponding to a direction north-northwest, with the greatest movement farthest away from Svalbard.

B. Comparisons

For comparison purposes we resample the ALS and ATM data to the CryoSat sampling rate. There exist 783 data points in study area 1, and 830 points in study area 2. First, data are divided into blocks of 25×25 m, where a median value for each block is determined. Second, a near neighborhood routine is used to grid data within a search radius of 152.5 m and 152.8 m corresponding to half the CryoSat sampling rate for study area 1 and study area 2, respectively. Due to ice drift, the satellite and the respective airborne data sets are outside each others footprint. To compensate for this, we have found the nearest great circle on Earth to the ATM track, and projected all the data onto this great circle. Finally, the CryoSat data point locations are tracked in the grid (Fig 5). We see an offset in the elevations of about 1 m, and requires a more detailed investigation.

Data are compared in scatter plots (Fig. 6) after ice drift is applied, and with results from the 40% threshold retracker, only. In study area 1, we get a correlation coefficient between ALS and ATM of $r = 0.816$ before the ice drift correction, and

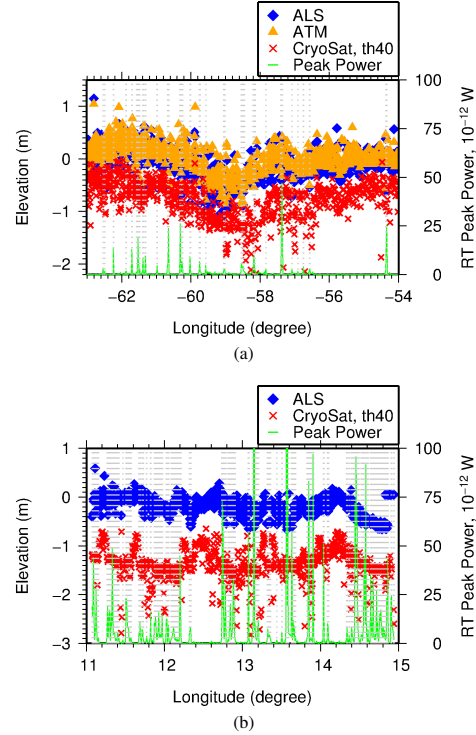


Fig. 5. Elevations above EGM08 from CryoSat (red crosses) and ALS (orange triangles) and ATM (blue diamonds) plotted together with the CryoSat retracked peak power (green), where the gray vertical dots indicate the presence of leads. (a) Study area 1 in the Lincoln Sea, and (b) study area 2 north of Svalbard.

$r = 0.905$ (Fig. 6(a)) after drift. Before the ice drift correction is applied, the correlation coefficient is $r = 0.484$ between CryoSat and ALS, and $r = 0.485$ between CryoSat and ATM. Correlation coefficients of $r = 0.530$ and $r = 0.513$ are found when comparing CryoSat (40% threshold retracker) with ALS and ATM, respectively (Fig. 6(b)-(c)). After drift the 50% threshold retracker yields a weaker correlation of $r = 0.492$ and $r = 0.507$ for ALS and ATM, respectively. In the second study area, the correlation coefficient between CryoSat (40% threshold retracker) and ALS after drift is $r = 0.428$ (Fig. 6(d)), we have in this case removed the very worst outliers with a rough cut off at -1.6 m. The correlation coefficient is $r = 0.258$ before drift, and $r = 0.326$ with a threshold of 50% after drift.

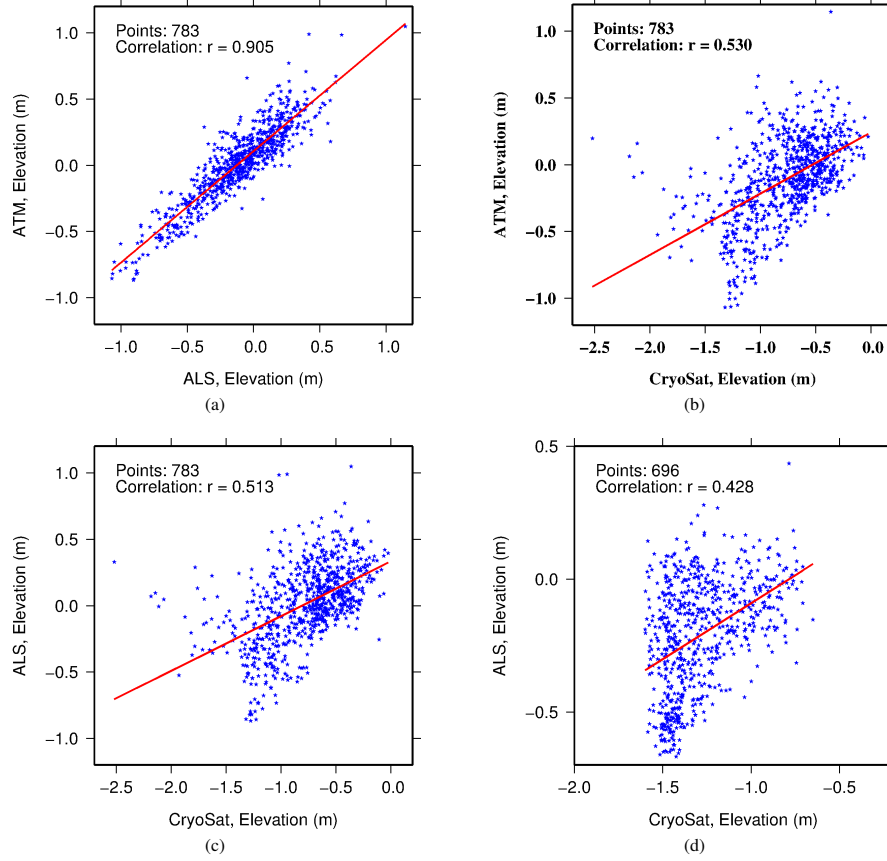


Fig. 6. Scatter plot of elevations above the EGM08 geoid from (a) ALS and ATM, (b) CryoSat and ATM elevations, (c) CryoSat and ALS from study area 1 and (d) CryoSat and ALS from study area 2.

V. SSH AND FREEBOARD ESTIMATION

The sea ice freeboard is defined as the ice and/or snow over the local sea surface. For laser freeboard the snow is included, and for radar freeboard snow is not included. The freeboard is estimated by

$$h_{fb} = h - h_{SSH}, \quad (1)$$

where h is the retracked range w.r.t. the geoid, and h_{SSH} is the SSH.

The SSH is determined for all data sets with an updated version of [32] SSH algorithm developed for airborne laser campaigns. They apply a lowest level filtering routine, by determine the lowest value

in a selected interval. A smooth surface is fitted to the lowest values in a given interval by least square collocation. This is defined as the local SSH. Instead of finding one minimum value in each interval, we tie the “true” leads as minimum values. When DMS images are available, they are examined to verify the minimum values as leads. In study area 2, where there is no DMS imagery, we use the CryoSat peak power as a lead discriminator.

We estimate the SSH of ALS and ATM in three steps. First, all the minimum values are routinely detected. Second, the minimum values are verified as leads in DMS images, and the values are filtered only to account for the lowest values. Third, the

SSH is determined with the SSH routine by constraining the leads.

To determinate the freeboard from CryoSat, we use five different methods to determine the SSH. In the first method (M1), we use a peak detection algorithm to detect the minimum values. We find the peak power of the retracked peak over a threshold of $1.5 \cdot 10^{-12}$ W, and afterwards select the measurement with the highest power, as being the lead. We are very conservative in this detection, because we only want the largest leads in the SSH determination. Second, we use the lead coordinates determined from CryoVEx (M2), and third, we use the leads determined from OIB (M3), forth and fifth, we take the SSH derived from ALS (M4) and ATM (M5) and average the SSH to the CryoSat elevation level.

A. Study area 1: Lincoln Sea

The freeboard is derived from (1). For ALS, and ATM, this gives a modal freeboard of 53 cm (Table I). This corresponds to a typical freeboard of multi-year ice. The SSH in M2 and M3 were calculated from 18 and 14 leads, respectively. A corresponding freeboard calculated from the OIB Quick Look product, where data are averages in 40 m by 40 m samples, gives a modal freeboard of 51 cm.

In the SSH determination for the CryoSat data, there is an overall consistency in the five methods (Fig. 7). The estimated freeboard ranges from 28 cm to 43 cm for the 40% threshold and from 13 cm to 33 cm for the 50% threshold (Table II). The peak detection algorithm used for M1 found in total 28 lead values. For the different methods, we get a penetration depth of 10-25 cm and 20-40 cm for a threshold of 40% and 50%, respectively, comparing the radar and laser freeboards (Table II). For several cases, the amount of data around the leads were so great, that the mode became a lead elevation.

TABLE I
ALS AND ATM MODAL LASER FREEBOARDS STATISTICS: MEAN, LEAST MEDIAN OF SQUARES (LMS) OR THE ESTIMATED MODE, THE STANDARD DEVIATION, AND THE OBSERVED MODE FOR 783 AVERAGED VALUES.

	Mean (m)	LMS (m)	SDev. (m)	Mode (m)
ALS	0.581	0.585	0.244	0.525
ATM	0.599	0.575	0.222	0.525

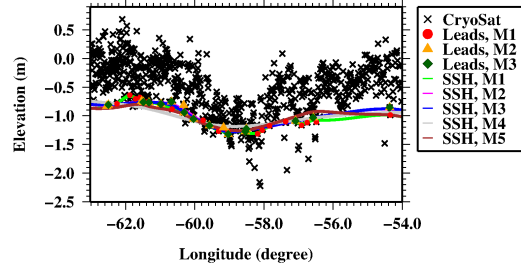


Fig. 7. CryoSat elevations, leads from M1, M2 and M3, together with SSH from M1-M5.

Therefore, we ended up ignoring these values in the freeboard determination. M1 gives the highest freeboard whereas M2 the lowest. M2-M5 are based on the ALS and ATM measurements which were conducted at different times. We have seen, that the ice in this period moved substantial distances, and we saw leads opening in the period from the OIB to the CryoVEx overflight. Therefore it may not exactly be the same ice measured in the three data collections. Furthermore, as already pointed out, the SSH from M2-M5 may have been measurement from the top of the snow if the leads were refrozen and with a snow layer on top.

The laser scanner data are measuring from the top of the snow surface, where the radar altimeter on board CryoSat theoretically is measuring down to the snow/ice interface. This may not be true in practice, and may vary depending e.g. on the snow density, but more studies have to be conducted to verify this.

To compensate for the snow layer, we use the snow depth from the OIB Quick Look product. We average the snow depth to match the CryoSat resolution, analogously to the laser elevation averaging, and add it to the CryoSat elevations. The modal snow depth in this area results in 23 cm. We are assuming the leads to be snow free. Snow loading will suppress a refrozen lead to a probably more correct SSH. The CryoSat data are compared to laser scanner data measuring to the snow/air interface, which may lead to an overestimation of the CryoSat freeboard compared with the airborne data sets.

Due to the presence of leads or ridges, it is not always possible to calculate the snow depth [26]. If these measurements are a lead, we set the

TABLE II
CRYOSAT MODAL FREEBOARD STATISTICS: MEAN, LEAST MEDIAN OF SQUARES OR THE ESTIMATED MODE, THE STANDARD DEVIATION, AND THE OBSERVED MODE FOR RADAR AND LASER FREEBOARD FOR A THRESHOLD OF 40% AND 50%.

	Mean	LMS	SDev.	Mode	Mean	LMS	SDev.	Mode
	(m)	No snow (m)	(m)	(m)	(m)	Snow (m)	(m)	(m)
CryoSat Method 1								
Threshold 40%	0.300	0.402	0.277	0.425	0.550	0.580	0.334	0.525
Threshold 50%	0.191	0.246	0.263	0.325	0.463	0.499	0.328	0.475
CryoSat Method 2								
Threshold 40%	0.251	0.269	0.273	0.275	0.519	0.562	0.346	0.425
Threshold 50%	0.150	0.155	0.260	0.175	0.420	0.456	0.328	0.275
CryoSat Method 3								
Threshold 40%	0.248	0.266	0.273	0.275	0.519	0.614	0.344	0.425
Threshold 50%	0.147	0.162	0.259	0.125	0.429	0.465	0.331	0.325
CryoSat Method 4								
Threshold 40%	0.304	0.374	0.293	0.375	0.559	0.676	0.359	0.525
Threshold 50%	0.203	0.258	0.282	0.225	0.466	0.555	0.347	0.525
CryoSat Method 5								
Threshold 40%	0.295	0.334	0.292	0.325	0.553	0.652	0.358	0.525
Threshold 50%	0.193	0.257	0.281	0.225	0.453	0.520	0.346	0.425

snow depth to zero, and if it is a non-lead the measurement is filtered out. From this the freeboard is now calculated based on 771 measurements. The two laser freeboards have been checked for the new measurement quantity, but the results did not give any change in the observed mode, and a minor change in the LMS of -0.1 cm and -0.5 cm for ALS and ATM, respectively. The new freeboard is recalculated (Table II) for all five methods and varies now from 43 cm to 53 cm with a 40% threshold and from 28 cm to 48 cm with a threshold of 50%. The methods M2 and M3 have a modal freeboard 10 cm lower than the laser freeboard measurements, but when looking at the least median of squares (LMS) or the estimated mode, M1 to M4 is closest to the ALS and ATM LSM freeboard.

In a selected region in the first study area, we plot the modal freeboards from ALS, ATM and CryoSat M1 (Fig. 8(a)), and the modal freeboard distribution of all the non-snow (Fig. 8(b)) and the snow calculations (Fig. 8(c)) for the 40% threshold results only.

B. Study area 2: North from Svalbard

In study area 2, we use the same strategy, as used in study area 1, but we do not have the OIB data to compare with, so only methods M1, M2, and M4 are used in deriving the freeboard from CryoSat.

The derived SSH (Fig. 9) varies considerably, and this may be a result of the large ice dynamics

in the area changing the sea ice conditions from the CryoSat to the CryoVEx overflight. 48 and 31 leads are used to determine the SSH in M1 and M2, respectively.

The ALS modal laser freeboard is calculated to 33 cm, which is typical for first-year ice. The freeboard is derived based on 458 measurements, after the lead values are filtered to be able to discriminate the ice from the leads. In deriving the freeboard from CryoSat, we get a modal radar freeboard between -3 and 13 cm from a threshold retracker of 40% and between -3 to 8 cm using the 50% retracker. The results and the statistics are summarized in Table III.

In the second study area, we do not have the OIB snow depth data to rely on. Instead snow depth from

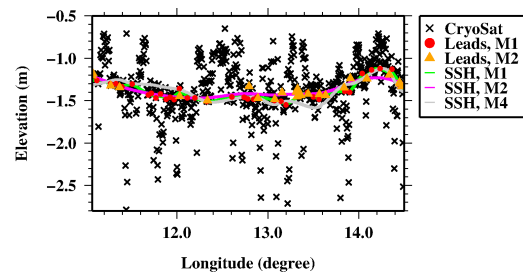


Fig. 9. CryoSat elevations with leads from M1 and M2, and SSH from M1, M2 and M4.

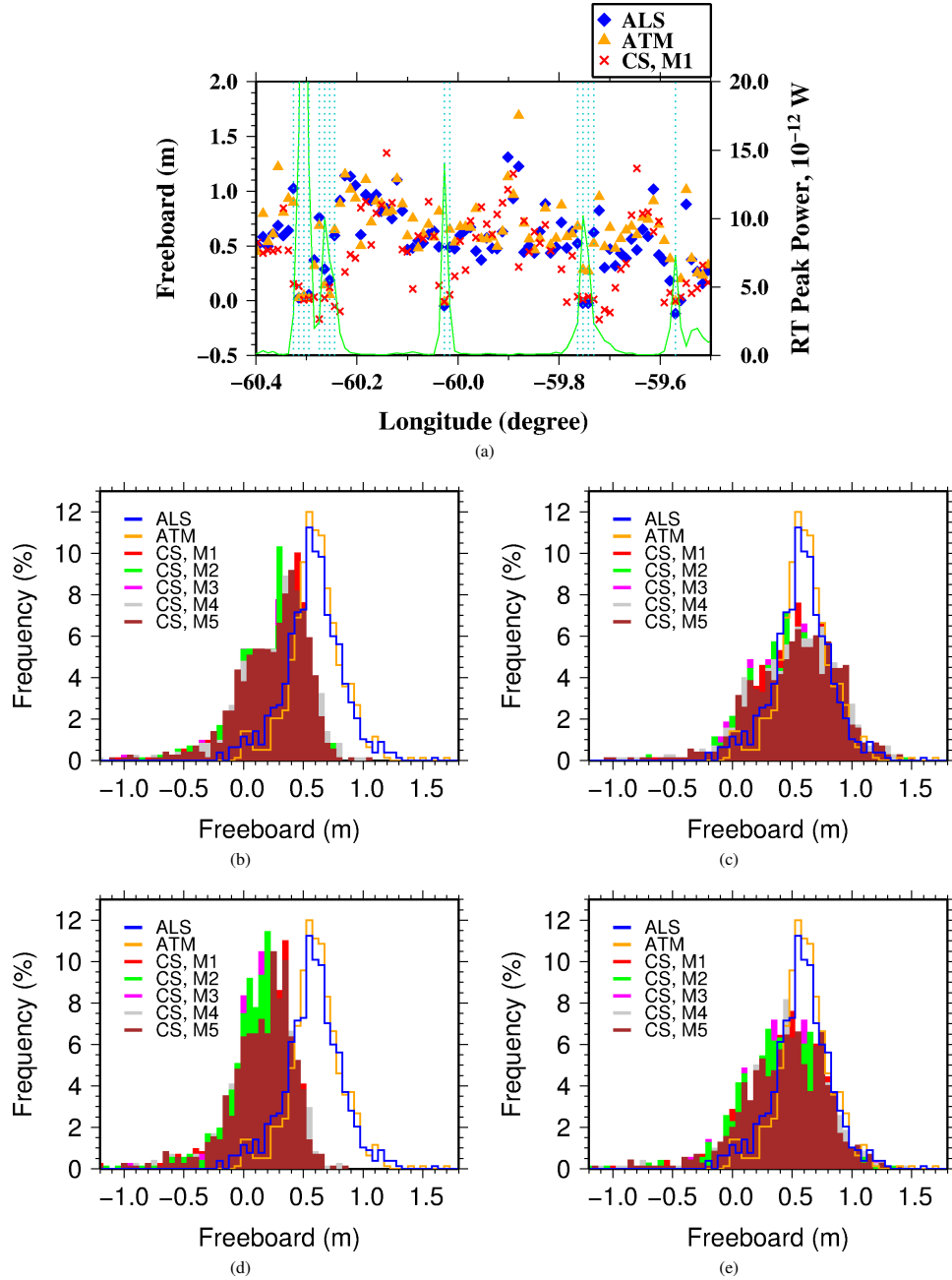


Fig. 8. (a) Comparison of ALS, ATM and CryoSat M1 freeboard. (b) distribution freeboard with bin size 0.05 m from ALS, ATM and CryoSat M1-M5, (c) same as ((b)) but with snow applied. (d)-(e) is the freeboard distribution (without and with snow) from the 50% threshold retracker.

Warren's climatology [33] is used, based on yearly data sets from in-situ measurements in 1954-1991, and it represents an Arctic Ocean primarily covered by multi-year ice. From this model a typical snow depth from study area 2 in April is approximately 38-40 cm, and for May it is 30-34 cm. Following OIB snow radar results [34], only half of the snow model should be applied over first-year ice, e.g. we would expect 15-20 cm of snow in this area. Haapala *et al.* [35] made an in-situ study North from Svalbard the April, 29 2011. They found a mean snow depth of 36 cm in the area stretching from 80 to 81°N, 12 to 21°E. In the western most area i.e. closest to study area 2, the snow depth seems to be smaller and around 10-28 cm with a freeboard of -15 to 10 cm.

In comparison of the modal freeboard (Fig. 10) from CryoVEx and CryoSat M1, M2 and M4, we find a penetration depth between 20-30 cm and 20-25 cm for the 40% and 50% threshold retracker, respectively. This corresponds to half of the [33] snow model depth, and the results from [35]. These 25 cm might be the mean snow layer from the second study area, indicating that the satellite is usually measuring to the snow/ice interface. The freeboard distribution of M1 (Fig. 10(b)) has a second peak around 33 cm, which corresponds to the ALS modal peak. This may be a reflection from the air/snow interface. We are in the end of April, and it is not unlikely that there are days of melt at this time of year, which would cause a wetter and warmer snow, whereas the K_u -band radar could not penetrate. The combination of melt followed by

freezing make frost flowers (thin ice layer) in the snow, less likely to be penetrated by the radar signal.

VI. DISCUSSION

It is necessary to average and sample the scanner data to best assimilate the CryoSat altimeter SIRAL, but a couple of things have to be considered in the averaging process. Important information about the sea ice cover may be lost. A lead can be averaged out because of its small size, where CryoSat is very sensitive towards leads even on very small scale. Due to the off-nadir scan angles, both the ATM and the ALS does not pick up the reflections from the very specular open leads. This is a problem, because these leads, representing the true SSH are the most important leads in the SSH determination. By tracking the CryoSat coordinates in the laser scanner data set, we may lose some important information if a lead is located in between the CryoSat samples.

The various SSH estimates gives a difference in the CryoSat radar freeboard of 15 cm for both areas with a threshold retracker of 40%. This demonstrates as shown in [36], how sensitive the freeboard retrieval is to the SSH determination.

The scatter plot between the laser and radar data from the first study area, showed a fair correlation, Laxon *et al.* [16] finds a correlation of $r = 0.608$ between CryoSat and OIB data. The result was weaker for the second study area north from Svalbard. This is probably a result of 1.) the changing ice cover in between the overpasses, 2.) the many snagging points due to many leads or 3.) because CryoSat in some areas reflects from different layers in the snow pack. It will be beneficial to investigate the CryoSat data in more details to filter out off-ranging elevations, and this may give better correlations.

VII. CONCLUSION

Comparisons of the CryoSat SAR altimeter and CryoVEx and OIB airborne laser altimeter measurements showed overall consistency. Various thresholds of the retracker reveal large differences in the CryoSat elevations, and we found, that a threshold of 40% resembled best the sea ice surface, both in the multi-year ice area, and in the first-year ice area. After a sea ice drift correction was applied, the results from April 2, 2012 for ALS and ATM gave a modal laser freeboard of 53 cm, which as

TABLE III
ALS MODEL LASER FREEBOARD AND CRYOSAT MODAL RADAR FREEBOARD STATISTICS: MEAN, LEAST MEDIAN OF SQUARES OR THE ESTIMATED MODE, THE STANDARD DEVIATION, AND THE OBSERVED MODE FOR RADAR AND LASER FREEBOARD.

	Mean (m)	LMS (m)	SDev. (m)	Mode (m)
ALS	0.312	0.344	0.163	0.325
CryoSat Method 1				
Threshold 40%	0.087	0.114	2.098	0.075
Threshold 50%	0.058	0.086	2.129	0.075
CryoSat Method 2				
Threshold 40%	0.086	0.046	2.103	-0.025
Threshold 50%	0.047	0.041	2.135	-0.025
CryoSat Method 4				
Threshold 40%	0.120	0.200	2.100	0.125
Threshold 50%	0.067	0.087	2.132	0.025

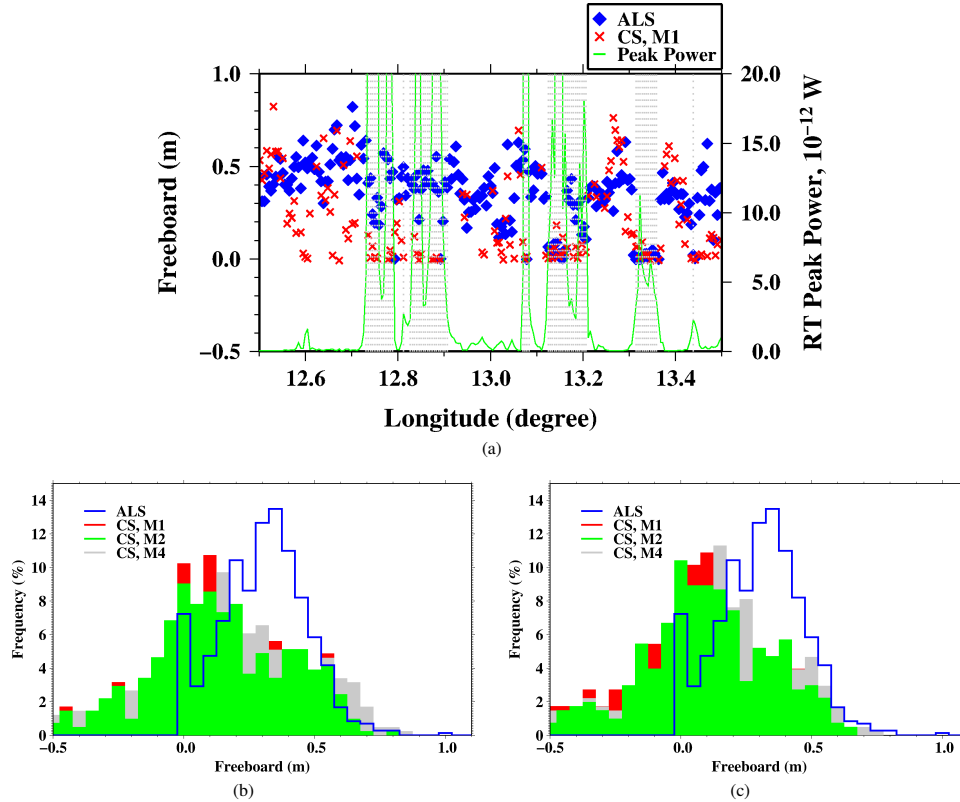


Fig. 10. (a) Comparison of ALS and CryoSat M1 freeboard. (b)-(c) distribution of freeboard (threshold 40% and 50%, respectively) with bin size 0.05 m from ALS and CryoSat M1, M2, M4.

expected corresponded to a multi-year ice area. We used the OIB Quick Look product to apply snow to the CryoSat data in this area.

The CryoSat freeboard was retrieved using five different methods to estimate the SSH, one only using a peak detection algorithm of the CryoSat retracked power. With this method, we found a freeboard of 43 cm without snow, and 53 cm when snow was applied from the OIB Quick Look product. In the second to the fifth methods, the SSH were determined from the laser scanner data, with either using the coordinates from the ALS and ATM leads, or by using the SSH derived from the laser freeboard retrieval. The resulting modal freeboard calculations were found to fit the laser altimeter modal freeboard within 10 cm when snow was applied.

The results from April 27, 2012 after the ice

drift correction was applied, gave for ALS a modal freeboard of 33 cm, corresponding to a first-year ice area, and a modal freeboard of CryoSat within 20-35 cm of this value. We did not have any available snow depth data from the site at this time, but regarding snow model results and in-situ measurements from the year before, indicate that this would be the modal snow depth for the area, i.e. CryoSat mainly penetrates to the snow/ice interface, but we also found a second peak interpreted as a reflection from the air/snow interface.

ACKNOWLEDGMENT

The contents of this paper are the views of the authors and should not be construed as an official NOAA or U.S. government statement of policy or position. We would like to acknowledge the DTU

Space and ESA's CryoVEx crew 2012, NASA's IceBridge Arctic 2012 team, the National Snow and Ice Data Center for distribution IceBridge data, and ESA for providing and processing CryoSat data.

REFERENCES

- [1] J. Comiso, P. Wadhams, W. Krabill, R. Swift, J. Crawford, and W. Tucker III, "Top/bottom multisensor remote sensing of Arctic sea ice," *J. Geophys. Res.*, vol. 96, no. C2, pp. 2693–2709, 1991.
- [2] M. Serreze, M. Holland, and J. Stroeve, "Perspectives on the Arctic's shrinking sea-ice cover," *Science*, vol. 315, no. 5818, pp. 1533–1536, 2007.
- [3] D. Perovich, W. Meier, M. Tschudi, S. Gerland, and J. Richter-Menge, "Sea Ice in Arctic Report Card: Update for 2012," http://www.arctic.noaa.gov/reportcard/sea_ice.html, December 2012. [Online]. Available: http://www.arctic.noaa.gov/reportcard/sea_ice.html
- [4] J. Comiso, C. Parkinson, R. Gersten, and L. Stock, "Accelerated decline in the Arctic sea ice cover," *Geophys. Res. Lett.*, vol. 35, no. 1, p. L01703, 2008.
- [5] J. Stroeve, M. Holland, W. Meier, T. Scambos, and M. Serreze, "Arctic sea ice decline: Faster than forecast," *Geophys. Res. Lett.*, vol. 34, no. 9, p. 9501, 2007.
- [6] M. Wang and J. Overland, "A sea ice free summer Arctic within 30 years," *Geophys. Res. Lett.*, vol. 36, no. 7, p. L07502, 2009.
- [7] C. Haas, S. Gerland, H. Eicken, and H. Miller, "Comparison of sea-ice thickness measurements under summer and winter conditions in the Arctic using a small electromagnetic induction device," *Geophysics*, vol. 62, no. 3, pp. 749–757, 1997.
- [8] D. Rothrock, Y. Yu, and G. Maykut, "Thinning of the Arctic sea-ice cover," *Geophys. Res. Lett.*, vol. 26, no. 23, pp. 3469–3472, 1999.
- [9] P. Wadhams, "Ice thickness in the arctic ocean: The statistical reliability of experimental data," *J. Geophys. Res.-Oceans*, vol. 102, no. C13, pp. 27951–27959, 1997.
- [10] H. Eicken, W. Tucker, and D. Perovich, "Indirect measurements of the mass balance of summer Arctic sea ice with an electromagnetic induction technique," *Ann. Glaciol.*, vol. 33, no. 1, pp. 194–200, 2001.
- [11] C. Haas, S. Goebell, S. Hendricks, T. Martin, A. Pfaffling, and C. von Saldern, "Airborne electromagnetic measurements of sea ice thickness: methods and applications," *Arctic Sea Ice Thickness: Past, Present and Future*, vol. 10, pp. 136–148, 2006.
- [12] S. Laxon, N. Peacock, and D. Smith, "High interannual variability of sea ice thickness in the Arctic region," *Nature*, vol. 425, no. 6961, pp. 947–950, 2003.
- [13] K. Giles, S. Laxon, and A. Ridout, "Circumpolar thinning of Arctic sea ice following the 2007 record ice extent minimum," *Geophys. Res. Lett.*, vol. 35, no. 22, p. L22502, 2008.
- [14] R. Kwok, H. Zwally, and D. Yi, "ICESat observations of Arctic sea ice: A first look," *Geophys. Res. Lett.*, vol. 31, no. 16, p. L16401, 2004.
- [15] R. Forsberg and H. Skourup, "Arctic Ocean gravity, geoid and sea-ice freeboard heights from ICESat and GRACE," *Geophys. Res. Lett.*, vol. 32, no. 21, 2005.
- [16] S. W. Laxon, K. A. Giles, A. L. Ridout, R. Wingham, D. J. and Willatt, R. T. Cullen, R. Kwok, A. Schweiger, J. Zhang, C. Haas *et al.*, "CryoSat-2 estimates of Arctic sea ice thickness and volume," *Geophys. Res. Lett.*, vol. 40, pp. 1–6, 2013.
- [17] P. Wadhams, W. Tucker III, W. Krabill, R. Swift, J. Comiso, and N. Davis, "Relationship between sea ice freeboard and draft in the Arctic Basin, and implications for ice thickness monitoring," *J. Geophys. Res.*, vol. 97, no. C12, p. 20325, 1992.
- [18] S. G. Beaven, G. L. Lockhart, S. P. Gogineni, A. R. Hosset-nmostafa, K. Jezek, A. J. Gow, D. K. Perovich, A. K. Fung, and S. Tjuatja, "Laboratory measurements of radar backscatter from bare and snow-covered saline ice sheets," *Int. J. Remote Sens.*, vol. 16, pp. 851–876, Mar. 1995.
- [19] R. Tonboe, S. Andersen, and L. Pedersen, "Simulation of the Ku-band Radar altimeter sea ice effective scattering surface," *IEEE Geosci. Remote S.*, vol. 3, no. 2, pp. 237–240, 2006.
- [20] R. Willatt, S. Laxon, K. Giles, R. Cullen, C. Haas, and V. Helm, "Ku-band radar penetration into snow cover on Arctic sea ice using airborne data," *Ann. Glaciol.*, vol. 52, no. 57, pp. 197–205, 2011.
- [21] K. Giles, S. Laxon, D. Wingham, D. Wallis, W. Krabill, C. Leuschen, D. McAdoo, S. Manizade, and R. Raney, "Combined airborne laser and radar altimeter measurements over the Fram Strait in May 2002," *Remote Sens. Environ.*, vol. 111, no. 2–3, pp. 182–194, 2007.
- [22] R. Tonboe, L. Pedersen, and C. Haas, "Simulation of the satellite radar altimeter sea ice thickness retrieval uncertainty," *Can. J. Remote Sens.*, vol. 36, no. 1, pp. 55–67, 2010.
- [23] H. Skourup, I. Einarsson, R. Forsberg, S. M. Hvidegaard, J. Nilsson, and A. Olesen, *ESA CryoVEx 2012 - Airborne field campaign, Data Acquisition Report*, National Space Institute (DTU Space), 2012, August 2012.
- [24] W. B. Krabill. (2012) IceBridge Narrow Swath ATM L1B Qfit Elevation and Return Strength [2012.04.12]. Digital media. NASA Distributed Active Archive Center at the National Snow and Ice Data Center. Boulder, Colorado USA. [Online]. Available: <http://nsidc.org/data/insat1b.html>
- [25] R. Dominguez. (2012) IceBridge DMS L1B Geolocated and Orthorectified Images, [2012.04.02]. National Snow and Ice Data Center. Boulder, Colorado USA. [Online]. Available: <http://nsidc.org/data/iodms1b.html>
- [26] S. Farrell, N. Kurtz, L. Connor, B. Elder, C. Leuschen, T. Markus, D. McAdoo, B. Panzer, J. Richter-Menge, and J. Sonntag, "A first assessment of IceBridge snow and ice thickness data over Arctic sea ice," *IEEE T Geosci Remote*, vol. 50, no. 6, pp. 2098–2111, 2012.
- [27] N. T. Kurtz, S. L. Farrell, M. Studinger, N. Galin, J. P. Harbeck, R. Lindsay, V. D. Onana, B. Panzer, and J. G. Sonntag, "Sea ice thickness, freeboard, and snow depth products from Operation IceBridge airborne data," *The Cryosphere Discussions*, vol. 6, no. 6, pp. 4771–4827, 2012. [Online]. Available: <http://www.the-cryosphere-discuss.net/6/4771/2012/>
- [28] D. Wingham, C. Francis, S. Baker, C. Bouzinac, D. Brockley, R. Cullen, P. de Chateau-Thierry, S. Laxon, U. Mallow, C. Mavrocordatos *et al.*, "CryoSat: A mission to determine the fluctuations in Earth's land and marine ice fields," *Adv. Space Res.*, vol. 37, no. 4, pp. 841–871, 2006.
- [29] ESA and UCL, "CryoSat Product Handbook," ESRIN - ESA and Mullard Space Science Laboratory - University College London, Tech. Rep., October 2012.
- [30] C. Davis, "A robust threshold retracking algorithm for measuring ice-sheet surface elevation change from satellite radar altimeters," *IEEE Trans. Geosci. Remote Sens.*, vol. 35, no. 4, pp. 974–979, 2002.
- [31] L. N. Connor, S. W. Laxon, A. L. Ridout, W. B. Krabill, and D. C. McAdoo, "Comparison of Envisat radar and airborne laser altimeter measurements over Arctic sea ice," *Remote Sens. of Environ.*, vol. 113, no. 3, pp. 563–570, 2009.
- [32] S. Hvidegaard and R. Forsberg, "Sea-ice thickness from air-

- borne laser altimetry over the Arctic Ocean north of Greenland," *Geophys. Res. Lett.*, vol. 29, no. 20, p. 1952, 2002.
- [33] S. G. Warren, I. G. Rigor, N. Untersteiner, V. F. Radionov, N. N. Bryazgin, Y. I. Aleksandrov, and R. Colony, "Snow depth on Arctic sea ice," *J. Climate*, vol. 12, no. 6, pp. 1814–1829, 1999.
- [34] N. T. Kurtz and S. L. Farrell, "Large-scale surveys of snow depth on Arctic sea ice from Operation IceBridge," *Geophys. Res. Lett.*, vol. 38, no. 20, 2011.
- [35] J. Haapala, M. Lensu, M. Dumont, A. H. Renner, M. A. Granskog, and S. Gerland, "Small-scale horizontal variability of snow, sea-ice thickness and freeboard in the first-year ice region north of Svalbard," *Annals of Glaciology*, vol. 54, no. 62, p. 261, 2013.
- [36] L. Connor, S. L. Farrell, D. C. McAdoo, W. B. Krabill, and S. Manizade, "Validating ICESat Over Thick Sea Ice in the Northern Canada Basin," *IEEE T. Geosci. Remote*, vol. 51, no. 4, pp. 2188–2200, 2013.

F.5 Ice mélange volume estimates from LiDAR - A snapshot of ice discharge in the Godthåbsfjord, Greenland

Ice mélange volume estimates from LiDAR - A snapshot of ice discharge in the inner Godthåbsfjord, Greenland

Stine K. Rose¹, Rene Forsberg¹, Sine M. Hvidegaard¹, Karina Nielsen², Leif T. Pedersen³, Louise S. Sørensen¹ and Sebastian B. Simonsen¹

¹ Div. of Geodynamics, DTU Space - National Space Institute, Elektrovej, Build. 327-328, 2800 Kgs. Lyngby, Denmark.
E-mail: stine@space.dtu.dk

² Div. of Geodesy, DTU Space - National Space Institute, Elektrovej, Build. 327-328, 2800 Kgs. Lyngby, Denmark.

³ Danish Meteorological Institute, Lyngbyvej 100, 2100 Copenhagen, Denmark.

ABSTRACT. Greenland fjords are regulating the exchange of water masses between the glaciers and the ocean, and the freshwater contribution from the Greenland ice sheet has a strong impact on the ecosystem in the fjords. In many fjords, the calving rate of icebergs from outlet glaciers has a large seasonal variability, as winter sea ice may trap large amounts of icebergs in front of the calving glacier; a phenomena known as ice mélange. Here, we present an estimate of the ice volume of icebergs calved predominately from the main glacier (Kangiata Nunata Sermia), and sea ice in Kangersuneq, southwest Greenland. We use airborne LiDAR to map the topography of the glacier, iceberg and sea ice freeboards in the fjord, to infer the overall volume of ice calved since the first ice mélange formation in the previous autumn. Satellite images are studied to assess the ice conditions in the fjord during the spring season. By applying the principle of isostatic equilibrium, we estimate the total ice mass in the fjord. From this snapshot (27 May, 2009), the ice mass in Kangersuneq is estimated to 1.70 ± 1.26 Gt ice, which accounts for more than a third of the annual discharge from the glaciers.

INTRODUCTION

The Greenland ice sheet (GrIS) is sensitive to changes in the climate. The melt rate of the ice sheet has accelerated during the last decade (Rignot and others, 2008; Shepherd and others, 2012), with corresponding increase in the freshwater flux from the GrIS to the surrounding ocean. The mass loss of the GrIS is ~ 230 Gt/year corresponding to a global sea level rise of ~ 0.6 mm/year (Sørensen and others, 2011; Shepherd and others, 2012; Sasgen and others, 2012). Large changes in the glacier dynamics have been observed, and half of this is due to glacier dynamics such as glacier thinning and calving. Glacier dynamics are to a high degree, affected by regional and local climate forcing (Howat and others, 2007; Moon and others, 2012).

The freshwater contribution from the melting of the GrIS has a global impact on both sea level and ocean salinity, and the amount of freshwater stored in the GrIS corresponds to a rise of the global sea level by about 7.36 m (Bamber and others, 2013). The changes in freshwater flux influence the marine and terrestrial ecosystem, and changes in the ecosystem, can affect the local fishery, and therefore the economy.

This paper focuses on a local area in southwest Greenland; the inner part of Nuup Kangerlua (Godthåbsfjord), the Kangersuneq, where the ice discharge from innermost glaciers Kangiata Nunata Sermia (KNS) and Akugdlerssúp Sermia (AS) are studied (Fig. 1). This paper link the ice sheet thinning, and oceanographic conditions to the changing climate.

Rignot and Kanagaratnam (2006) showed that the outlet glaciers in Kangersuneq have increased their velocity over the last decade, with KNS and Narssap Sermia (NS), located further out in the same fjord system, having a net volume loss of 6 km^3 ice yr^{-1} . They found that KNS experienced an acceleration of mass loss of 6% in the period 1996-2000, and 27 %

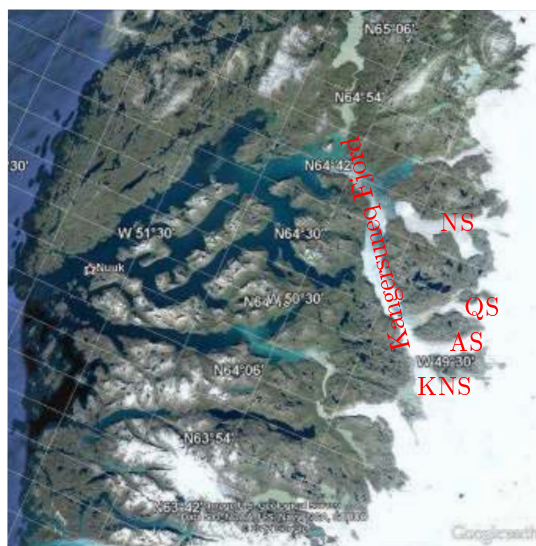


Fig. 1. Site map of the Godthåbsfjord, including Kangersuneq and surrounding area. Image is from U.S Geological Survey Google Earth, data SIO, NOAA, U.S. Navy, NGA, GEBCO adapted from Google Earth 2012. Kangersuneq and the associated glaciers (NS: Narssap Sermia, QS: Qamanârssúp Sermia, AS: Akugdlerssúp Sermia, and KNS: Kangiata Nunata Sermia) are mark with red. NS, AS and KNS are tidewater glaciers, QS is land-terminating. In this image sea ice can be seen in the fjord.

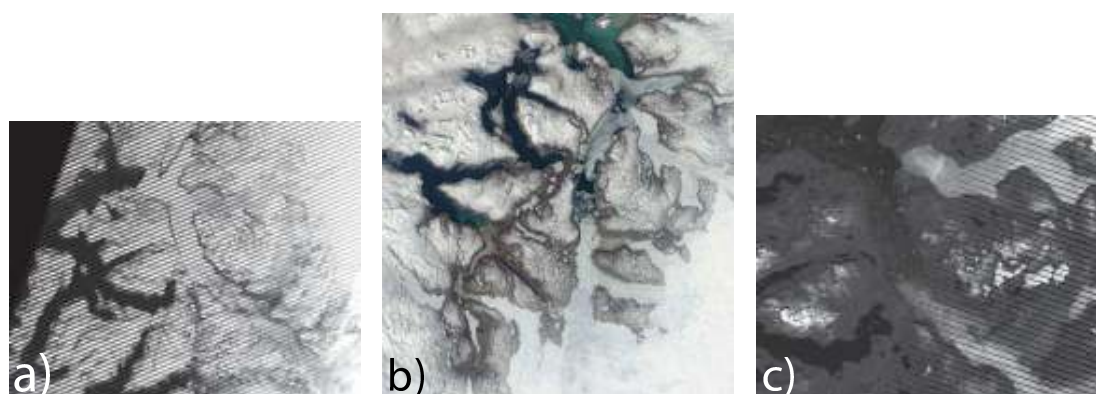


Fig. 2. a) Landsat-7 image from 14 May 2009; sea ice is covering the inner fjord. b) MODIS image from the Terra satellite on 26 May, 2009; a patch with open water is visible in the fjord, and c) Landsat-7 image from 22 June, 2009; a lot of the sea ice have melted or moved out of the inner fjord. All images are cropped to the desired region. The lines in the Landsat images are a satellite artifact.

in 2000–2005. Whereas, the NS glacier had a 68% and 150% acceleration in the same time periods. This acceleration of mass loss are also verified in more recent studies by Joughin and others (2010), Mortensen and others (2013) and Fitzner and others (2013, Pers. com.). In a study by Box and Decker (2011), the KNS glacier front is found to have retreated by 0.1 km/year on average in the period from 2000–2010. Sole and others (2011) show that KNS is controlled by subglacial hydrodynamic forcing rather than by changes in the calving front, and that the calving rate show interannual variation, with the highest rate in summer. From a study in the south-western Greenland based on GPS measurements, an increase in the summer velocity of up to 220% above winter values are found (Bartholomew and others, 2010).

In this paper, we study the icebergs calved of the KNS and AS glaciers, which are a major contributor to the mass loss of the glaciers. Airborne LiDAR measurements supported by precise geodetic GPS positioning and inertial navigation attitude observations, were collected in the Kangersuneq and associated parts of the GrIS in the period 26 – 28 May, 2009. The processed data provide elevation data from the ice sheet margin together with sea ice and iceberg freeboards (height of the ice above the sea local level). This is done by measuring the amount of ice above sea level, assuming isostatic equilibrium and applying an ice density to estimate the total mass.

REGIONAL SETTINGS

The Kangersuneq branch of the Godthåbsfjord is approximately 50 km long, 5 km wide, and has an average depth of 250 m (Mortensen and others, 2013). The Kangersuneq is connected to the GrIS via glaciers in its innermost parts, including the tidewater glaciers KNS, NS, and AS (Fig. 1).

In November new sea ice starts to form in Kangersuneq. The sea ice in the fjord is either first-year ice or fast ice (i.e. frozen into the coast). In winter icebergs are frozen-in in front of the glaciers by sea ice. This is called ice mélange. At this time the glacier front is relative inactive. By May–June, the fast ice starts to break up, releasing rafted and ridged ice together with calved glacial ice accumulated during winter. In summer when the sea ice disappears, the icebergs drift away

from the glacier, where they melt, usually before leaving the mouth of the fjord.

The size of the glacial ice in the fjord reaches its maximum in July, and becomes smaller towards winter. Large amounts of the sea ice and glacial ice in the fjord melt away during summer due to a warm intermediate layer in the fjord. The increased heat in the summer, is equivalent to a melt of about 2.1 km³ glacial ice from the KNS glacier (Mortensen and others, 2011). Estimates of the total ice volume of frozen-in icebergs, held together with mass loss of the glacier, indicate the amount of melt from the relative warm fjord water (Mortensen and others, 2011).

We examine Landsat and MODIS imagery of the fjord, provided by NASA and US Geological Survey, before and after the date of LiDAR measurements to observe if there has been ice movement out of the fjord, i.e. if the ice mélange has broken up. These images show that the ice is still laying in the fjord 14 May, 2009 (Fig. 2a). By 26 May, an open water patch is visible on a MODIS images (Fig. 2b) between the KNS and the NS glacier. This may indicate the start of ice discharge out of the fjord. In the end of June, there is definitely ice movement in the fjord, maybe from newly calved ice (Fig. 2c).

DATA

Airborne data

The measurements were acquired from the Air Greenland Twin-Otter OY-POF, operating from Kangerlussuaq Airport. The DTU-Space hardware consisted of a Riegl Q240 LiDAR, capable of swath mapping the heights of the ice surface at 2 – 3 cm accuracy for a swath width roughly equal to the flight attitude (nominally 1200 ft above the surface). The position of the aircraft was determined by Global Positioning System (GPS) receivers (Trimble and Javad), and the attitude by a Honeywell H764 integrated Inertial Navigation System (INS)/GPS.

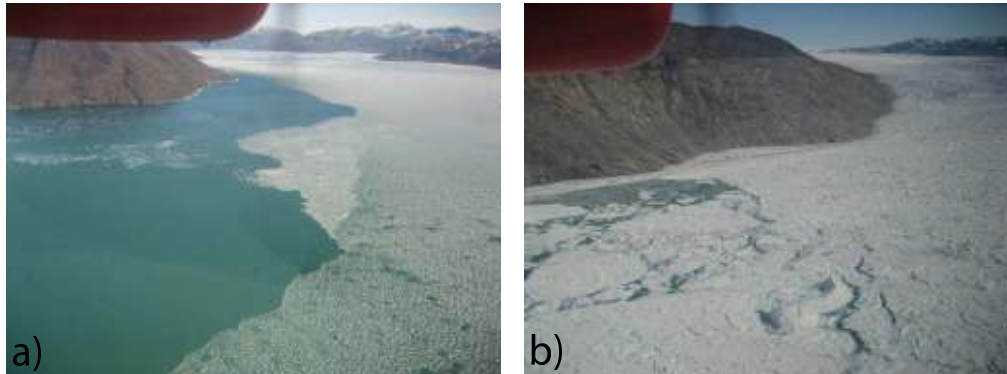


Fig. 3. Ice conditions in the Kangarsuneq fjord. a) Thin sea ice, and b) small icebergs locked in the sea ice, this is the ice mélange.

METHOD

GPS and LiDAR Processing

The position of the aircraft was processed with differential GPS using dual-frequency. The International Global navigation satellite system Service (IGS) station at Kellyville (Kely) was used as reference GPS station. The solution was based on static processing of the base station to fix the coordinates, and kinematic differential processing to archive the position of the aircraft. The position of the permanent station Kely was determined using the online processing service AUSPOS operated by the Australian Government's agency, Geoscience Australia. The GPS data were processed with the longest baseline being approximately 280 km. Data were processed w.r.t. the WGS84 ellipsoid. The average standard deviation of the vertical height, calculated from every processed point was 5.91 cm, and the average 3D Positional Dilution of Precision (PDOP) was calculated to 1.66. The position and attitude information were extracted from INS data packets and averaged to 10 Hz. The GPS and INS data were merged by draping the INS derived positions onto the post processed GPS positions to form a uniform navigation and attitude file for the LiDAR. The accuracy on the vertical height from airborne GPS measurements in the Arctic are usually better than 10 cm (Skourup and others, 2013a), and in individual cases down to 3 cm (Skourup and others, 2013b).

The LiDAR were geolocated and the position derived in the earth fixed system from GPS, and the attitude information. Calibration of the LiDAR misalignment angles were performed by overflight of a building in the airport with known GPS coordinates, as well as scanning of the runway. These calibrations indicated some problems and reduced the accuracy of the INS, likely due to problems with the real time kalman filter. This affected the accuracy of pitch and roll, and the point cloud accuracy, was estimated to 20 – 30 cm root mean square (RMS) instead of the usual 5 – 10 cm (Forsberg and others, 2007).

Estimating the floating ice volumes

From a visual inspection from the aircraft, the amount of ice in the fjord was quite small, with only the inner 5 km in front of the glaciers choked with icebergs. The rest of the inner fjord was covered with thin, melting sea ice and scattered small icebergs (Fig. 3).

In the floating ice volume determination, the ellipsoidal heights obtained from the LiDAR measurements are converted into heights above sea level (geoid heights) by using the Arctic Gravity Project (ArcGP) geoid (Forsberg and others, 2006). A rough filtering of data were applied, in which elevations below –1 m and above 60 m were rejected. Tie points of local sea surface between ice floes were selected, based on a lowest level filtering algorithm performed by a least-square collocation function (Hvidegaard and Forsberg, 2002), to minimize geoid and system errors in the LiDAR. To lower the variability in the along-track LiDAR data, these were averaged into grid cells with a resolution of $0.02^\circ \times 0.01^\circ$.

A volume estimate is obtained by interpolating the ice heights above sea level using ordinary local neighborhood kriging (Nielsen and others, 2013) onto a regular grid with a resolution of $0.02^\circ \times 0.01^\circ$ spanning about -52.2°E to -49.5°E and 64.2°N to -64.5°N . The grid is bounded by the coastline and the calving front which are derived from the Landsat image (Fig. 2c). The distribution of the ice height is strongly positive skewed and to account for this the heights are log-transformed before the kriging procedure. After prediction a back-transformation is necessary to obtain the estimated heights at their original level. The uncertainty of the total ice volume above sea level is estimated by summing the elements of the kriging covariance matrix.

The total floating ice volume (sail and keel) in the fjord was determined by assuming isostatic equilibrium with the surrounding fjord water. The total ice volume is given by

$$V_i = kV_f, \quad (1)$$

where $k = \frac{\rho_w}{\rho_w - \rho_i}$, V_i is the total ice volume, and V_f is the volume of ice above the sea surface, ρ_w and ρ_i are the water and ice densities, respectively.

ICE VOLUME RESULTS

The elevation data w.r.t the geoid were filtered and interpolated to a local sea level. The location of the glacier termini was extracted by the Landsat image, and the resulting elevation data from the LiDAR (see Fig. 4) are interpolated by kriging to cover the whole fjord. The interpolated ice height map is shown in Fig. 5. The ice heights are largest near the calving front and decreases gradually away from the front.

4

Rose and others: Ice mélange volume estimates

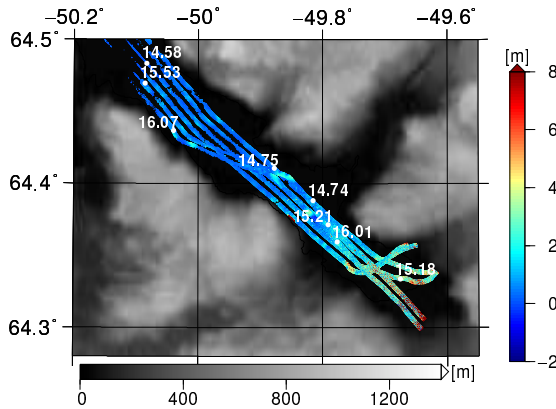


Fig. 4. Elevations in the innermost fjord relative to the local sea level, where the LiDAR data are cut at the glacier terminus. The background is the full resolution the Advanced Spaceborne Thermal Emission and Reflection Radiometer (ASTER) Global Digital Elevation Model (GDEM) produced at the US Geological Survey EROS Data Center. The numbers in the map indicate the time of the overflight given in UTC hours.

A regular distribution of sea ice is seen across the fjord, and this is supported by visible inspection of sea ice and icebergs from the aircraft (Fig. 3)

The mean ice freeboard volume in the fjord is $0.19 \pm 0.14 \text{ km}^3$. A standard value for the ice density of $\rho_i = 917 \text{ kg m}^{-3}$ (Paterson, 1981), is used, together with a density of $\rho_w = 1023.15 \text{ kg m}^{-3}$ for the top layer of the Godthåbsfjord based on measurements from July 2008 in Mortensen and others (2011). This gave a proportionality constant of $k = 9.63 \pm 0.52$, when using uncertainties of 0.5 kg m^{-3} and 5 kg m^{-3} for water and ice densities, respectively (Wadhams and others, 1992). However, these uncertainties are too small to influence the total uncertainty. The proportionality constant yields a total ice volume in the fjord of $1.86 \pm 1.37 \text{ km}^3$, corresponding to $1.70 \pm 1.26 \text{ Gt}$ ice.

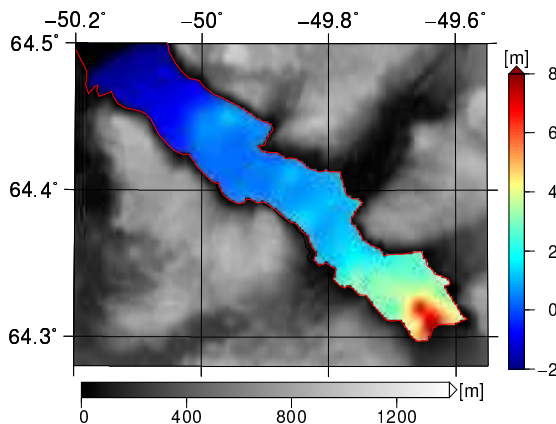


Fig. 5. The interpolated ice conditions in the fjord system w.r.t the local sea level. The thin red line indicate the coastline extracted from the Landsat image.

DISCUSSION

The LiDAR data have an accuracy of 20 – 30 cm RMS, due to the problems with the INS. This has caused more noise on the measurements than normally (Forsberg and others, 2007). Through this study, we made assumptions of the ice volume estimate, i.e. that the sampling profiles were representative for the fjord as a whole, and about the icebergs and ice and water densities. We have kept the ice density constant, but actually the density of the ice differs from region to region and season to season. Rothrock (1986) writes, that the most uncertain estimate in the sea ice volume determination is the density. In a recent study by Alexandrov and others (2010), they use field measurements, and find an ice density of first-year sea ice of $916.7 \pm 35.7 \text{ kg m}^{-3}$ and $882 \pm 23 \text{ kg m}^{-3}$ from perennial sea ice. We would expect the glacial ice to be very close to 917 kg m^{-3} , which is ice in its most pure form, and furthermore the sea ice in the fjord is first-year ice. A density of 830 kg m^{-3} is usually associated with the pore-close off in firn, and may define the transition from firn to ice (Paterson, 1981). If we assume, that the ice volume in the fjord, had a density of 850 kg m^{-3} , the total volume would be $\sim 1.12 \text{ km}^3$ or 0.95 Gt ice with $k = 5.9$.

Also the water density varies in the fjord; Mortensen and others (2011) discuss the density variation in the Godthåbsfjord, and how the density profile is observed to vary due to the bottom topography and tidal currents. We use water densities from the local fjord survey, which we expect to be the best density for this study. But water densities for the surface water varies locally and with seasons between 120 to 129 kg m^{-3} , and it varies especially in the inner fjord due to freshwater run-offs from the glaciers. The fjord is in general less saline in the Arctic due to river run-off from the glaciers, where the salinity increases with depth. We take the ratio of the ice volume density and seawater as constant, but as Bass (1980) pointed out the ratio can change up to 10%, due to air in the ice, though 2% is more likely in the Arctic. Our derived k -ratio is in good agreement with other studies (Dowdeswell and Bamber, 2007).

The uncertainty on the resulting ice volume is large, and the interpolation of the ice elevation from the coarse flight tracks of the LiDAR data point and the natural variability gave rise to a large variance. To improve this, we would need a more dens flight pattern over the fjord.

During winter sea ice holds back the glacial ice from moving out of the fjord. Even though sea ice and glacial ice will be melting during the winter season (Mortensen and others, 2013), we would expect the ice volume in the fjord to be larger in late winter, than average estimates. From Fig. 2 and 3, it was evident that the sea ice already started to melt away by May, 2009.

Our result of $1.86 \pm 1.37 \text{ km}^3$ is a snapshot of the ice conditions in the Kangarsuneq 27 May, 2009, which include ice discharge from KNS and AS and sea ice situated in the fjord. It is therefore difficult directly to compare the results with the KNS/NS yearly flux of $6 \text{ km}^3 \text{ yr}^{-1}$ reported by Rignot and Kanagaratnam (2006). Scaling the glacial meltwater flux found by Fitzner and others (2013, Pers. com.) with inter-annual changes in glacier surface velocity (Joughin and others, 2011) the 2008–2009 glacial flux was found to be $4.4 \text{ km}^3 \text{ yr}^{-1}$ and $0.4 \text{ km}^3 \text{ yr}^{-1}$ from the KNS and the AS glaciers, respectively.

We measure a volume equivalent of 38% of the yearly glacial flux from the two glaciers, which is a large portion of the

flux captured by one LiDAR snapshot, even with sea ice included. Accounting for seasonal changes in calving fluxes, the ice volume we measure in the ice mélange are most likely, ice trapped from the previous summer speed-up, apart from the ice melted during winter. Furthermore, implies that the ice mélange in front of KNS and AS, only slowly release ice into the outer Kangarsuneq, but this is only speculations.

SUMMARY AND CONCLUSION

In this study, we have used airborne LiDAR data in Kangarsuneq, southwest Greenland, in front of the KNS and the AS glaciers, to observe the calved glacial ice and the sea ice floating in the fjord.

A lowest level filtering algorithm was used to determine the local sea level to obtain freeboard heights of the glacial ice and sea ice in the fjord. The freeboard height where interpolated to cover the whole fjord by kriging. We found a snapshot of the floating ice volume in Kangarsuneq 27 May 2009 to yield 1.70 ± 1.26 Gt ice, predominately from the two tidewater glaciers KNS and AS.

From airborne altimetry it is possible to estimate the ice volume in the fjord, but we need more data, preferably sampled during the year, to compare the method to other studies with yearly estimates. It should then be possible to monitor the ice volume in the fjord by satellites. The presented study are then timely as data from CryoSat-2 and future data from ICESat-2 will emerge, and contribute to the understanding of the freshwater flux into fjords originating from land ice.

ACKNOWLEDGMENT

The flights of the project were sponsored by the Freshlink project, supported by the Danish Natural Science Research council. We thank NASA and US Geological Survey for providing the Landsat and MODIS images.

REFERENCES

- Alexandrov, V., S. Sandven, J. Wahlin and OM Johannessen, 2010. The relation between sea ice thickness and freeboard in the Arctic, *The Cryosphere*, **4**, 641–661.
- Bamber, Jonathan L, J A Griggs, R T W L Hurkmans, J A Dowdeswell, S.P. Gogineni, I Howat, J Mouginot, J Paden, S Palmer, E. Rignot and D Steinhage, 2013. A new bed elevation dataset for Greenland, *The Cryosphere*, **7**(2), 499–510.
- Bartholomew, Ian, Peter Nienow, Douglas Mair, Alun Hubbard, Matt A King and Andrew Sole, 2010. Seasonal evolution of subglacial drainage and acceleration in a Greenland outlet glacier, *Nat. Geosci.*, **3**(6), 408–411.
- Bass, DW, 1980. Stability of icebergs, *Ann. Glaciol.*, **1**, 43–47.
- Box, J.E. and D.T. Decker, 2011. Greenland marine-terminating glacier area changes: 2000–2010, *Ann. Glaciol.*, **52**(59), 91–98.
- Dowdeswell, J. A. and J. L. Bamber, 2007. Keel depths of modern Antarctic icebergs and implications for sea-floor scouring in the geological record, *Mar. Geol.*, **243**(1–4), 120–131.
- Fitzner, A, D van As, J Bendtsen, D. Dahl-Jensen, X Fettweis, J Mortensen and S Rysgaard, 2013. Estimating the glacial meltwater contribution to the freshwater budget from salinity and $\delta^{18}\text{O}$, *Journal of Geophysical Research(In prep.)*, 1–17.
- Forsberg, R., H. Skourup, O. Andersen, P. Knudsen, S. W. Laxon, A. Ridout, A. Braun, J. Johannessen, C. C. Tscherning and D. Arabelos, 2006. Arctic Ocean Geoid, Ice Thickness and Mean Sea Level - The ARCGICE Project, Proceedings ESA workshop "15 years of progress in radar altimetry", Venice.
- Forsberg, R., H. Skourup, O. B. Andersen, P. Knudsen, S. W. Laxon, A. Ridout, J. Johannessen, F. Siegismund, H. Drange, C. C. Tscherning, D. Arabelos, A. Braun and V. Renganathan, 2007. Combination of Spaceborne, Airborne and In-Situ Gravity Measurements in Support of Arctic Sea Ice Thickness Mapping, *Technical report no 7*, Danish National Space Center.
- Howat, I.M., I. Joughin and T.A. Scambos, 2007. Rapid changes in ice discharge from Greenland outlet glaciers, *Science*, **315**(5818), 1559.
- Hvidegaard, SM and R. Forsberg, 2002. Sea-ice thickness from airborne laser altimetry over the Arctic Ocean north of Greenland, *Geophys. Res. Lett.*, **29**(20), 1952.
- Joughin, I, B Smith, I Howat and T Scambos, 2011. MEASUREs Greenland Ice Velocity: Selected Glacier Site Velocity Maps from InSAR. (Updated 2013), *National Snow and Ice Data Center, Boulder, Colorado, USA*.
- Joughin, Ian, Ben E Smith, Ian M Howat, Ted Scambos and Twila Moon, 2010. Greenland flow variability from ice-sheet-wide velocity mapping, *J. Glaciol.*, **56**(197), 415–430.
- Moon, T, I Joughin, B Smith and I Howat, 2012. 21st-century evolution of Greenland outlet glacier velocities, *Science*, **336**(6081), 576–578.
- Mortensen, J, J Bendtsen, RJ Motyka, K Lennert, M Truffer, M Fahnestock and S Rysgaard, 2013. On the seasonal freshwater stratification in the proximity of fast-flowing tidewater outlet glaciers in a sub-Arctic sill fjord, *J. Geophys. Res.-Oceans*.
- Mortensen, J, K Lennert, J Bendtsen and S Rysgaard, 2011. Heat sources for glacial melt in a sub-Arctic fjord (Godthåbsfjord) in contact with the Greenland Ice Sheet, *J. Geophys. Res.-Oceans*, **116**(C1).
- Nielsen, Karina, Shfaqat A Khan, Giorgio Spada, John Wahr, Michael Bevis, Lin Liu and Tonie Dam, 2013. Vertical and horizontal surface displacements near Jakobshavn Isbræ driven by melt-induced and dynamic ice loss, *J. Geophys-Solid Earth*, 1–9.
- Paterson, W.S.B., 1981. The physics of glaciers, Pergamon, New York.
- Rignot, E., JE Box, E. Burgess and E. Hanna, 2008. Mass balance of the Greenland ice sheet from 1958 to 2007, *Geophys. Res. Lett.*, **35**(10.1029).
- Rignot, E. and P. Kanagaratnam, 2006. Changes in the velocity structure of the Greenland Ice Sheet, *Science*, **311**(5763), 986–990.
- Rothrock, DA, 1986. Ice thickness distribution-measurement and theory, *The geophysics of sea ice*, 551–575.
- Sasgen, I., M. van den Broeke, J. L. Bamber, E. Rignot, . Sandberg Sørensen, B. Wouters, Z. Martinec, I. Velicogna and S. B. Simonsen, 2012. Timing and origin of recent regional ice-mass loss in Greenland, *Earth Planet Sc Lett*, **333**, 293–303.
- Shepherd, A., E. R. Ivins, A. G., V. R. Barletta, M. J. Bentley, S. Bettadpur, K. H. Briggs, D. H. Bromwich, R. Forsberg, N. Galin and others, 2012. A reconciled estimate of ice-sheet mass balance, *Science*, **338**(6111), 1183–1189.
- Skourup, H., V. Barletta, I. Einarsson, R. Forsberg, C. Haas, V. Helm, S. Hendricks, S. M. Hvidegaard and L. S. Srensen, 2013a. ESA CryoVEx 2011, Airborne field campaign with ASIRAS radar, EM induction sounder and laser scanner, National Space Institute (DTU Space), Tech. report.
- Skourup, H., I. Einarsson, R. Forsberg, S. M. Hvidegaard, J. Nilsson and A.V. Olesen, 2013b. ESA CryoVEx 2012 - Airborne field campaign, Data Acquisition Report, National Space Institute (DTU Space), TEch. report.
- Sole, A. J., D. W. F. Mair, P. W. Nienow, I. D. Bartholomew, M. A. King, M. J. Burke and I. Joughin, 2011. Seasonal speedup of a Greenland marine-terminating outlet glacier forced by surface melt-induced changes in subglacial hydrology, *J. Geophys. Res.-Earth*, **116**(F3).

- Sørensen, LS, SB Simonsen, K Nielsen, P Lucas-Picher, G Spada, G Adalgeirsdottir, R Forsberg and CS Hvidberg, 2011. Mass balance of the Greenland ice sheet (2003-2008) from ICESat data-the impact of interpolation, sampling and firn density, *Cryosphere*, **5**, 173–186.
- Wadhams, P., WB Tucker III, WB Krabill, RN Swift, JC Comiso and NR Davis, 1992. Relationship between sea ice freeboard and draft in the Arctic Basin, and implications for ice thickness monitoring, *J. Geophys. Res.*, **97**(C12), 20325.

Appendix G

Posters

This appendix contains the posters presented at various conferences and workshops during the Ph.D study.

CryoSat-2 Validation and Preliminary Results



S. Kildegaard Poulsen^{(*)1}, S. M. Hvidegaard¹, L. Stenseng¹, H. Skourup¹, L. T. Pedersen², R. Forsberg¹
 1. National Space Institute, DTU Space, Juliane Maries Vej 30, DK-2100 Copenhagen Ø, Denmark
 2. Danish Meteorological Institute, Lyngbyvej 100, DK-2100 Copenhagen Ø, Denmark
 (*stine@space.dtu.dk)

CryoSat-2 Validation Up to Now

CryoVEx

DTU Space is part of the CryoSat Calibration and Validation team (CryoVEx), the object of which is to provide pre-launch reference datasets for CryoSat-2. We undertake measurements of ice sheets elevations and sea-ice thickness and make ice profiles from measurements. The campaign is aimed in particular at understanding miscellaneous sources of error: snow loading, ice density, radar penetration, preferential sampling and various freeboard measurement errors. CryoVEx is a joint effort of ESA, DTU Space and other European and Canadian research groups.

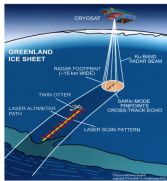


Fig 1. CryoSat validation principles.

CryoSat-2

CryoSat-2 is aimed at observing changes in the Earth's cryosphere, i.e. changes to the ice- and snow-covered parts of the Earth. The satellite was launched on 8 April 2010, it has an inclination angle of 92° and a mean altitude of 717 km. CryoSat-2 is carrying the SIRAL instrument, which is a radar altimeter, able to measure in SAR mode over sea-ice, interferometric mode (SARin) over rapidly varying topographic features on the ice sheet margins and low-resolution mode (LRM) over the interior of the ice sheet and over ocean.

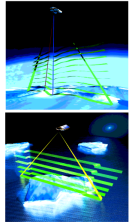


Fig 2. Top figure: SAR. Bottom figure: SARin

Airborne and In-situ Measurements

Extensive validation campaigns to gather a multitude of ground truth measurements were carried out in the Arctic prior to the launch of the first CryoSat mission and now continue for CryoSat-2. The campaigns consist of airborne radar/laser altimetry, EM sounding, and in-situ observations.



Fig 3. Airborne radar and laser measurements.



Fig 4. Measurement of sea-ice thickness.



Fig 5. Corner reflector and helicopter with EM-bird



Fig 6. Snow probe measurement.

CryoSat-2 Validation 2011

Plans for CryoVEx 2011

The CryoVEx 2011 Arctic campaign will be carried out during April and early May. Underflights of CryoSat will be performed together with overflights of ground teams. The main sites will be over sea-ice near CFS Alert, Canada and north of Svalbard (coordinated with RV Lance cruise) and over ice in central Greenland, Devon Ice Cap, Canada and Nordaustfonna, Svalbard.

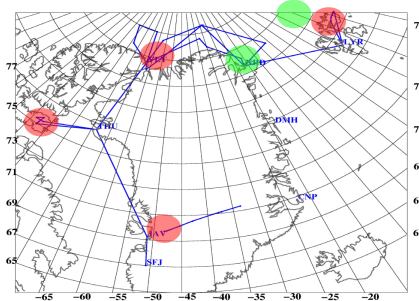


Fig 7. Figure: CryoVEx 2011 main sites (coloured dots) with CryoVEx 2008 as background.

The preliminary schedule is:
 Mid April: Sea ice flights with airborne radar, laser and EM sounding with ground teams directly on the sea ice.
 End of April to Early May: Land ice flights of EGIG line (Central Greenland), Austfonna Svalbard together with sea ice north of Svalbard, and over Devon Ice Cap.

The airborne surveying will be done with the Twin Otter carrying radar and laser altimeters observing the surface elevation and with the German Polar 5 (DC3) with EM sounding measuring the total sea ice thickness.

The results from CryoVEx 2011 will be analysed together with CryoSat-2 data.

Preliminary Results from CryoSat-2

CryoSat-2 data

The following data described, is from a SAR line (82.7N, 9.4E - 84.5N, 3.7E), the 09.13.2010 at 20:28:52 - 20:39:34. The echo is retracked with an OCOG retracker. There are large deviations in the height and we see a saw-tooth-like appearance this is probably due to, that most of the energy is concentrated in one sample bin. We need a better retracker!

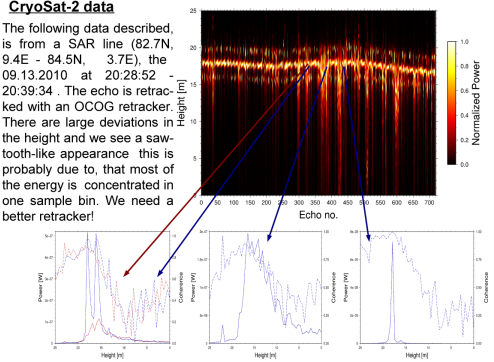
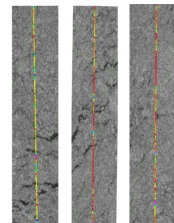


Fig 8. Top: Radargram showing the normalized power as a function of echo and height. Bottom: four waveforms, no. 325 (red), 330, 385, 449. Solid line: power, Dotted line: coherence between interferometric channels.

The two peaks in the waveform no. 325 are from two separate reflectors, because the coherence is almost 1. The slow increase in no. 385 around the leading edge, and decrease with the trailing edge, could indicate a smooth surface. In waveform no. 449, it clearly shows, how the power is sampled in one bin. The return signal is almost 200 times larger, than in the other signals.



The SAR image shows a region with sea-ice. There is apparently no correspondence between the freeboard heights (the sea-ice height over the sea surface), given by the CryoSat-2 data, and the leads (open water between ice floes) visible in the SAR image as black features. However, no correction for possible ice drift, doing the three hours, has been made.

Fig 10. Freeboard from the CryoSat line plotted on the SAR pictures from 17:21 UTC. The color scale increases from blue to orange. It is difficult to distinguish ice types in late Summer, but based on the knowledge of ice conditions in this region before Summer, we assume it is multi-year ice, measuring 1.5-3 m in thickness.

Initial results of CryoSat-2 data from the Arctic

Stine K. Poulsen^{1*}, Lars Stenseng³, Henriette Skourup¹, Leif T. Pedersen², Rene Forsberg¹, Louise S. Sørensen¹

¹Div. of Geodynamics, DTU Space, National Space Institute, Copenhagen, Denmark.

²Danish Meteorological Institute, Copenhagen, Denmark.

³Div. of Geodesy, DTU Space, National Space Institute, Copenhagen, Denmark.

*E-mail: stine@space.dtu.dk



Introduction

In this study, we present initial results of lead detection in sea-ice from CryoSat-2 commissioning phase L1b SAR data. Data are retracked with an 80% threshold and a 5 parameter β -retracker. The threshold retracker showed the best results. Furthermore, freeboard values are calculated by interpolating the DTU10 Mean Sea Surface (MSS) model [1]. The results are compared with an Envisat ASAR image.

CryoVEx

DTU Space is part of the CryoSat Calibration and Validation team (CryoVEx), the object of which is to provide reference datasets for CryoSat-2. We undertake measurements of ice sheet elevations and sea-ice thicknesses. The CryoVEx campaign is, aimed at understanding miscellaneous sources of error: snow loading, ice density, radar penetration, preferential sampling and various freeboard measurement errors. CryoVEx is a joint effort of ESA, DTU Space and other European and Canadian research groups.

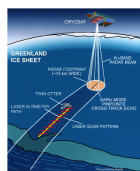


Figure 1: CryoSat validation principles.

CryoVEx 2011

The CryoVEx 2011 Arctic campaign will be carried out during April and early May. Underflights of CryoSat will be performed together with overflights of ground teams performing in-situ measurements. The main sites will be over sea-ice near CFS Alert, and north of Svalbard (coordinated with RV Lance cruise), and over continental ice in central Greenland, Devon Ice Cap, and Nordaustfonna. The airborne surveying will be done from a Twin Otter carrying radar and laser altimeters observing the surface elevation, and with the German Polar 5 (DC3) with EM sounding measuring the total sea ice thickness. The results from CryoVEx 2011 will be analyzed together with CryoSat-2 data.

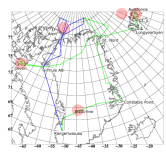


Figure 2: CryoVEx 2011 main sites (red dots). The work will be carried out during April and early May.

Retracking

- The shape of the returned radar echo; is a combination of the range to the different illuminated reflectors, scattering properties and position within the antenna beam pattern.
- The complexity of the returned echo is related to the complexity of the illuminated surface.
- The echo is affected by thermal, speckle noise and impulse response of the radar.
- We have used an 80% threshold and a five parameter β -retracker [2].
- The threshold retracker developed by [3], is intended for measuring ice-sheet elevations. The position of the leading edge of the return waveform is derived by locating the first range bin to exceed a percentage of the maximum waveform amplitude. This is here achieved by the OCOG amplitude.
- The β -retracker, developed by [4], is a fitting algorithm with 5- or 9-parameter functional form of the returned power, to fit single or double-ramped waveforms, respectively.

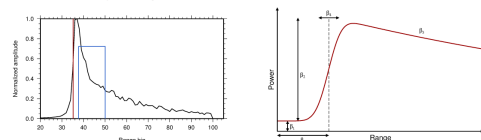


Figure 3: Left: 80% threshold retracker, where the position of the leading edge is determined with OCOG retracker. Right: Five parameter β -retracker.

Sea-ice north of Svalbard, Fall

The data used, is from a CryoSat-2 SAR L1b line, from the 2010.10.08 at 19:08:00 UTC, going north from Svalbard. Echo no. 1300-1800.

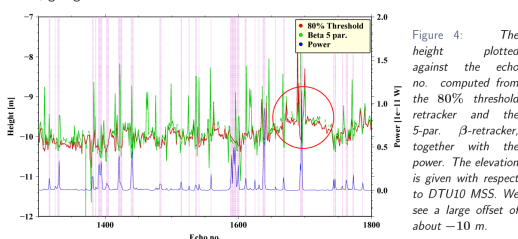


Figure 4: The height plotted against the echo no. computed from the 80% threshold retracker and the 5-par. β -retracker, together with the power. The elevation is given with respect to DTU10 MSS. We see a large offset of about -10 m.

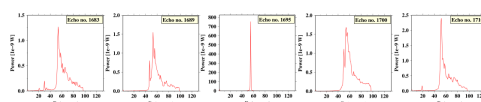


Figure 5: Waveforms showing rough surface (echo 1683), very rough ice (echo 1689), very smooth surface i.e. lead (echo 1695), very rough ice (echo 1700) and rough ice (echo 1710).

- The five waveforms plotted in Fig. 5, are associated with echoes within the red circle in Fig. 4 and 6.
- The ASAR image, 19:17 UTC, Fig. 6, shows a region with multi-year ice.
- The CryoSat-2 track is delayed nine minutes compared to the image, i.e. assuming no movements in the ice.
- Height extracted from the 80% retracker, and with respect to DTU10 MSS [1].
- A lowest level least square collocation filtering procedure [5], is used to detect the local sea surface heights.
- There is a clear correspondence between the freeboard heights, and the leads visible in the ASAR image as black features.
- Large freeboard around the leads, resembling pressure ridges. Fig. 6.

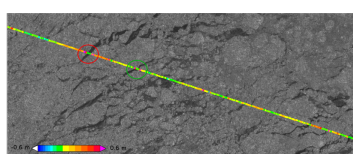


Figure 6: Freeboard calculated from the CryoSat-2 line plotted on an Envisat ASAR 100 m resolution image from 19:17 UTC. Based on the knowledge of the ice conditions in this region in spring, and the found heights, we assume it is multi-year ice, measuring 1.5-3 m in thickness.

Conclusion

The SAR CryoSat-2 track was compared with the Envisat ASAR image, and it showed good agreement. It was possible to detect leads, and they were verified with waveforms around one lead. This work will be improved, and further investigations of the data and retracking procedure, will be undertaken, to give more reliable results. Finally, these studies will be validated after the CryoVEx campaign 2011.

References

- [1] O. B. Andersen and P. Knudsen. The DTU10 global Mean sea surface and Bathymetry. In *Geophysical Research Abstracts*, volume 10. European Geophysical Union, 2008.
- [2] L. Stenseng and O. B. Andersen. First Results of Recovery of Short Wavelength Gravity Field Signals from CryoSat-2 Data. In *ESA CryoSat Validation Workshop*, February 1-3 2011.
- [3] CH Davis. A robust threshold retracking algorithm for measuring ice-sheet surface elevation change from satellite radar altimeters. *Geoscience and Remote Sensing, IEEE Transactions on*, 35(4):974-979, 2002.
- [4] T.V. Martin, H.J. Zwally, A.C. Brenner, and R.A. Bindaschadler. Analysis and retracking of continental ice sheet radar altimeter waveforms. *Journal of Geophysical Research*, 88(C3):1608-1616, 1983.
- [5] Henriette Skourup. A study of Arctic sea ice freeboard heights, gravity anomalies and dynamic topography from ICESat measurements. PhD thesis, University of Copenhagen, 2009.

Arctic tides from GPS on sea-ice

Stine K. Rose^{1*}, Henriette Skourup¹, Rene Forsberg¹

¹Div. of Geodynamics, DTU Space, National Space Institute, Kgs. Lyngby, Denmark.

*E-mail: stine@space.dtu.dk

DTU Space
National Space Institute

Introduction

The presence of sea-ice in the Arctic Ocean plays a significant role in the Arctic climate. Sea-ice dampens the ocean tide amplitude up to 40%, and can have a phase shift up to 1 h [1], with the result that global tidal models perform less accurately in the polar regions. This study presents, a kinematic processing of Global Positioning System (GPS) placed on sea-ice, at six different sites north of Greenland for obtaining the Sea Surface Height (SSH), and to improve tide models in the Central Arctic. The GPS measurements are compared with the Arctic tide model AOTIM-5, which assimilates tide-gauges and altimetry data. This work was carried out as a test study for the ongoing SATICE project, where a long-term tidal network of GPS buoys will be deployed in the Arctic Ocean north of Greenland and northeast of Canada. More details about this work are found in [2].

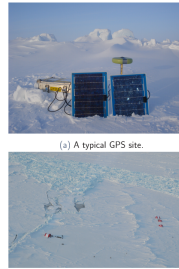


Figure 1

Method

In the period from 20 March to 1 May 2009, a GPS network with six receivers was established north of Greenland on drifting sea-ice and on fast ice close to the coast. Fig. 2, together with a corresponding measurement from a 2006 campaign. The GPS data were processed differential using the kinematic baseline processor Waypoint GrafNav 8.20 from Novatel. For more details see [2].

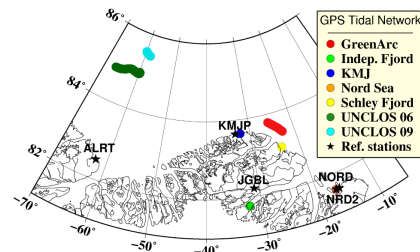


Figure 2: The location of GPS receivers in the tidal network. The black stars represent the permanent GPS reference stations, and the DTU Space deployed reference station (NRD2).

SSH and Geophysical parameter corrections

The SSH (h_{SSH}) can be measured directly by GPS (h) with respect to a reference ellipsoid. In terms of ellipsoidal height (h), SSH is expressed as

$$h_{SSH} = h - h_{AH} - h_{FB} \quad (1)$$

where h_{AH} is the GPS antenna height over the sea-ice, and h_{FB} is the sea-ice freeboard, defined as the part of the sea-ice above the sea surface. The SSH can also be expressed by various geophysical parameters;

$$h_{SSH} = N + h_{tides} + h_{DT} + h_{IBE} + h_{errors} \quad (2)$$

The parameters are; the geoid (N), the tides (h_{tides}) including the ocean tide, load tide, solid earth tide and the permanent tide, the dynamic topography (h_{DT}), the inverse barometric effect (h_{IBE}) caused by atmospheric loading, and height corrections (h_{errors}) from instrument and model inaccuracies.

Tides are not defined in a geodetic reference frame, but to an averaged zero sea level without any explicit reference frame. We expect the GPS tidal observations to be biased by about 71 cm in the study area relative to the actual mean SSH, because the reference ellipsoid of the WGS84 system refers to an Earth ellipsoid larger than the "best" mean Earth ellipsoid (as approximated by the T/P ellipsoid) [3]. This bias is added to Equation (1).

Site	\bar{h} (m)	\bar{N} (m)	h_{AH} (cm)	h_{FB} (cm)	h_{DT} (cm)	h_{IBE} (cm)	h_{tide} (cm)	h_{perm} (cm)
GreenArc	28.28	28.21	50	20	59.5	-7.05 to -1.25	-5.58 to 1.03	-11.86
Independence Fjord	31.17	32.59	15	20	60.4	-10.72 to 10.41	-5.77 to 8.33	-11.71
KMJ	27.24	27.39	14	20	58.5	-8.21 to -0.050	-3.99 to 5.55	-11.86
Nord Sea	29.24	28.94	96	Negative	61.9	-9.27 to -0.610	-5.77 to 4.07	-11.70
UNCLOS 06	20.89	20.98	46	16	56.1	-15.37 to 20.63	-5.43 to 6.81	-11.97
UNCLOS 09	22.60	21.79	65	50	58.3	-25.29 to 1.37	-2.17 to 3.28	-11.97
Uncertainty	0.05	0.15	0.1	1 to 3	20	5	-	-

Table 1: Mean ellipsoidal height (\bar{h}), mean EGM08 geoid (\bar{N}), antenna height (h_{AH}), freeboard of the sea-ice (h_{FB}), dynamic topography (h_{DT}), inverse barometric effect (h_{IBE}), solid earth tides (h_{tide}), and permanent (mean) tide correction (h_{perm}).

GPS tides versus AOTIM-5 tide model

The SSH given by Equation (1) and Eq. (2), were calculated together with the difference between the two SSH values h_{error} (Table 2).

Site	Eq. (1) h_{SSH} (m)	Eq. (2) h_{SSH} (m)	$h_{error}(SSH)$ (m)
GreenArc	28.29	28.60	0.31
Independence Fjord	32.54	33.06	0.52
KMJ	27.40	27.80	0.19
Nord Sea	29.29	29.35	0.06
UNCLOS 06	20.98	21.40	0.42
UNCLOS 09	22.16	22.13	0.03

Table 2

The ocean tide (including the load tide) is extracted from Eq. (1) and (2). The resulting GPS tidal heights in the mean-tide system, are shown in Figure 3 (red), and plotted together with the predicted vertical component of the tides from the AOTIM-5 tide model (blue).

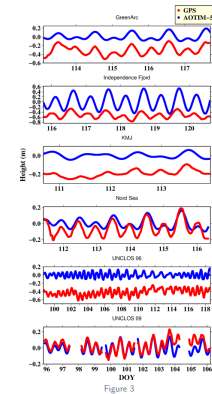


Figure 3

Tidal analysis

Tidal analysis of the GPS tides was made by a least squares harmonic analysis routine *t.tide* [4]. Combining the M_2 amplitude and phase gives a Root Sum of Squares (RSS) of 3.2 cm (GreenArc), 30.4 cm (Independence Fjord), 1.71 cm (KMJ), 5.8 cm (Nord Sea), 5.5 cm (UNCLOS 06), and 2.3 cm (UNCLOS 09). This demonstrates, that we can estimate the accuracy with less than 6 cm in the Arctic basin. In the Independence Fjord site, AOTIM-5 does not work well - likely a result of missing tide information and depth of the ocean floor in the fjord.

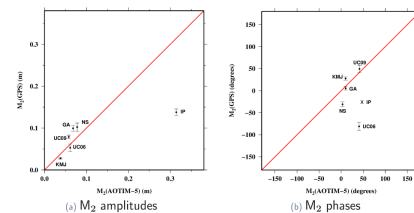


Figure 4: M_2 amplitudes, and (b) M_2 phases of the GPS tides plotted against AOTIM-5 from the six sites GreenArc (GA), Independence Fjord (IF), KMJ, Nord Sea (NS), UNCLOS (UC) 06 and 09.

Conclusions

- It is possible to interpolate the ellipsoidal height from GPS to the vertical tidal defined zero level, with an offset of 3 to 52 cm.
- The large offsets are due to errors in the geoid, gps processing, DT and/or measurement errors in the freeboard and antenna height.
- Furthermore, we were able to reproduce the ocean and load tide from the six GPS sites, compared with the tide model AOTIM-5.
- The total amplitude of the GPS tides was dampened due to sea-ice.
- The tide model AOTIM-5 seems to work well over sea-ice covered areas, but is lacking in fjord systems.
- Greater accuracy and longer time series are needed, and hopefully this will be achieved when the SATICE project is realized.

Acknowledgement

We thank Jørgen Skaffte, and the Danish UNCLOS project, for running the GPS stations north of Alert. The authors also acknowledge the discussions and comments by Ole B. Andersen from DTU Space on the tidal analysis.

References

- [1] S. J. Prinsenberg. Damping and phase advance of the tide in western Hudson Bay by the annual ice cover. *J. Phys. Oceanogr.*, 18(11):1744–1751, 1988.
- [2] S.K. Rose, H. Skourup, and R. Forsberg. Arctic Tides from GPS on Sea-ice. *J. Geodyn.*, 2012. IN PRESS.
- [3] N.K. Pavlis, S.A. Holmes, S.C. Kenyon, and J.K. Factor. An earth gravitational model to degree 2160: Egm2008. *EGU General Assembly*, pages 13–18, 2008.
- [4] R. Pawlowicz, B. Beardsley, and S. Lentz. Classical tidal harmonic analysis including error estimates in matlab using *t.tide*. *Computers & Geosciences*, 28(8):929–937, 2002.

C51A-0763: Assessment of Lead Discrimination from CryoSat-2

Stine K. Rose^{1*}, Laurence Connor², Thomas Newman^{2,3}, Walter H.F. Smith², Sinead L. Farrell^{2,3}, Rene Forsberg¹

¹Div. of Geodynamics, DTU Space, National Space Institute, Kgs. Lyngby, Denmark.

²NOAA Laboratory for Satellite Altimetry, College Park, MD.

³Cooperative Institute for Climate and Satellites, Earth System Science Interdisciplinary Center (ESSIC), University of Maryland, College Park, MD.

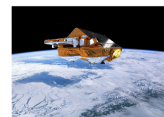
*E-mail: stine@space.dtu.dk

DTU Space
National Space Institute



Introduction

Sea ice is strongly affecting the global climate, and the sea ice extent has been monitored by satellites since 1979 [1]. In order to estimate the Arctic sea ice volume, ice thickness must be determined. Measurements of sea ice thickness are, however, difficult to achieve as they encounter limitations due to spatial and temporal variability. The measurements of sea ice freeboard may be used to estimate sea ice thickness, when combined with examination of leads between ice floes to determine the local sea surface height. With CryoSat-2 (CS), we have the opportunity to measure much more of the Arctic Ocean due to its high sampling rate and geographical coverage to 88°N/S. Validation of the CS retrievals are very important for verifying the derived sea ice thickness and understanding the associated error sources.



(a) Illustration of CryoSat-2.



(b) Operation IceBridge logo.
Figure 1

This study

- We present a comparative analysis of CS elevations with the Operation IceBridge (OIB) Airborne Topographic Mapper (ATM) laser altimeter data gathered on April 2, 2012, where the NASA P-3 completed an underflight of CS orbit number 10520 north of Alert, Nunavut, Canada.
- We present a lead detecting algorithm, which was developed using the CS Level1b (L1b) waveforms, and we analyze its capabilities via comparisons with Envisat's ASAR imagery, OIB Digital Mapping System (DMS) L1B geolocated and orthorectified imagery and ATM elevations.
- Using CS L1b waveforms we have developed a method to find misplaced CS Level 2 (L2) elevations and correct them to remove any elevation bias.
- All data have been corrected for sea ice drift, however the drift in the study area was minor.

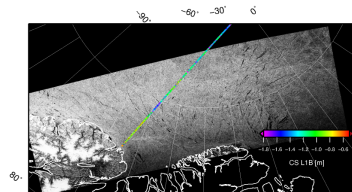


Figure 2: ASAR image over study area with CS track.

CryoSat overlaying an Envisat ASAR image

The CS elevations are obtained by a 75% threshold re-tracker. The elevations are given w.r.t. the EGM08 geoid, and corrected for atmospheric and geophysical parameters.

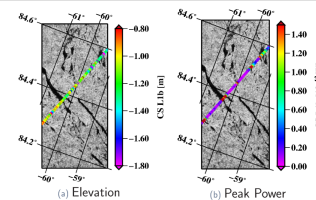


Figure 3:

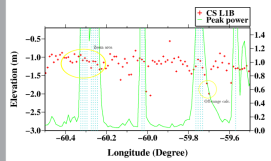


Figure 4:

When the peak power is very large it is an indication of a specular surface, i.e. a (re-frozen) lead. Peak power $> 1.5 \cdot 10^{-12} W$ is marked in Fig 4 with blue dots. CS clearly sees the lead (Fig. 3b), but the retracked height

is not realistic. Also beam parameters (not shown), are good indicators of a lead, e.g. a stack kurtosis > 50 indicates a lead.

CryoSat versus Operation IceBridge's ATM

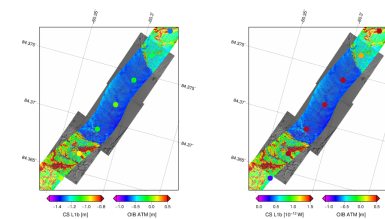


Figure 5: CS elevations and peak power overlaid DMS images of a refrozen lead.

- The OIB ATM data are averaged to be comparable with CS points.
- ATM data are average by dividing the data into blocks of 25 m, after which a near neighborhood routine is used to grid the data within a search radius of 200 km. Finally, the CS locations are tracked in the grid.
- ATM data are corrected for EGM08, Inverse Barometric effect, Ocean tide, Long Periodic Tide, Solid Earth tide (as the CS data.)
- The CS and ATM elevation color scales are of same length.

CryoSat versus Operation IceBridge's ATM... continued

- CS not corrected for snow. Following [2], one could apply a snow model over multi year ice, and half the snow model over first year ice.

- CS offset by approx. 1 m, snow layer is not the whole answer!

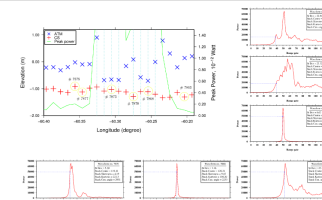


Figure 6: Expansion of Fig. 5, and six selected waveforms.

Off-range calculation

The CS L2 elevation is off-ranging, when the first peak is short followed by a tall peak. This is probably due to a lead off-nadir, calculated to 3.4 km away from nadir, which is still in the CS footprint. By making a simple calculation of the distance between the first and second peak, the CS2 elevation is corrected. The numbered yellow circles represent the waveforms below. An other example of off-ranging data,

which has not been corrected in the L1b product is shown in a yellow circle in Fig. 4. These are artifacts from the lead close by.

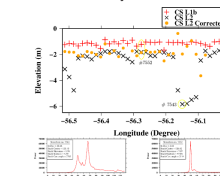


Figure 7: CS L1b, L2, and corrected L2 elevations.

Conclusions

- Leads are detected in CS data by looking at the peak powers greater than $1.5 \cdot 10^{-12} W$. Also, the beam parameters are good indicators of leads.
- The retracker needs to be improved!
- The averaged OIB ATM data can data also detect leads.
- CS L2 data are in this stage not useful.

Acknowledgement

The authors thank NASA Wallops Flight Facility for processing and providing the ATM and DMS data. ESA for applying Envisat and CS data. The authors also thank Roberto Saldo from DTU Space, who have provided the drift data.

References

- [1] JC Comiso, P. Wadhams, WB Krabill, RN Swift, JP Crawford, and WB Tucker III. Top/bottom multisensor remote sensing of Arctic sea ice. *J. Geophys. Res.*, 96(C2):2693-2709, 1991.
- [2] S.L. Farrell, N. Kurtz, L.N. Connor, B.C. Elder, C. Leuschen, T. Markus, D.C. McAdoo, B. Panzer, J. Richter-Menge, and J.G. Sonntag. A first assessment of icebridge snow and ice thickness data over arctic sea ice. *IEEE T Geosci Remote*, 50(5):2098-2111, 2012.